DISSIPATIVE PROCESSES IN SUPERCONDUCTING NANODEVICES: NANOWIRE-RESONATORS, SHUNTED NANOWIRES, AND GRAPHENE PROXIMITY JUNCTIONS

BY

MATTHEW W. BRENNER

DISSERTATION

Submitted in partial fulfillment of the requirements
for the degree of Doctor of Philosophy in Physics
in the Graduate College of the
University of Illinois at Urbana-Champaign, 2011

Urbana, Illinois

Doctoral Committee:

Professor Russell W. Giannetta, Chair
Professor Alexey Bezryadin, Director of Research
Professor Paul G. Kwiat
Professor Anthony Leggett

Abstract

The topic of superconducting nanowires has recently been an interesting field of research which has included the study of the superconductor to insulator transition (SIT), the observation of macroscopic quantum behavior such as quantum phase slips (QPS), and the potential use of nanowires as qubits. Superconducting coplanar microwave waveguide resonators have also become a popular way of studying superconducting junctions and qubits, as they provide an extremely low noise environment. For example, superconducting two-dimensional Fabry-Perot resonators have been used by other groups to make non-demolition measurements of a qubit. The motivation of this thesis will be the merging of the fields of superconducting nanowires and the technique of using superconducting microwave resonators to study junctions by incorporating a nanowire into the resonator itself at a current anti-node. By doing this, the nonlinear effects of the nanowire can be studied which may find application in single photon detectors, mixers, and the readout of qubits. We also employ the technique of molecular templating to fabricate some of the thinnest superconducting nanowires ever studied (down to ~ 5 nm in diameter in some cases).

In this thesis, we extend the understanding of the nonlinear properties of a nanowire-resonator system and investigate a new type of nonlinearity that involves a pulsing regime between the superconducting and normal phases of the nanowire. We develop a model, which describes the results quantitatively and by modeling the system, we are able to extract information regarding the relaxation time of the nanowire back into the superconducting state. We also study double nanowire-resonator systems where two closely spaced parallel nanowires

interrupt the resonator center conductor and form a loop where vortex tunneling processes can occur. Using a double nanowire-resonator we are able to observe the Little-Parks effect at low temperatures (where the resistance of the wires is immeasurably low) and are able to confirm the multivalued nature of the current phase relationship (CPR) in nanowires. Additionally, we observe an anomalous transmission regime where the periodic pulsing is replaced by stochastic amplitude fluctuations.

In addition to microwave measurements on nanowires, we also study the normal state in resistively shunted nanowires with dc measurements where the inclusion of a shunt resistor is observed to change the nature of the normal state from the Joule heated state to a state that preserves phase coherence. Finally, the statistics on switching current events in graphene proximity junctions are analyzed and compared to the well known results for Josephson junctions. Only thermal activation (and no macroscopic quantum tunneling) is observed in graphene proximity superconducting junctions down to temperatures of ~ 300 mK.

To my family.

Acknowledgements

There are many people who have assisted me in many ways and without their help, this dissertation could not have been completed. First, I would like to thank my advisor Alexey Bezryadin who helped me each step of my journey through my research career so far. In particular, he has helped come up with many interesting ideas and has taught me countless experimental techniques as well as guided me in how to analyze data and present results in a clear and understandable way. I would also like to thank some of the older Alumni of our group: Tony Bollinger, Ulas Coskun, David Hopkins, and Andrey Rogachev for training me in nanowire fabrication, measurement techniques, data analysis, and teaching me how to program in Labview. Additionally, I would also like to thank Thomas Aref, Mitrabhanu Sahu, Jaseung Ku, Myung-Ho Bae who have spent countless hours with me in fruitful discussions, teaching me new experimental techniques, and training me on various instruments. I also would like to thank Andrey Belkin, Robert Dinsmore, Mikeas Remeika, Bob Colby, C. J. Lo, Anil Nandyala, Sean Daugherty, Emily Sprague, and Thomas Hymel, who have also provided many ideas, answers, encouragement, and an enjoyable atmosphere in the lab. I would also like to thank Paul Goldbart, Nayana Shah, and Sarang Gopalakrishnan for their input and discussions and help in understanding the physics of some of my experiments. The sample fabrication was an integral part of my research and could not have been completed without the help of the Materials Research Laboratory staff. Many of the staff members spent numerous hours patiently training me and giving me advice. Therefore I would like to thank Tony Banks, Vania Petrova, Mike Marshall, Bharat Sankaran, and Kevin Colravy. I also could not have completed this work

without the constant support of my family and friends and for always encouraging me in my difficult times. Finally, I would like to thank God for his constant gifts of grace and love that have enabled me to complete this thesis. This work was supported by the U.S. Department of Energy under Grant No. DE-FG0207ER46453. This work was carried out in part in the Frederick Seitz Materials Research Laboratory Central Facilities, University of Illinois, which are partially supported by the U. S. Department of Energy under Grant Nos. DEFG0207ER46453and DE-FG0207ER46471.

Table of contents

Chapter 1

Introduction

The physics of superconducting nanowires has recently been an interesting field of research. In particular, nanowires have been applied as photon-number-resolving-detectors [1, 2, 3] and have been proposed as candidates to be used in current standard applications [4]. Other exotic behavior interesting to the subject of nanowires are the superconductor to insulator transition (SIT), the observation of macroscopic quantum behavior such as quantum phase slips (QPS), and the use of QPS in nanowires to achieve qubit devices [4, 5]. The SIT, which has been proposed and observed on Josephson junctions [6, 7, 8, 9, 10, 11, 12, 13], has also been observed with nanowires [14, 15, 16, 17, 18] where the normal state resistance of the nanowire is one such parameter that has been observed to control the state of the nanowire. The SIT is characterized by the change in behavior of the resistance as the temperature is lowered. In superconducting nanowires, the resistance decreases according to the Arrhenius law as the temperature is reduced and finally goes to an infinitesimally low value at zero temperature. In contrast, the resistance of insulating nanowires increases as the temperature is decreased. In short nanowires, like those studied in this thesis, the transition from the superconducting to insulating state is observed to be a sharp function of the quantum resistance for Cooper pairs $R_Q = h/4e^2$. If the normal state resistance is less than R_Q, the wire is observed to be superconducting at low temperature and if the normal state resistance of the nanowire is greater than R_Q, the wire is observed to be insulating. While the observation of the SIT can clearly be noticed from the resistance versus temperature (R vs. T) curves, the exact nature of the insulating state is still not clearly

understood. In thin inhomogeneous wires, the insulating state can arise due to oxidation of the metal resulting in granularities or non-uniformity. However, even in homogeneous junctions, the insulating state can arise. This could occur to do the Coulomb interaction [19, 20] or weak localization [21], which results in the complete destruction of superconductivity by driving T_c to zero. The insulating state can also arise due to the loss of coherence due to QPS and thus the capacity for a supercurrent to flow [13, 22, 23]. Thus, the exact nature of the SIT in short MoGe still remains an unsolved and open question.

The topic of QPS in nanowires is a continuation of the work introduced by Leggett [24] to study macroscopic quantum behavior. Most observations of QPS in nanowires have been carried out by the observation of a resistive tail in the resistance vs. temperature plots of superconducting nanowires [25, 26, 27, 28, 29, 30]. However, to add controversy to the existence of QPS in nanowires, not all nanowires, especially homogeneous short nanowires, show a resistive tail [17, 18, 31, 32, 33]. The resistive tails in longer nanowires have also been attributed to inhomogeneities [34] in the nanowire or to noise in the experimental setup. Also, unlike Josephson junction where there is an insulating oxide barrier to tunnel through, no such obvious barrier exists in nanowires. This has fueled the debate over whether QPS exist in short nanowires. A conclusive demonstration of macroscopic quantum tunneling (MQT) in Josephson junctions was done by Martinis, Devoret, and Clark [35] where excellent agreement between the measured switching current statistics and an MQT model for Josephson junctions was observed. Additionally, the predicted splitting of the switching current distribution was observed when the frequency of the driven microwave radiation matched the energy splitting between the two discrete quantum states. To date, no such demonstration in nanowires has been reported. However, Sahu *et al*. [36] have adopted the method of analyzing switching currents to observe

QPS in nanowires. At high temperatures they were able to fit their switching current distributions with a model involving only thermally activated phase slips (TAPS), while at low temperatures they had to include QPS to account for the data. They were not able to measure the distribution splitting with an applied microwave source because the plasma frequency in nanowires is ~ 100 GHz where microwave engineering becomes difficult. The debate over QPS in nanowires was advanced one more step though the experiments of T. Aref [37] where he observed a region of saturation of the standard deviation as a function of temperature of the switching currents at low temperatures indicating the presence of QPS. The presence of QPS in superconducting nanowires still remains a debate as the observations could be related to noise in the experimental setup and there is still a lack of a more definitive proof of QPS such as the switching current distribution splitting.

The field of superconducting coplanar microwave waveguide resonators has become a popular way of studying superconducting junctions (including nanowires) as they offer novel techniques to probe various classical and quantum properties of the junctions. Superconducting microwave transmission lines have been introduced by Anderson *et al*. [38] and can be transformed, by making two interruptions in the center conductor, into a superconducting Fabry-Perot resonator (SFPR) with a high quality factor, Q ≈ 500,000 [39, 40]. SFPRs have been developed for the purpose of measuring the impedance and rf surface resistance of high-T_c thin films [41,42]. Additionally, Josephson junctions have been coupled to SFPRs and showed microwave emission and voltage steps corresponding to the modes of the resonator [43, 44]. Because there are no leads attached to the SFPR, as there is a capacitive coupling (and because the signal can be filtered with attenuators against unwanted noise), there is expected to be low noise in the SFPR, which is ideal for the study of QPS and other quantum phenomena which can

lose coherence from the presence of environmental noise. Two of the most exciting applications of SFPRs is their use in making non-demolition measurements of a qubit [39, 45] and in the possible fabrication of qubits [33, 46]. A SFPR can be used to make a qubit by introducing a Josephson junction or nanowire as a nonlinear inductive element (see Fig. 1.1), where the inductance is dependent on the supercurrent amplitude [46, 47]. Without the nonlinear inductor, the SFPR has equally spaced energy levels and cannot be used as a qubit, but with its inclusion, it forces the energy spectrum to be anharmoic and can be used as a qubit if the anharmonicity is such that it satisifies the relationship [46] $\delta\omega/N > \Gamma$, where $\delta\omega$ is the maximum shift in the resonance frequency, N is the number of photons in the cavity corresponding to the shift, and Γ is the bandwidth at -3 dB from the maximum transmission value.

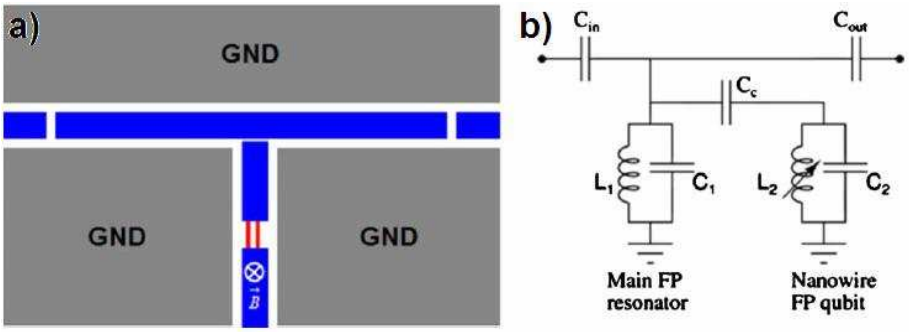

Figure 1.1: (a) Schematic of a nanowire-SFPR based qubit design proposed by J. Ku et al. [46]. The nanowires in the center act as a nonlinear inductor resulting in an anharmonic energy level spacing allowing the device to be used as a qubit. Two nanowires are used to tune the critical current [48, 49] allowing the anharmonicity to be controlled. The main resonator (top) is used in the "readout" scheme. (b) The simplified equivalent circuit of the qubit and main SFPR "readout" device. This figure is taken from [46].

The motivation of this thesis will be the merging of the fields of superconducting nanowires and SFPRs by incorporating a nanowire into the resonator itself at a current anti-node. The technique of introducing a nanowire in a SFPR offers a chance to observe nanowire physics

in a new way and also new nanowire physics that could not be observed previously in DC measurements. It allows the possibility of a low noise level environment for the observation of QPS in new ways that couple with the resonator modes. The nanowire-resonator systems can, in principle, be cooled to the cavity QED regime, as the following heuristic argument shows. The r.m.s. amplitude of the antinodal current corresponding to a single photon is given by the equipartition theorem $\left\langle LI^2/2 \right\rangle = \hbar\omega_0/2$: here, ω_0 is the resonator's natural frequency ($\omega_0/2\pi$ = 10 GHz) and L = 1 nH is the order of magnitude of a typical circuit inductance, corresponding to an impedance of Z_0 = 50 Ω). For these values, $I_{\text{r.m.s.}} \approx \omega_0\sqrt{\hbar/Z_0} \cong 100$ nA , which is of the same order of magnitude as the critical current of a nanowire: e.g., a critical current of ~200 nA was previously reported [50, 51]. Thus, the *quantum* regime is, in principle, achievable [46]. This regime would, e.g., feature coherent superpositions of states having distinct currents and cavity-photon numbers and be useful in making a nanowire-based qubit.

Another interesting effect of a SFPR-nanowire system is the generation of large nonlinearities. Nonlinear effects in the microwave regime of superconductors can be used to study quantum squeezing [52, 53, 54] and the dynamical Casimir effect [55] and may also find application in single-photon detectors [56], mixers [57, 58], and the readout of qubits [59, 60, 61]. Strong nonlinear effects have been observed in microbridges in SFPRs [62, 63] including the observation of amplification via intermodulation gain, period doubling [63], and strong coupling between modes [64]. Thus, the investigation of strong nonlinearities may lead to new interesting physics and applications. By incorporating a nanowire in a SFPR, J. Ku *et al.* has already identified some nonlinear properties of the system such as a Duffing behavior [46]. In this thesis, we extend the understanding of the nonlinear properties of a SFPR-nanowire system and investigate a new type of nonlinearity that involves a pulsing regime between the

superconducting and normal phases of the nanowire. By modeling the system, we are able to extract information regarding the relaxation time of the nanowire back into the superconducting state. We also study double nanowire-SFPR systems where two closely spaced parallel nanowires interrupt the resonator center conductor and form a loop where vortex tunneling processes can occur. Using a double nanowire-SFPR we are able to observe the Little-Parks [65, 66] effect at low temperatures (where the resistance of the wires is immeasurably low) and are able to confirm the multivalued nature of the current phase relationship (CPR) in nanowires. Additionally, we observe an anomalous transmission regime where the extreme nonlinear pulsing is replaced by stochastic amplitude fluctuations. Thus, the placing of a nanowire inside a resonator is demonstrated to reveal new physics and new ways of understanding superconducting nanowires.

The organization of the thesis will now be described. In chapter 2, the basic nanowire and resonator theory is described and in some cases derived. The theory presented in this chapter will be used throughout the remaining chapters in the thesis. Chapter 3 contains the fabrication and measurement techniques used to make and measure the nanowires for both the DC and microwave type samples. The single nanowire-SFPR samples are discussed in chapter 4 including a description of the pulsing state observations with the corresponding model and fits, which give information about the relaxing process of the nanowire back into the superconducting state. Chapter 5 continues the investigation of the nanowire based resonator, except that in this chapter, we focus on double nanowire-SFPRs and study vortex thermal activation, the Little-Parks effect at low temperatures, the multivalued nature of the CPR, and the anomalous transmission effect, which occurs at half flux quantum values of the magnetic field. In chapter 6, we switch from microwave to DC measurements of nanowires. Here we study the effect of

adding an external resistive shunt to nanowire(s). We observe trends consistent with an increased dissipation and a crossover from a joule heated normal state (JHNS) to a state that preserves phase coherence. In Chapter 7, we present the statistics on switching current events in graphene proximity junctions and compare them to the well known results for Josephson junctions.

---

[1] Aleksander Divochiy, Francesco Marsili, David Bitauld, Alessandro Gaggero, Roberto Leoni, Francesco Mattioli, Alexander Korneev, Vitaliy Seleznev, Nataliya Kaurova, Olga Minaeva, Gregory Gol'tsman, Konstantinos G. Lagoudakis, Moushab Benkahoul, Francis Lévy & Andrea Fiore, Nature Photonics **2,** 302 (2008).
[2] A.J. Kerman, E. A. Dauler, W. E. Keicher, J. K. W. Yang, K. K. Berggren, G. Gol'tsman, B. Voronov, Appl. Phys. Lett. **88,** 111116 (2006).
[3] A D Semenov, P Haas, B Günther, H-W Hübers, K Il'in, M Siegel, A Kirste, J Beyer, D Drung, T Schurig and A Smirnov, Supercond. Sci. Technol. **20**, 919 (2007).
[4] Mooij J E and Nazaron Y V, Nature Physics **2,** 169 (2006).
[5] J. E. Mooij and C. J. P. M. Harmans, New J. Phys. **7**, 219 (2005).
[6] A. Schmid, Phys. Rev. Lett. **51,** 1506 (1983).
[7] S. A. Bulgadaev, JETP Lett. **39,** 315 (1984).
[8] S. Chakravarty, Phys. Rev. Lett**. 49,** 681 (1982).
[9] J.S. Penttilä, Ü. Parts, P. J. Hakonen, M. A. Paalanen, E. B. Sonin, Phys. Rev. Lett. **82,** 1004 (1999).
[10] D. Meidan, Y. Oreg and G. Refael, Phys Rev. Lett. **98**, 187001 (2007).
[11] H. P. Büchler, V. B. Geshkenbein, G. Blatter, Phys. Rev. Lett**. 92**, 067007 (2004).
[12] P. Werner and M. Troyer, Phys. Rev. Lett. **95**, 060201 (2005).
[13] A. D. Zaikin, D. S. Golubev, A. van Otterlo, G. T. Zimányi, Phys. Rev. Lett. **78**, 1552 (1997).
[14] F. Sharifi, A. V. Herzog, and R. C. Dynes, Phys. Rev. Lett. **71**, 428 (1993
[15] P. Xiong, A. V. Herzog, and R. C. Dynes, Phys. Rev. Lett. **78**, 927 (1997).
[16] A. Bezyradin, C. N. Lau, and M. Tinkham, Nat. **404**, 971 (2000).
[17] A. T. Bollinger, R. C. Dinsmore III, A. Rogachev, and A. Bezyradin, Phys. Rev. Lett. **101**, 227003 (2008).
[18] A. Rogachev and A. Bezryadin, Appl. Phys. Lett. **83**, 512 (2003).
[19] Y. Oreg and A. M. Finkel'stein, Phys. Rev. Lett. **83**, 191 (1999).
[20] H. Ebisawa, H. Fukuyama, and S. Maekawa, J. Phys. Soc. Jpn. **55**, 4408 (1986).
[21] Y.-J. Kim and K. J. Chang, Mod. Phys. Lett. B **12**, 763 (1998).
[22] N. Giordano, Phys. Rev. Lett. **61**, 2137 (1988).
[23] D. S. Golubev, and A. D. Zaikin, Phys. Rev. B **64**, 014504 (2001).
[24] A. J. Leggett, Prog. Theor. Phys. (Suppl.), **69**, 80 (1980).
[25] C. N. Lau, N. Markovic, M. Bockrath, A. Bezryadin, and M. Tinkham, Phys. Rev. Lett. **87**, 217003 (2001).
[26] N. Giordano, Phys. Rev. Lett. **61**, 2137 (1988).
[27] N. Giordano, Phys. Rev. Lett. **43**, 160 (1991).
[28] M. Zgirski, K.-P. Riikonen, V. Touboltsev, and K. Arutyunov, Nano Lett. **5**, 1029 (2005).
[29] M. Zgirski, K.-P. Riikonen, V. Touboltsev, and K. Arutyunov, Phys. Rev. B **77**, 054508 (2008).
[30] F. Altomare, A. M. Chang, M. R. Melloch, Y. Hong, and C. W. Tu, Phys. Rev. Lett. **97**, 017001 (2006).
[31] A. Rogachev, A. T. Bollinger, and A. Bezryadin, Phys. Rev. Lett. **94**, 017004 (2005).
[32] A. T. Bollinger, A. Rogachev, A. Bezryadin, EuroPhys. Lett. **76**, 505 (2006).
[33] A. Bezryadin, J. Phys.:Condens Matter **20,** 043202 (2008).
[34] A. T. Bollinger, A. Rogachev, M. Remeika, and A. Bezryadin, Phys. Rev. B **69**, 180503 (2004).
[35] J. M. Martinis, M. H. Devoret, and J. Clarke, Phys. Rev. B **35**, 4682 (1987).
[36] M. Sahu, M.-H. Bae, A. Rogachev, D. Pekker, T.-C. Wei, N. Shah, P. M. Goldbart, and A. Bezryadin, Nature Physics **5**, 503-508 (2009).
[37] T. Aref, PhD thesis, *University of Illinois at Urbana-Champaign* (2010).
[38] A. C. Anderson, R. S. Withers, S. A. Reible, and R. W. Ralston, IEEE Trans. Magn. **MAG-19**, 485 (1983).

[39] A. Wallraff, D. Schuster, A. Blais, L. Frunzio, R.-S.Huang, J. Majer, S. Kumar, S. M. Girvin, and R. J. Schoelkopf, Nature (London) **431,** 162 (2004).
[40] L. Frunzio, A. Wallraff, D. Schuster, J. Majer, and R. Schoelkopf, IEEE Trans. App. Supercond. **15**, 860 (2005).
[41] D. E. Oates, P. P. Nguyen, Y. Habib, G. Dresselhaus, M. S. Dresselhaus, G. Koren, and E. Polturak, Appl. Phys. Lett. **68,** 705 (1996).
[42] M. S. DiIorio, A. C. Anderson, and B. Y. Tsaur, Phys. Rev. B **38**, 7019 (1988).
[43] H. D. Jensen, A. Larsen, and J. Mygind, IEEE Trans. Magn. **27**, 3355 (1991).
[44] A. Larsen, H. D. Jensen, and J. Mygind, Phys. Rev. B **43**, 10179 (1991).
[45] R. J. Schoelkoph and S. M. Girvin, Nat. **451**, 664 (2008).
[46] J. Ku, V. Manucharyan, and A. Bezryadin, Phys. Rev. B **82**, 134518 (2010).
[47] E. Boaknin, V. Manucharyan, S. Fissette, M. Metcalfe, L. Frunzio, R. Vijay, I. Siddiqi, A. Wallraff, R. Schoelkopf, and M. H. Devoret, arXiv: 0702445 (2007).
[48] D. S. Hopkins, D. Pekker, P. M. Goldbart, and A. Bezryadin, Science **308**, 1762 (2005).
[49] D. Pekker, A. Bezryadin, D. S. Hopkins, and P. M. Goldbart, Phys. Rev. B **72**, 104517 (2005).
[50] A. Bezryadin, A. Bollinger, D. Hopkins, M. Murphey, M. Remeika, and A. Rogachev, "Superconducting Nanowires Templated by Single Molecules," review article in *Dekker Encyclopedia of Nanoscience and Nanotechnology*, James A. Schwarz, Cristian I. Contescu, and Karol Putyera, eds. (Marcel Dekker, Inc. New York, 2004), 3761–3774.
[51] T. Aref and A. Bezryadin, arXiv:1006.5760v2 (2011).
[52] R. Movshovic, B. Yurke, P. G. Kaminsky, A. D. Smith, A. H. Silver, R. W. Simon, and M. V. Schneider, Phys. Rev. Lett. **65**, 1419 (1990).
[53] B. Yurke and E. Buks, J. Lightwave Technol. **24**, 5054 (2006).
[54] E. Buks and B. Yurke, Phys. Rev. A **73**, 023815 (2005).
[55] E. Arbel-Segev, B. Abdo, O. Shtempluck, and E. Buks, quant-ph/0606099 (2006).
[56] G. N. Goltsman, A. Korneev, I. Rubtsova, I. Milostnaya, G. Chulkova, O. Minaeva, K. Smirnov, B. Voronov, W. Sysz, A. Pearlman, A. Verevkin, and R. Sobolewski, Phys. Status Solidi C **2**, 1480 (2005).
[57] A. Skalare, W. R. McGrath, B. Bumble, H. G. LeDuc, P. J. Burke, A. A. Verheijen, R. J. Schoelkoph, and D. E. Prober, Appl. Phys. Lett. **68**, 1558 (1996).
[58] F. D. Wilms, E. Miedema, T. M. Klapwijk, and J. R. Gao, Appl. Phys. Lett. **74**, 433 (1999).
[59] I. Siddiqi, R. Vijay, F. Pierre, C. M. Wilson, M. Metcalfe, C. Rigetti, L. Frunzio, and M. H. Devoret, Phys. Rev. Lett. **93**, 207002 (2004).
[60] K. Wiesenfeld and B. McNamara, Phys. Rev. A **33**, 629 (1986).
[61] J. C. Lee, W. D. Oliver, T. P. Orlando, and K. K. Berggren, IEEE Trans. Appl. Supercond. **15**, 841 (2005).
[62] E. Segev, B. Abdo, O. Shtempluck, and E. Buks, J. Phys.: Condens. Matter **19**, 096206 (2007).
[63] E. Arbel-Segev, B. Abdo, O. Shtempluck, and E. Buks, cond-mat/0607262 (2006).
[64] E. Arbel-Segev, B. Abdo, O. Shtempluck, and E. Buks, cond-mat/0607259 (2006).
[65] W. A. Little and R. D. Parks, Phys. Rev. Lett. **9**, 9 (1962).
[66] W. A. Little and R. D. Parks, Phys. Rev. **133**, A97 (1963).

Chapter 2

Theory

It is our objective in this chapter to present the foundational theoretical background of Josephson junctions and quasi one-dimensional superconducting nanowires necessary to understand the experimental results presented in this thesis. Superconductivity arises when some fraction of electrons pair up due to an attractive interaction. The superconducting state can be understood through the theory of Bardeen, Cooper, and Schrieffer (the BCS theory) at its microscopic level [1]. However, a simpler limiting case of the BCS theory formulated to allow a theoretical analysis of a superconductor whose superconducting gap contains an inhomogeneous spatial profile, was developed by Ginzburg and Landau [2] and later reformulated by Gor'kov [3]. The Ginzburg and Landau (GL) theory is a mean field theory and only valid close to the superconducting transition temperature T_c. Within the GL theory, the phenomena of phase slips [4] in one-dimensional superconductors can be characterized, which give rise to resistance even below T_c. These phase slips can either be thermally induced or can occur by quantum tunneling through the energy barrier. In this thesis, measurements are sometime performed on nanowires interrupting the center of a superconducting coplanar waveguide resonator. Thus, some basic resonator theory is also presented in this section.

2.1 Ginzburg-Landau theory and phase slips

The collection of paired electrons are called Cooper pairs and are bosons (i.e. spin-1 particles) and the condensate is their collective energy state. In GL theory, the superconducting condensate can be described by a pseudowavefunction called the complex order parameter,

$$\psi = |\psi| e^{i\phi}, \tag{2.1}$$

where $|\psi|$ is the amplitude and ϕ is the phase of the order parameter. The density of superconducting electrons is given by: $n_s = |\psi^2|$, which is zero above the critical temperature T_c. Assuming that ψ is small and varies slowly in space, the GL free energy per unit volume can be expanded in a series such that:

$$f = f_{no} + \alpha|\psi|^2 + \frac{\beta}{2}|\psi|^4 + \frac{1}{2m^*}\left|\left(\frac{\hbar}{i}\nabla - \frac{e^*}{c}\mathbf{A}\right)\psi\right|^2 + \frac{h^2}{8\pi}, \tag{2.2}$$

where f_{no} is the free energy density of the normal state in the absence of any fields, $m^* = 2m$ is the mass of a Cooper pair, $\hbar$ is Planck's constant divided by 2π, $e^* = 2e$ is the Cooper pair charge, c is the speed of light, $\mathbf{A}$ is the vector potential, and h is the magnetic field density. The parameters α and β are temperature-dependent expansion constants which are defined as follows:

$$\alpha(T) = -\frac{e^{*2}}{m^* c^2} H_c^2(T) \lambda_{eff}^2(T) \tag{2.3}$$

$$\beta(T) = \frac{4\pi e^{*4}}{m^{*2} c^4} H_c^2(T) \lambda_{eff}^4(T) \tag{2.4}$$

$$\lambda_{eff}^2 = \frac{m^* c^2}{4\pi |\psi|^2 e^{*2}}. \tag{2.5}$$

Here, H_c is the critical magnetic field and λ_{eff} is the London penetration depth. In the absence of fields, the parameter β must be positive; however, the α parameter can change signs, which indicates that the temperature has passed through T_c. Above T_c, the minimum free energy occurs at $|\psi|^2 = 0$, corresponding to the normal state; however when α is negative, the minimum occurs when $|\psi|^2 = -\frac{\alpha}{\beta}$.

When fields are present, the order parameter is adjusted to minimize the total free energy. Eq. 2.2 can be minimized using a variational method to reveal the GL differential equations:

$$\alpha\psi + \beta|\psi|^2\psi + \frac{1}{2m^*}\left(\frac{\hbar}{i}\nabla - \frac{e^*}{c}\mathbf{A}\right)^2\psi = 0 \tag{2.6}$$

$$\mathbf{J} = \frac{e^*}{m^*}|\psi|^2\left(\hbar\nabla\phi - \frac{e^*}{c}\mathbf{A}\right) = e^*|\psi|^2\mathbf{v}_s, \tag{2.7}$$

where **J** is the supercurrent density and $\mathbf{v}_s$ is the supercurrent velocity defined by:

$$\mathbf{v}_s = \frac{\hbar}{m^*}\nabla\phi. \tag{2.8}$$

If again we take there to be no fields (**A** = 0), then the order parameter is real and we can write Eq. 2.6 in terms of a normalized wavefunction $f = \psi/\psi_\infty$, where $\psi_\infty = -\alpha/\beta > 0$:

$$\frac{\hbar^2}{2m^*|\alpha(T)|}\frac{d^2 f}{dx^2} + f - f^3 = 0. \tag{2.9}$$

Thus, a characteristic length is obvious from the above equation and can be notated as $\xi(T)$, which is the length of variation of the order parameter and is defined as:

$$\xi^2(T) = \frac{\hbar^2}{2m^*|\alpha(T)|} \propto \frac{\xi(0)}{1-t}, \qquad (2.10)$$

where $t = T/T_c$.

A one-dimensional superconductor has two of its dimensions less than the coherence length and one dimension greater than it. However, most of the nanowires studied in this thesis have a diameter between 5-25 nm and a length of ~ 100 nm while the coherence length is ~ 7 nm. Thus, strictly speaking, our nanowires are not one-dimensional. However, it has been theoretically demonstrated [5] that superconductors that have two dimensions less than 4.4ξ and one dimension greater than it, still display the properties of a one-dimensional superconductor as the dimensions are still too small to support a vortex core. We call these superconductors quasi one-dimensional superconductors and classify most of our nanowires in this category.

In dirty superconductors, (where the mean free path l satisfies $l << \xi$(T)) the GL coherence length is related to the Pippard and BCS coherence length ξ_o by:

$$\xi(T) = 0.855\frac{(\xi_o l)^{1/2}}{(1-t)^{1/2}}, \qquad (2.11)$$

where $\xi_o = \hbar v_F/\pi\Delta(0)$ is the Pippard or BCS coherence length, $\Delta(0) = 1.76k_BT_c$ and v_F is the Fermi velocity. Our nanowires, mostly made from MoGe, are in this dirty limit as they have a mean free path of ~ 3 Å and a coherence length of ~ 7 nm.

As stated before, within the GL theory, the superconducting condensate can be described by the complex order parameter, $\psi = |\psi| e^{i\phi}$, which can be plotted in polar coordinates and visualized as a wound helix oriented perpendicular to the x-axis (see Fig. 2.1). Little [4] developed the idea that fluctuations of the phase can cause the order parameter to locally go to zero at some spot along the length of the wire and create a normal core the size of ~ one coherence length. During this process, the phase across the wire changes by +/- 2π and one coil of the helix is added or subtracted (see Fig. 2.1). Due to current conservation as can be seen from Eqs. 2.7 and 2.8, the constraint $|\psi|^2 \nabla\phi = \text{constant}$ shows that when a phase slip occurs and $\psi \to 0$, the phase gradient can vary rapidly in time [6]. This results in a voltage pulse and a mechanism for the nanowire to dissipate the kinetic energy of the condensate through heat [7].

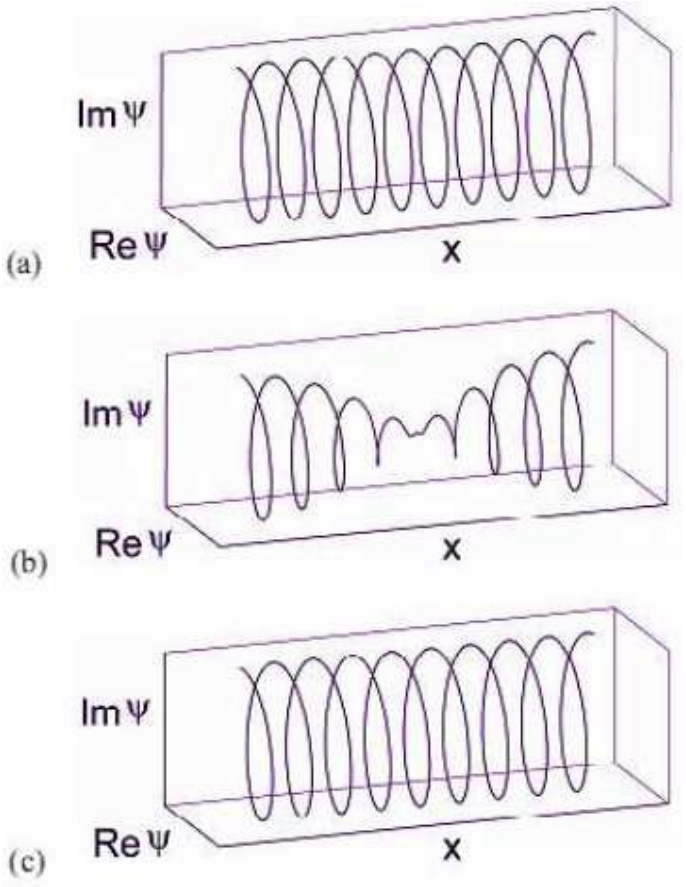

*Fig. 2.1: The chronology of a phase slip event. (a) Before the phase slip event, there are 10 coils or helical turns along the length of a wire such that the total phase difference between the ends of the wire is 10*2π = 20π. (b) The order parameter goes to zero at some point along the length of the wire causing the phase to slip by 2π. (c) After the phase slip event, one helical turn has been subtracted so that the total phase difference across the wire is now 9*2π = 18π. This picture is taken from Ref. [8].*

An applied voltage would cause a tightening of the helix as the phase increases according to:

$$\frac{d\phi}{dt} = \frac{2eV}{\hbar}. \qquad (2.12)$$

As the supercurrent is accelerated, stochastic phase slips reduce the supercurrent through the loss mechanism discussed above and the evolution of the phase is allowed without the current

reaching the critical current. Thus, the energy that is being supplied to the nanowire at a rate of IV is dissipated through heat and the wire remains in the superconducting state. This dynamic non-equilibrium steady state results in the wire having a finite resistance due to the phase slip process and this will depend on the rate of phase slips, which can be related to the voltage through the following equation: $V = \frac{\hbar}{2e} 2\pi\Gamma$. The wire resistance follows an Arrhenius type equation with a temperature-dependent free energy barrier. The free energy barrier is determined as the difference of the corresponding free energies of the wire with a constant amplitude of the order parameter and the state with a phase slip crossing the wire, namely with zero order parameter at some place on the wire. In what follows, this free energy barrier and the resistance of the nanowire due to phase slips will be derived.

2.2 Free energy barrier for phase slips in nanowires

The free energy barrier for phase slips was first calculated by Langer and Ambegaokar [6]. Using the GL theory, they found the final result that the energy barrier for a phase slip to be:

$$\Delta F(T) = \frac{8\sqrt{2}}{3} \frac{H_c^2(T)}{8\pi} A\xi(T), \qquad (2.13)$$

where H_c is the thermodynamic critical field, A is the cross sectional area of the nanowire, and ξ is the GL coherence length. This equation can be understood by considering the volume $\sim \xi A$ of a nanowire that becomes normal during a phase slip process (assuming the wire is thin enough so that the whole diameter goes normal) and then multiplying it by the condensation energy per unit volume $f_n - f_s = H_c^2/8\pi$. The result is apparent in Eq. 2.13 with an extra factor of order unity.

Near T_c, we have the following GL temperature dependencies for the critical field and the coherence length:

$$H_c(T) \propto \left(1-\frac{T}{T_c}\right) \quad \text{and} \quad \xi(T) \propto \left(1-\frac{T}{T_c}\right)^{-1/2}. \tag{2.14}$$

Thus, we can write the temperature-dependent free energy barrier as:

$$\Delta F(T) = \Delta F(0)\left(1-\frac{T}{T_c}\right)^{3/2}, \tag{2.15}$$

where

$$\Delta F(0) = \frac{8\sqrt{2}}{3}\frac{H_c^2(0)}{8\pi} A\xi(0). \tag{2.16}$$

The objective now is to derive a more useful form of $\Delta F(0)$ that can be more easily compared to the experiment and also one that reduces the number of fitting parameters. By expressing the free energy as $\Delta F(T) = \Delta F(0) f(T)$, where $f(T)$ is the temperature dependence of the free energy barrier, and relating it to the critical current and finding expressions for $H_c(T)$ and $\xi(T)$ that are valid in a wider temperature range, we will also be able to formulate a more expansive form of the free energy temperature dependence that will be valid farther from T_c than the GL theory normally allows. We begin by eliminating $H_c^2(0)$ through the GL expression for the coherence length:

$$\xi^2(T) = \frac{\hbar^2}{4m|\alpha(T)|},$$

where

$$\alpha(T) = -\frac{2e^2}{mc^2} H_c^2(T) \lambda_{eff}^2(T).$$

We can solve for $H_c^2(T)$ in these last two equations and evaluate it at zero temperature:

$$H_c^2(0) = \frac{\hbar^2 c^2}{8e^2 \xi^2(0) \lambda_{eff}^2(0)}.$$

The free energy at zero temperature is now:

$$\Delta F(0) = \frac{\sqrt{2}\hbar^2 c^2 A}{24\pi e^2 \xi(0) \lambda_{eff}^2}.$$

At this point, the effective penetration depth must be replaced. We use the effective penetration depth in the dirty limit because for MoGe $l \sim 3$ Å $<< \lambda_L(0) \sim 18.5$ nm, here $\lambda_L(0)$ is the London penetration depth at zero temperature. We now proceed as:

$$\lambda_{eff}^2(T) = \lambda_L^2(T) \frac{\xi_o}{J(0,T) l}. \qquad (2.17)$$

Evaluating this at zero temperature we have $J(0,0) = 1$ (where $J(0,T)$ is the real space Fourier transform of the BCS kernel $K(0,T)$ for the nonlocal relation between $\vec{A}$ and $\vec{J}$ evaluated at $\vec{R} = 0$), and now the free energy barrier at zero temperature is:

$$\Delta F(0) = \frac{\sqrt{2} A \hbar^2 c^2 l}{24\pi e^2 \lambda_L^2(0) \xi(0) \xi_o}.$$

Now, the London penetration depth can be eliminated by using the following equation:

$$\lambda_L^2(T) = \frac{mc^2}{4\pi n_s(T)e^2} \ . \tag{2.18}$$

Evaluating this at zero temperature we get:

$$\lambda_L^2(0) = \frac{mc^2}{4\pi ne^2}, \tag{2.19}$$

where n is the number density of normal electrons. In the limit of zero temperature, all the electrons are paired and therefore we are able to use the relation that $n = n_s(0)$. The free energy barrier now becomes:

$$\Delta F(0) = \frac{\sqrt{2}A\hbar^2 nl}{6m\xi(0)\xi_o}.$$

The next step is to replace the BCS coherence length using:

$$\xi_o = \frac{\hbar v_F}{\pi\Delta(0)}, \tag{2.20}$$

where v_F is the Fermi velocity and $\Delta(0)$ is the superconducting gap at zero temperature. So now the free energy barrier becomes:

$$\Delta F(0) = \frac{\sqrt{2}\pi\hbar Anl\Delta(0)}{6mv_F\xi(0)}.$$

Using the Drude theory, the force exerted on a normal metal can be given by the following equation:

$$m\frac{dv}{dt} = eE - \frac{mv}{\tau}, \tag{2.21}$$

where v is the electron velocity, E is the electric field, and τ is the elastic scattering time. In the steady state the condition $dv/dt = 0$ can be used in conjunction with the previous equation to arrive at Ohm's law:

$$j = nev = \frac{ne^2\tau}{m}E = \sigma E\,. \tag{2.22}$$

The conductivity σ can be defined and related to the resistivity ρ as:

$$\sigma = \frac{ne^2\tau}{m} = \frac{ne^2 l}{mv_F} = \frac{1}{\rho}\,. \tag{2.23}$$

Thus, the resistivity can be introduced to the free energy barrier by using the previous equation and the free energy barrier now has the form:

$$\Delta F(0) = \frac{\sqrt{2}\pi\hbar A\Delta(0)}{6e^2\xi(0)\rho}\,.$$

The BCS expression for the superconducting energy gap at zero temperature is given by:

$$\Delta(0) \cong 1.76k_B T_c\,. \tag{2.24}$$

Thus we have the free energy barrier as:

$$\Delta F(0) = \frac{0.415\pi\hbar A k_B T_c}{e^2\xi(0)\rho}\,.$$

The quantum resistance of Cooper pairs and normal-state resistance of the nanowire are given by the following expressions:

$$R_q = \frac{h}{4e^2} \quad \text{and} \quad R_N = \frac{\rho L}{A}. \tag{2.25}$$

Inserting these into the previous form for the energy barrier, the free energy barrier at zero temperature takes on its final form for nanowires as:

$$\Delta F(0) = 0.83 \frac{R_q}{R_N} \frac{L}{\xi(0)} k_B T_c. \tag{2.26}$$

The GL temperature dependence of the free energy described in Eq. 2.15 is only valid near T_c. A free energy temperature dependence valid at all temperatures below T_c can be found from the two-fluid temperature dependence of the coherence length which can be expressed as:

$$\frac{\xi(T)}{\xi(0)} = \sqrt{\frac{1+(T/T_c)^2}{1-(T/T_c)^2}}. \tag{2.27}$$

The temperature dependence of the critical field H_c can also be expressed by a polynomial fit to numerical work done by Muhlschlegel [7, 9, 10].

$$\frac{H_c(T)}{H_c(0)} = 1.73(1-T/T_c) - 0.40089(1-T/T_c)^2 - 0.33844(1-T/T_c)^3 + 0.00722(1-T/T_c)^4. \tag{2.28}$$

Alternatively, the temperature dependence of the free energy barrier can be found by relating it to the critical current. We can begin by finding a useful expression for H_c^2 which can then be substituted into Eq. 2.13. From GL theory, the critical current density (depairing current) in a wire can be shown to be expressed as:

$$J_c = \frac{cH_c}{3\sqrt{6}\pi\lambda}. \tag{2.29}$$

With the usual definition of $I_c = J_c A$. Additionally, GL theory gives us the following expression for the flux quantum:

$$\Phi_o = \frac{hc}{2e} = 2\sqrt{2}\pi H_c \lambda\xi. \tag{2.30}$$

Both Eqs. 2.29 and 2.30 can be solved for H_c, which can then both be substituted into Eq. 2.13 to result in the following relationship between free energy and the critical current:

$$\Delta F = \frac{\sqrt{6}\hbar I_c}{2e}. \tag{2.31}$$

Using the expression Bardeen derived for the temperature dependence of the critical current of nanowires [11], the free energy barrier temperature dependence can also be expressed as:

$$\frac{\Delta F(T)}{\Delta F(0)} = \left(1 - \left(\frac{T}{T_c}\right)^2\right)^{3/2}. \tag{2.32}$$

In the case of high bias currents, the free energy barrier is slightly modified according to a closed form approximation Tinkham [12] found from the work of Langer and Ambegaokar [6].

$$\Delta F(I,T) = \frac{\sqrt{6}\hbar}{2e} I_c(T)\left(1 - \frac{I}{I_c(T)}\right)^{5/4}. \tag{2.33}$$

2.3 Little and LAMH fits for the $R(T)$ vs. T curve

To calculate the resistance as a function of temperature for a nanowire experiencing phase slips, Little devised a method [4] where the nanowire is broken into segments each having a length equal to the coherence length. Each segment of the wire is assumed to be in only one of two states: (i) the superconducting state (where there is presumed to be zero resistance), which exists in a time interval in between phase slip events and (ii) the normal state (where the segment has a finite resistance), which exists for the duration of the phase slip event. We express the number of phase slips that occurs per second as an Arrhenius law:

$$\Omega_{PS} = \Omega_o \exp\left(-\frac{\Delta F}{k_B T}\right), \tag{2.34}$$

where Ω_o is the phase-fluctuation attempt frequency and ΔF is the energy barrier for a phase slip event. The fraction of the time that an individual segment is in the normal state is simply the product of the time duration τ of the phase slip event (or equivalently the relaxation time of the order parameter) and the phase slip frequency Ω_{PS}:

$$f = \pi\Omega_o \exp\left(-\frac{\Delta F}{k_B T}\right) = \exp\left(-\frac{\Delta F}{k_B T}\right). \tag{2.35}$$

In this equation, the product $\pi\Omega_o \approx 1$ as we assume that the energy scales for both of these parameters are equal. Each individual segment in the nanowire has a resistance given by:

$$R_i = \frac{R_N \xi(T)}{L}, \tag{2.36}$$

where R_N is the normal state resistance of the nanowire. In this model, during each unit of time, the wire is in the normal state for a time f and in the superconducting state for a time (1-f). The phase slip fluctuations are fast and thus only the average value of the resistance can be measured. The average value of the resistance in a single segment can be modeled by the following expression:

$$\langle R_i \rangle = R_i f + R_o (1 - f), \tag{2.37}$$

here, $R_o = 0$ is the resistance of a segment in the superconducting state. Thus, the total resistance can be found by summing the average resistance of each segment:

$$R_{Little}(T) = \frac{L}{\xi(T)} \langle R_i \rangle = \frac{L}{\xi(T)} \left(R_i f + R_o (1 - f) \right).$$

The result is the equation for the Little prediction of the resistance of a nanowire as a function of temperature.

$$R_{Little}(T) = R_N \exp\left(-\frac{\Delta F}{k_B T} \right). \tag{2.38}$$

At temperatures close to T_c, this equation is not as accurate as it predicts that the nanowire resistance should be R_N, while it should be less then R_N due to superconducting fluctuations [13]. However, in the LAMH theory, the normal state resistance is only included explicitly after the LAMH resistance is found from considering the time evolution of the superconducting phase. To find the LAMH resistance, we consider the case where the bias current can be large, which has the effect of "tilting" the free energy landscape. When a thermal fluctuation occurs, the phase jumps over the barrier and the phase is changed by 2π. Due to the tilt in the free energy,

the energy barrier is different depending on the direction of the phase jump. The difference in the energy barrier can be found by considering the work done by the source during a phase slip:

$$\delta F = \Delta F_+ - \Delta F_- = \int IVdt = \int_0^{2\pi} \frac{\hbar I}{2e} d\phi = \frac{hI}{2e}. \tag{2.39}$$

The energy barrier when the phase changes by 2π is denoted as ΔF_+, while the energy barrier when the phase changes by -2π is given the symbol ΔF_-. These energy barriers are given by:

$$\Delta F_+ = \Delta F - \frac{\delta F}{2} = \Delta F - \frac{hI}{2e} \tag{2.40}$$

$$\Delta F_- = \Delta F + \frac{\delta F}{2} = \Delta F + \frac{hI}{2e}. \tag{2.41}$$

The system attempts to go over the barrier with a frequency Ω and successively makes it over the barrier with a probability given by the Boltzmann factors $\exp(-\Delta F_\pm / k_B T)$. The phase will change as a function of time according to:

$$\begin{aligned}
\frac{d\phi}{dt} &= \Omega_+ - \Omega_- = \Omega\left(\exp\left(-\frac{\Delta F_+}{k_B T}\right)\right) - \exp\left(-\frac{\Delta F_-}{k_B T}\right) \\
&= \Omega\left(\exp\left(-\frac{\Delta F - hI/2e}{k_B T}\right) - \exp\left(-\frac{\Delta F + hI/2e}{k_B T}\right)\right) \\
&= 2\Omega e^{-\Delta F/k_B T} \sinh\left(\frac{hI}{4ek_B T}\right).
\end{aligned}$$

The voltage can be found by using the Josephson relation [7]:

$$\frac{d\phi}{dt} = \frac{2eV}{\hbar} = 2\Omega e^{-\Delta F/k_B T} \sinh\left(\frac{hI}{4ek_B T}\right)$$

$$V = \frac{\hbar\Omega}{e} e^{-\Delta F/k_B T} \sinh\left(\frac{hI}{4ek_B T}\right). \tag{2.42}$$

Finally, the resistance is found by differentiating the voltage with respect to the current:

$$R_{LAMH} = \frac{dV}{dI} = \frac{\pi\hbar^2\Omega}{2e^2 k_B T} e^{-\Delta F/k_B T} \cosh\left(\frac{hI}{4ek_B T}\right). \tag{2.43}$$

At small bias currents such that $I << 4ek_B T / h$, the hyperbolic cosine becomes equal to one and the zero-bias resistance is given as:

$$R_{LAMH} = R_q \frac{\hbar\Omega}{k_B T} e^{-\Delta F/k_B T}. \tag{2.44}$$

The attempt frequency for the phase slips was found by McCumber and Halperin [14] using GL theory:

$$\Omega = \frac{L}{\xi}\left(\frac{\Delta F}{k_B T}\right)^{1/2} \frac{1}{\tau_{GL}}, \tag{2.45}$$

where τ_{GL} is the GL relaxation time and is given by:

$$\frac{1}{\tau_{GL}} = \frac{8k_B(T_c - T)}{\pi\hbar}. \tag{2.46}$$

In Eq. 2.45, the factor $1/\tau_{GL}$ sets the frequency scale, L/ξ is the number of independent wire segments in which the phase slips can occur, and $(\Delta F/k_B T)^{1/2}$ accounts for the overlap of the segments. Thus, the full LAMH resistance can be written as:

$$R_{LAMH}(T) = Bt^{-3/2}(1-t)^{9/4} e^{\left(c(1-t)^{3/2}/t\right)}. \qquad (2.47)$$

where

$$B = \frac{8}{\pi}\frac{L}{\xi(0)} R_q \sqrt{c} \quad \text{and} \quad c = 0.83\frac{R_q}{R_N}\frac{L}{\xi(0)} \quad \text{and} \quad t = \frac{T}{T_c}. \qquad (2.48)$$

Near T_c, the normal quasiparticles present in the wire provide a parallel conduction channel (resistive shunt) and thus the total resistance of the nanowire can be found according to:

$$R^{-1} = R_{LAMH}^{-1} + R_N^{-1}. \qquad (2.49)$$

2.4 Josephson junctions

Our nanowires typically have a length that is much greater than the coherence length ($L >> \xi$) giving rise to a multi-valued current phase relation [5] and allowing the phase to build up past 2π allowing phase slips. When the junction length is on the same order or smaller than the coherence length, the junction can be classified as a Josephson junction (JJ) which obeys a sinusoidal current phase relation and follows the Josephson relation for phase evolution [15, 16]:

$$I_s = I_c \sin\phi \qquad (2.50)$$

$$\frac{d\phi}{dt} = \frac{2eV}{\hbar}, \tag{2.51}$$

where I_s is the supercurrent, I_c is the critical current, ϕ is the phase across the junction, and V is the voltage across the junction. If the Josephson junction is shunted by a capacitor C and a resistor R and the system is biased with a total current I, then the following relationship holds true for this resistively and capacitively shunted junction (RSCJ) [17]:

$$I = I_c \sin\phi + \frac{V}{R} + C\frac{dV}{dt}. \tag{2.52}$$

Inserting the Josephson relation for the voltage we can derive the following equation for the phase evolution across the junction:

$$\frac{d^2\phi}{dt^2} + \frac{1}{RC}\frac{d\phi}{dt} + \frac{2e}{\hbar C}\left(I_c \sin\phi - I\right) = 0. \tag{2.53}$$

A qualitative analysis of the dynamics described by the previous equation reveals that this system is similar to a particle in a "tilted washboard" (see Fig. 2) moving in an effective potential given by:

$$U(\phi) = -E_J \cos\phi - \frac{\hbar I}{2e}\phi, \tag{2.54}$$

where $E_J = \hbar I_c / 2e$. The energy barrier for the phase particle to thermally escape from a potential well in this model can be expressed as [7, 18]:

$$\Delta U \cong \frac{4\sqrt{2}}{3} E_J \left(1 - \frac{I}{I_c}\right)^{3/2}. \tag{2.55}$$

In the "tilted washboard" model used here, as the current I is increased, the tilt increases. In the limit where $I \to I_c$, the energy barrier for a phase slip by 2π decreases to zero and the phase particle is allowed to run down the washboard and the "runaway" or voltage state has been achieved. The mass of the particle in this model and the viscous drag force are given by:

$$m = C\left(\frac{\hbar}{2e}\right)^2 \quad \text{and} \quad F_{drag} = \left(\frac{\hbar}{2e}\right)^2 \frac{1}{R}\frac{d\phi}{dt}. \tag{2.56}$$

The quality factor and plasma frequency are given by:

$$Q = \omega_{po} RC \quad \text{and} \quad \omega_{po} = \sqrt{\frac{2eI_c}{\hbar C}}. \tag{2.57}$$

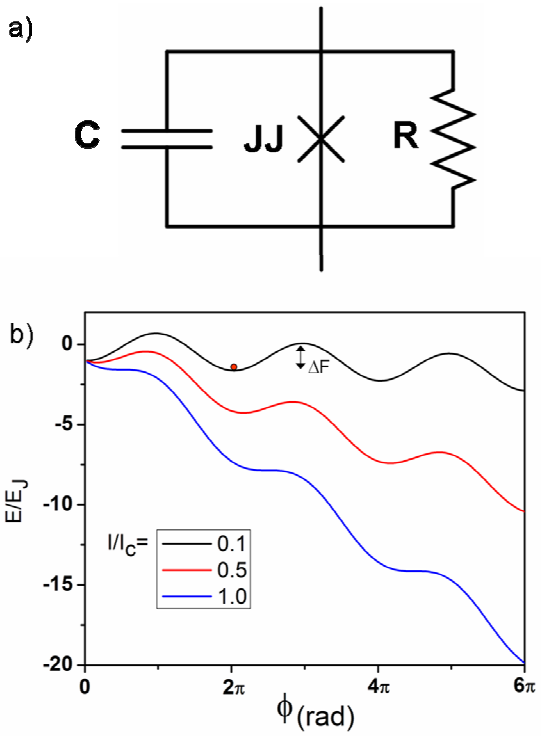

Fig. 2.2: (a) The equivalent circuit of the RCSJ model showing the JJ shunted by a capacitor and a resistor. (b) The tilted washboard representation of the RCSJ model. As the current is increased, the washboard potential tilt increases and correspondingly the free energy barrier ΔF for phase slips decreases.

The current phase relationship for the JJ can be recovered by finding the minimum in the potential from Eq. 2.54. The result is the current phase relationship given in Eq. 2.50:

$$\frac{dU}{d\phi} = 0 \rightarrow I_s = I_c \sin\phi .$$

Additionally, the plasma frequency and its current dependence can be derived by solving for the frequency of small oscillations centered at the minimum of the effective potential according to:

$$\omega^2 = \frac{1}{m}\frac{d^2U}{d\phi^2}\bigg|_{\phi\min}, \tag{2.58}$$

where $\phi_{\min} = \sin^{-1}(I/I_c)$. This results in the following expression for the current-dependent plasma frequency:

$$\omega_p(I) = \omega_{po}\left[1-\left(\frac{I}{I_c}\right)^2\right]^{1/4}. \tag{2.59}$$

Once the phase particle has escaped a potential minimum and has begun running down the washboard, the damping force can cause the particle to "retrap" back into a potential well and thus back into the superconducting state. The condition for this is that the energy dissipated through the resistor is equal to the energy input from the current source. The energy dissipated through the resistor can be found by the following:

$$\int \frac{V^2}{R}dt = \frac{\hbar}{2eR}\int_{-\pi}^{\pi} V(\phi)d\phi ,$$

where the voltage can be found through the kinetic energy $1/2\,CV^2 = E_J\left(1+\cos\phi\right)$ and thus the previous equation becomes:

$$\frac{\hbar}{2eR}\sqrt{\frac{2E_J}{C}}\int_{-\pi}^{\pi}\sqrt{1+\cos\phi}\,d\phi = 5.657\,\frac{\hbar}{2eR}\sqrt{\frac{2E_J}{C}}\,.$$

The right hand side can by set equal to the input energy from the current source and solved for the retrapping current:

$$5.657\,\frac{\hbar}{2eR}\sqrt{\frac{2E_J}{C}} = \frac{hI_r}{2e}$$

$$I_r \cong \frac{4I_c}{\pi Q}\,. \qquad (2.60)$$

The inductance of a JJ can also be found using the Josephson relation and the voltage across an inductor:

$$V = \frac{\hbar}{2e}\frac{d\phi}{dt} = \frac{\hbar}{2e}\frac{d\phi}{dI}\frac{dI}{dt} = L\frac{dI}{dt}\,,$$

thus,

$$L = \frac{\hbar}{2e}\left(\frac{dI}{d\phi}\right)^{-1}\,. \qquad (2.61)$$

Applying this to the current phase relationship expressed in Eq. 2.50, the kinetic inductance of a JJ is:

$$L = \frac{\hbar}{2eI_c \cos\phi}. \tag{2.62}$$

For small currents:

$$L = \frac{\hbar}{2eI_c}. \tag{2.63}$$

2.5 Heating effects in superconducting nanowires

The hysteresis observed in the voltage-current (*VI*) curves of Josephson junctions and nanowires has been attributed to the dynamics of the particle in the tilted washboard model where the inertia of the phase particle carries it down the washboard potential until it is retrapped. However, Tinkham *et. al.* [12] proposed an alternative model involving heating to describe the hysteresis. In this model, the fraction of the wire that is in the normal state is given by $x = l/L$, where l is the length of the normal part of the wire (which is located at the center of the nanowire) and L is the length of the nanowire. The total power dissipated in this region therefore is $P_{dis} = I^2 R_N x$, where I is the current through the nanowire and R_N is the normal resistance of the entire nanowire. The heat that is generated is then carried out through the ends of the superconducting section of the wire which has a length given by $\frac{L}{2}(1-x)$. The rate of heat conduction through the wire is $H = KA\Delta T / t$, where K is the thermal conductance, A is the cross sectional area, t is the length of the superconducting section of the nanowire where heat will pass, and ΔT is the temperature difference ($T_c - T_b$) where T_c is the superconductor critical temperature and T_b is the bath temperature. Equating the rate of heat production (the power

dissipated in the normal section of the nanowire) and the rate of heat conduction out of the nanowire leads to the following relationship:

$$I^2 R_N x = \frac{4K_s A(T_c - T_b)}{(1-x)L}. \tag{2.64}$$

This expression can be rearranged to give a quadratic equation for the fraction of the wire that is in the normal state:

$$x(1-x) = \frac{4K_s A(T_c - T_b)}{LI^2 R_N} \equiv \beta. \tag{2.65}$$

This can be solved for *x*:

$$x = \frac{1 \pm \sqrt{1-4\beta}}{2}. \tag{2.66}$$

The solution is only defined for $\beta \le 1/4$, which leads to the equation for the retrapping current:

$$I_r = 4\sqrt{\frac{K_s A(T_c - T_b)}{LR_N}}. \tag{2.67}$$

The voltage can also be written as:

$$V = IR_N x = R_N \left(\frac{I + \sqrt{I^2 - I_r^2}}{2} \right), \quad I > I_r. \tag{2.68}$$

This model can made more accurate by dividing the nanowire wire into many segments and implementing a finite-difference equation for each segment. By doing this and then

incorporating the measured *R(T)* vs. *T* curve a more accurate simulation of the hysteretic *V-I* curve can be found.

A heating model for nanowires can also be constructed in which the experimental *R(T)* vs. *T* curve is unnecessary [19, 20, 21]. Here, the nanowire switches to the Joule-heated normal state (JHNS) due to self-sustained heating induced by phase slips. The basic elements are the same as outlined in [12]; however, here the stochastic phase slip process and the corresponding thermal and quantum phase slip rates are included instead of the experimental *R(T)* vs. *T* curve. The result shows that in general a few phase slips are necessary to induce thermal runaway, but that there are some domains in temperature and current (low temperature and high current) where even the energy deposited by one phase slip is enough to trigger the JHNS.

2.6 Current phase relationship and kinetic inductance in superconducting nanowires

In the case of strong applied currents, the free energy density takes on a more simple form given by:

$$f = f_{no} + \alpha|\psi|^2 + \frac{\beta}{2}|\psi|^4 + |\psi|^2 \frac{1}{2} m^* v_s^2 + \frac{h^2}{8\pi}. \qquad (2.69)$$

When the diameter of the nanowire is small compared to the penetration depth, the kinetic energy of the current is much larger than the field energy and the term $h^2/8\pi$ can be neglected. For a given v_s, Eq. 2.69 can be minimized and the value of the order parameter that does that is given by:

$$|\psi|^2 = \psi_\infty^2\left(1-\frac{m^* v_s^2}{2|\alpha|}\right). \tag{2.70}$$

This can be inserted into the GL equation for the supercurrent density:

$$\mathbf{J} = \frac{e^*}{m^*}|\psi|^2\left(\hbar\nabla\phi - \frac{e^*}{c}\mathbf{A}\right) = e^*|\psi|^2\mathbf{v}_s\,.$$

Using the value of $\psi_\infty^2 = -\alpha/\beta$ the equation for the supercurrent density now becomes:

$$J_s = -2e\frac{\alpha}{\beta}\left(1-\frac{m^* v_s^2}{2|\alpha|}\right)v_s\,. \tag{2.71}$$

The supercurrent velocity can be expressed as:

$$v_s = \frac{\hbar}{m^*}\nabla\phi = \frac{\hbar}{m^*}\frac{\phi}{L}\,. \tag{2.72}$$

Now, inserting this into the supercurrent density gives the new form of the supercurrent density:

$$J_s = -2e\frac{\alpha}{\beta}\left[\frac{\hbar\phi}{m^* L} - \frac{m^*}{2|\alpha|}\left(\frac{\hbar\phi}{m^* L}\right)^3\right].$$

The parameter α can be eliminated using the expression:

$$\xi^2(T) = \frac{\hbar^2}{2m^*|\alpha(T)|}\,. \tag{2.73}$$

So, the new form of the supercurrent density is:

$$J_s = -2e\frac{\alpha}{\beta}\sqrt{\frac{2|\alpha|}{m^*}}\left[\frac{\xi}{L}\phi - \left(\frac{\xi}{L}\phi\right)^3\right]. \tag{2.74}$$

In order to find the critical current, we must find the maximum in the supercurrent density by the setting $\partial J_s/\partial v_s = 0$. This results in the following expression for the critical current density:

$$J_c = -2e\frac{2\alpha}{3\beta}\sqrt{\frac{2|\alpha|}{3m^*}}. \tag{2.75}$$

Using the fact that $I = JA$, we can express the supercurrent as a function of the phase according to:

$$I_s = \frac{3\sqrt{3}}{2}I_c\left[\frac{\xi}{L}\phi - \left(\frac{\xi}{L}\phi\right)^3\right]. \tag{2.76}$$

This is the nanowire current phase relation (CPR) and is the same one derived by Likharev [5]. Using the equation for the kinetic inductance of a nanowire given by Eq. 2.61, the kinetic inductance of a nanowire is:

$$L_{NW} = \frac{\hbar}{3\sqrt{3}eI_c}\left[\left(\frac{\xi}{L}\right) - 3\left(\frac{\xi}{L}\right)^3\phi^2\right]^{-1}. \tag{2.77}$$

Thus, the kinetic inductance of the nanowire like that of the Josephson junction is nonlinear. At low bias currents, the kinetic inductance of the nanowire can simply be expressed as:

$$L_{NW} = \frac{\hbar L}{3\sqrt{3}eI_c\xi}. \tag{2.78}$$

2.7 Switching and retrapping rates and distributions

The thermal switching rate from the superconducting state to the running state (voltage) or normal state is given by the Arrhenius law:

$$\Gamma_{TAPS} = \frac{\Omega_{TAPS}}{2\pi} \exp\left(-\frac{\Delta F}{k_B T}\right), \tag{2.79}$$

where Ω_{TAPS} is the attempt frequency for thermally activated phase slips (TAPS) and ΔF is the free energy barrier for TAPS to occur. Instead of thermal hopping over the barrier, the phase particle can also quantum tunnel through the barrier and a simple model for the quantum phase slip (QPS) rate was proposed by Giordano [22, 23]. In this model, the thermal energy scale $k_B T$ is replaced by the quantum energy scale $\hbar\omega_P/2\pi$, where ω_P is the plasma frequency. The simple relationship $k_B T_{QPS} = \hbar\omega_P/2\pi$ results in the QPS rate taking on a similar form as the TAPS rate except where $T \to T_{QPS}$:

$$\Gamma_{QPS} = \frac{\Omega_{QPS}}{2\pi} \exp\left(-\frac{\Delta F}{k_B T_{QPS}}\right). \tag{2.80}$$

After a Josephson junction or nanowire is driven out of the superconducting state into the voltage state, the system can be retrapped back into the superconducting state, for example, by sufficiently reducing the bias current. If the JJ or nanowire has entered into the Joule-heated normal state through overheating the sample above T_c, then the retrapping process does not have a noticeable stochasticity and the system returns to the superconducting state when the current is reduced past a critical value to reduce the heating in the nanowire, allowing its temperature to

drop below T_c. However, if the system is in the running state, then dissipation can aid the phase particle in the retrapping process by directing its trajectory back into a potential well on the tilted washboard, and stochasticity is observed. The work of Ben-Jacob *et al.* [24] can be useful in determining the retrapping rate from the running state as they derived the transition rate of a system in a stable oscillatory steady state to another steady state under the influence of large fluctuations. They have come up with the following analytical approximation under the limit of small dissipation:

$$\frac{1}{\Gamma_{RT}} = \tau_{RT} \cong \frac{\sqrt{\pi}}{G}\left(\frac{k_B T}{\Delta W}\right)^{1/2} \exp\left(\frac{\Delta W}{k_B T}\right), \tag{2.81}$$

where, Γ_{RT} is the rate of retrapping, τ_{RT} is the life time of the retrapping process, and the function W is the solution of a Hamilton-Jacobi type equation. The function ΔW is found to be:

$$\Delta W = \frac{1}{2}\left[\frac{I}{G} - \frac{I}{G_M(I)}\right] \cong \frac{1}{2}\left[\frac{I}{G} - \frac{4}{\pi}\right], \tag{2.82}$$

where G is the friction coefficient $G_M(I)$ is the value of G corresponding to the minimum value of I possible for the system not to switch states, and I is the external drive. $G_M(I)$ is given by:

$$G_M(I) = \pi I/4\,. \tag{2.83}$$

For a Josephson junction, the external drive I and friction force G are characterized by:

$$I = I_{dc}/I_c \quad \text{and} \quad G = (\omega_P RC)^{-1}, \tag{2.84}$$

where I_{dc} is the bias current, R is the RCSJ resistance, and C is the RCSJ capacitance. Using these relations as well as the identity of $I_{\min} = I_{RT}$, the rate of retrapping into the superconducting state can be expressed as:

$$\Gamma_{RT} = (I - I_{ro})\sqrt{\frac{1}{\pi C k_B T}} \exp\left(-\frac{(I - I_{ro})R^2 C}{k_B T}\right). \tag{2.85}$$

In our experiments, we measure the distribution of switching and retrapping currents. In order to compare our experimental data to the theoretical rates for the switching and retrapping currents, a relationship between the switching distributions and rates must be used. We start by writing an equation governing the change in the persistence probability $W(t)$ (i.e. the probability that there is no escape):

$$dW(t) = -\Gamma(I(t))W(t)dt\,. \tag{2.86}$$

In this model, the escape rate Γ is assumed to have a current dependence. Solving for the persistence probability we get:

$$W(t) = \exp\left(-\int_0^t \Gamma(I(t'))dt'\right). \tag{2.87}$$

A change of variables can be made through the relationship $\dot{I} = dI/dt$, where I is the current resulting in:

$$W(t) = \exp\left(-\int_0^I \frac{\Gamma(I)}{\dot{I}} dI\right). \tag{2.88}$$

The escape probability $P(I)$ can be found by summing the probability that the particle escapes or does not escape (persists):

$$\int_o^I P(I)dI + W(T) = 1. \tag{2.89}$$

By differentiating this expression in I we get:

$$P(I) + \frac{dW}{dI} = 0. \tag{2.90}$$

We can solve this for $P(I)$ [25]:

$$P(I) = \frac{\Gamma(I)}{\dot{I}} \exp\left(-\int_0^I \frac{\Gamma(I)}{\dot{I}} dI \right) = \frac{\Gamma(I)}{\dot{I}} W. \tag{2.91}$$

Using Eqs. 2.89 and 2.91 the probability of escape can by expressed:

$$P(I) = \frac{\Gamma(I)}{\dot{I}} \left(1 - \int_0^I P(u)du \right), \tag{2.92}$$

which is the form used by Fulton and Dunkelberger [26] and is the essential relationship between our experimentally measured distributions and transforming that representation into a rate to be compared with the theory. For this expression to be more useful, we must divide the current into small bins (denoted by K) where we assume the rate is constant and that the bin is small enough so that $\Delta I = \dot{I}\Delta t$. The bin corresponding to the maximum switching current will be the bin where $K = 1$. Therefore $t = 0$ corresponds to bin K while $t = \Delta t$ corresponds to bin $K - 1$ and so on. Thus looking at the persistence probability we have the following equation:

$$\Delta W = \exp\left(-\Gamma(K)\Delta t\right) = 1 - \int_{I(K)}^{I(K-1)} P(I)dI \,. \tag{2.93}$$

Using the fact that the probability must sum to equal one, we can rewrite this expression as:

$$\exp\left(-\Gamma(K)\Delta t\right) = \int_{I(K-1)}^{\infty} P(I)dI \Big/ \int_{I(K)}^{\infty} P(I)dI \,. \tag{2.94}$$

By taking the logarithm, replacing the integrals with sums, and replacing Δt we have the experimentally useful equation to find the switching or retrapping rate given the corresponding distribution (histogram).

$$\Gamma(K) = \frac{\dot{I}}{\Delta I} \ln\left(\sum_{n=1}^{K} P(n) \Big/ \sum_{m=1}^{K-1} P(m) \right). \tag{2.95}$$

The sweep speed used in our experiments can easily be found from the expression for a sinusoidal current with frequency f and amplitude I_o:

$$I(t) = I_o \sin\left(2\pi f t\right). \tag{2.96}$$

The time derivative of the current is given by:

$$\dot{I}(t) = 2\pi f I_o \cos\left(2\pi f t\right). \tag{2.97}$$

By using the trigonometric identity $\cos^2\theta + \sin^2\theta = 1$, the sweep speed is found to obey the following relationship:

$$\dot{I} = 2\pi f I_o \sqrt{1 - \left(I/I_o\right)^2} \,. \tag{2.98}$$

2.8 Bardeen critical current

The temperature dependence of the critical current in a nanowire can be found from Eq. 2.75, which gives the critical current density in a nanowire:

$$J_c = -2e\frac{2\alpha}{3\beta}\sqrt{\frac{2|\alpha|}{3m^*}}.$$

Using the expressions given in section 2.1 for $\alpha(T)$ and $\beta(T)$, the critical current density can be expressed as:

$$J_c = \frac{cH_c(T)}{3\sqrt{6}\pi\lambda(T)},$$

where c is the speed of light. The temperature dependence of the critical field $H_c(T)$ can be approximated by a parabolic law according to:

$$H_c(T) \cong H_c(0)\left[1-\left(\frac{T}{T_c}\right)^2\right]. \qquad (2.99)$$

The temperature dependence of the penetration depth can be well approximated by the two-fluid approximation given by:

$$\lambda(T) \cong \frac{\lambda(0)}{\left[1-(T/T_c)^4\right]^{1/2}}. \qquad (2.100)$$

Using the temperature dependences given by Eqs. 2.99 and 2.100, the temperature dependence of the critical current is given by:

$$J_c \propto \frac{H_c(T)}{\lambda(T)} \propto \left[1-\left(\frac{T}{T_c}\right)^2\right]\left[1-\left(\frac{T}{T_c}\right)^4\right]^{1/2} = \left[1-\left(\frac{T}{T_c}\right)^2\right]^{3/2}\left[1+\left(\frac{T}{T_c}\right)^2\right]^{1/2}. \qquad (2.101)$$

The $\left[1+(T/T_c)^2\right]^{1/2}$ can be dropped as it is within the uncertainty of the two approximations used to derive the temperature dependence and results in a negligible effect on J_c. Finally, using the fact that $J_c \propto I_c$, the critical current temperature dependence can be expressed as:

$$I_c = I_c(0)\left[1-\left(\frac{T}{T_c}\right)^2\right]^{3/2}. \qquad (2.102)$$

This equation is referred to as the Bardeen equation [11] throughout the thesis. The $I_c(0)$ factor can also be approximated in terms of experimentally useful parameters using GL and BCS theory [27]. We start with an expression for the critical current that is derived within GL theory:

$$I_c = \frac{A\Phi_o}{3\sqrt{3}\pi\lambda^2\xi}, \qquad (2.103)$$

where A is the cross sectional area, Φ_o is the flux quantum, λ is the penetration depth, and ξ is the coherence length. From the BCS theory we know:

$$\frac{1}{\lambda^2} \cong \frac{1}{\lambda_L^2}\frac{l}{\xi_o} = \frac{\pi\Delta}{\hbar\rho_n}, \qquad (2.104)$$

where λ_L is the London penetration depth, ξ_o is the Pippard coherence length, l is the mean free path, Δ is the energy gap, and ρ_n is the normal state resistivity. Inserting this into Eq. 2.103 and

using the relations $R_N = \rho_n L/A$ (L is the nanowire length) and $\Delta(0) \cong 1.76 k_B T_c$, the critical current at zero temperature can be expressed as:

$$I_c(0) \cong (92\mu A)\frac{LT_c}{R_N \xi(0)}. \qquad (2.105)$$

2.9 Magnetic field period in double nanowire samples

When a magnetic flux penetrates a superconducting ring, oscillations in various superconducting parameters can be observed. For example, Little and Parks [28] discovered that when magnetic flux threads a hollow cylinder, the superconducting transition temperature T_c is observed to oscillate. They have also developed a theory, which is based on the fact that the free energy of the cylinder oscillates with the applied flux due to the vorticity of the cylinder changing in a periodic fashion, to minimize the free energy. Also, when a superconducting ring containing two Josephson junctions is pierced by a magnetic field [29], the system critical current oscillates between $(I_{c1} + I_{c2})$ and $|I_{c1} - I_{c2}|$, where I_{c1} and I_{c2} are the critical currents of the Josephson junctions. These effects are a result of the single-valued nature of the order parameter and thus the constraint that the phase change around any closed path must be an integer value of 2π:

$$\oint \nabla\phi \cdot d\mathbf{s} = 2\pi n, \qquad (2.106)$$

where n is an integer. When applied to a double nanowire sample, where the nanowires connect to long rectangular electrodes on either side, this constraint leads to the following relation [30, 31]:

$$\theta_{1,L\leftarrow R} - \theta_{2,L\leftarrow R} + 2\delta(B) = 2\pi n_v , \tag{2.107}$$

where $\theta_{1,L\leftarrow R}$ and $\theta_{2,L\leftarrow R}$ are the phase accumulation along the length of the wires, $\delta(B)$ is the phase difference due to the Meissner currents in the leads, and n_v is the vortex number. For the particular gauge used here ($\mathbf{A} = By\mathbf{e}_x$) the vector potential is always parallel to the nanowires and the phase difference $\theta_{1,L\leftarrow R} - \theta_{2,L\leftarrow R}$ is given by:

$$\theta_{1,L\leftarrow R} - \theta_{2,L\leftarrow R} = \frac{2\pi}{\Phi_o} 2abB , \tag{2.108}$$

where Φ_o is the flux quantum, $2a$ is the distance between the nanowires, b is the length of the nanowires, and B is the magnetic field. To find the phase accumulation due to the Meissner current in the leads we start with the form of the supercurrent density given from the GL theory:

$$\mathbf{J} \propto \left(\nabla\phi(\mathbf{r}) - \frac{2e}{\hbar}\mathbf{A}(\mathbf{r}) \right) . \tag{2.109}$$

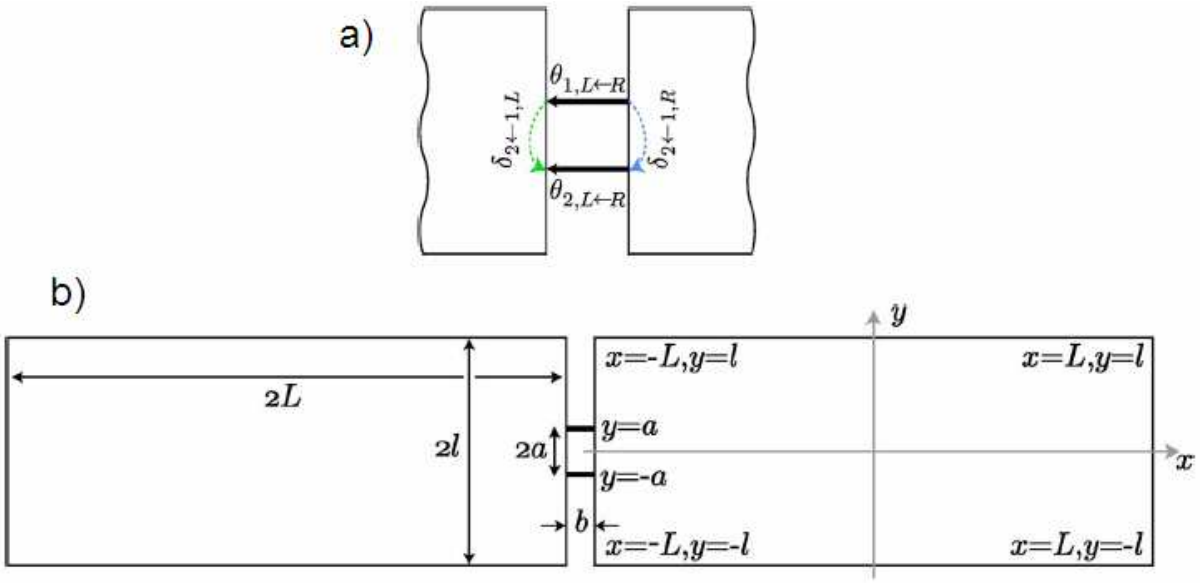

Fig. 2.3: (a) A schematic view of the nanowires and leads showing the phase accumulation in each wire ($\theta_{L\leftarrow R}$) and in each lead ($\delta_{2\leftarrow 1}$). (b) The geometry of the system showing the dimensions and coordinates used in the calculation of the magnetic field period. The figure is taken from [31].

In the *x*-direction, there is no phase difference between the wires and thus only the second term in Eq. 2.109 is nonzero. Thus, we have the following relationship for the magnitude of the supercurrent density in the *x*-direction:

$$J_x \propto \frac{2e}{\hbar} A_x = \frac{2e}{\hbar} Bl \,. \tag{2.110}$$

where 2*l* is the width of the leads. As the current circulates, it eventually flows in the *y*-direction as it passes the two nanowires. The vector potential has no component in the *y*-direction and thus the magnitude of the supercurrent density follows the relation:

$$J_y \propto \nabla \phi_y \,. \tag{2.111}$$

Current is conserved and thus $J_x = J_y$, which gives the following relationship for the phase gradient in the *y*-direction:

$$\nabla \phi_y = \frac{2\pi}{\Phi_o} Bl . \tag{2.112}$$

Now the phase accumulation due to the Meissner current can be found by integrating the phase gradient along the *y*-direction:

$$\delta(B) = \int_{-a}^{a} \nabla \phi_y dy = \frac{2\pi}{\Phi_o} 2alB . \tag{2.113}$$

The phase accumulations $\theta_{1,L\leftarrow R} - \theta_{2,L\leftarrow R}$ and $\delta(B)$ from Eqs. 2.108 and 2.113 can be inserted into Eq. 2.107 to get:

$$\frac{2\pi}{\Phi_o} 2abB + \frac{2\pi}{\Phi_o} 4alB = 2\pi m ,$$

where *m* is an integer. The lowest energy state of this system is when there is no Meissner current. Whenever the magnetic field satisfies this relation, there is no screening current in the ground state. Thus, the previous equation can be used to find the magnetic field period:

$$\Delta B = \left[\left(\frac{\Phi_o}{4al} \right)^{-1} + \left(\frac{\Phi_o}{2ab} \right)^{-1} \right]^{-1} . \tag{2.114}$$

When the condition $b << l$ is true, the magnetic field period reduces to:

$$\Delta B = \frac{\Phi_o}{4al} c_1 , \tag{2.115}$$

where c_1 is of order unity and a function of a/l that takes into account how the current flows around the corners of the leads. When $a << l$, c_1 is constant and the magnetic field period takes on the exact form:

$$\Delta B = \frac{\pi^2}{8G}\frac{\Phi_o}{4al}, \qquad (2.116)$$

where $G = 0.916$ is the Catalan number.

2.10 Superconductor-insulator transition and the insulating state in nanowires

So far, we have discussed the superconducting state in nanowires. However, under certain conditions, a nanowire may become insulating as opposed to superconducting as the temperature is reduced even though it is made out of superconducting material. The normal state resistance is one such parameter that has been observed to control the state of a nanowire and thus play an important role in understanding the superconductor to insulator transition (SIT) in nanowires [32, 33]. The SIT has also been observed on the same type of MoGe nanowires studied in this thesis [34, 35] as well as on similar nanowires made from superconducting Nb [36]. It is characterized by the change in behavior of the resistance as the temperature is lowered. In superconducting nanowires, the resistance decreases according to the Arrhenius law as the temperature is reduced and finally goes to exactly zero at zero temperature. In contrast, the resistance of insulating nanowires increases as the temperature is decreased (see Fig. 2.4). In short nanowires, like those studied in this thesis, the SIT is observed to be a sharp function of the

quantum resistance for Cooper pairs $R_Q = h/4e^2$. If the normal state resistance is less than R_Q, the wire is observed to be superconducting at low temperature and if the normal state resistance of the nanowire is greater than R_Q, the wire is observed to be insulating.

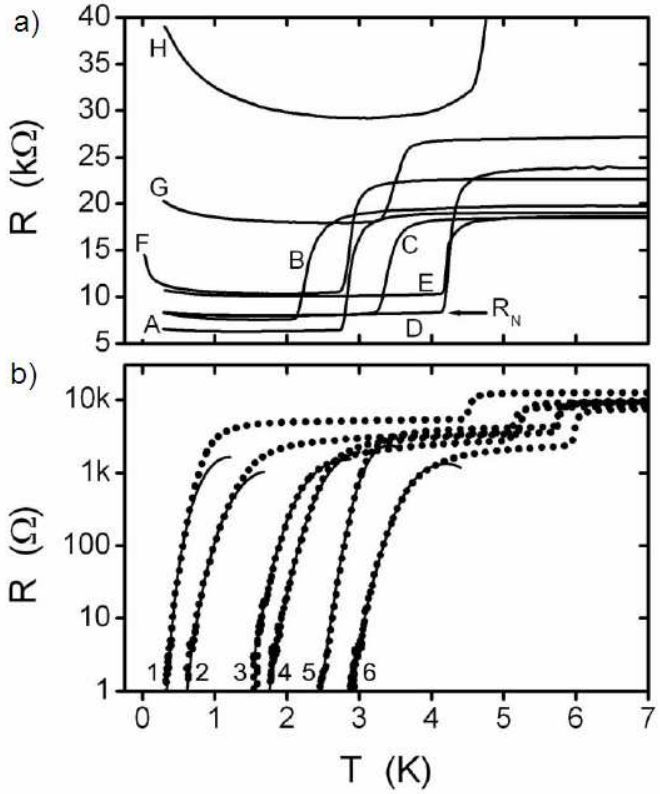

Fig. 2.4: Graph taken from [37]. Resistance vs. temperature for MoGe nanowires showing the insulating and superconducting behavior. The first transition at higher temperature is where the film transitions to the superconducting state. (a) Insulating nanowire behavior characterized by an increase in the resistance at low temperature. (b) Superconducting nanowire behavior characterized by a decrease of resistance to below the noise level at low temperature. The transition from superconducting to insulating behavior occurs when the nanowire normal state resistance is equal to R_Q.

While the observation of the SIT can clearly be noticed from the *R* vs. *T* curves, the exact nature of the insulating state is still not clearly understood. In thin inhomogeneous wires, the insulating state can arise due to oxidation of the metal resulting in granularities or non-uniformity. However, even in homogeneous junctions, the insulating state can arise. This could occur to do the Coulomb interaction [38, 39] or weak localization [40], which results in the

complete destruction of superconductivity by driving T_c to zero. The insulating state can also arise due to the loss of coherence due to QPS and thus the loss of the capacity for a supercurrent to flow [41, 42, 43]. Within the latter category, Golubev and Zaikin (GZ) [43] calculated the time in between single QPS events ($\tau_{GZ} = \Gamma_{GZ}^{-1}$) for the type of MoGe nanowires studied in this thesis. When the parameter $A_{GZ} = 2$, Golubev and Zaikin found that for insulating samples (like those studied in this thesis) $10^{-8}\text{s} \le \tau_{GZ} \le 10^{-4}\text{s}$ and for superconducting samples $10^{-1}\text{s} \le \tau_{GZ} \le 10^{14}\text{s}$. Thus, the superconducting samples only appear to be superconducting because QPS events are rare while in insulating samples they occur often. However, when Golubev and Zaikin used $A_{GZ} = 1$, they found that for insulating samples $10^{-11}\text{s} \le \tau_{GZ} \le 10^{-9}\text{s}$ and for superconducting samples $10^{-6}\text{s} \le \tau_{GZ} \le 10^{0}\text{s}$. Thus, both the insulating and superconducting samples should show an insulating behavior due to the proliferation of QPS. However, QPS can still be damped [44] resulting in a dissipative phase transition [45] similar to that observed in the RCSJ model for Josephson junctions. In many cases, it may be difficult to distinguish. Some evidence such as the resistance at the transition between the superconducting and insulating state occurring at R_Q points to the dissipative phase transition for the MoGe nanowires studied here. However, this is not firmly established yet.

In the insulating state, the behavior of the resistance vs. temperature curves in our MoGe nanowires follows the predictions of the theory of Coulomb blockade. Weak Coulomb blockade was first demonstrated in tunnel junctions [46] but was then observed in homogeneous normal wires [47]. Thus, even if our nanowires have no breaks, they can still show Coulomb blockade effects. Golubev and Zaikin [48] were able to extend this understanding by using an effective action technique to derive the temperature dependence of the conductance ($G = R^{-1}$) as well as

the current voltage $I(V)$ characteristics. The weak Coulomb blockade occurs when the temperature is high compared with the charging energy E_C. The conductance is given by GZ as:

$$\frac{G(T)}{G_0} \cong 1 - \beta\left[\frac{E_C}{3k_BT} - \left(\frac{3\zeta(3)}{2\pi^4}g + \frac{1}{15}\right)\left(\frac{E_C}{k_BT}\right)^2\right], \qquad (2.117)$$

where G_0 is the conductance in the absence of Coulomb effects, $\beta = 1/3$ for diffusive wires, $\zeta(3) \cong 1.202$, and $g = 4G_0R_Q$. By expanding this expression about E_C, the previous equation can be rewritten as and compared to the experimental data:

$$\frac{G_0}{G_0 - G(T)} = \frac{3k_BT}{\beta E_C} + \frac{9}{\beta}\left(\frac{3\zeta(3)}{2\pi^4}g + \frac{1}{15}\right). \qquad (2.118)$$

2.11 Superconducting coplanar waveguide resonator properties

In this section, we will explore some of the basic characteristics of superconducting coplanar waveguide resonators, which are used in this thesis. Much of the information presented in this section is taken from M. Göppl *et. al.* [49], where an analysis of many of the physical properties of coplanar waveguide resonators is given. We use superconducting metal to construct our resonators because it is the same material that we use to fabricate our nanowires and thus can be processed in one step, but also because they have small resistance and thus have higher quality factors. To design a resonator in the microwave frequency range, we make use of the relationship between the length of the resonator and its fundamental mode:

$$f_0 = \frac{v_P}{2l}, \tag{2.119}$$

where f_0 is the fundamental mode frequency, l is the length of the resonator ($2l = \lambda_0$) which we control to achieve the desired frequency, and v_P is the phase velocity given by:

$$v_p = c/\sqrt{\varepsilon_{eff}} = 1/\sqrt{L_l C_l}, \tag{2.120}$$

where c is the speed of light in a vacuum and ε_{eff} is the effective permittivity. The parameters L_l is the inductance per unit while C_l is the capacitance per unit length and are both given by the use of conformal mapping techniques [50, 51]:

$$L_l = \frac{\mu_0}{4}\frac{K(k_0')}{K(k_0)} \quad \text{and} \quad C_l = 4\varepsilon_0\varepsilon_{eff}\frac{K(k_0)}{K(k_0')}, \tag{2.121}$$

where μ_0 is the permeability of free space, ε_0 is the permittivity of free space, and $K(k)$ are the complete elliptic integrals of the first kind with the arguments $k_0 = w/(w+2g)$ and $k_0' = \sqrt{1-k_0^2}$; here w is the width of the center conductor and g is the gap between the center conductor and the ground plane (see Fig. 2.5). The characteristic impedance of the resonator is given by $Z_0 = \sqrt{L_l/C_l}$ and is chosen to result in a value of ~ 50 Ω. The calculations of inductance so far have only described the magnetic inductance but in thin MoGe films, the kinetic inductance significantly contributes to the total inductance and cannot be ignored. The total inductance of the resonator is given by $L = L_m + L_k$, where L_m is the contribution due to the magnetic (geometric) inductance and L_k is the kinetic inductance due to the inertia of the Cooper pairs.

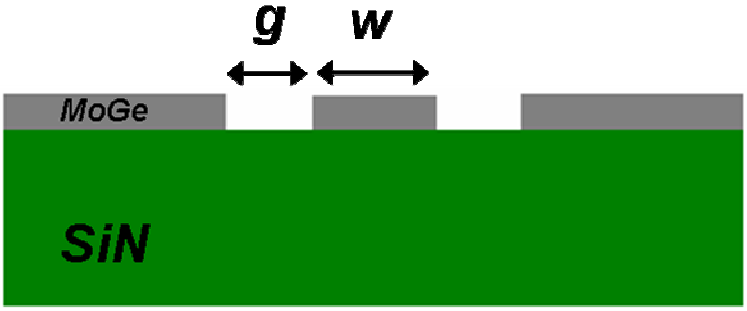

Fig. 2.5: Side view of coplanar waveguide resonator. The ground plane and center conductor are fabricated with MoGe and the center conductor is a width w and is separated from the ground plane by a gap of width g. The entire resonator sits on top of a SiN layer.

The resonance frequency and loaded quality factor can be experimentally determined by fitting a Lorentzian line shape to the transmission characteristics:

$$S_{21} = \frac{A_0}{(f_0/Q)^2 + 4(f - f_0)^2}, \tag{2.122}$$

where A_0 is a constant, f_0 is the resonance frequency, and Q is the loaded quality factor. While the Lorentzian line shape can fit the data well, it is not an exact fit and is only valid near the resonance frequency. The transmission characteristics can be fit more precisely by a transmission line (TL) model for the resonator. In this scheme, the resonator is modeled as a distributed circuit with the circuit elements given per unit length and where the circuit is given by a resistor in series with an inductor which are both in parallel with a capacitor (see Fig. 2.6(a)). The impedance of such a circuit is given by [52]:

$$Z_{TL} = Z_0 \frac{1 + i \tan \beta l \tanh \alpha l}{\tanh \alpha l + i \tan \beta l} \approx \frac{Z_0}{\alpha l + i \frac{\pi}{\omega_0}(\omega - \omega_n)}, \tag{2.123}$$

with $\beta = \omega_n / v_p$ and $\omega_n = n\omega_0$, where α is the attenuation constant l is the TL length, and n is the mode number. The impedance Z_{TL} can be approximated as in the second expression given in

Eq. 2.123 by considering small losses and frequencies close to the resonance frequency of the n^{th} mode. Near the resonance frequency, the TL model can be approximated by lumped circuit elements consisting of a parallel combination of a resistor R, inductor L, and capacitor C (see Fig. 2.6(b)) where the impedance is given by:

$$Z_{RCL} = \left(\frac{1}{i\omega L} + i\omega C + \frac{1}{R} \right)^{-1} \approx \frac{R}{1 + 2iRC(\omega - \omega_n)}. \qquad (2.124)$$

Thus the two models have a similar form for the impedance near the resonance frequency. The internal and quality factor of the RCL model is due to losses due to the resonator itself and is given by:

$$Q_{\text{int}} = \omega_n RC. \qquad (2.125)$$

The external quality factor is dominated by losses through the coupling capacitor and resistive and radiative losses and is given by:

$$Q_{ext} = \omega_n R'C/2, \qquad (2.126)$$

where R' is given by:

$$R' = \frac{1 + \omega_n^2 C_k^2 R_L^2}{\omega_n^2 C_k^2 R_L^2}, \qquad (2.127)$$

here, C_k is the coupling capacitor and R_L is the load resistor in series with the coupling capacitor. The loaded quality factor is a combination of the internal and external quality factors:

$$Q^{-1} = Q_{\text{int}}^{-1} + Q_{ext}^{-1}. \qquad (2.128)$$

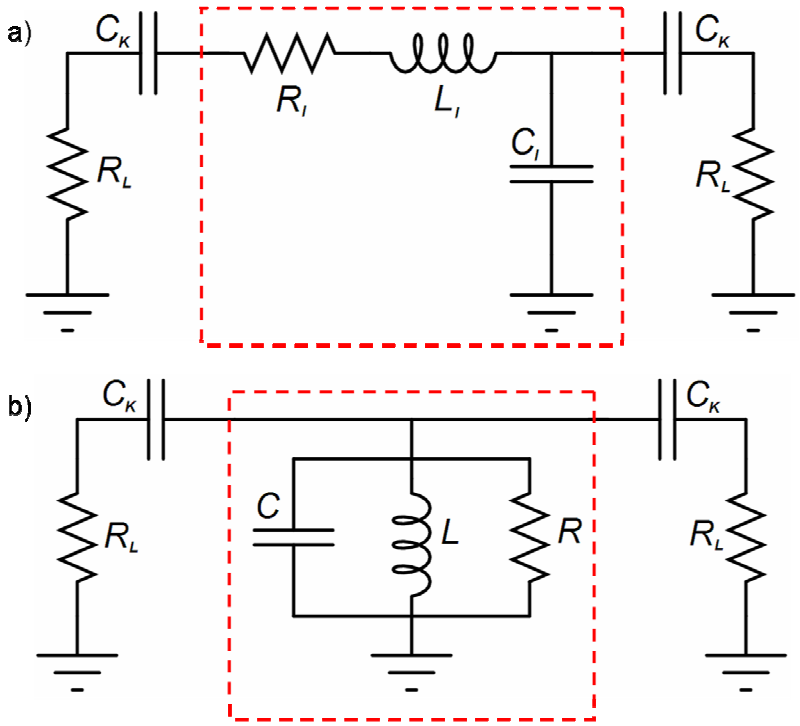

Fig. 2.6: (a) The TL model of the resonator showing the distributed element circuit in the dashed red box. The resonator is coupled to the input and output through a capacitor C_k and resistor R_L. (b) The RCL model of the resonator (in dashed red box) coupled to the input and output.

The insertion loss of the resonator is the shift in dB of the peak from unity and is a function of the quality factor of the resonator:

$$L_0 = -20\log\left(\frac{g}{g+1}\right) \text{ dB}, \qquad (2.129)$$

where g is defined by $g = Q_{\text{int}}/Q_{ext}$.

2.12 Duffing oscillator

The physics of a Duffing oscillator, that is an oscillator containing a non-linearity and displaying a bifurcation, can be understood through the prototypical example of a simple pendulum with a damping term (see Fig. 2.7). Following much of [53], the equation of motion can be written as:

$$ml^2\ddot{\theta}(t) + \gamma\dot{\theta}(t) + mgl\sin\theta = F\cos\omega t + F_N, \qquad (2.130)$$

where m is the mass of the pendulum, l is the length, θ is the angle of deflection, γ is the viscous damping coefficient, g is the acceleration due to gravity, F is an externally applied force at frequency ω, and F_N is an external noise source.

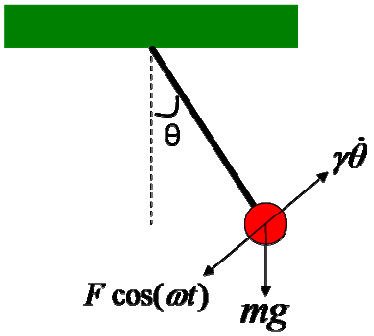

Fig. 2.7: Schematic of a simple non-linear pendulum that is subject to a driving force $F\cos(\omega t)$ *and damping* $-\gamma\dot{\theta}$. *This is the prototypical example of a Duffing oscillator, which is a non-linear oscillator that shows bifurcation.*

When the oscillations are small, $\sin(\theta)$ can be expanded as

$\sin(\theta) \cong \theta - \frac{1}{6}\theta^3 + O(\theta^5) = \theta - \frac{1}{6}\theta^3$ and the equation of motion can be written as:

$$\ddot{\theta}(t) + 2\Gamma\dot{\theta}(t) + \omega_0^2\theta\left(1 - \frac{1}{6}\theta^2\right) = \frac{F}{ml^2}\cos\omega t + \frac{F_N}{ml^2}, \qquad (2.131)$$

where the resonance bandwidth is given by $2\Gamma = \gamma/ml^2$ and the resonance frequency is $\omega_0 = \sqrt{g/l}$. For a weak non-linearity, the first harmonic of the amplitude oscillation can be solved for using the rotating wave approximation by substituting the following into Eq. 2.131:

$$\theta(t) = A(t)e^{i\omega t} + c.c., \tag{2.132}$$

where $A(t)$ varies slowly on the time scale of ω^{-1} and *c.c.* is the complex conjugate. After neglecting $\ddot{A}(t)$, averaging over the period $2\pi/\omega$, and some rescaling, we have:

$$\dot{B}(\tau) + \left(\frac{1}{\Omega} - i\frac{\varsigma}{\Omega} + i|B|^2\right)B = -i\sqrt{\beta} + \tilde{v}_N(\tau), \tag{2.133}$$

where $B(\tau)$ is the rescaled slow oscillation amplitude and is given by:

$$B(\tau) = \sqrt{\frac{\omega_0^2}{4\omega\delta\omega}}A(\tau), \tag{2.134}$$

where $\Omega = \delta\omega/\Gamma$ is the reduced detuning, $\varsigma = \frac{\omega + \omega_0}{2\omega}\Omega \approx \Omega$, $\delta\omega = \omega_0 - \omega$ is the detuning, $\tilde{v}_N(\tau)$ is the rescaled noise, $\tau = \delta\omega t$ is the rescaled time, and the rescaled drive power is given by:

$$\beta = \frac{gF^2}{64m^2l^5\omega^3\delta\omega^3}. \tag{2.135}$$

By setting $\dot{B}(\tau) = 0$, ignoring the noise term, and taking the modulus squared of both sides of Eq. 2.133, the steady state solution can be found:

$$|B|^2\left(\frac{1}{\Omega}+\left(\frac{\varsigma}{\Omega}-|B|^2\right)^2\right)=\beta. \qquad (2.136)$$

The solutions to this equation are shown in Fig. 2.8, which shows the dependence of the reduced dimensionless oscillation amplitude $|B|^2$ on the detuning Ω. The typical Lorentzian profile is observed at low input powers. Due to the non-linearity, as the input power β is increased, the resonance frequency bends towards lower frequencies. Eventually, an overhang appears indicating that there are three possible oscillating states. The dashed middle part of the curve shows the unstable solution and gives rise to hysteresis. As the frequency is increased from left to right, the system first follows the lower branch until it jumps at frequency f_1 to the upper branch when it reaches the instability. However, as the frequency is reduced from right to left, the system follows the upper branch and then jumps at frequency f_2 to the lower branch. Thus, the Duffing oscillator is hysteretic and the jumps in transmission is the bifurcation discussed above. The behavior of the Duffing oscillator discussed in this section can be applied to any linear oscillator to which a cubic nonlinearity is added to the "position" coordinate or any of its derivatives.

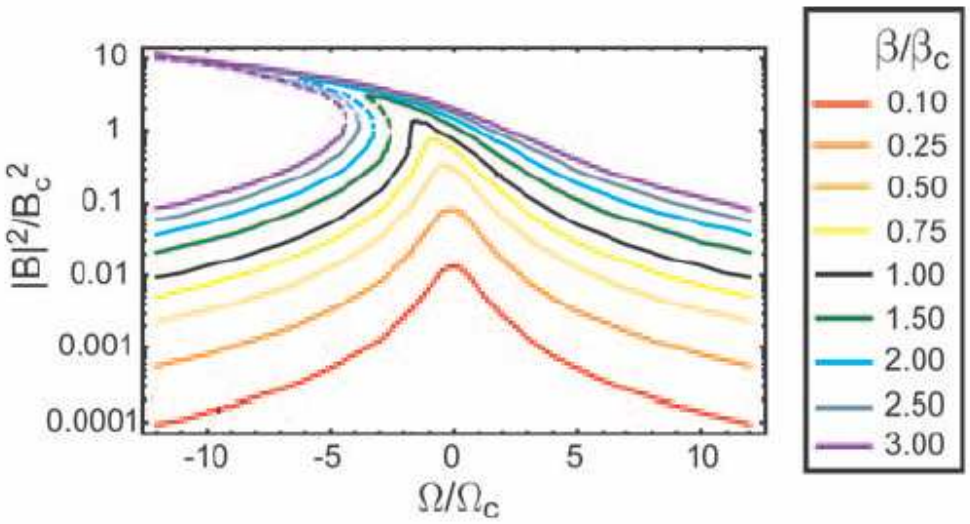

Fig. 2.8: A plot of the dependence of the dimensionless oscillation amplitude $|B|^2$ normalized to the amplitude at the ciritcal point B_c^2 on the normalized detuning Ω. The black curve corresponds to the critical input power. The dashed part of each curve is the unstable zone. The graph is taken from [53].

2.13 Equation of motion for phase evolution in a biased resistively and capacitively shunted junction with a series inductance

Our resonator can be modeled using the lumped circuit approximation since the characteristic length scale of the circuit is much less than the wavelengths considered in the experiments. Using this approach, the nanowire-interrupted resonator can be modeled using the circuit described in Fig. 2.9. In this model, the values of the resistance *R*, capacitance *C*, and inductance *L* are derived from the properties of the resonator itself. The effect of the nanowire is taken into account through its kinetic inductance by the insertion of a Joesphson junction (JJ) in series with the inductor. (The model presented is exactly correct only for short wires, for which the CPR is sinusoidal. For longer wires we expect that the model is at least approximately correct, based on our numerical simulations.) This schematic allows the ratio of the inductances from the

resonator and nanowire to be adjusted allowing for various strength Duffing nonlinearity effects. In the model, the circuit is biased with a current I_{bias}, which is a sinusoidal current with a frequency in the microwave spectrum.

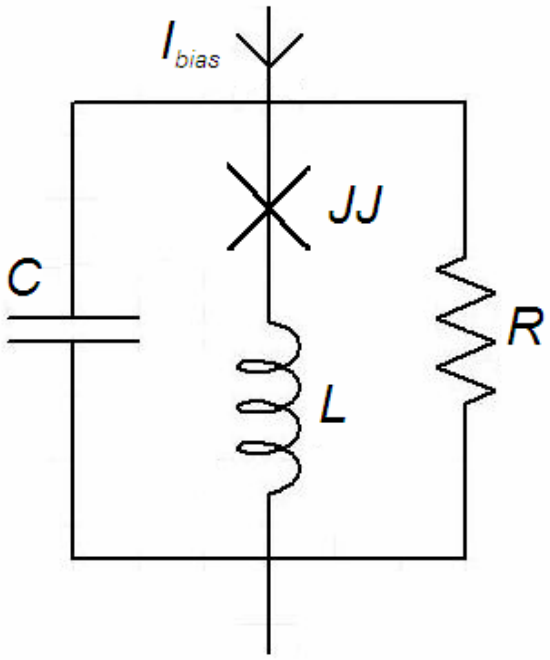

Fig. 2.9: The nanowire-resonator is modeled as a resistively and capacitively shunted junction with an inserted inductance in series with the junction. It is biased by a sinusoidal current with a frequency in the microwave spectrum.

To solve this circuit, a numerical method is employed. The goal is to find an equation to evolve the superconducting phase ϕ of the circuit as a function of time. We start by solving for the current through the capacitor:

$$I_{CAP} = I_{bias} - I_s - I_R , \qquad (2.137)$$

where I_s is the supercurrent through the junction given by $I_s = I_c \sin\phi$ and I_R is the current through the resistor and is given by Ohm's law $I_R = V/R$, here I_c is the critical current of the junction and V is the voltage across the resistor given by:

$$V = \frac{\hbar}{2e}\dot{\phi} + L\dot{I}_s . \tag{2.138}$$

The first- and second-order time derivatives of the supercurrent through the junction are:

$$\dot{I}_s = I_c\dot{\phi}\cos\phi \quad \text{and} \quad \ddot{I}_s = I_c\left(\ddot{\phi}\cos\phi - \dot{\phi}^2\sin\phi\right).$$

The time derivative of the voltage can be found and related to the current through the capacitor:

$$\dot{V} = \frac{\hbar}{2e}\ddot{\phi} + L\ddot{I}_s = \frac{\hbar}{2e}\ddot{\phi} + LI_c\left(\ddot{\phi}\cos\phi - \dot{\phi}^2\sin\phi\right) = \frac{I_{CAP}}{C} .$$

Solving for the second time derivative of the phase results in:

$$\ddot{\phi} = \left[\frac{I_{CAP}/C + LI_c\dot{\phi}^2\sin\phi}{\hbar/2e + LI_c\cos\phi}\right]. \tag{2.139}$$

Now we can numerically solve for the circuit phase and its first derivative by initializing them to zero and then evolving them according to:

$$\dot{\phi}_n = \dot{\phi}_{n-1} + \tau\ddot{\phi}_n \quad \text{and} \quad \phi_n = \phi_{n-1} + \tau\dot{\phi}_n , \tag{2.140}$$

where τ is the time step of the numerical integration and n is the step number. The voltage and supercurrent can all be solved as a function of time knowing the phase and its first derivative according to Eqs. 2.138 and 2.50.

---

[1] J. Bardeen, L. N. Cooper, and J. R. Schrieffer, Phys. Rev. **108**, 1175 (1957).
[2] V. L. Ginzburg and L. D. Landau, Zh. Eksperim. i. Teor. Fiz. **20**, 1064 (1950).
[3] L. P. Gor'kov, Zh. Eksperim. i. Teor. Fiz. **36**, 1918 (1959) [Soviet Phys.—JETP **9**, 1364 (1959)].
[4] W. A. Little, Phys. Rev. **156**, 396 (1967).
[5] K. K. Likharev, Rev. of Mod. Phys. **51**, 101 (1979).
[6] S. Langer and V. Ambegaokar, Phys, Rev. **164**, 498 (1967).
[7] Michael Tinkham, *Introduction to superconductivity* (Dover, 2004).

[8] A. T. Bollinger, PhD thesis, University of Illinois at Urbana-Champaign (2005).
[9] M. Sahu, M.-H. Bae, A. Rogachev, D. Pekker, T.-C. Wei, N. Shah, P. M. Goldbart, and A. Bezryadin, Nature Physics **5**, 503-508 (2009).
[10] B. Muhlschlegel, Z. Phys. **155**, 313 (1959).
[11] J. Bardeen, Rev. Mod. Phys**. 34,** 667 (1962).
[12] M. Tinkham, J. U. Free, C. N. Lau, and N. Markovic, Phys. Rev. B **68**, 134515 (2003).
[13] A. Bezryadin, J. Phys.:Condens Matter **20,** 043202 (2008).
[14] D. E. McCumber and B. I. Halperin, Phys. Rev. B **1**, 1054 (1970).
[15] B. D. Josephson, Phys. Lett. **1**, 251 (1962).
[16] B. D. Josephson, Advan. in Phys. **14**, 419 (1965).
[17] D. E. McCumber, J. App. Phys. **39**, 3113 (1968).
[18] J. M. Martinis, M. H. Devoret, and J. Clarke, Phys. Rev. B **35**, 4682 (1987).
[19] N. Shah, D. Pekker, P. M. Goldbart, Phys. Rev. Lett. **101**, 207001 (2008).
[20] D. Pekker, N. Shah, M. Sahu, A. Bezryadin, and P. M. Goldbart, Phys. Rev. B **80**, 214525 (2009).
[21] M. Sahu, M.-H. Bae, A. Rogachev, D. Pekker, T.-C. Wei, N. Shah, P. M. Goldbart, and A. Bezryadin, Nature Physics **5**, 503-508 (2009).
[22] N. Giordano, Phys. Rev. Lett. **61**, 2137 (1988).
[23] N. Giordano and E. R. Schuler, Phys. Rev. Lett. **63**, 2417 (1989).
[24] E. Ben-Jacob, D. J. Bergman, B. J. Matkowsky, and Z. Schuss, Phys. Rev. A **26,** 2805 (1982).
[25] A. Garg, Phys. Rev. B **51**, 15592 (1995).
[26] T. A. Fulton and L. N. Dunkleberger, Phys. Rev. B **9** 4760 (1974).
[27] M. Tinkham, C. N. Lau, App. Phys. Lett. **80**, 2946 (2002).
[28] W. A. Little and R. D. Parks, Phys. Rev. Lett. **9**, 9 (1962).
[29] R. Jaklevic, J. Lambe, A. Silver, and J. Mercereau, Phys. Rev. Lett. **12**, 159 (1969).
[30] D. S. Hopkins, D. Pekker, P. M. Goldbart, and A. Bezryadin, Science **308**, 1762 (2005).
[31] D. Pekker, A. Bezryadin, D. S. Hopkins, and P. M. Goldbart, Phys. Rev. B **72**, 104517 (2005).
[32] F. Sharifi, A. V. Herzog, and R. C. Dynes, Phys. Rev. Lett. **71**, 428 (1993).
[33] P. Xiong, A. V. Herzog, and R. C. Dynes, Phys. Rev. Lett. **78**, 927 (1997).
[34] A. Bezyradin, C. N. Lau, and M. Tinkham, Nat. **404**, 971 (2000).
[35] A. T. Bollinger, R. C. Dinsmore III, A. Rogachev, and A. Bezyradin, Phys. Rev. Lett. **101**, 227003 (2008).
[36] A. Rogachev and A. Bezryadin, Appl. Phys. Lett. **83**, 512 (2003).
[37] A. T. Bollinger, A. Rogachev, and A. Bezryadin, EuroPhys. Lett. **76**, 505 (2006).
[38] Y. Oreg and A. M. Finkel'stein, Phys. Rev. Lett. **83**, 191 (1999).
[39] H. Ebisawa, H. Fukuyama, and S. Maekawa, J. Phys. Soc. Jpn. **55**, 4408 (1986).
[40] Y.-J. Kim and K. J. Chang, Mod. Phys. Lett. B **12**, 763 (1998).
[41] N. Giordano, Phys. Rev. Lett. **61**, 2137 (1988).
[42] A. D. Zaikin, D. S. Goluvev, A. van Otterlo, and G. T. Zimányi, Phys. Rev. Lett. **78**, 1552 (1997).
[43] D. S. Golubev, and A. D. Zaikin, Phys. Rev. B **64**, 014504 (2001).
[44] A. O. Caldeira and A. J. Leggett, Phys. Rev. Lett. **46**, 211 (1981).
[45] J. S. Penttilä, Ü. Parts, P. J. Hakonen, M. A. Paalanen, and E. B. Sonin, Phys. Rev. Lett. **82**, 1004 (1999).
[46] J. P. Pekola, K. P. Hirvi, J. P. Kauppinen, and M. A. Paalanen, Phys. Rev. Lett. **77**, 3889 (1994).
[47] Y. V. Nazarov, Phys. Rev. Lett. **82**, 1245 (1999).
[48] D. S. Golubev and A. D. Zaikin, Phys. Rev. Lett. **86**, 4887 (2001).
[49] M. Göppl, A. Fragner, M. Baur, R. Bianchetti, S. Filipp, J. M. Fink, P. J. Leek, G. Puebla, L. Steffen, and A. Wallraff, J. of Appl. Phys. **104**, 113904 (2008).
[50] S. Gevorgian, L. J. P. Linnér, and E. L. Kollberg, IEEE Trans. Microwave Theory Tech. **43**, 772 (1995).
[51] K. Watanabe, K. Yoshida, T. Aoki, and S. Kohjiro, Jpn. J. Appl. Phys. Part 1 **33**, 5708 (1994).
[52] D. M. Pozar, *Microwave Engineering* (Addison-Wesley, 1993).
[53] M. B. Metcalfe, PhD thesis, *Yale University* (2008).

Chapter 3

Fabrication and transport measurements of nanowire devices

3.1 Fabrication of nanowires by metal coating of carbon nanotubes

Throughout the history of superconducting nanowires, a variety of fabrication techniques have been used to make ultra-thin, one-dimensional nanowires which include: using single crystals of tin [1,2], step edge [3], stencil mask [4], and e-beam lithography in conjunction with Ar-ion milling [5]. With each of these methods it is difficult to make thin nanowires that are homogeneous, superconducting at low temperatures, and make seamless contact to the electrodes to prevent issues associated with contact resistance. Many interesting phenomena including the superconductor to insulator transition (SIT) [4] and the observation of quantum phase slips (QPS) [6] in nanowires requires the diameter of the nanowires to be small and easily controlled, which was difficult with these older methods. However, the molecular templating technique developed by Bezryadin et al. and refined by other members of his group [7,8,9,10] can achieve such ultra-thin and highly-homogeneous nanowires with no contact resistance.

All the nanowires used in this thesis were fabricated by the molecular templating technique. In short, the molecular templating technique consists in using a molecular object—such as glue molecules [10], DNA [8,11], WS_2 nanorods [12], carbon nanotubes [7,13], or fluorinated carbon nanotubes [14,15] (which were primarily used in this thesis)—as a scaffolding

to support the superconducting material, which forms the nanowire. Using the molecular templating technique has many advantages including: controlling the diameter and length of nanowire, the availability of many wires to choose from, and the option of making wires out of any material that can be sputtered or evaporated. Additionally, this method allows one to make multi-wire devices and nanowires situated in superconducting Fabry-Perot resonators, as was done in this thesis. All of the fabrication presented in this section was performed at the Center for Microanalysis of Materials (CMM) and the Microfabrication Facility, which are both part of the Frederick Seitz Materials Research Laboratory (MRL).

3.1.1 Preparation of the substrate

The first step in fabricating superconducting nanowires using the molecular templating method is to prepare a substrate containing a ~100-500 nm trench which will be used to suspend a scaffolding to build the nanowire upon (see Fig. 3.1). We start by purchasing a 4 inch in diameter Si (100), which is typically 500 μm thick (sometimes we use doped Si so that a gate electrode can be used at low temperatures). On top of the Si wafer there are two layers of oxide. The bottom layer is a 100 nm SiO_2 film grown by dry oxidation and the top layer is a 400 nm film of SiO_2 grown by wet oxidation. Above the oxide we deposit a 60 nm thick layer of low stress SiN by a low-pressure chemical vapor deposition process. Before being shipped from James River Semiconductor, Inc., the wafer is coated with a PMMA protective layer, which must be removed by submerging the entire wafer in acetone and agitating or swirling it for 30-45 seconds until it is clean. The wafer is then rinsed in isopropanol and blown dry with nitrogen. The entire wafer is then coated with an e-beam sensitive resist (PMMA) and then brought to the e-beam writing facility. Here fine lines with widths of ~100-500 nm and spaced a distance of 4.8 (6mm for resonator samples) mm apart are written. In order to locate the position

of the nanowire along the trench in later identification and optical lithography processes, number markers are written next to each line, from -119 to +119, and are spaced 20 μm apart. Additionally, larger crosses (visible to the naked eye) are drawn at the midpoint between the written lines (soon to be trenches) to help guide the subsequent dicing of the wafer into usable chips.

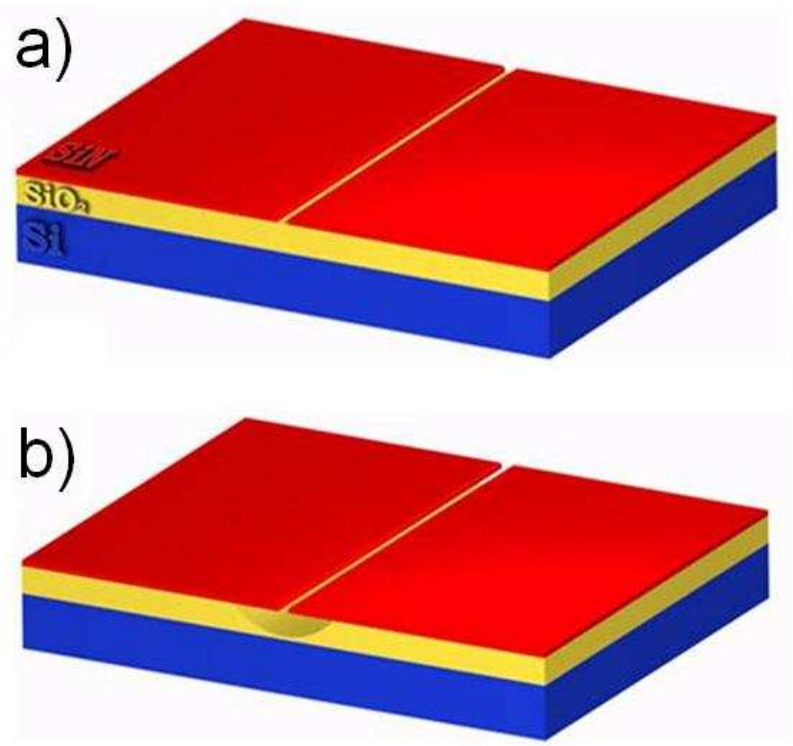

Figure 3.1: Preparation of the substrate: (a) Si (0.5 mm) - SiO_2 (500 nm) - SiN (60 nm) substrate with a 100-500 nm wide trench, which is defined by e-beam lithography and reactive ion etched in SF_6 plasma. (b) Substrate with an under-cut in the SiO_2 layer produced by a HF wet etch, which etches SiO_2 much faster than SiN.

After the e-beam pattern has been developed, the pattern is transferred to the SiN layer using reactive ion etching (RIE) (see Fig. 3.2). We first break the wafer into four quarters including a small test chip using a diamond tip. The test chip is then put in a Uniaxis 790 series reactive ion etching system where a plasma is generated and used to etch the exposed areas of

the SiN film using SF_6 gas at a 20 sccm flow rate, 60 mT of pressure, 75 W of power, and over 2.5-5 minutes of time. Once the correct etching interval is determined, RIE is done on the rest of the quarter wafer under the same conditions. At this point, the trenches have developed in the SiN layer. The wafer is then cleaned by submersion and agitation in acetone for 30 seconds, isopropanol for 30 seconds, and finally blown dry with nitrogen gas. A layer of photoresist (AZ5214) is then applied on top of the entire wafer to protect the surface from damage that can occur from the Si "dust" during the dicing process. An automated dicing saw is then used to cut the sample into 4.8 mm X 4.8 mm chips for standard nanowire samples, and 4.8 mm X 12 mm chips for nanowire-resonator samples. Once this process is complete, the chips can be easily divided and are stored in a drawer at room temperature, ready to be cleaned as they are needed to make nanowires.

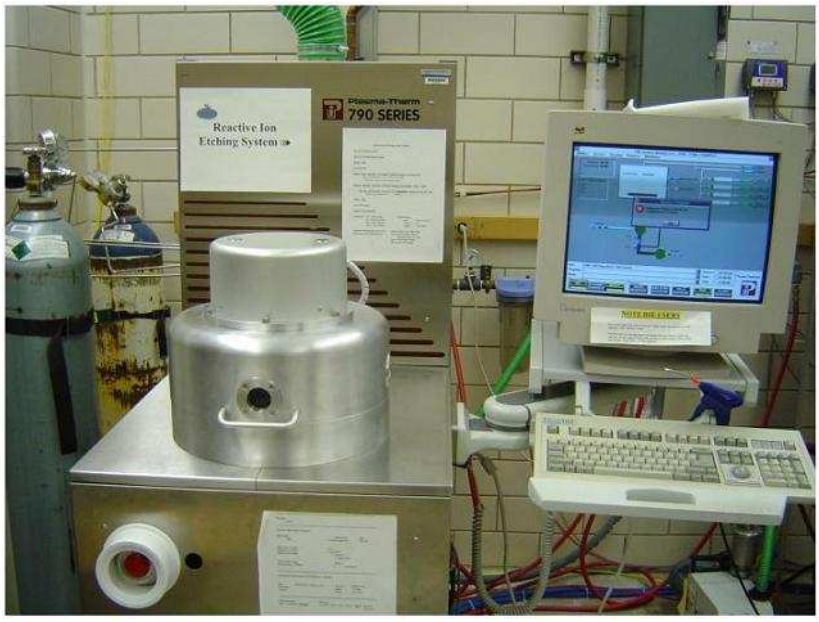

Figure 3.2: The Uniaxis 790 Series Reactive Ion Etching System located in the Materials Research Laboratory's Microfabrication facility.

To begin the cleaning process, 9 new and clean scintillation vials (used as simple glass beakers here) are opened and blown with nitrogen gas to expel any dirt or dust particles. They are placed in the fume hood and filled in order with (1) Acetone, (2) Acetone, (3) deionized (DI)

H_20, (4) Nitric Acid, (5) DI H_20, (6) DI H_20, (7) Nitric Acid, (8) DI H_20, and (9) Isopropanol. In between (5) and (6) a plastic cup is filled partly with a 49% solution of Hydroflouric Acid (HF). The chip is then grasped with tweezers and immersed and agitated in acetone (1) for ~30 s to remove the majority of the photoresist that was deposited on the wafer to protect it from the dicing process. Because of the large chunks of photoresist now present in the solution of acetone, the chip is placed in a new vial of acetone (2) and sonicated for ~5 min to remove the remaining photoresist from the surface of the chip. The chip is then immersed and agitated in DI H_20 (3) for ~30 s to remove the acetone and is then placed in a vial of Nitric Acid (4) and sonicated for ~5 min to remove organic contaminants. A DI H_20 rinse is done again to remove the Nitric Acid (5) and then the sample is immersed and agitated (i.e., just moved back and forth slowly, but not sonicated) in the HF for ~10 s, to form an undercut in the SiO_2 layer near the trench; this helps to prevent electrical leakage between the electrodes that will be formed in a later step. The undercut forms because the HF etches the SiO_2 at a much faster rate than the SiN. Another DI H_20 rinse is done (6) to remove the HF and stop the etching process. At this point, the sample is immersed and agitated in Nitric Acid (7) for ~2 min to remove any remaining organic contamination and then agitated in DI H_20 (8) for ~30 s to remove the Nitric Acid. The chip is then immersed and agitated in isopropanol (9) for ~30 s to remove the DI H_20, and finally blown dry with pressurized nitrogen gas. The chip is now ready for the deposition of carbon nanotubes or another molecular agent capable of being used as a scaffolding to form the nanowire(s).

3.1.2 Deposition of fluorinated single-wall carbon nanotubes

When using the molecular templating technique, it is important that the scaffolding has a small diameter and a high resistance (insulating) to prevent the scaffolding from influencing the

electrical measurement of the nanowire. Thus when fabricating our nanowires, we primarily use fluorinated single-wall carbon nanotubes (FSWNTs). These nanotubes adhere to the SiN surface and can be as long as a few microns long, giving them the potential to bridge the trench and form a molecular scaffolding to support a nanowire. They also have a small diameter, ~1 nm, allowing us to fabricate nanowires with small diameters and test the limits of superconductivity and the effects of quantum phase slips (QPS). They have also been demonstrated to be insulating [16] which eliminates any possible parallel conduction channel through the nanotube itself. They are insulating because the conduction electrons that are free in the unfluorinated nanotubes are bound to the fluorine atoms in the fluorinated nanotubes. This important property of the nanotube prevents other sources of environmental dissipation, which otherwise would play a strong role in studying the rate of QPS and the effect of resistive shunting on the superconducting nanowire. There are many other materials that can also adhere to the nanotube, especially with the aid of a thin sticking layer, thus allowing one to fabricate various types of nanowires.

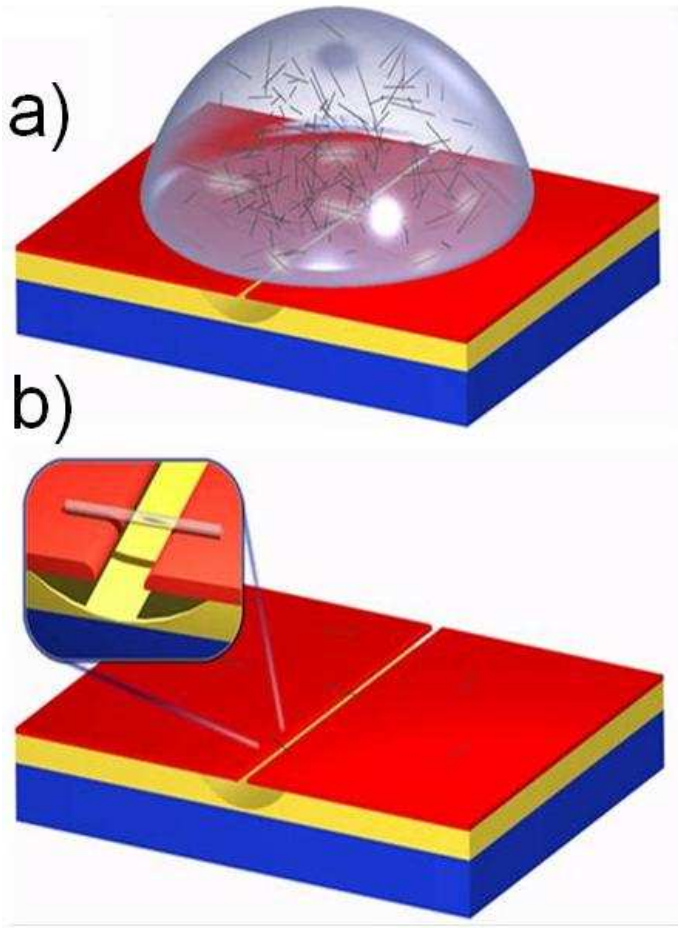

Figure 3.3: Deposition of fluorinated single-walled carbon nanotubes: (a) Carbon nanotubes are suspended in isopropanol and dropped onto the surface of the substrate. The nanotubes are allowed to settle for ~1 min and stick to the surface of the substrate. (b) The substrate is dried with forced nitrogen gas, and the nanotubes that settled onto the surface of the substrate adhere to the surface. Randomly, some of these nanotubes may span the trench.

The FSWNTs also have the advantage that they do not need to be grown in the lab but are commercially available from Carbon Nanotechnologies, Inc. They can also easily be placed in solution by dissolving them in isoproponal, which is the first step in our nanotube deposition process. We begin by preparing a "master solution", which is usually highly concentrated with nanotubes. To do this, we insert a clean capillary tube into the FSWNT container and tap the black, soot-like powder which results in a small quantity of FSWNT powder sticking inside the capillary tube. The tube is then placed over a clean scintillation vial filled with laboratory-grade

isoproponal and tapped a few times to release the FSWNT into the scintillation vial. The solution is then sonicated for about 20 min which breaks up the FSWNT cluster and promotes their dissolving. After sonication, the solution is typically a dark murky grey color and more sonication is performed if there are still visible chunks of FSWNTs. If not, then the master solution is ready and a dilution process needs to be carried out to reduce the concentration.

If the master solution has not been used recently, then sonication for ~10 min is necessary to dissolve any FSWNTs that have settled out of solution. Once this is done, the master solution is diluted anywhere from 1:5 to 1:20 in isoporponal, depending on the initial concentration of FSWNTs. To check the concentration, nanotubes are deposited onto one prepared and cleaned chip from section 3.1.1 and then analyzed under a scanning electron microscope (SEM). With the chip on a clean, dust-free paper, the nanotubes are deposited with two drops of the diluted FSWNT solution dispensed from a clean pipette. The drop is allowed to sit on the chip (see Fig. 3.3(a)) for ~1 min. If the drop slides off the chip, another one is dispensed to replace it. Forced nitrogen gas is then used to blow the drop off the chip. Some nanotubes will have fallen out of solution and rest on the chip. Randomly, a small percentage of precipitated nanotubes will have landed across the gap, thus spanning the trench (see Fig. 3.3(b)). Ideally, we would like to have ~1 nanotube across the trench for every 20 μm of trench length. This concentration is then checked in the SEM and the solution is diluted appropriately if the concentration is too high or remade from the master solution if the concentration is too low. This process can be used to determine the concentration for a given trench width; however, if nanowires of a different length are desired, the concentration will have to be altered by increasing (decreasing) it for wider (narrower) trenches. If the FSWNT solution is not used for a while in order to maintain the correct concentration, a mark should be made to indicate the volume of the solution and extra

isoproponal added, as the isoproponal slowly evaporates over time. Once the correct concentration is achieved, the deposition process can be followed as outlined above and the sample is now ready for metal deposition.

3.1.3 Sputter coating with superconducting metal

Once the molecular agent (i.e., the fluorinated nanotube) is deposited across the trench, the sample is ready for metal deposition. The goal of this molecular templating process has been to make superconducting nanowires that are thin, homogeneous, and simultaneously well-connected to the electrodes. It is also necessary that the critical temperature (T_c) is high enough so that the various superconducting properties of the nanowire can be studied using our standard ^{4}He and ^{3}He cryostats. Thus, the specific choice of using the MoGe alloy has been set by these conditions and the heavy historical influence of our group, which has used MoGe as the metal of choice in forming superconducting nanowires using nanotubes [9,14,17,18], DNA [8,11], and polymers [10] as the scaffolding.

Previous studies on $Mo_{1-x}Ge_x$ have shown that the T_c of $Mo_{1-x}Ge_x$ increases linearly as the concentration of Ge is reduced until $x < 0.2$ (see Fig. 3.4), where there is a structural change in the MoGe from an amorphous state to a body-centered-cubic (BCC) crystalline structure [19,20]. We have chosen to use $Mo_{1-x}Ge_x$ (purchased from Williams Advanced Materials) with $0.21 < x < 0.24$, to obtain the maximum possible T_c while avoiding the structural transition. Table 3.1 presents some typical parameters of this material that are relevant to our work.

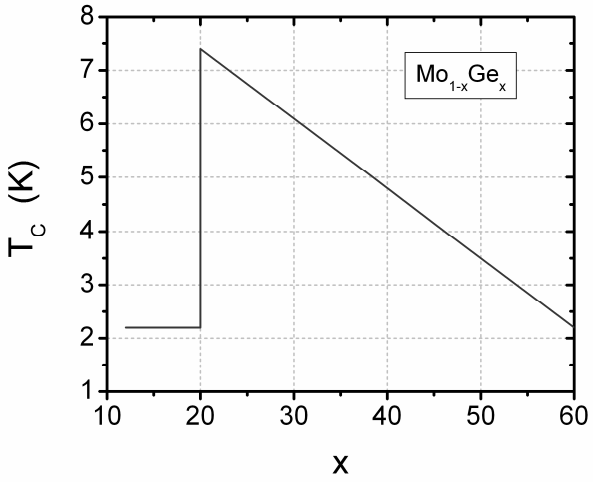

Figure 3.4: Bulk T_C as a function of germanium content, x, for $Mo_{1-x}Ge_x$.

Table 3.1: Properties of MoGe: (*) Measured and derived physical parameters of MoGe from [20].

Resistivity (ρ)	~ 180 μ Ω cm
Mean Free Path (l)	~ 3 Å
Fermi Velocity (v)	~ 10^6 m/s
Transition Temperature (T_c)	~ 7.4 K (bulk)* 0-7.4 K (film; the T_c drops as the film thickness is reduced)*
Energy Gap ($\Delta(0)$)	~ 1.1 meV (bulk)* ~ 1.0 meV (film)*
Ginzburg-Landau coherence length ($\xi(0)$)	~ 4.4 nm (bulk)* ~ 4.9 nm (film)*
Magnetic Penetration Depth ($\lambda_{eff}(0)$)	~ 424 nm (film)*
Lower Critical Field (H_{C1})	~ 2 mT (film)
Upper Critical Field (H_{C2})	~ 12.2 T (bulk)* ~ 6.7 T (film)*

We sputter the MoGe using the AJA ATC 2000 custom four-gun co-sputtering system located in the Frederick Seitz Materials Research Laboratory's Microfabrication and Crystal Growth Facility (see Fig. 3.5(a)). The system is equipped with a liquid nitrogen cold trap that is essential for reducing oxygen, oil, and water impurities in the sputtered films, which can heavily reduce or eliminate the superconducting properties of the sputtered films. The main chamber base-pressure is typically below ~10^{-7} Torr before sputtering is commenced. The MoGe target is always pre-sputtered ~5 min (usually with the sample chuck inserted) before any sample is placed in the chamber, to reduce contamination from other materials and to clean the target from any oxide layer that may have formed since its last use. The chuck is then retrieved from the sputtering chamber and vacuum carbon tape is placed on its surface and touched a few times with latex gloves to decrease the adhesion, so that the samples can be extracted later without damaging the substrate. The samples are then placed on the carbon tape and inserted into the sample chamber and left to pump to low pressure. At this point, they are inserted into the sputtering chamber and set to rotate at ~20 rpm to ensure a better uniformity of the deposited films.

When the pressure in the sputtering chamber reached less than ~10^{-7} Torr, the films are sputtered using a DC power source of 150 W and an argon gas pressure of 3 mT, with a flow rate of 20 sccm into the chamber. Before opening the sample shutter, a visual check for the observation of a purple glow in the chamber is done to ensure a plasma is forming. Following the above mentioned procedure results in a sputtering rate of ~1 nm per 8 seconds (or 1.25 Å/s), which is subsequently determined by profilometry. We typically sputter ~5-25 nm of MoGe to make wires that are consistently superconducting or insulating, but are not wide enough for a two-dimensional fluctuation (i.e., a vortex) to reside in the wire. Note that we had to replace the

MoGe target with one from SCM Inc., when the previous sputtering conditions did not result in superconducting films. The problem was solved by creating higher sputtering rates. This was achieved by increasing the DC power to 300-400 W and decreasing the argon chamber pressure to below ~1 mT. Under these new conditions the sputtering rate increased to ~3 Å/s. However, with this new method a new problem periodically arose—at high powers the indium seal that binds the MoGe to the copper back plate can begin to melt and short the target. This problem was fixed by scrapping the indium short until it was fully removed. Indium-contaminated samples can be detected during the photolithography step when the metal does not etch in a hydrogen peroxide solution.

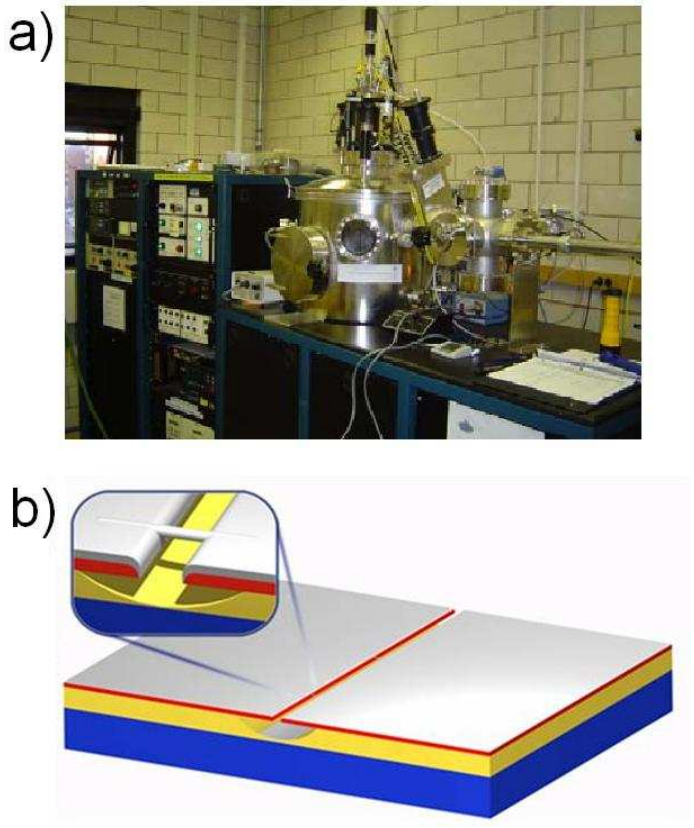

Figure 3.5: (a) The AJA ATC 2000 custom four-gun co-sputtering system located in the Materials Research Laboratory's Microfabrication Facility. (b) Deposition of metal: The surface of the substrate including the nanotubes are sputter coated with several nanometers of superconducting metal.

At this point, the samples now have a uniform layer of MoGe covering the SiN surface and the nanotube as can be seen in Fig. 3.5(b). When exposed to air, the MoGe film is weakly affected by oxidation, which can go as deep as ~2.5 nm initially, but which subsequently progresses at a much slower rate. Thus, we always store the sputter-coated samples in a dessicator until we are ready to perform other processes on the chip. The next step in the molecular templating method is to select the desired nanowire(s) that will be measured.

3.1.4 Scanning electron microscope and focused ion beam

After the sputtering process is complete, the two electrodes formed by the superconducting film on either side of the trench is connected by many nanowires along the length of the trench. For most of our measurements, only one or two high quality nanowires are desired to be measured. Thus, we scan the trench along its whole length (4.8 mm) searching for the identification, characterization, and location of the desired nanowire(s). This is done using a Hitachi S-4700 scanning electron microscope (SEM) and the SEM built into the FEI DB235 focused ion beam (FIB). Both of these instruments are capable of obtaining images with high resolution of ~5 nm. These instruments (see Fig. 3.6) are both located in the Center for Microanalysis of Materials (CMM).

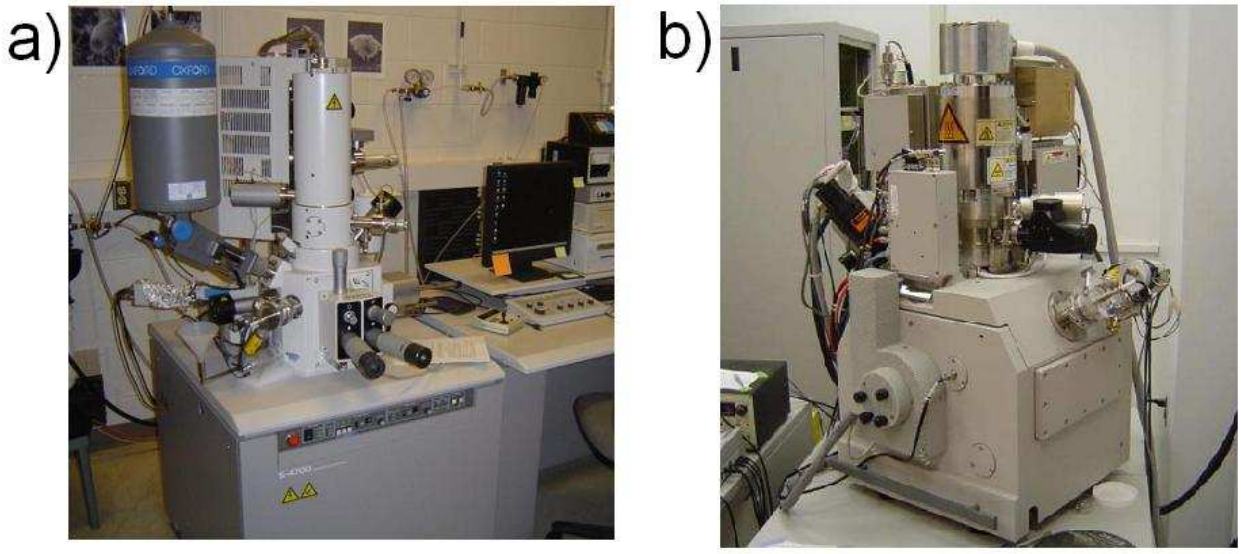

Figure 3.6: (a) The Hitachi S-4700. (b) The FEI DB235 FIB. Both instruments are part of the Material Research Laboratory's Center for Microanalysis of Materials facility.

The first step is to attach the samples to the sample stage using vacuum-compatible carbon tape that has been tapped a few times with a latex glove to reduce the adhesion to the sample. Once the sample is loaded and pumped to low pressure, we begin by finding the trench, focusing the electron beam, and then searching the trench. We typically begin the search at least 0.5 mm from the edge of the chip to reduce the probability of the electrode pattern contacting the outer ring of metal that is usually present after the photolithography step, and to avoid potential leakage for doped substrates. When searching the trench, our goal is to identify wire(s) that are visibly homogeneous, contain no breaks or granularity, and are well connected to both electrodes preventing issues associated with contact resistance. When wires are less than ~200 nm in length, we look for bright spots on the ends of the wires, indicating that a second surface is below the wire (reflecting more electrons) and that the wire is straight, stays in the plane of the upper surface of the SiN film, is well connected and firmly suspended across the trench. We also look for wires that are isolated from other wires or contamination by at least ~10 μm on either side. This is necessary because our photolithography mask has a bridge width of 20 μm, and all

nanowires protected under this mask will survive the subsequent H_2O_2 etching of MoGe. Additionally, there is a difficulty in some applications where the markers used for recording locations of the wires may cause defects in the film; such defects can become important when the magnetic screening current profile in the leads has an observable effect. Thus, whenever possible, the wires that are nearly halfway in between the markers were chosen for photolithography patterning (see Fig. 3.7(a)). Once the locations of all the potential nanowire(s) have been recorded, the SEM images are compared and the highest quality nanowire is chosen. The SEM images are then used to measure the length and width of the nanowire(s).

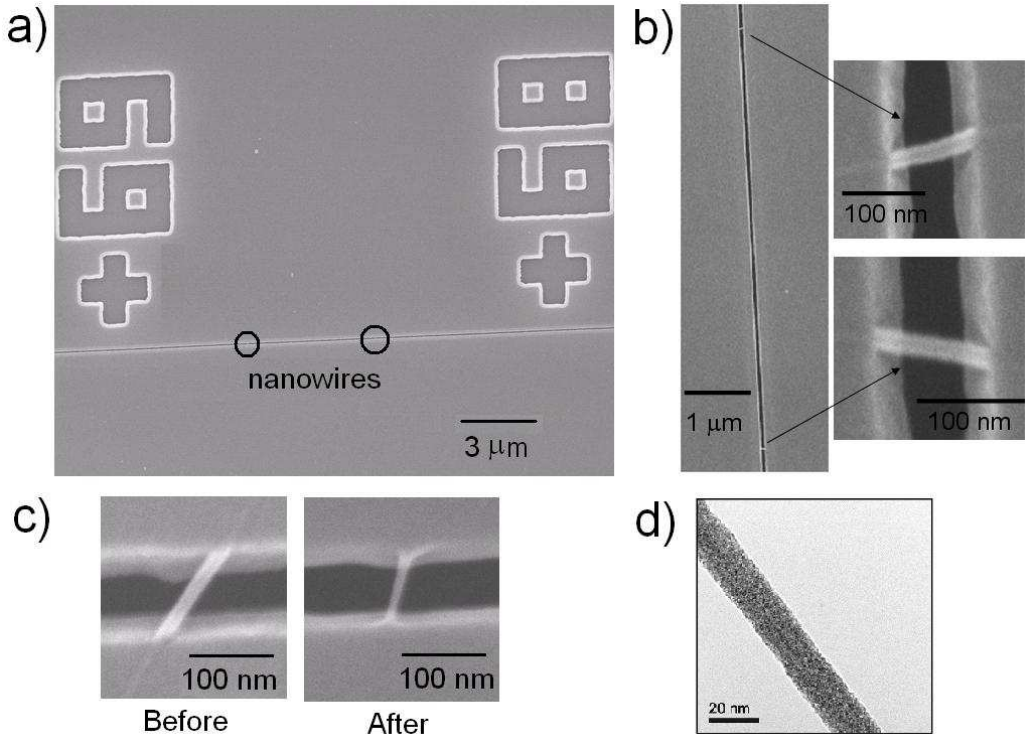

Figure 3.7: (a) Scanning Electron Microscope (SEM) image of alignment markers separated by 20 μm. The markers are large enough to be seen with an optical microscope during the photolithography mask alignment. The two black circles reveal the location of the two nanowires found between these markers. (b) A set of parallel nanowires separated by 6.8 μm. The wires cross a 100 nm wide trench (black line). The nanowires are 109 nm long and 25 nm wide (top) and 107 nm long and 23 nm wide (bottom). (c) A nanowire 130 nm long and 22 nm wide before focused ion beam (FIB) modification. After exposure to the ion beam, the width of the nanowire varies between 11 and 16 nm. (d) Transmission Electron Microscope (TEM) image of a nanowire demonstrating the amorphous structure of the MoGe alloy [21].

When the FIB is used to image the wires, it is possible to use the ion beam to remove undesired wires, contamination across the trench, or any remaining SiN bridges that were left from the stitching process of the e-beam writer. This process is performed by first aligning the electron and ion beam using a piece of dust, a marker, or the trench as a visual aid. In order for the ion beam to be aligned, the sample stage must be tilted by 52°. With this same tilt, the ion beam is focused using a similar aid within ~25 μm from the undesired object. For most modifications the 2.2 μA ion current is sent through a much smaller current aperture of ~10-30 pA to reduce damage and gallium contamination to the nearby film and nanowire(s). To perform the ion milling, the line tool is used to define the cut at a zoom of ~50 kX in the "electron mode". The stage is then tilted 52° and the cut is made with the ions. This technique may also be used to reduce the switching current of a nanowire by following the above procedure and substituting the definition of the cutting pattern from the line tool to a single screen image with the current aperture set between 1-10 pA and an exposure time of less than 0.3 sec (see Fig. 3.7(c)). This may be a useful tool to study the dependence of the nanowire critical current on the overall resonator properties in microwave nanowire-resonator applications.

3.1.5 Photolithography and etching

After the desired nanowires have been selected, imaged, and located, each sample is taken to the class-100 clean room located in the Materials Research Laboratory's Microfabrication and Crystal Growth Facility for photolithography (see Fig. 3.8). A hotplate in the clean room is covered with Al foil to help generate a uniform surface temperature. A glass microscope slide is placed on the aluminum foil, and the hotplate temperature is set to 120° C. After a few minutes, the hot plate has reached the desired temperature and the samples are placed on the glass slide

and heated for ~5 min to evaporate any water vapor that may be on the surface. The samples are then placed in a flow of dry nitrogen for ~5 min to cool down, which will allow the photoresist to stick more efficiently. Then, sequentially, each sample has a drop of photoresist (Shipley 1805 or 1813 positive resist) placed on top of the sample, which is then spun for ~25 sec at 8000 rpm. Once this step is complete the upper surface of the sample is uniformly coated with ~5 μm of photoresist. The relatively fast speeds for spinning are necessary for our small samples to get an even thin coat of resist as opposed to slower speeds that are sufficient for larger wafers. The sample is then placed back on the glass slide on the hotplate and soft-baked for 2 min at 120° C. At this point, the photoresist has hardened and the sample is ready for photolithography.

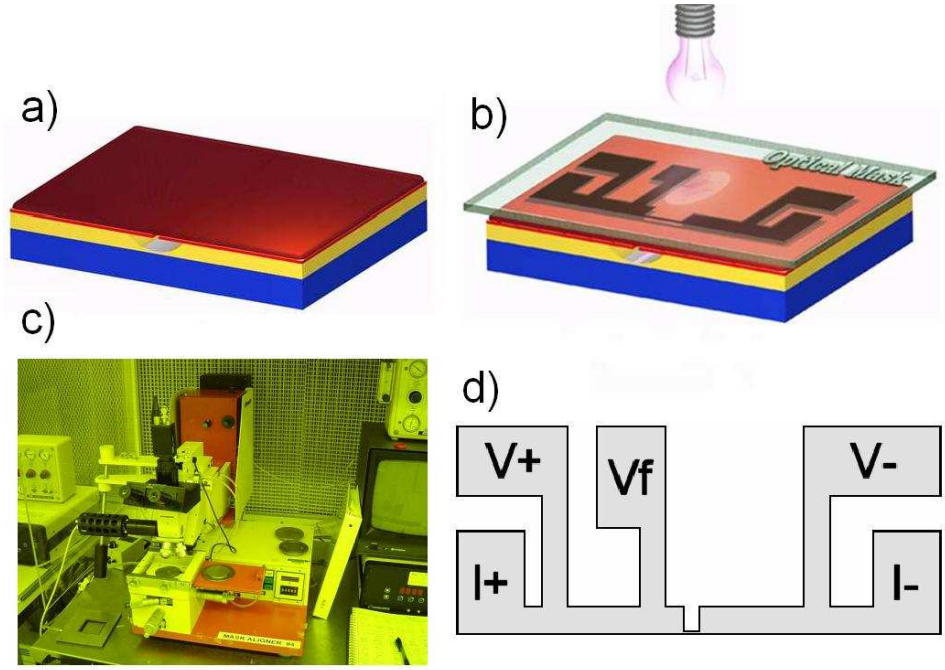

Figure 3.8: Photolithography process: (a) Photoresist is spin-coated onto the entire surface of the substrate. (b) An optical mask is aligned over the substrate and the sample is exposed to UV light. The mask is designed to isolate a single (or pair of) nanowire(s) and simultaneously create an electrode pattern for later measurements. (c) The Karl Suss MJB3 Mask Aligner located in the Microfabrication Clean Room in the Materials Research Laboratory. (d) The shape of our Cr mask used in photolithography. The thinnest region is designed in one of four sizes-5, 10, 15, and 20 μm, which is the portion that covers the nanowire. The outermost electrodes (I+, I-) are used to inject current while the next pair of inner electrodes (V+, V-) are used to measure the voltage across the wire. There is a fifth electrode (V_f) that can be used to measure the film portion of the pattern.

To perform photolithography, we use a Karl Suss MJB3 Mask Aligner with a UV wavelength of 365 nm. The photomask, which has the electrode pattern drawn in Cr on glass, is used to transfer the pattern from the mask to the photoresist and eventually to the MoGe. After aligning our mask by using the markers in conjunction with the recorded position of the chosen wire(s), the sample is exposed to UV light for 7.2 sec. The exposed resist is then developed by immersing and agitating the sample in a developer solution, which is mixed from 1 part by volume of Shipley 351 Microposit Developer to 4 parts by volume of DI water, for ~30 sec (~10 sec after the pattern becomes fully visible). The sample is then rinsed in DI water for ~30 sec to remove all the developer. The sample is dried using forced nitrogen and then analyzed under an optical microscope to inspect the quality and location of the photoresist mask covering the MoGe. If the mask has any major defects such as: the lines are not straight, the width of the bridge varies significantly, the mask has holes, or the bridge does not cover the nanowire(s), then the patterned photoresist is removed by immersing and agitating the sample in acetone for ~2 min and the photolithography process is repeated. Additionally, for the resonator samples, the capacitive coupling between the center conductor and the input, output, and grounding planes needs to remain free of any dirt or metal deposits along their entire length. If the sample is free of any major defects, then the sample is placed in a 3% solution of H_2O_2 for 5-25 sec to remove the portions of the MoGe film and MoGe wire(s) that are not protected by the photoresist pattern. The etch rate of MoGe in a 3% solution of H_2O_2 is ~ 1 nm/sec. The photoresist mask is removed by agitating the sample in acetone for ~2 min and then the sample is rinsed in isopropanol for ~30 sec and dried in a flow of forced nitrogen gas. The sample is now ready for the mounting process.

3.2 Cryostat measurement systems

Once the electrode pattern on the sample has been finished, the sample needs to be mounted on a chip carrier that can be directly inserted into a socket on the ^{4}He or ^{3}He system. As part of this process, gold wires need to be connected to the contact pads using indium dots for the samples that will be used in DC measurements. Once all the mounting is complete, the chip carrier is inserted into one of our measurement systems. The ^{4}He systems for DC and microwave measurements can both reach temperatures of ~1.4 K and involve inserting samples into a ^{4}He transfer dewar. The ^{3}He system, which has both DC and microwave lines, can reach temperatures down to ~0.27 K. The dewar for the ^{3}He system is also equipped with a superconducting magnet, allowing us to generate magnetic fields up to 9 T (and 11 T if the helium bath is pumped on).

3.2.1 Sample mounting for dc measurements

Once the sample electrodes have been formed and any modifications made to the nanowire, the sample must be mounted for electrical measurements (see Fig. 3.9). During this process, it is possible to "burn" nanowires by static discharges. To help minimize this problem, we electrically ground ourselves by wearing a grounding wristband and spray anti-static solutions around the work area. We mount the chip on a 6-pin plastic chip carrier, which is secured in a socket that is grounded through 100 kΩ resistors. Short lengths of gold wire (50 μm in diameter and ~1 cm in length) are soldered to the pins of the chip carrier using a small amount of indium to reduce the melting temperature of the solder, reducing the chance of breaking the gold wire. A small piece of double-sided sticky carbon tape is secured in the center of the chip carrier, where the sample is then placed with tweezers. We use indium dots (average diameter of

250 μm) to connect the gold wires to the electrode pattern. The indium dot is placed in a particular location on the sample electrode pattern by using the flat end of a small drill bit or the end of a metal lead from a commercial resistor or capacitor. The indium dot is pressed down firmly with the drill bit to secure the indium dot to the metal electrode. Using tweezers, a gold wire attached to a pin is moved over the indium dot and pressed into it. Then, another indium dot is placed on top of the pressed-in-gold wire and pressed down firmly to secure the gold wire in place. The result is a gold wire sandwiched in between two indium dots and connected to the contact pad on the electrode pattern. This helps to maintain a good electrical contact and minimizes the possibility that the gold wire will become detached when the sample is cooled.

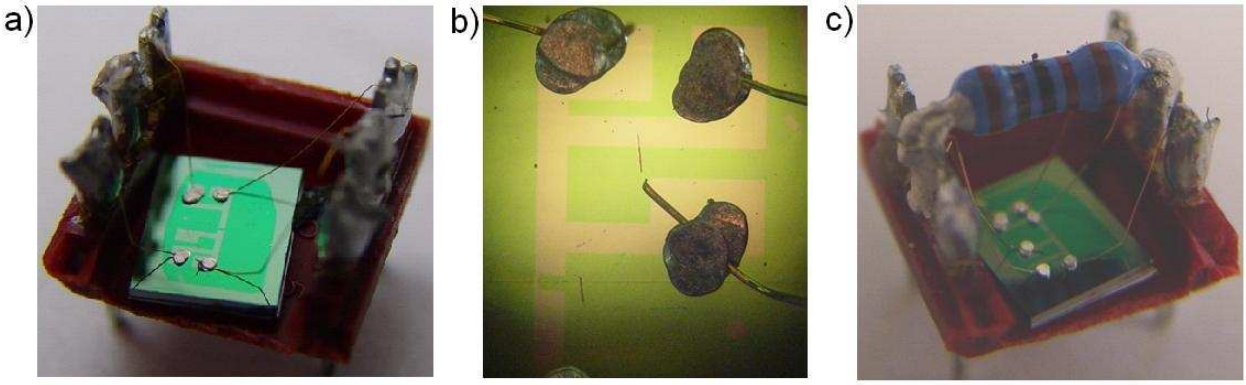

Figure 3.9: Mounted DC nanowire samples. (a) Four of the pins are connected through gold wires that are bonded by indium dots to the MoGe contact pads that were formed by sputtering and photolithography. These pads will be used in four-probe DC electrical measurements of the nanowire. The outer pads are for injecting current (I+, I-) and the inner pads are for measuring the voltage across the wire (V+, V-). (b) A zoomed-in view of the contact between some MoGe pads and the gold wire through the indium dot. (c) A view of the resistive shunt connected to the mounted nanowire sample through silver paste. The resistor is connected to the two free pins which are in turn connected to either side of the electrodes through gold wire that is indium-bonded to the surface.

To add a resistive shunt to the sample, a drop of fast drying silver paint is applied to each of two unused pins on either side of the chip carrier. The excess leads of a commercial resistor (5-200 Ω) are then cut and the ends of the resistor are then placed on the silver paint and left to dry. Once dry, the sample can then be mounted in either our ^{3}He or ^{4}He system to be measured.

3.2.2 Sample mounting for microwave measurements

Once the resonator pattern has been formed and any modifications made to the nanowire(s), the sample must be mounted for electrical measurements (see Fig. 3.10). We use two methods of mounting the resonator sample. The first is to use a wire-bonder to connect to the input/output ports and the ground plane. Using this method, the sample is glued to a copper plate that has been machined in the Materials Research Labortory's Machine Shop with four holes in the corners. The sample is glued to the copper plate using GE varnish. Once the sample is secure, it is taken to the Aluminum wire wedge bonder (K&S) where connections are made between the sample and the sample holder. The ground planes of the resonator are wire-bonded to the copper back plate while the input and output leads of the resonator are wire-bonded to the center conductor of a printed circuit board (PCB), which consists of a microstrip-type transmission line with 50 Ω characteristic impedance.

The second method is used when the wire-bonder is not available or is broken and involves using indium dots and silver paste to connect to the input/output and ground planes. Using this method, the excess Si must be cut away from the portions of the sample that do not contain part of the resonator pattern. This is done by first gluing the sample to a Si wafer by spinning Shipley 1813 photoresist on the wafer at 4000 rpm, pressing the sample into the thin film of photoresist, then baking it on a hotplate at 120 °C for ~2 min. The wafer is taken to an automated dicing saw where the sample is aligned by the naked eye and the excess Si is cut away from the resonator. The resonator is then detached from the Si wafer by swirling the wafer in acetone for ~2 min and then cleaned by immersing and agitating it in isoproponal for ~30 sec before drying it with forced nitrogen gas. After this, an indium dot must be pressed on the input

and output leads to ensure a solid connection between the SMA connecter pin and the contact pad, especially at low temperatures. Caution must be taken in the process as there is a danger of shorting the capacitive connection between the input/output and the center conductor or ground plane as the size of the indium dot grows from ~250 μm to over twice that size as it is pressed into the contact pad. Once the indium dots are secure, the sample is placed on a copper plate that has been machined in the Materials Research Labortory's Machine Shop to the proper length (12 mm, the length of the chip supporting the resonator device after the dicing process) with four holes drilled in the corners.

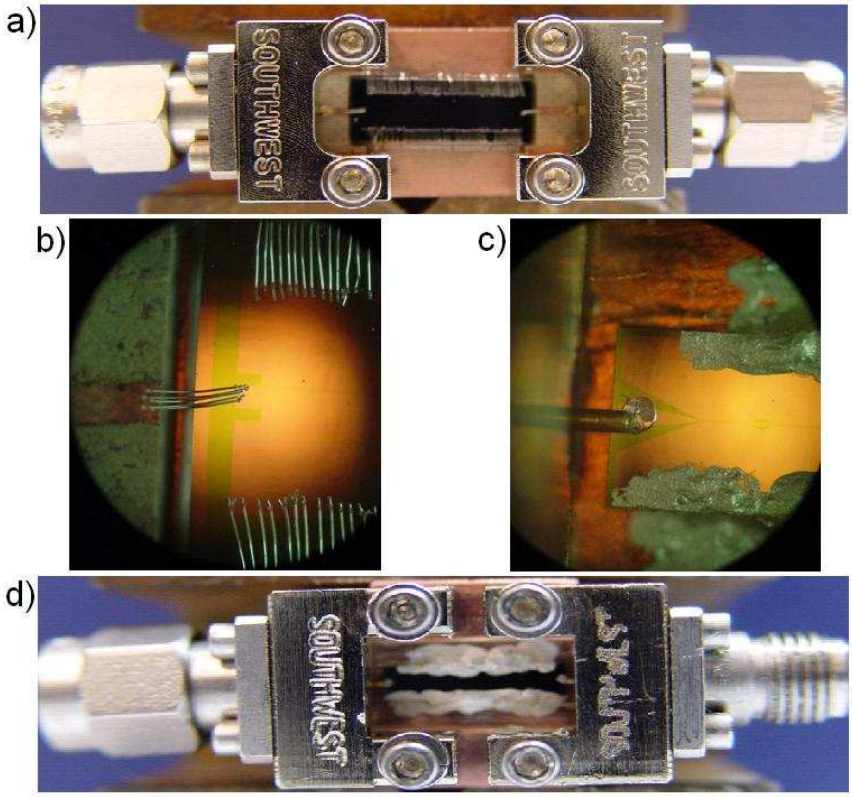

Figure 3.10: Mounted resonator-nanowire samples. (a) A mounted resonator-nanowire sample produced from method I. This picture shows the finished, mounted sample where all wire-bonding is complete and the resonator-nanowire is mounted with SMA connectors. (b) A zoomed-in view from (a) that shows the input, output, and ground planes connected to copper using wire-bonding. (c) A mounted resonator-nanowire sample produced from method II. This picture shows the finished, mounted sample where all dicing, silver pasting, and placement of indium dots is complete and the resonator-nanowire is mounted with SMA connectors. (d) A zoomed-out view from (c) that shows the ground planes connected to copper using silver paste and the input and output connected to the center pin through contact with an indium dot.

At this step, for both mounting methods, an SMA component containing a connector on one side and a pin on the other is screwed in at both ends of the copper plate through the four holes. It is important that the pin of the SMA connector contacts the copper center conductor of the PCB transmission line (method 1) or the indium dot (method II) securely without being shorted to the surrounding ground planes. The ground plane in method II is now ready to be connected to the copper plate using silver paste. A thin wooden stick is used to extract some silver paint from the bottle, which is placed on a glass slide. The stick is then broken into a few pieces, thus creating much finer tips, and is cautiously used to transfer the silver paint from the glass slide to the edges of the ground planes. Slowly, the silver paint is applied across the entire length of both ground planes and connected to the copper ground plane. After ~30 min, the silver paint is dry and ready for the next step. If the sample undergoes multiple thermal cycling between cryogenic and room temperatures, it is observed that the silver paint loses its conduction quality and makes a bad connection to the copper plate and thus the mounting process involving the silver paste needs to be repeated.

At this point, the differences between mounting methods I and II are over and the sample is analyzed under an optical microscope for any dust or contamination causing shorts in the resonator. If no problem is found, the sample is wrapped in a flexible Cu sheet for further shielding from electro-magnetic stray noise and to protect it from accidentally being touched and from dust. When being measured in the ^{4}He system, the thermometer and a resistor used for heating are tightly wound around the Cu enclosed sample and then wrapped in aluminum foil to hold the secure everything in place and hold in any generated heat. The sample is now ready to be cooled in either the ^{4}He or the ^{3}He cryostat and measured.

3.2.3 ^{4}He dc transport system

The ^{4}He system DC system (see Fig. 3.11) was built by U. C. Coskun from our laboratory in order to provide an inexpensive setup in which samples can be quickly measured at cryogenic temperatures. A more extensive discussion of this setup can be found in Ref. [22]. A socket, where the chip carriers can be inserted, is located at the bottom of the dipstick. There are ten measurement leads that run from the room temperature portion of the stick down to the bottom (cold) portion of the dipstick and are thermally connected to a copper block by silver paste. The silver paste also serves as a high-frequency electro-magnetic noise filter. The temperature is measured by measuring the resistance of a calibrated Cernox thermometer, to which four of the measurement leads are attached, located next to the socket on the copper plate. A copper can is used to cover the sample and thermometer, which is wound with a resistive twisted pair of Stableohm wire to serve as a heater. A stainless steel pipe covers the length of the dipstick so that a vacuum can be created around the sample. Once a sample has been placed in the socket, the air in the dipstick is then pumped out and a small amount of He gas (thermal exchange gas) is introduced to help in the cooling process.

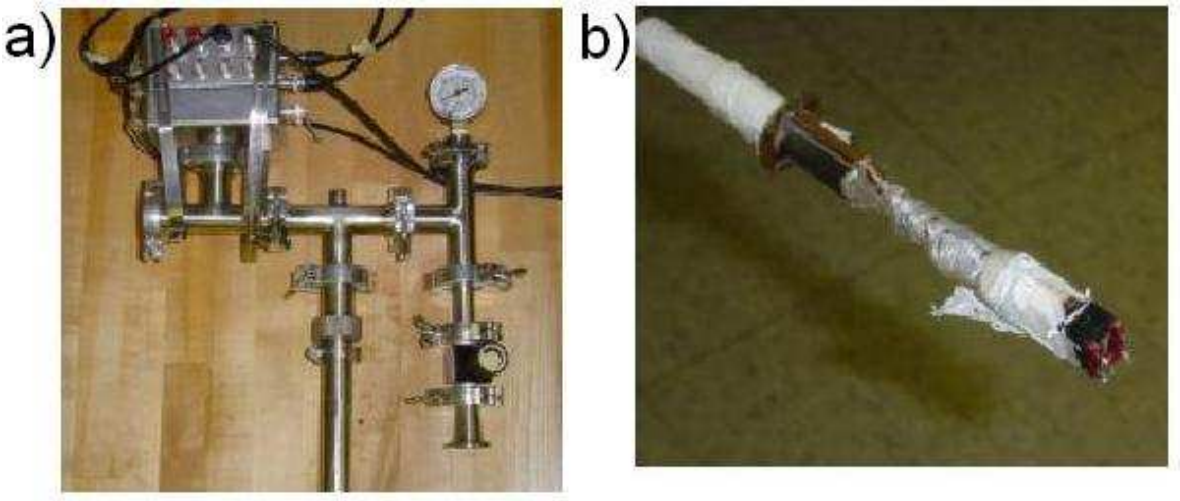

Figure 3.11: ^{4}He measurement system. (a) The room temperature portion of the ^{4}He dipstick. (b) The socket area of the ^{4}He dipstick.

The bottom portion of the dipstick is then immersed into a bath of liquid nitrogen until it cools to 77 K. By cooling first in liquid nitrogen, we save on the total amount of liquid helium necessary to cool the sample to 4.2 K. Then, we transfer the dipstick into a 35-liter capacity liquid He transfer dewar filled with ~4 liters of liquid helium and let it cool to 4.2 K. By pumping on such a small volume of liquid helium (~4 liters), we are able to quickly reduce the temperature to ~1.4 K in ~2 hours. Once the base temperature of 1.4 K has been achieved, we can measure our samples for ~15 hours before the liquid helium has completely evaporated. Also, once at base temperature, the sample can be heated to a desired temperature by passing current through the heater and the appropriate measurements can be performed.

3.2.4 ^{4}He microwave system

The ^{4}He system that we use for microwave measurements (see Fig. 3.12) was built by Jaseung Ku and is an inexpensive system that can quickly be cooled down to ~1.4 K for low temperature measurements. The system contains a pair of input and output microwave semi-rigid cables: either UT-085B-SS (outer conductor: stainless steal, inner conductor: beryllium copper) or UT-085-SS (outer conductor: stainless steel, inner conductor: silver-plated copperweld (SPCW)). The input line semi-rigid cable is connected to a ~20 dB attenuator or isolator and then leads to the sample, which is located near the bottom of the dipstick. The output of the resonator is connected through a semi-rigid cable to another 20 dB attenuator or an isolator, which then feeds into a low-noise cryogenic amplifier that is connected to a room-temperature output hermetically-sealed SMA connector. The temperature is measured by measuring the resistance of a calibrated Cernox thermometer, to which four measurement leads are attached. The thermometer, as well as a resistor that functions as a heater, are wrapped around the sample and

secured in place with aluminum foil, which also helps to maintain a uniform temperature and efficient heating. Three additional DC lines are used to carry the Ground (GND), V_g, and V_d signal to power the low temperature amplifier, which is located at cryogenic temperatures in the bottom section of the dipstick. Thus, there are a total of 9 DC and 2 microwave lines that extend from room temperature to cryogenic temperatures. The room temperature connections are located in a BNC box on the top of the stick.

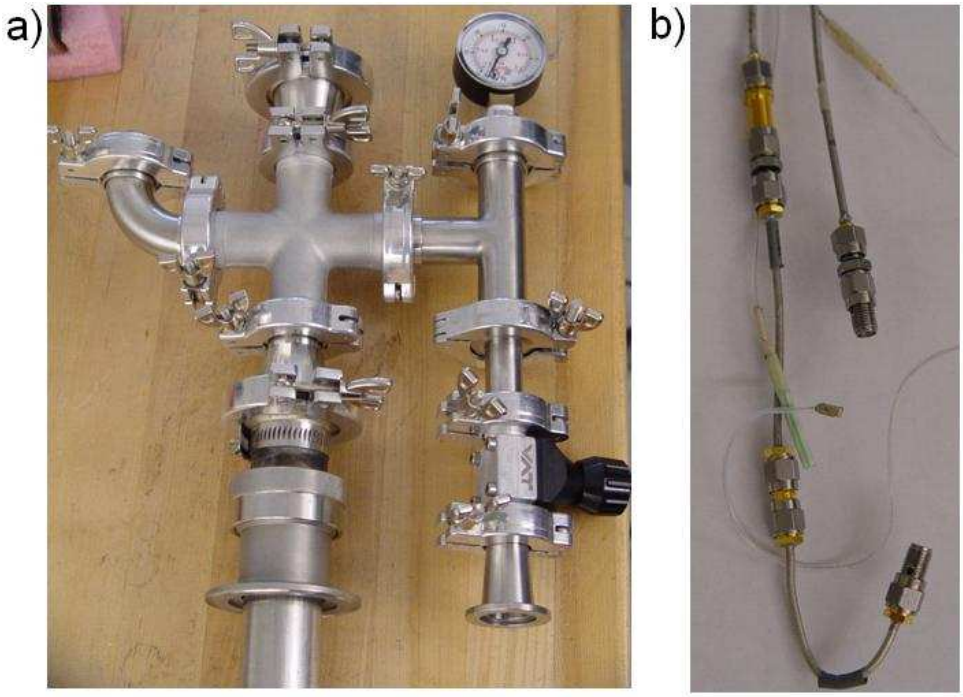

Figure 3.12: ^{4}He microwave measurement system. (a) The room temperature portion of the ^{4}He microwave dipstick. The upper-left connectors are for temperature measurements and control of the heater while the upper-center connectors contain the microwave input and output lines. (b) The socket area of the ^{4}He microwave dipstick. The sample connects to the open SMA connectors while the heater and thermometer that are shown are wrapped in aluminum foil around the sample.

A stainless steel pipe then covers the length of the dipstick so that a vacuum can be created around the sample. Once a sample has been screwed into the SMA connector and the steel pipe placed around the dipstick, the air in the dipstick is pumped out and a small amount of He gas (exchange gas) is introduced to help in the cooling process. The bottom portion of the dipstick is then immersed into a bath of liquid nitrogen until it cools to 77 K. By cooling first in

liquid nitrogen, we save on the total amount of liquid helium necessary to cool the sample to cryogenic temperatures. Then, we transfer the dipstick into a 35-liter capacity liquid He transfer dewar filled with ~4 liters of liquid helium and let it cool to 4.2 K. By pumping on such a small volume of liquid helium (~4 liters), we are able to quickly reduce the temperature to ~1.4 K in ~2 hours. Once the base temperature of 1.4 K has been achieved, we can measure our sample for ~15 hours before the liquid helium has completely evaporated. Also, once at base temperature, the sample can be heated to a desired temperature by passing current through the heater and the appropriate measurements can be performed.

3.2.5 ^{3}He dc/microwave system

When temperatures lower than 1.4 K are necessary, the ^{3}He system is used, which can reach temperatures down to ~0.27 K. After the cryostat was purchased from Janis Research Company, a number of modifications were made to allow multiple samples to be mounted and measured and to insert microwave lines into the system, which will be discussed later. The ^{3}He system also contains a superconducting magnet from Cryomagnetics that is capable of producing fields up to 9 T. To achieve such low temperatures the system relies on the condensation and evaporation properties of the ^{3}He isotope as well as an immersion in a bath of ^{4}He. In order to measure a sample in this system, the samples must first be loaded into the cryostat.

When doing DC measurements, there is a capacity of three samples. There are two side sockets and one bottom socket for samples. These are chosen based on the desired orientation of the magnetic field. Typically, one side socket is used to hold the calibrated ruthenium oxide thermometer which is measured in a four-probe configuration. After the mounted samples have been inserted into the sockets, a mounted microwave resonator sample can also be attached to the

microwave lines. Once this is complete, a faraday cage is placed over the samples and the system is vacuum sealed using an indium gasket and pumped down to ~10^{-5} Torr to remove any moisture or air that could freeze and cause undesired thermal linkage or damage to the electronics or sample at low temperature. At this point, a small amount of He gas (exchange gas) is added to the cryostat to aid in the cooling process.

With the samples loaded, the cryostat is sealed and filled with exchange gas, the cryostat is lowered into the dewar. If the dewar is already filled with ^{4}He, then helium gas is flowed through the 1K pot and sorption pump (to prevent air freezing inside the lines) as the cryostat is slowly lowered into the dewar. This is done until the cryostat is fully inserted into the dewar and sealed. If the dewar is near room temperature, then the cryostat is fully inserted in the dewar and vacuum sealed. The air is then pumped out and replaced with nitrogen gas. Liquid nitrogen is then pumped into the dewar until the 1K pot and sorption pump temperatures both are ~77 K. Then the liquid nitrogen is forced out and the dewar is pumped free of nitrogen gas. Helium gas is then introduced to the dewar through the 1K pot and sorption pump lines. Once the dewar is slightly over pressurized, liquid helium is pumped into the dewar until the 1K pot and sorption pump temperatures reach 4.2 K and the dewar is filled to the appropriate level. Then, the exchange gas is pumped out of the internal vacuum chamber (IVC) until the pressure inside the cryostat is ~10^{-6} Torr, in order to prevent additional thermal leakage from the sample stage. The pumping is done using a turbopump.

When the cryostat is at 4.2 K and evacuated and at least 10% of the dewar is full of ^{4}He, the condensation process can begin. At temperatures above ~27 K, ^{3}He begins to be released from the carbon charcoal in the sorption pump. Thus the sorption pump is heated to ~45 K resulting in the outgassing of the ^{3}He. Additionally, a ~2 mm wide tube connects the ^{4}He bath to

the 1K pot, allowing liquid ^{4}He to enter the 1K pot at a controllable rate (by the use of a valve). A vacuum pump can quickly cool the 1K pot to ~1 K by removing the ^{4}He vapor. The 1K pot surrounds an inner tube containing the ^{3}He gas that has outgassed from the sorption pump, which begins to condense once the 1K pot reaches a temperature below ~2 K. The condensed ^{3}He liquid collects in the ^{3}He pot located just above the sample. This process is continued for ~ 30 min to condense the majority of the ^{3}He. The heat is then removed from the sorption pump and a valve is opened to allow a controllable amount of ^{4}He gas to cool the sorption pump. As the temperature of the sorption pump decreases, an effective "pumping" on the ^{3}He is achieved as the ^{3}He vapor begins to bind back to the charcoal. This results in a base temperature of ~ 0.27 K, which can be maintained for ~24 hours if the 1K pot remains cold.

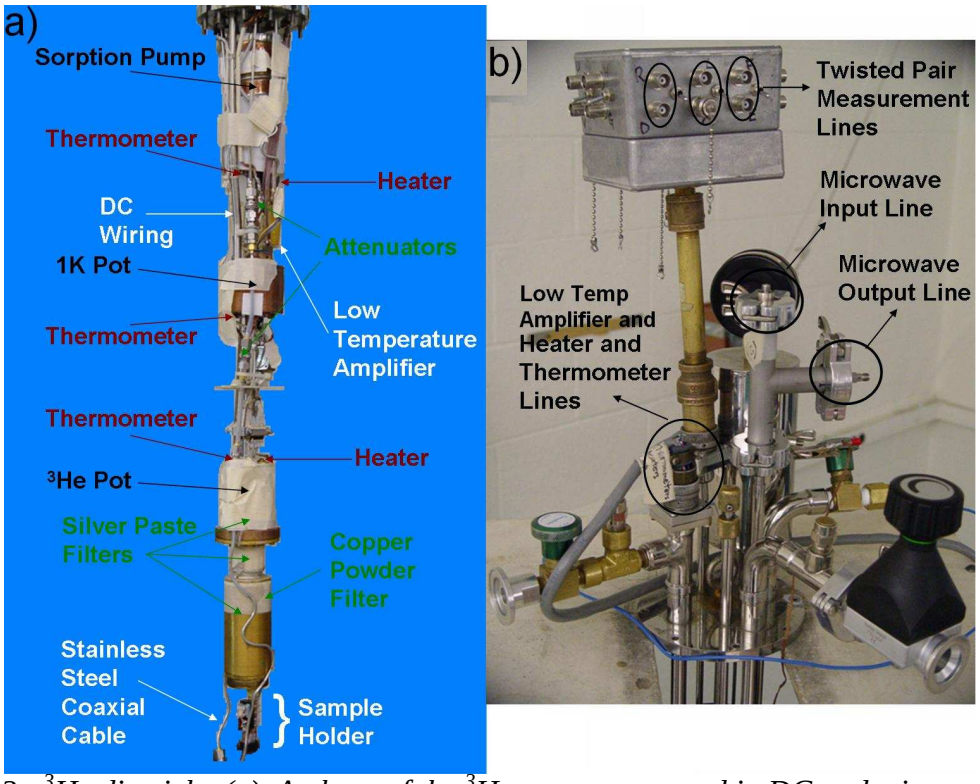

Figure 3.13: ^{3}He dipstick. (a) A photo of the ^{3}He cryostat as used in DC and microwave nanowire experiments showing the various thermometers, pots, heaters, filters, cables, and other components involved in the system. (b) A picture of the top portion of the ^{3}He dipstick showing the BNC box with 3 of the 8 twisted DC lines (upper black ovals), the connection for the low temperature amplifier, heaters, and component thermometers (lower black oval), and the microwave input and output line connections (middle two black ovals).

The wiring of all the thermometers, heaters, and the 16 DC measurement lines, as well as the fabrication of the sample holder (see Fig. 3.13 and Fig. 3.15) was done by Andrey Rogachev (now at the University of Utah). The measurement lines coming from the BNC electrical box at the top of the cryostat are high-resistance wires and are thermally anchored to the 1K pot to minimize heat transfer from room temperature to the 1K pot location. Each measurement line connection to the BNC box has a π-filter to help reduce high frequency noise. The BNC box also has connections to power the sorption pump and ^{3}He pot heater as well as connections to the thermometers to measure the temperature of the sorption pump, 1K pot, and sample. All the measurement lines are grouped as eight sets of twisted pairs and eventually pass through three silver paste filtering stages and a copper powder filtering stage to limit unwanted high frequency noise for DC measurements. High resistance wires are also located between the 1K pot and the ^{3}He pot and between the ^{3}He pot and the RC filters located at the top of the copper measurement attachment that is mounted directly below the ^{3}He pot. There is ~1 m of lower resistance wire that is used after the RC filters and is wrapped many times around the attachment and thermally anchored with silver paste. Low resistance wire is also used to attach to the sample stage, which helps the sample to thermalize to the thermometer temperature. Two pairs of measurement lines go to the upper side connection where we put our commercially calibrated RuO thermometer from Lakeshore to measure the sample temperature. Three other pairs of measurement lines go to the lower side connection, which is used for measurements with a magnetic field parallel to the sample film. The remaining three pairs go to the bottom slot, which is used for measurements with a magnetic field perpendicular to the sample film. For additional shielding, a copper can is then placed over these three connection sites.

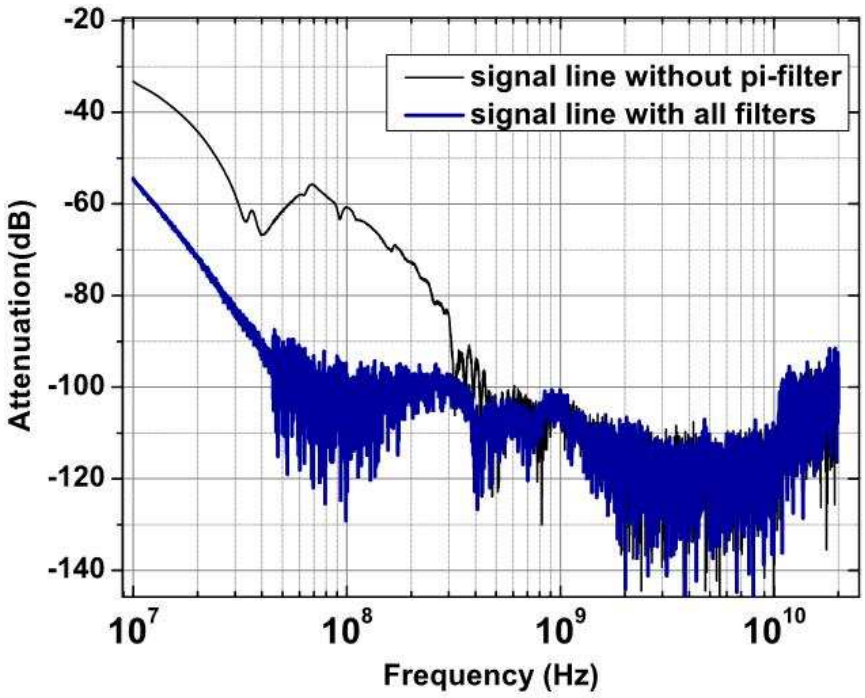

Figure 3.14: Attenuation of a signal line in our ^{3}He system measured at room temperature. With all filters in place (blue curve) the attenuation is larger than 90 dB for frequencies higher than 40 MHz. For frequencies higher than 6 GHz (roughly corresponding to our base temperature of (T ~ 0.29 K), the attenuation is larger than 110 dB and the signal falls below the noise level of the network analyzer. The attenuation of the signal lines without the π-filteris also shown (black curve). The π-filters provide an attenuation of 20 dB for frequencies larger than 10 MHz.

It is essential that any high-frequency noise coming from the outside environment (which is on the order of the QPS rate) be minimized. This noise could easily be interpreted as QPSs. Each measurement line has three stages of filtering including a π-filter at room temperature, a copper-powder filter (Cu-F) at base temperature (similar to the one developed by Martinis, Devoret, and Clarke [23]), and a silver paste filter (Ag-F), also at base temperature. These filters help suppress noise ranging from low frequency to high microwave frequencies. The compact powder filters (i.e. Cu-F and Ag-F) rely on skin-effect damping for attenuation of high frequencies. At room temperature, commercially available π-filters (Spectrum Control, SCI 1201-066) are placed on each electrical lead inside an aluminum box (Hammond Manufacturing)

before they enter the cryostat. These π-filters are low-pass filters with a rated 7 dB cutoff frequency of 3 MHz. For frequencies larger than 10 MHz, the measured attenuation of these filters is more than 20 dBm. The Copper-powder filters are fabricated using three feet of coiled insulated Constantan wire [Cu(55%)Ni(45%) alloy, resistance 18.4 Ω/foot, diameter 0.004 inch] embedded in a mixture of copper powder (~325 mesh, Alfa Aesar) and epoxy (Stycast #1226, Emerson and Cuming). Similarly, the silver paste filters are fabricated using three feet of coiled insulated Constantan wire in silver paste (fast drying silver paint, Ted Pella Inc.). A network analyzer (Agilent N5230A) was used to measure the signal lines with all the filters. We found the attenuation to be larger than 100 dB for frequencies larger than 1 GHz (see Fig. 3.14). For frequencies above 6.25 GHz, which corresponds to a temperature of 0.3 K, the attenuation is more than 110 dB and falls below the noise floor of our network analyzer. This level of attenuation is similar to the attenuation used in previous experiments involving QPS [23].

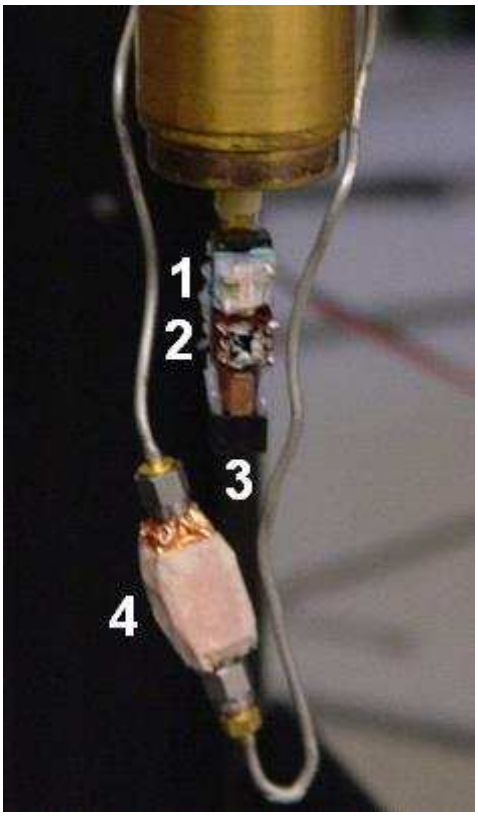

Figure 3.15: The sample socket of the ^{3}He dipstick showing the location of the thermometer and various types of samples: (1) thermometer, (2) DC nanowire sample with B-field parallel to film, (3) DC nanowire sample with B-field perpendicular to film, (4) microwave resonator sample with measured tilt to allow B-field to thread a double-wire sample.

The microwave lines were added to the ^{3}He cryostat by Robert Dinsmore and Jaseung Ku [24]. The signal is fed in through a 0.85 inch diameter SS coaxial cable (UT-085-SS-SS), which was purchased from Micro-Coax. The cables have a stainless steel jacket, a PTFE dielectric, and a stainless steel center conductor. The cables were connected to SMA connectors with snap-on center conductor pins and solder-on male outer conductor connectors. Two cables to be used as input and output lines for the microwave resonator experiments were inserted through an empty feed-through at the top of the cryostat. Isolators and attenuators were installed along each line to limit the amount of thermal radiation coming from room temperature and also to thermalize the center conductor to cryogenic temperatures. A total of three attenuators are thermally anchored on the input line, one at each temperature stage (20, 3, and 11 dB at 4, 1, and 0.3 K, respectively), and are connected by stainless steel semi-rigid cables. On the output line, two isolators (4-8 GHz) are thermally anchored at 0.3 K and 1 K. Three additional DC lines (ground, V_g, and V_d) were added to the BNC box and brought down to power the low temperature amplifier (4-8 GHz), which was thermally linked to the 4 K stage. When the system was cooled, the average base temperature changed from ~275 mK to 310 mK, indicating that only a small amount of thermal noise was reaching the sample.

3.3 Electrical measurements

3.3.1 dc transport measurements

We carry out DC electrical transport measurements in a four-probe configuration using either the ^{4}He or ^{3}He system described above with each pair of voltage and current lines in a twisted pair (see Fig. 3.16). The bias current is supplied by an ultra-low distortion function generator

(Stanford Research Systems DS 360), which applies a voltage that is passed through a known standard resistor (typically ~1 MΩ). The large value of the resistance compared to the resistance of the nanowire effectively makes the measurement current-biased. The voltage across the standard resistor can be measured, which is amplified through a battery-powered pre-amplifier (Princeton Applied Research model 113 or Stanford Research Systems model SR 560) that provides additional low-pass and high-pass filtering, and then is connected to a data acquisition card (National Instruments model PCI-MIO-16XE-10). Thus, knowing the voltage and resistance, the value of the current can be calculated through Ohm's Law: $V=IR$. Then, using another pre-amplifier and slot on the data acquisition card, we measure the voltage across the sample. In this manner, we can measure voltage as a function of current, *V(I)*. We define the resistance of the sample, *R*, as the slope of the *V(I)* curve in the limit of zero current. To measure the resistance, we typically use an AC measuring current with an amplitude of ~10 nA at a frequency of ~12 Hz, centered at zero bias. Using a measuring current that is too low leads to a noisy measurement of *R*, while using a measuring current that is too large results in an incorrect value of *R* if the *V(I)* curve is no longer linear. The value of *R* is determined in LabVIEW by line-fitting the measured *V(I)* curves.

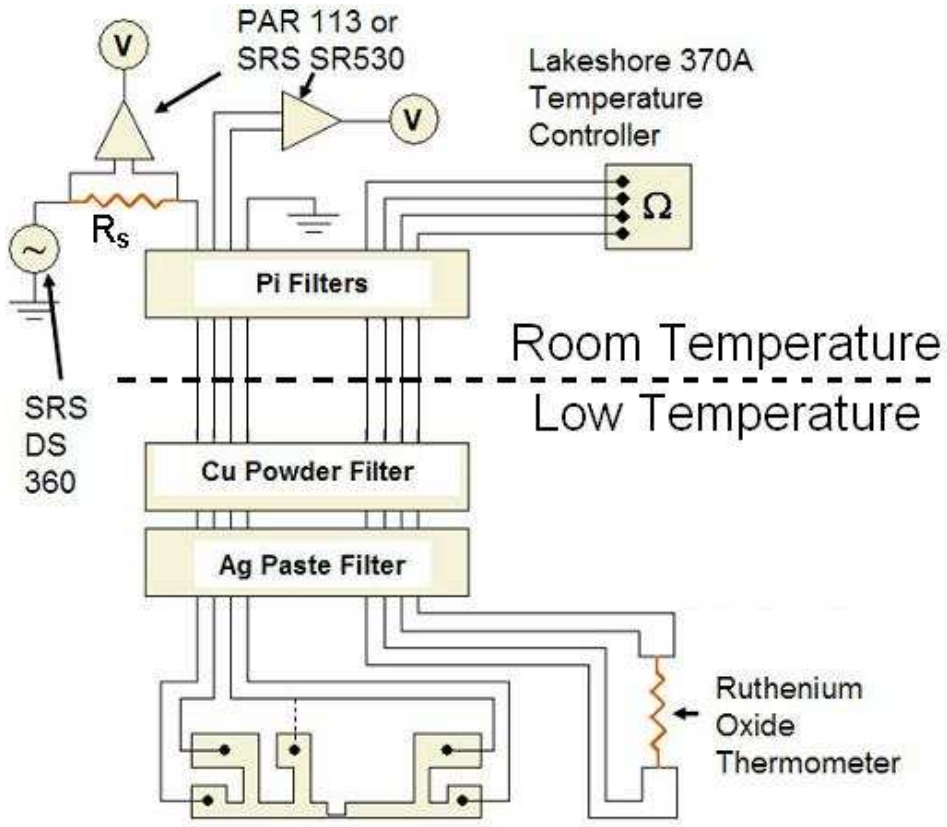

Figure 3.16: Schematic of the four-probe transport DC measurements of nanowires. The sample is current-biased by applying a voltage across a standard resistor (R_s) using the SRS DS 360 function generator. The current is measured by measuring the voltage across the standard resistor using a PAR 113 or a SRS SR530 battery powered preamp. The outputs of these preamps are wired to a BNC box that is connected to a computer via a DAQ board. The temperature of the sample is measured through a four-probe configuration using a calibrated thermometer. To reduce noise, π-filters are employed at room temperature while Cu-powder and Ag-paste filters are used at low temperature.

To measure a *V(I)* curve, the function generator is set to a slow frequency of ~100 mHz and a relatively high voltage (~1 V) in order to generate large bias current values on the order of a few μA (this value depends on the critical current of the nanowire). Caution must be taken when performing these measurements because there is a risk of burning the wires when currents much larger than the critical current of the nanowires are used. We also measure *dV(I)/dI* vs. *I* curves by measuring the slope of the *V(I)* curve in a narrow range centered around a nonzero DC bias current. For temperatures low enough for the nanowire to be superconducting, we can also

measure the switching current, I_{SW} (the current at which the sample jumps from a low-voltage state to a resistive state), and the retrapping current, I_R (the current at which the resistive wire returns to the low-voltage state). We can also measure any of these parameters as a function of magnetic field and temperature. The magnetic field is generated by passing a current (Cryomagnetics Inc. Bipolar Superconducting Magnet Power Supply for high fields or Keithley 2400 SourceMeter for small fields) through a superconducting solenoid and converting the current to magnetic field through solenoid ratio of 4.481 A/T. We measure the resistance of the thermometer with a Keithley 2000 multimeter (^{4}He system) or a Lakeshore 370 AC resistance Bridge (^{3}He system) with a four-probe configuration. The temperatures can also be fixed during these measurements through a LabVIEW controlled feedback loop (^{4}He system) or a PID temperature controller which can maintain the target temperature within ~5 mK (^{3}He system). On the ^{3}He system, the output current is either wired to the ^{3}He pot or the sorption pump heater. The 1K pot and sorption pump temperatures are measured using a Keithley 2001 multimeter.

3.3.2 Microwave measurements

We carry out most of our microwave electrical transport measurements using an Agilent N5230A vector network analyzer (NA) connected to the sample through 50 Ω SMA transmission lines (see Fig. 3.17) in either the ^{4}He or ^{3}He system, which is described in Sections 3.2.4 and 3.2.5. This device is capable of sending microwaves at various powers (-90 to +20 dBm with a minimum step size of 0.01 dB) and frequencies (10 MHz - 20 GHz with a frequency resolution of 1 Hz) and receiving microwaves in these same ranges. The NA can also sweep power from -90 to +20 dBm at fixed frequency or sweep frequency between 10 MHz – 20 GHz with fixed power. To perform the sweep, the NA measures S_{21} at a particular single frequency, which is the

ratio of power at the NA input and output. The measurement S_{21} is done in units of dB and is thus defined by: $S_{21}(\text{dB}) = P_{in}\ (\text{dB}) - P_{out}\ (\text{dB})$, where P_{in} is the power at the NA input and P_{out} is the power that the NA device is outputting. We use this device to characterize the transmission properties of our nanowire-embedded resonator samples (typically measure S_{21} vs. NA frequency to do this) where an S_{21} value of 1 (in the linear scale) or zero (measured in dB) means perfect transmission. Even for a resonator with perfect transmission, this number is often different than 1 because of the gain and loss mediums of the amplifiers, transmission lines, attenuators, and isolators. The sweep time over a particular frequency interval can be controlled by adjusting the IF bandwidth and ranges from 0.001s – 24 hrs.

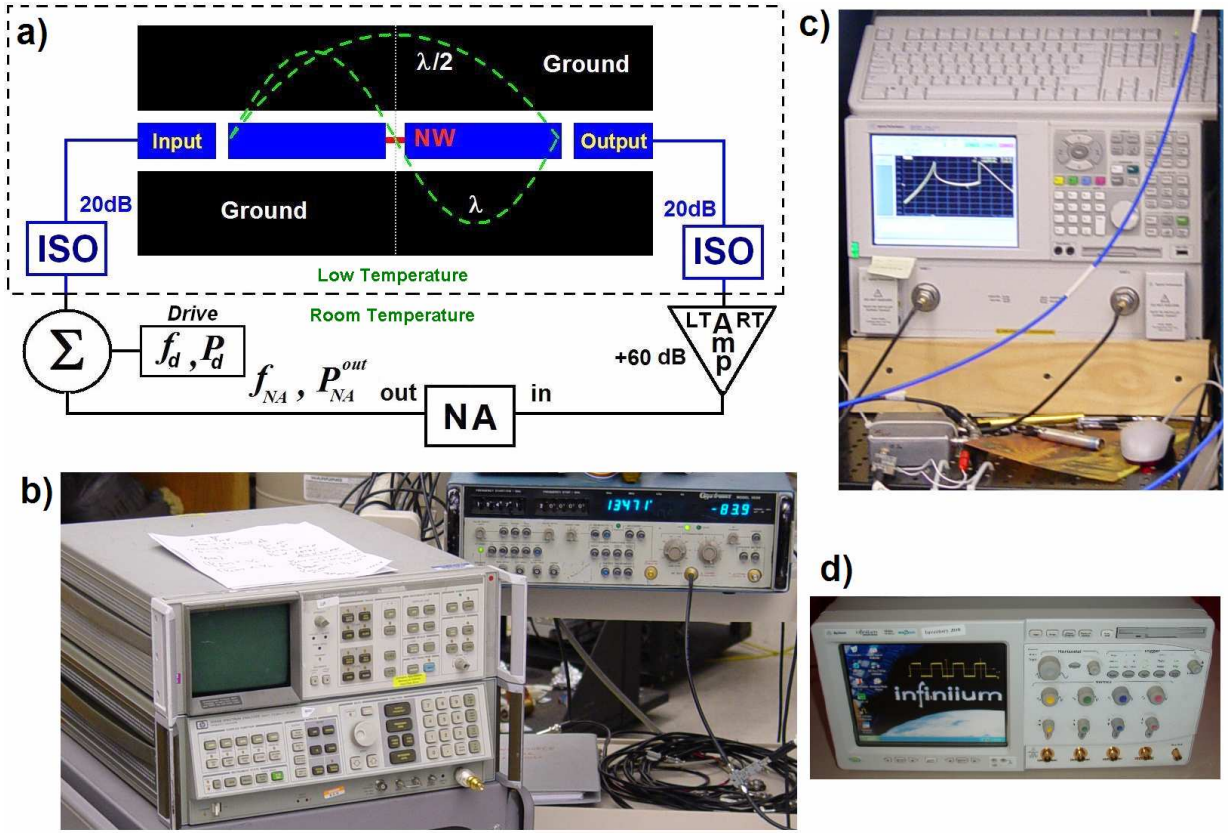

Figure 3.17: (a) Nanowire-embedded resonator system and measurement setup. Two microwave signals can be added together through a power combiner (∑) and sent to the input of the resonator through a 20 dB isolator. The first signal is sent from the network analyzer (NA) and has a frequency f_{NA} and power P_{NA}^{out} while the second signal is sent from the Gigatronics microwave source at a frequency f_P and power P_P. The input and output of the resonator are capacitively coupled to the center conductor through coupling capacitors of ~40 fF formed by a 3 μm gap in the MoGe film. The center conductor (blue) is ~25 nm thick and ~20 μm wide. It is interrupted in the middle by the trench, and connected through the nanowire. The output of the resonator travels through another 20 dB isolator and then a series of low and room temperature amplifiers, which have a combined gain of ~ +60 dB, before going to the NA input, where the transmitted power is measured. The amplitudes of the supercurrent oscillations corresponding to the λ/2 and λ modes are shown by dashed lines. (b) A picture of the Agilent N5230A vector network analyzer used in this thesis. (c) (Left) The Agilent 8566B spectrum analyzer used in this thesis. (Right) The Gigatronics 1026 microwave function generator used in this thesis. (d) The Infinium oscilloscope HP/Agilent DSO81004A-001, 10 GHz, 4CH, 40GSa/s.

In addition to using the NA, we can also measure the output spectrum of the nanowire resonator samples using a 22 GHz Agilent 8566B spectrum analyzer. To do this, we simply connect the output transmission line from the resonator to the input of the spectrum analyzer. This device measures its input power as a function of frequency in either a linear or logarithmic

scale. We can also send more than one signal to the resonator sample simultaneously. We use the Gigatronics 1026 microwave function generator as our second microwave source, which can be sent separately or can be added to the output of the NA through a power combiner, which has a loss of ~ 4 dB. Using a LabVIEW program, we can also measure S_{21} vs. NA frequency curves as a function of the frequency and/or power of the Gigatronics source. The S_{21} vs. NA frequency curves as well as all the other curves we can measure using the NA, spectrum analyzer, and the Gigatronics source can all be measured as a function of temperature and magnetic field. The temperature and magnetic field can all be measured and controlled in the same way as is detailed in Section 3.3.1.

---

[1] J.E. Lukens, R.J. Warburton, and W.W. Webb, Phys. Rev. Lett., **25**, 1180 (1970).
[2] R.S. Newbower, M.R. Beasley, and M. Tinkham, Phys. Rev. B, **5**, 864 (1972).
[3] N. Giordano. Phys. Rev. Lett., **61**, 2137 (1988).
[4] F. Sharif , A.V. Herzog, and R.C. Dynes, Phys. Rev. Lett., **71**, 428 (1993).
[5] M. Savolainen, V. Touboltsev, P. Koppinen, K.-P. Riikonen, and K. Arutyunov, Appl. Phys. A: Mater. Sci. Process. **79**, 1769 (2004).
[6] N. Giordano, Phys. Rev. Lett., **61**, 2137 (1988).
[7] A. Bezryadin, C. N. Lau, and M. Tinkham, Nature (London), **404**, 971 (2000).
[8] D.S. Hopkins, D. Pekker, P.M. Goldbart, and A. Bezryadin, Science, **308**, 1762 (2005).
[9] A. Bezryadin, J. Phys.:Condens Matter **20**, 043202 (2008).
[10] M.-H. Bae, R.C. Dinsmore III, T. Aref, M. Brenner, and A. Bezryadin, Nano Lett., **9**, 1889 (2009).
[11] D.S. Hopkins, D. Pekker, T.C. Wei, P.M. Goldbart, and A. Bezryadin, Phys. Rev. B, **76**, 220506 (2007).
[12] A. Johansson, G. Sambandamurthy, D. Shahar, N. Jacobson, and R. Tenne, Phys. Rev. Lett., **95**, 116805 (2005).
[13] C.N. Lau, N. Markovic, M. Bockrath, A. Bezryadin, and M. Tinkham, Phys. Rev. Lett., **87**, 217003 (2001).
[14] A.T. Bollinger, A. Rogachev, M. Remeika, and A. Bezryadin, Phys. Rev. B, **69**, 180503 (2004).
[15] K.F. Kelly, I.W. Chiang, E.T. Mickelson, R.H. Hauge, J.L. Margrave, X. Wang, G.E. Scuseria, C. Radloff, and N.J. Halas, Chem. Phys. Lett., **313**, 445 (1999).
[16] E.T. Mickelson, C.B. Huffman, A.G. Rinzler, R.E. Smalley, R.H. Hauge, and J.L. Margrave, Chem. Phys. Lett., **296**, 188 (1998).
[17] A. Rogachev, A.T. Bollinger, and A. Bezryadin, Phys. Rev. Lett., **94**, 17004 (2005).
[18] A. Rogachev, T.C. Wei, D. Pekker, A.T. Bollinger, P.M. Goldbart, and A. Bezryadin, Phys. Rev. Lett., **97**, 137001 (2006).
[19] J.M. Graybeal and M.R. Beasley, Phys. Rev. B, **29**, 4167 (1984).
[20] J.M. Graybeal, PhD thesis, *Stanford University* (1985).
[21] A. T. Bollinger, PhD thesis, *University of Illinois at Urbana-Champaign* (2005)
[22] U.C. Coskun, PhD thesis, *University of Illinois at Urbana-Champaign* (2005).
[23] J.M. Martinis, M.H. Devoret, and J. Clarke, Phys. Rev. B, **35**, 4682 (1987).
[24] R.C. Dinsmore III, PhD thesis, *University of Illinois at Urbana-Champaign* (2009).

Chapter 4

Cratered Lorentzian response of driven microwave superconducting single nanowire-bridged resonators

We report on observations of a superconductor-normal pulsing regime in microwave (GHz) coplanar waveguide resonators consisting of superconducting MoGe films interrupted by a gap that is bridged by one or more suspended superconducting nanowires. This regime, which involve MHz-frequency oscillations in the amplitude of the supercurrent in the resonator, are achieved when the *steady-state* amplitude of the current in the driven resonator exceeds the critical current of the nanowires. Thus we are able to determine the temperature dependence of the critical current, which agrees well with the corresponding Bardeen formula [1]. The pulsing regime manifests itself as an apparent "crater" on top of the fundamental Lorentzian peak of the resonator. Once the pulsing regime is achieved at a fixed drive power, however, it remains stable for a range of drive frequencies corresponding to subcritical steady state currents in the resonator. We develop a phenomenological model of resonator-nanowire systems, from which we are able to obtain a quantitative description of the amplitude oscillations and also, *inter alia*, to investigate thermal relaxation processes in superconducting nanowires. For the case of resonators comprising *two* parallel nanowires and subject to an external magnetic field, we find field-driven oscillations of the onset power for the amplitude oscillations, as well as the occurrence (for values of the magnetic field that strongly frustrate the nanowires) of a distinct

steady state in which the pulsing is replaced by stochastic amplitude-fluctuations. We conclude by giving a brief discussion of how circuit-QED-based systems have the potential to facilitate nondestructive measurements of the current-phase relationship of superconducting nanowires and, hence, of the rate at which quantum phase-slips take place in superconducting nanowires.

4.1 Introduction

A variety of recent advances in quantum computing and related fields have involved circuit-QED systems [2, 3], which consist of mesoscopic elements (e.g., "artificial atoms") that are strongly coupled to microwave resonators. Circuit-QED has the advantage over *cavity* QED [4], which involves atoms coupled to an optical cavity, in that the strong-coupling regime, in which the resonance frequency shifts appreciably when a single photon is added to the cavity, is easier to attain [2]. The condition for cavity QED effects to become significant is that the relevant excitation energy scales of the "atomic" system should be similar to those of a single cavity photon. To date, most of the mesoscopic elements employed in circuit-QED settings have been "artificial atoms" (e.g., Cooper-pair boxes [5]), capacitively coupled to the resonator; in addition, a Josephson junction has, in certain experiments, been integrated into the resonator itself in order to facilitate the "weak" measurement [6] of the internal states of the artificial atoms [7, 8, 9]. Both artificial atoms and Josephson junctions are essentially zero-dimensional quantum systems; the present work is motivated by the possibility of extending the circuit-QED paradigm to spatially extended systems, which have more complex internal structure and thus richer excitation spectra. In particular, we focus on superconducting nanowires, which are believed to exhibit many-body phenomena such as Little's phase slips [10], which can occur either by thermal activation or by quantum tunneling [11, 12, 13, 14, 15, 16]. It was recently shown that

superconducting nanowires act as nonlinear inductive elements, so they have been proposed as building blocks for qubits [17]. Circuit-QED systems involving superconducting nanowires thus raise the possibility of bringing the physics of *many-body cavity QED*—which involves, e.g., Bose-Einstein condensates (BECs) coupled to optical cavities [18, 19, 20, 21, 22]—to the solid-state setting. It is known that, in the context of atomic and optical physics, the cavity QED element offers new routes for probing the quantum dynamics of the BEC [23], as well as generating coupled matter-light phases that cannot be achieved with the BEC alone [20, 21]. Specifically, resonator-induced collective behavior, which has been studied in the cavity QED case and which we focus on in the present work, has no direct analog, to date, in circuit-QED.

Further motivation for the present work comes from the following points. First, the strategies used to date to probe quantum phase slips in superconducting nanowires are complicated by the need to measure very small resistances. Other experiments have bypassed this difficulty by studying the phase-slip induced formation of a Joule-heated quasi-normal state [14, 15, 16]. The new avenues opened up by circuit-QED-based experiments should enable the complications of measuring small resistances to be by-passed and compliment the studies done by measuring switching rates into the Joule-heated quasi-normal state. In addition, working with superconducting nanowires, rather than oxide-based superconducting tunnel junctions, should ameliorate complications due to trapped charges in the oxide material.

Thin-film superconducting resonators have been extensively studied [24, 25, 26] including a situation that incorporates a Josephson junction as a nonlinear inductive element into the resonator [27]. In the present work we study systems involving a microwave coplanar waveguide resonator having either one or two superconducting nanowires integrated into it [17] (see Fig. 4.1). The nanowires, as well as the central conductor of the resonator, are made of

MoGe, and are fabricated by molecular templating, as discussed in Refs. [13, 28]. The nanowires are suspended over a trench, rather than resting on a substrate. The nanowire-resonator systems that we have fabricated can, in principle, be cooled to the cavity QED regime, as the following heuristic argument shows. The energy cost of a phase slip vanishes as the current through the nanowire approaches its critical value. The r.m.s. amplitude of the antinodal current corresponding to a single photon is given by the equipartition theorem as $\left\langle LI^2/2 \right\rangle = \hbar\omega_0/2$: here, ω_0 is the resonator's natural frequency ($\omega_0/2\pi$ = 10 GHz) and L = 1 nH is the order of magnitude of a typical circuit inductance, corresponding to an impedance of $Z_0 = 50\ \Omega$). For these values, $I_{\text{r.m.s.}} \approx \omega_0\sqrt{\hbar/Z_0} \cong 100$ nA , which is of the same order of magnitude as the critical current of a nanowire: e.g., a critical current of ~200 nA was previously reported [29, 30]. Thus, the *quantum* regime is, in principle, achievable [17]. This regime would, e.g., feature coherent superpositions of states having distinct currents and cavity-photon numbers.

Here, we present measurements on a microwave coplanar waveguide resonator containing one superconducting nanowire at various temperatures and photon populations. These measurements, though not in the cavity QED regime *per se*, nevertheless reveal several puzzling features that are related to the physics of superconducting nanowires, and that ought to be understood and accounted for before the *quantum* dynamics of the composite system is addressed. These phenomena are related to the existence, for a strongly driven resonator, of a nonequilibrium, time-domain pulsing regime (which, in the frequency domain, we term the "crater") in which the nanowire is found to switch, periodically, between its normal and superconducting states (resonators integrated with micro-bridges have been studied in [31]). We develop a simple, quantitative model of this pulsing regime, which captures all of its salient

features; the success of our model poses constraints on how far neglected features, such as supercurrent dissipation can influence the behavior of a nanowire in a resonator.

4.2 Experiment

The nanowire-resonator samples were fabricated using the molecular templating technique [13, 28]. The nanowire is integrated into a superconducting coplanar waveguide (CPW) resonator using optical lithography. To make the nanowire, single-walled carbon nanotubes were deposited on a Si-SiO_2-SiN substrate, which contained a 100 nm wide trench across the center of the chip. The trench is produced through a process involving e-beam lithography, reactive ion etching, and wet etching in HF (to produce an undercut). The trench was aligned with the center of the resonator, in order to create a gap in the resonator's center conductor [see Fig. 4.1(a)]. Then a thin film (here 10 or 25 nm) of $Mo_{0.76}Ge_{0.24}$ (from Super Conductor Materials Inc.) was deposited across the surface of the sample using an AJA DC magnetron sputtering system (ATC 2000 from AJA International Inc.). The nanotubes that cross the trench became substrates for superconducting MoGe nanowires, as a result of the metal sputtering. Following Boaknin *et al.* [27], the resonator was patterned by photolithography, and the photo-mask was positioned so that just one or two nanowire(s) (as in chapter 5) connect the two halves of the center conductor which, as mentioned above, is interrupted by the trench (see Fig. 4.1).

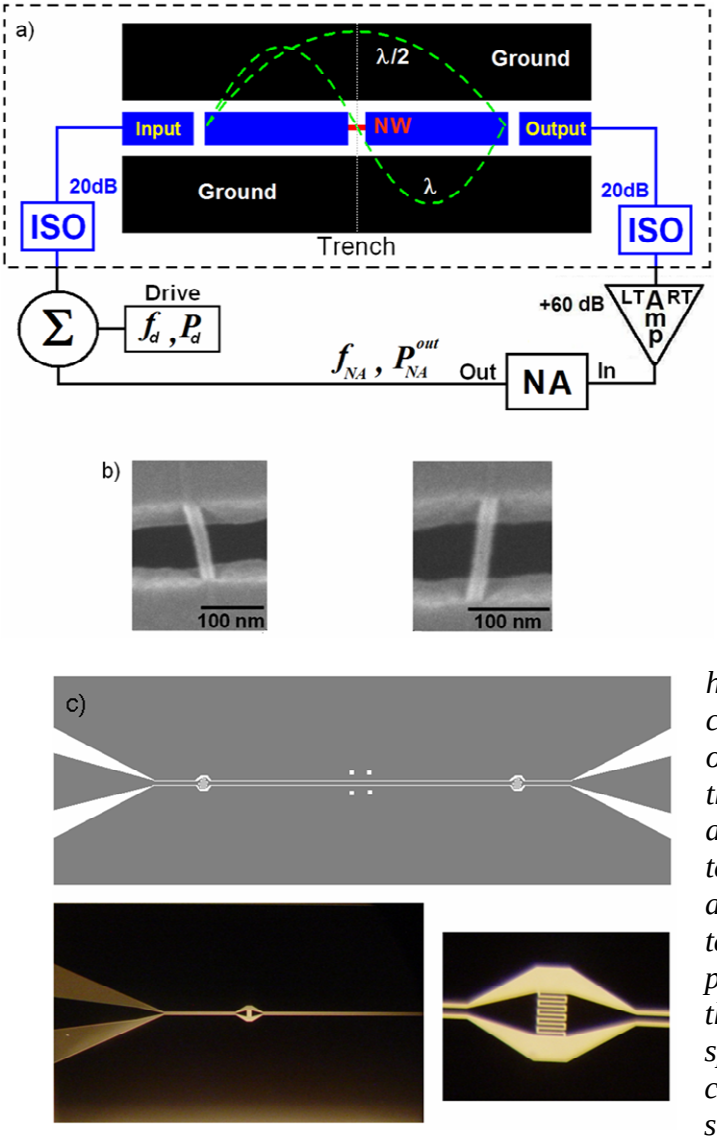

Fig. 4.1: (a) Resonator-nanowire schematic and measurement setup. The microwave signal, composed of one or two sinusoidal waves [added through a power combiner (denoted ∑)], is directed to the input of the Fabry-Perot resonator through a total of ~30 dB of isolators and attenuators, that are maintained at a cryogenic temperature. The input and output of the resonator are capacitively coupled to the center conductor (blue) through coupling capacitors of ~45 fF, formed by a 3 μm gap in the MoGe film. The center conductor is either 10 or 25 nm thick and 10 μm wide. It is interrupted, halfway along its length, by a trench, and connected through the nanowire(s). The output signal of the resonator travels through ~20 dB of isolators and attenuators (also at a cryogenic temperature) and then ~60 dB of amplifiers, including one at a cryogenic temperature, before arriving at the input port of the network analyzer (NA), where the transmitted power is measured. The spatial profiles of the supercurrents corresponding to the λ/2 and λ modes are shown as dashed lines. (b) Examples of two individual, 25 nm wide, MoGe nanowires. The trench, over which the wires are suspended, appears black. (c) Top panel: Schematic of photomask used to define the resonator. Bottom panel: photograph of one side of the resonator with a zoomed in view of the capacitive coupling.

This fabrication technique results in high-quality nanowires, which seamlessly connect the two halves of the resonator. The center conductor of the resonator is either 10 or 25 nm thick and ~10 μm wide, and the gap between the ground plane and center conductor is ~5 μm. A Fabry-Perot resonator is formed by gaps of ~3 μm between the center conductor and the input and output ports of the resonator. These gaps form two capacitors having capacitances of about

45 fF each, which act as two semi-transparent mirrors to impose a rigid boundary condition such that the supercurrent through these gaps is exactly zero. The total length of the center conductor between the two coupling gaps is 10 mm and the expected fundamental resonant frequency was ~10 GHz; however, the measured resonant frequency at low temperature was ~4 GHz, due to the kinetic inductance contributed by the MoGe film. All samples were designed to be overcoupled to have quality factors that are dominated by external dissipation from the energy leakage thorough the capacitive mirrors to the input and output ports, rather than by internal dissipation in the resonators.

Figure 4.1(b) shows scanning electron micrograph (SEM) images of typical superconducting MoGe nanowires (here having lengths and widths of ~105 nm and ~25 nm, respectively). The supercurrent oscillations in the resonator are excited by applying a microwave signal to the input, which is coupled to the resonator via the capacitive mirror. If desired, this signal can be a sum of two such waves (via a power combiner). The signal power that is transmitted through the resonator and escapes through the coupling capacitor at a given frequency is measured using an Agilent N5230A vector network analyzer (NA), on the output port of the resonator, after the signal has passed through a series of isolators, attenuators, and amplifiers. The transmission coefficient for this process, which we call the *S*-parameter, is defined via $S_{21} = 10\log_{10}\left(P_{\mathrm{NA}}^{\mathrm{in}} / P_{\mathrm{NA}}^{\mathrm{out}}\right)$ [or, equivalently, $S_{21} = P_{\mathrm{NA}}^{\mathrm{in}} - P_{\mathrm{NA}}^{\mathrm{out}}$, if $P_{\mathrm{NA}}^{\mathrm{in}}$ and $P_{\mathrm{NA}}^{\mathrm{out}}$ are expressed in dBm, which is an absolute unit where 0 dBm equals 1 mW], where $P_{\mathrm{NA}}^{\mathrm{out}}$ is the power of the signal sent *from* the NA *to* the resonator input, and $P_{\mathrm{NA}}^{\mathrm{in}}$ is the power measured *on* the NA input port which arrives *from* the resonator ouput port through a series of isolators, attenuators, and amplifiers. Isolators and attenuators adding up to ~30 dB on both the input line and output line from the resonator are inserted at low temperatures, in order to eliminate the

thermal noise impact from the environment. A cryogenic low noise amplifier (from Low Noise Factory) and room-temperature amplifiers are also employed in order to increase the signal-to-noise ratio. For all curves showing a crater behavior, the input power corresponds to the power sent from the NA to the input port of the resonator and the drive power is set to zero. For all curves showing a periodic set of peaks, a single drive source is used where the input power corresponds to the drive power and the NA power is negligibly small.

4.3 Experimental results

For low values of the input signal power (e.g., around –60 dB), the transmitted power shows sharp, Lorentzian, resonance peaks centered at signal wavelengths, λ, obeying $L = \lambda/2$ (fundamental mode), = λ (first harmonic), = 3λ/2 (second harmonic),… , where L is the length of the resonator defined as the distance between the two mirrors [see Fig. 4.2(a), (b), and (c)]. The various modes can be fit to the Lorentzian lineshape, as in Fig. 4.2(b) and (c) according to $S_{21} = 10\log\left(\frac{A}{(f_0/Q)^2 + 4(f - f_0)^2}\right) = const - 10\log\left((f_0/Q)^2 + 4(f - f_0)^2\right)$ [dB], where Q is the quality factor, A is a constant, f_0 is the resonance frequency, and f is the frequency. The quality factor at higher modes decreases because the capacitive loss mechanisms are inversely proportional to frequency. In a MoGe resonator such as those measured in this work, the resonance frequency increases with a reduction in temperature until it begins to saturate at low temperatures of ~ 1 K [see Fig. 4.2(d)]. This occurs due to the fact that in MoGe the kinetic inductance is not negligible and changes as a function of temperature. Similarly, the quality factor in our MoGe resonators increase as the temperature is reduced [see Fig. 4.2(e)]. The

quality factor is related to the number density of cooper pairs in the condensate and as the temperature is lowered, it increases as the quasi-particle number density decreases due to a lower thermal energy causing less cooper pairs to break up.

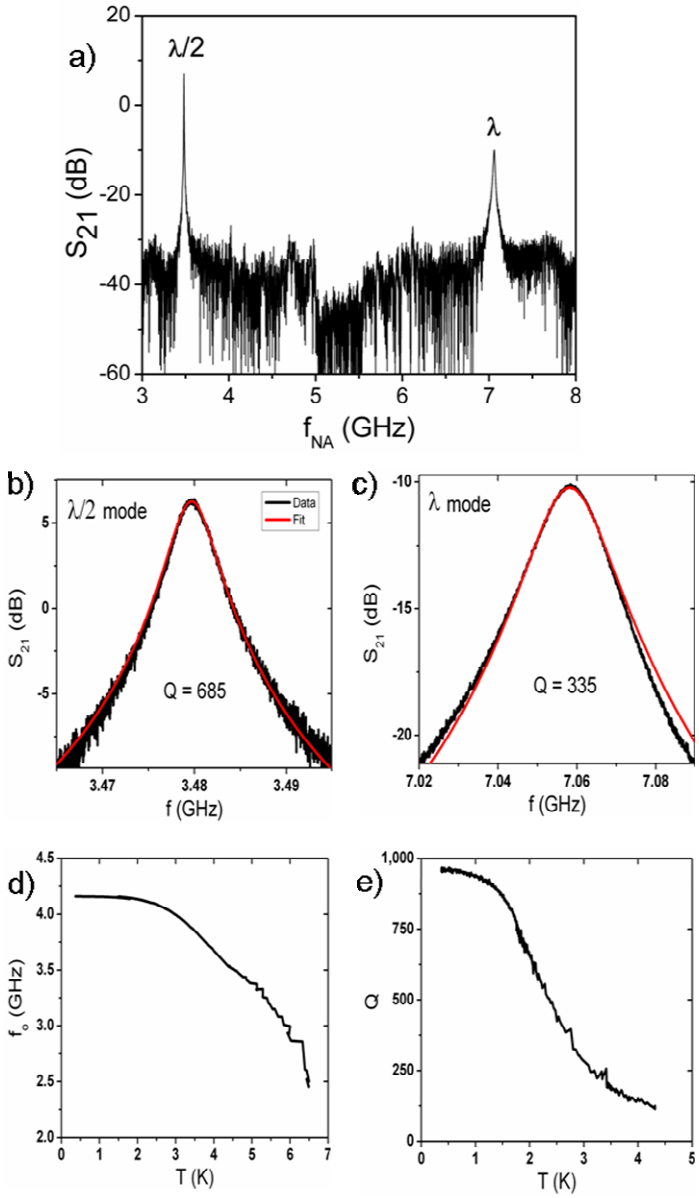

Fig. 4.2: (a) Transmission characteristic of sample S1, showing peaks at the fundamental frequency, corresponding to $L = \lambda / 2$, and the first harmonic, at $L = \lambda$. (b) The λ/2 transmission peak measured at low power with the corresponding Lorentzian lineshape fit resulting in Q = 685. (c) The λ transmission peak measured at low power with the corresponding Lorentzian lineshape fit resulting in Q = 335. (d) The resonance frequency of a 25 nm thick MoGe resonator as a function of temperature. (e) The temperature dependence of the quality factor for the same resonator as described in (d).

As the power is increased from -60 towards -47 dB, the frequency-dependent response near the λ/2 resonance first bends over towards lower frequencies, as shown in Fig. 4.3(a), doing so in a manner consistent with the behavior of the Duffing oscillator [17]. The nonlinear inductance of the nanowire, $L_{NW} = \frac{\hbar}{2e}\left(\frac{dI}{d\varphi}\right)^{-1}$, is the source of the Duffing nonlinearity, in which e is the electronic charge, $\hbar$ is Planck's constant divided by 2π, I is the supercurrent, and φ is the superconducting phase difference between the ends of the wire. At a certain critical power, a bifurcation is observed where there is a noticeable jump in the transmission, which can be as large as 5 dB in our samples as in Fig. 4.3(b). As the frequency is swept in the opposite direction, hysteresis is observed. The bifurcation in a nanowire embedded MoGe resonator sample and its corresponding hysteretic behavior has been previously studied [17]. As the power is increased further, the resonance then develops a marked *dip* in transmission near the center of the shifted peak [see Fig. 4.3(a)]. In what follows, we refer to this dip as a *Lorentzian crater*. By contrast, we note that the resonance corresponding to the λ mode remains Lorentzian up to much higher input powers (i.e., by a factor of ~3000). This difference in behavior is not accounted for by the difference in *Q*-factors (i.e., quality factors) between the resonances [32]. Indeed, the 3λ/2 resonance, which is of still smaller *Q* than the λ mode, develops a crater at a lower input power [see Fig 4.8(a)]. The frequency width of the crater at this mode is larger than in the λ/2 mode because the crater width is inversely proportional to the quality factor. The crater width also grows with an increasing input power. Thus, one is led to regard the crater as being related to the properties of the *nanowire itself*, and as being manifested at resonances that have an *antinode* at the location of the nanowire (the λ/2, 3λ/2,…etc. modes) [17]. The properties of the film are expected to be observed at the λ, 2λ,…etc. modes where there exists a

node at the location of the nanowire. This view is corroborated by the relationship between the threshold power for crater formation, P_c, and the temperature (see Fig. 4.4), which has the form

$$P_c(T) \propto \left(1-(T/T_c)^2\right)^3, \qquad (4.1)$$

where T_c is the critical temperature for the onset of superconductivity in the nanowire. Equation (1) matches the temperature dependence predicted by the Bardeen formula [1] for the *square* of a nanowire's critical current given by $I_c(T) = I_c(0)\left[1-(T/T_c)^2\right]^{3/2}$, where $I_c(0)$ is the critical current at zero temperature and T_c is the critical temperature of the nanowire. Thus, the crater is a result of dissipation triggered when the nanowire current exceeds it's critical current, resulting in Joule heating. The argument presented above is based on the assumption that, in general, the power carried through the resonator or a coplanar waveguide in general is proportional to the square of the amplitude of the supercurrent, i.e. $P \sim I^2$.

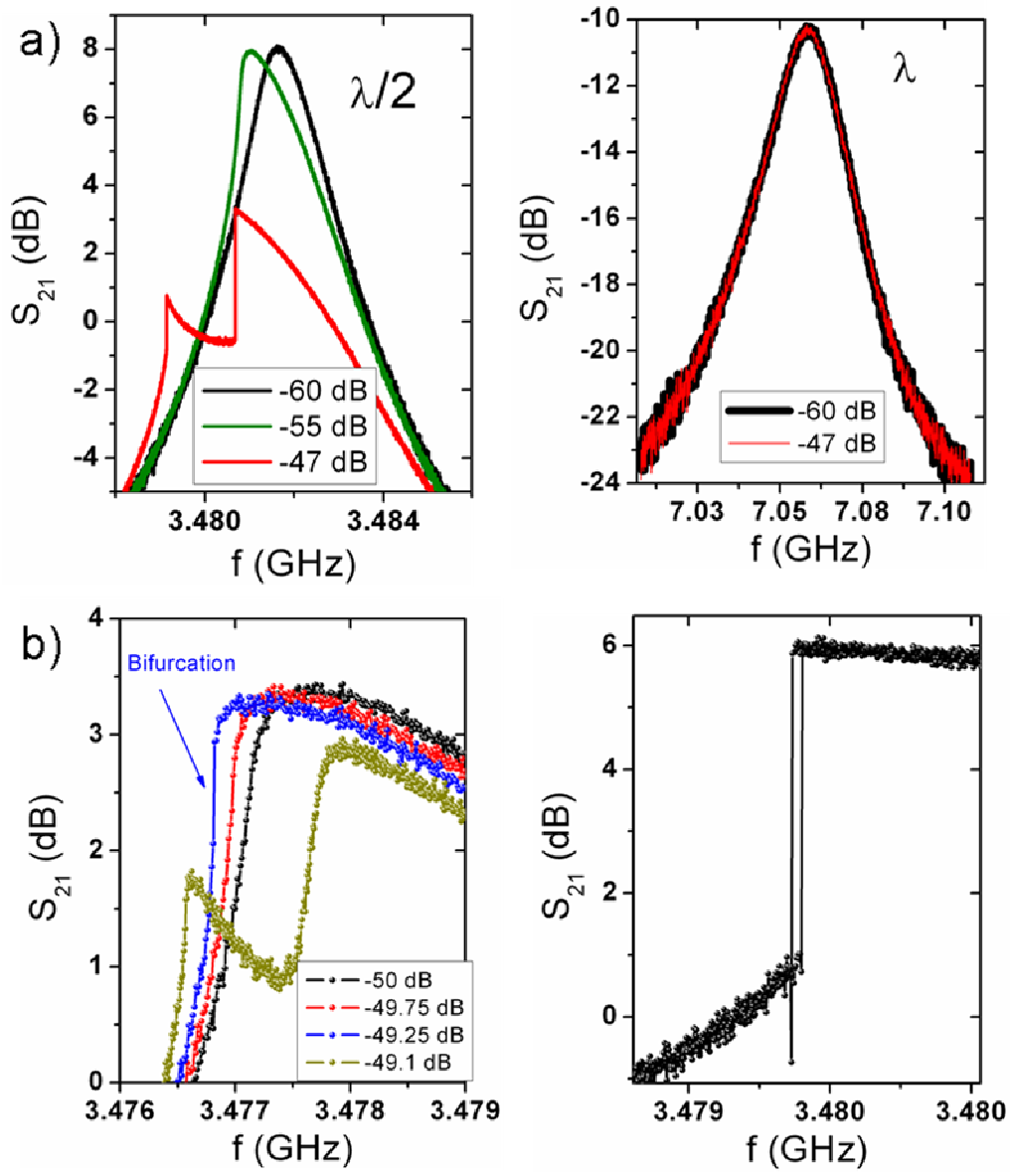

Fig. 4.3: (a) (left) Shape of the λ/2 transmission peak for sample S1 for a relatively low power (black curve) and for a relatively high power (red curve). The peak becomes more asymmetrical and develops a "crater." (right) Shape of the λ peak (Q = 335) for the same powers as in the left panel; unlike the λ/2 peak, the λ peak shows no appreciable dependence on the input power in this regime. Note that the vertical axis is on a logarithmic scale, and that the quality factor is found by fitting the transmission curve to the Lorentzian lineshape:

$S_{21} = 10\log\left(\frac{A}{(f_0/Q)^2 + 4(f - f_0)^2}\right)$*, where A is a scaling factor and* f_0 *is the resonance frequency. (b) (left) Transmission vs. frequency showing the transition from a bent over Lorentzian curve to one showing bifurcation and eventually to one with a crater. (right) An example of a transmission curve showing bifurcation where hysteresis is observed as the frequency is first swept in the positive and then in the negative direction.*

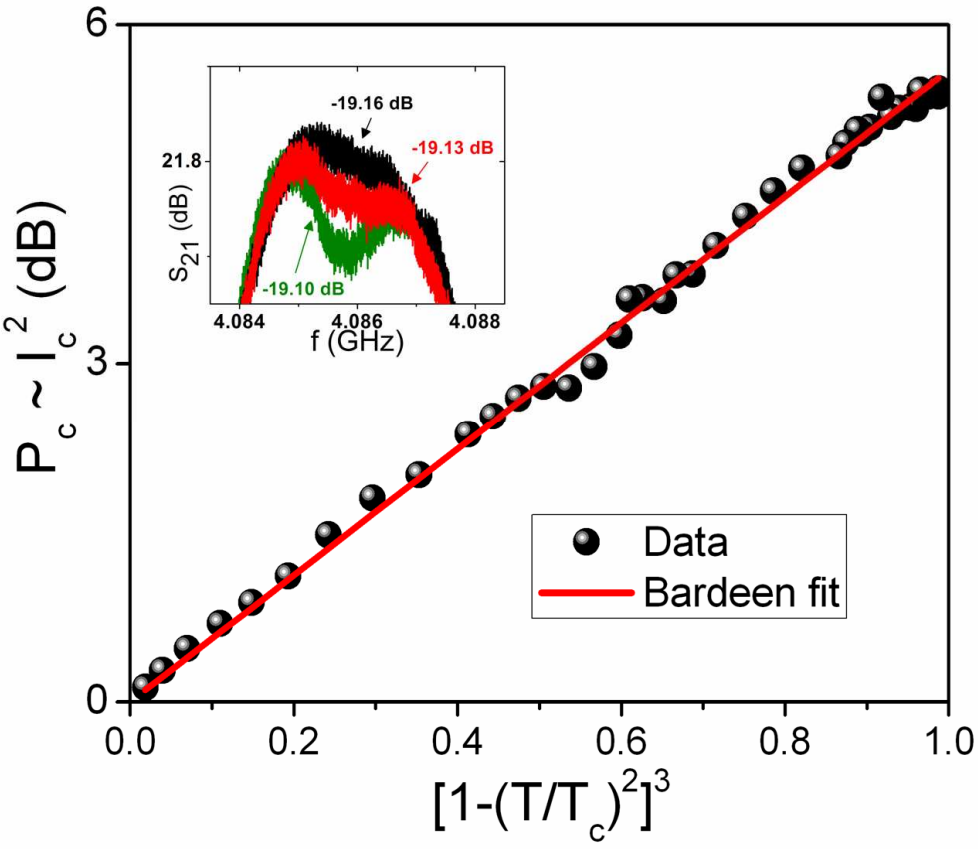

Fig. 4.4: Temperature dependence of the threshold input power, P_c, required for the onset of a crater for sample S2. That the onset power, P_c, is proportional to $\left[1-(T/T_c)^2\right]^3$ suggests that it is proportional to I_c^2, where I_c is the critical current of the nanowires, and hence that the crater is a consequence of the nanowire current being driven past its critical value. Such a conclusion follows from the fact that according to Bardeen [1], the critical current of a nanowire depends on temperature as $\left[1-(T/T_c)^2\right]^{3/2}$, at all measured temperatures. In the fit, a value of 5.54 K was used for T_c, which is close to the T_c values of other measured and similarly dimensioned nanowires. The quality factor of sample S2 at a temperature of 1.5 K was 725. The inset illustrates how the threshold power is determined: the red curve is taken to be the threshold, as it constitutes the power at which a crater just becomes observable. The uncertainty of the determined P_c is about 0.05 dB.

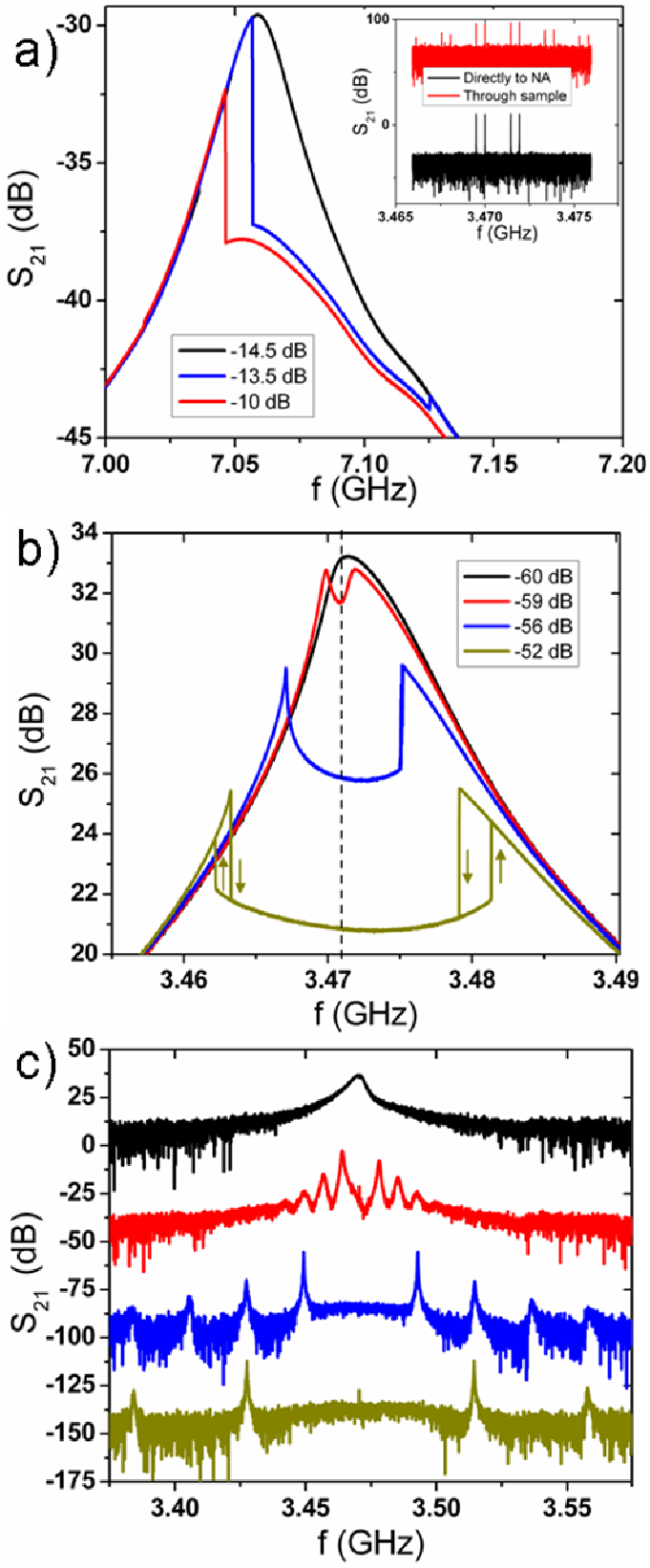

Fig. 4.5: (a) Transmission curve at the λ resonance as the input signal power is increased, showing the onset and expansion of the "crater" for sample S1. Note that there is no Duffing-type nonlinear behavior at this resonance, and that for powers above the threshold, the shape of the "crater" is concave-down. Inset: The transmission spectrum for two drive sources separated by 2 MHz sent directly to the NA (black) and through the nanowire-resonator sample to the NA (red). The non-linearity of the system is demonstrated by observing idler tones at the same separation of 2 MHz from the stronger signal frequency produced by mixing. (b) Evolution of the transmission curve at the λ/2 resonance as the input power is increased, showing the onset and expansion of the crater. Note that, for powers well above the threshold for crater formation, the transmission curve becomes hysteretic (i.e., irreversible with frequency sweeping). The vertical dashed line is the frequency at which the driving source is tuned in (c). (c) The transmission spectrum [or, equivalently, in the time domain the supercurrent amplitude oscillations (see main text)] when the drive frequency is fixed at 3471 MHz. The four curves, from top to bottom, correspond to drive powers with the same values as given in panel (b). The curves in panel (c) have been translated vertically for ease of viewing.

Note that the positive curvature of the bottom of the crater at the λ/2 resonance [see Figs. 4.3(a) and 4.5(b)] is incompatible with a scenario (such as that presented for the simpler case of a resonator without any nanowires in Ref. [33]) in which the *Q*-factor of the resonance decreases abruptly at some critical input power, and the system thus enters a dissipative *stationary* state. The behavior at the λ resonance is, however, consistent with this scenario [see Fig. 4.5(a)]: this is to be expected because, for this resonance, the current amplitude is very small in the region where the nanowire is located, so that the nanowire dynamics do not participate strongly to this resonance. Under the simple *Q*-factor reduction scenario, the transmission coefficient would jump to a smaller value when the current exceeds the switching current (the value of the supercurrent at which the wire switches to the normal state) of the nanowire [34] and rise to its original level when the current falls below the retrapping current, but the lineshape would exhibit a negative curvature, as a perfect Lorentzian peak does. In other words, regardless of the *Q*-factor, there would be more transmission at the resonance than away from it.

A more striking inconsistency with the *Q*-factor reduction scenario is the occurrence of *current-amplitude oscillations* when the input power exceeds the threshold for crater formation. In this regime, the frequency spectrum of power transmitted by the resonator exhibits a periodic array of satellite peaks [see Fig. 4.5(c)], spaced at integer multiples of a certain frequency Δf away from the drive frequency; Δf increases with input power, and the height of these satellite peaks scales approximately as $1/n$, where n is the n^{th} peak, counting from the drive frequency. As the Fourier coefficients associated with a function that is periodic and has discontinuities decay as $1/n$ [35], the behavior of the satellite peak heights indicates that, in the *time* domain, the transmitted power exhibits periodic jumps. In Fig. 4.6, color plots of the transmission characteristics of the behavior of the following can be observed: the satellite peak spacing

evolution dependency on drive power, the crater formation as a function of NA power, and the satellite peak evolution dependency on the drive frequency.

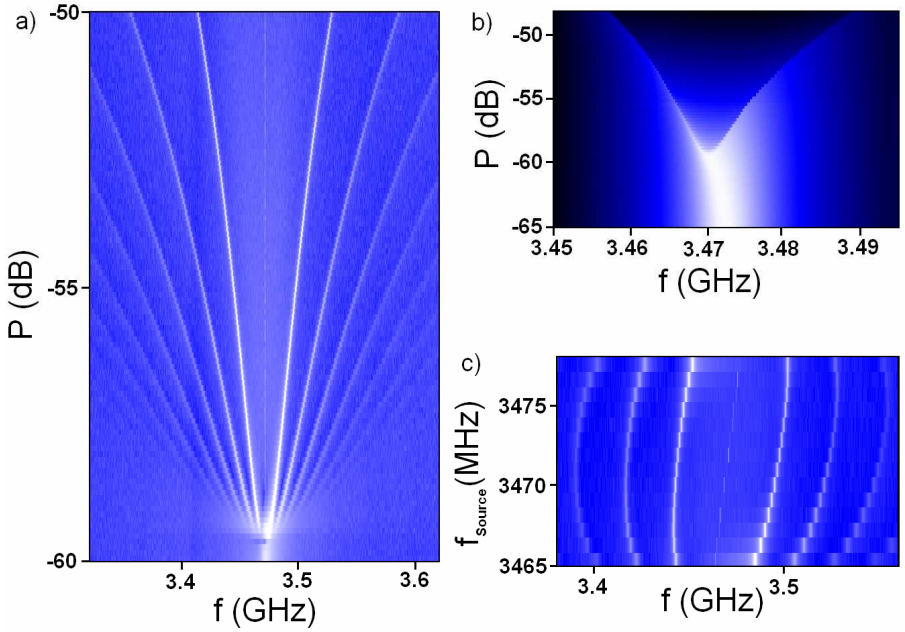

Fig. 4.6: Color plots of the transmission characteristics of sample S1 at 1.5 K. (a) A drive signal is fixed at a frequency of 3471 MHz while the drive power is varied. As the drive power increases, the satellite peak spacing increases. Lighter color shows higher transmission. (b) The evolution of the Lorentzian peak into a crater. As the NA power is increased, the Lorentzian peak first bends over to lower frequencies, then a crater in the Lorentzian forms and continues to grow in width. (c) A drive signal is fixed at a power of -55 dB while the frequency is varied. The satellite peak spacing varies as a function of the drive frequency.

For input powers near the threshold for crater formation, the crater is non-hysteretic; as the input power is increased further, however, hysteresis appears on the high-frequency side of the crater, and for still higher powers on the low-frequency side as well. Besides using a quasi-one-dimensional nanowire as opposed to a microbridge, the coexistence of hysteresis and amplitude oscillations is an important difference between our results and those presented in Ref. [31]. The hysteresis that we observe does not appear to be sensitive to the sweep rate (see Fig. 4.7). Additionally, there is a noticeable stochasticity in the switching frequency into the normal state (into the crater) and retrapping frequency back to the superconducting state (jump

back to the Lorentzian curve) as seen in the inset of Fig. 4.7. This switching is presumably caused by random thermal fluctuation of the superconducting phase across the nanowire.

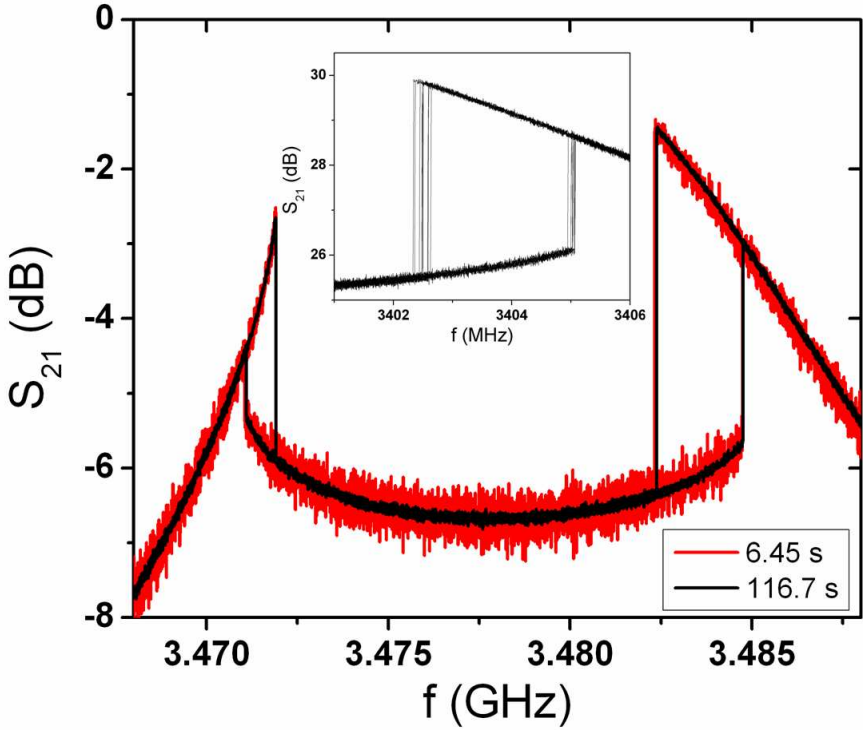

Fig. 4.7: Typical transmission characteristics, corresponding to two widely separated sweep speeds (red fast; black slow) for sample S1. The width of the hysteretic region (as well as the entire shape of the curve) does not depend noticeably on the sweep rate, at least for the sweep rates used in these measurements. Inset: Transmission plot of sample S2 showing a noticeable distribution of switching frequencies (10 sweeps are included) into and out of the crater.

Whereas nearly all of the data that we present is for a sample containing a MoGe nanowire of diameter 25 nm at the λ/2 resonance, we have observed essentially identical phenomena at the 3λ/2 resonance (see Fig. 4.8), and also for even thinner nanowires (see Fig. 4.18). In addition, similar phenomena have been observed in resonators having much larger *Q*-factors, which incorporate much longer, thicker, and wider, Nb wires, where the width is much larger than the coherence length (Fig. 4.9).

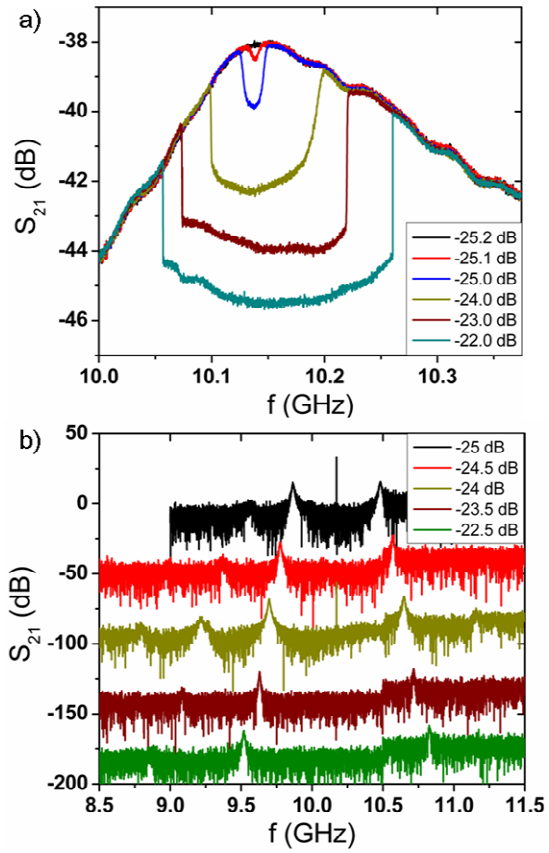

Fig. 4.8: (a) Transmission characteristics of sample S2 (25 nm thick MoGe) at 1.45 K at its 3λ/2 resonance, as the input signal power is increased. In this case, the crater is qualitatively similar to that at the λ/2 resonance; however, it exhibits additional features, such as secondary dips near the edges of the crater. We attribute these new features to the fact that the 3λ/2 resonance is relatively broad (Q ~60), and therefore requires higher input power for a crater to form. At these high input powers, the nonlinearities in the rest of the resonator (i.e., not the nanowire part), and the associated parasitic resonances, can no longer be neglected. (b) The satellite peaks when the driving frequency and power [which is in the same range as in panel (a)] resides in the crater (for the same sample S2). When the drive frequency is in the crater, the satellite peaks are qualitatively similar in shape to those at the λ/2 resonance. The curves in this panel have been vertically translated for ease of viewing.

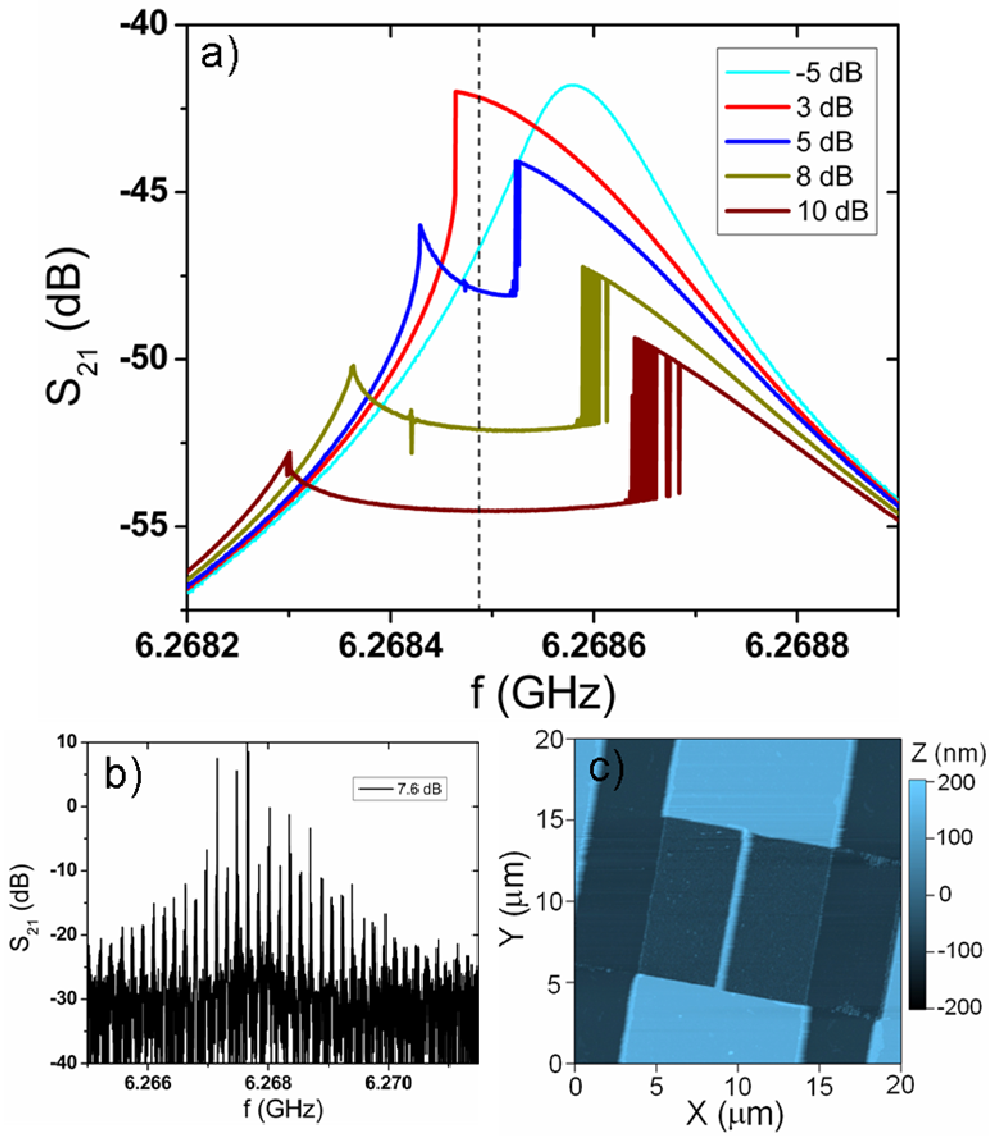

Fig. 4.9: Microwave measurements on sample S3, which is a Nb film resonator with an incorporated microbridge. The wire is 200 nm thick, 1 μm wide, and 10 μm in length and was fabricated using e-beam lithography. (a) Transmission characteristics of sample S3 at its λ/2 resonance, for a range of input powers. At the measurement temperature of 1.5 K, the quality factor of the low-power curve is 43,500. The shape of the crater that forms is similar to that for the MoGe case. (b) Satellite peaks when the driving frequency and power lie inside the crater. The driving frequency is indicated by the vertical dashed line in panel (a), and has a power of 7.6 dB. (c) Superconducting Nb resonator, grown on a sapphire substrate and containing a microbridge. The Nb resonator sample presented here was fabricated by T. J. McArdle at the University of Illinois in Urbana-Champaign.

A further proof can be given that only the resonances that have an *antinode* at the location of the nanowire (the λ/2, 3λ/2,…etc. modes) result in the crater behavior. In Fig. 4.10(a), a plot is shown of the transmission power versus the NA frequency as the NA source is swept across the fundamental resonance peak with a power tuned to -50 dB, which is a few dB less than the critical power P_c. A second microwave source was fixed at the 3λ/2 resonance peak (10.434 GHz) and its power was varied. Because the 3λ/2 resonance peak also has a current antinode at the location of the nanowire, the microwave power from the source fixed at this frequency will cause a crater. The small, distorted "sawtooth" like curves inside the crater are a result of the interference of the two strong signals at a constantly changing frequency difference.

In Fig. 4.10(b) and (c), the magnitude and phase are shown as the NA frequency is swept across the fundamental mode of sample S1 at an input power of -60 and -50 dB. When the power is -60 dB, a Lorentzian profile is observed in the magnitude vs. frequency measurement. The phase vs. frequency measurement shows a phase change of ~180° as the resonance peak it traversed. Had the measurement been carried out in a greater frequency range or with a higher quality factor resonator, the full 180° would be observed. The behavior of the phase of the S_{21} parameter as a function of frequency can be explained via the phase of a RLC circuit by the following equation: $\phi = \arctan\left(\frac{X_L - X_C}{R}\right) = \arctan\left(\frac{4\pi^2 f^2 LC - 1}{2\pi fRC}\right)$, where X_L and X_C are the inductive and capacitive reactances, respectively. When the power is set to -50 dB, a bifurcation jump is observed in the magnitude vs. frequency plot. At the bifurcation frequency, a ~ 90° jump in the phase is measured and ~ the full 180° is measured across the entire resonance peak.

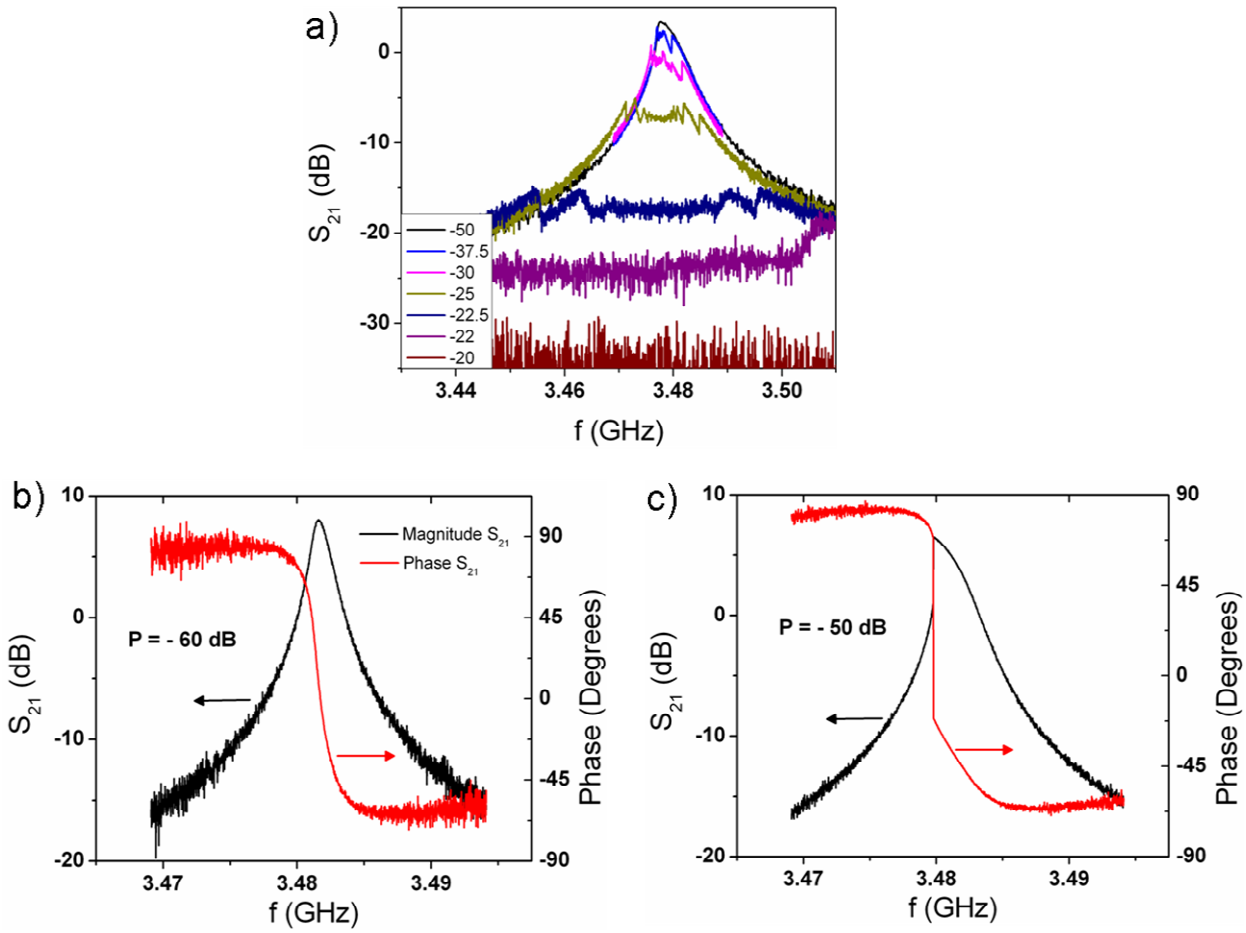

Fig. 4.10: (a) Transmission spectrum with two strong microwave sources. The NA source frequencies are swept near the λ/2 resonance frequency at an output power of -50 dB while a second source is fixed at the resonance frequency of the 3λ/2 where f = 10.434 GHz while the power is varied. Peak structures are observed in the same frequency range where the crater exists. (b) The magnitude and phase as the NA frequency is swept across the fundamental mode of sample S1 at an input power of -60 dB where a Lorentzian is noticeable. (c) The magnitude and phase as the NA frequency is swept across the fundamental mode of sample S1 at an input power of -50 dB where a Lorentzian profile with a bifurcation jump is observed. At the bifurcation frequency, a ~ 90 degrees jump in the phase is measured, however, this value is power dependent.

4.4 Theoretical model

We have developed a phenomenological model for resonators with integrated nanowires, which may be summarized as follows. The resonator is modeled as a Duffing nonlinear oscillator

[17, 36] via the identification of the amplitude of oscillation with the supercurrent through the nanowire. We add to the model the following element, which we term a "switching rule": if the amplitude of oscillation exceeds a certain critical value (which corresponds to the switching current of the nanowire), the oscillation amplitude is instantaneously reset to zero. This switching rule is meant to capture the fact that when the current in the nanowire exceeds its switching current, the nanowire enters the normal state, in which it has a normal resistance of the order of 1 kΩ; while the nanowire is in its resistive state, the effective Q-factor of the resonator is very small; hence, the steady-state amplitude of the supercurrent is essentially zero. The switching rule represents the underlying assumption that as the wire switches to the normal state it will dissipate all the energy stored in the resonator (which is stored in two forms, namely the kinetic energy of the moving condensate and the potential energy of the electric field between the center conductor and the ground planes of the resonator). An additional element of the switching rule is that, after switching, the amplitude of the oscillator is held at zero for a fixed time t_{hold}, which corresponds to the time the nanowire takes to cool down and relax to its equilibrium superconducting state. (Alternatively, one can describe t_{hold} as the duration for which the Q-factor of the resonator is taken to be zero.) At the end of t_{hold}, the Q-factor is returned to its original value, and the oscillation amplitude regrows according to the Duffing oscillator equation of motion.

An important aspect of the model, which is necessary for it to describe the observed hysteresis, is the continuous manner in which we take the drive frequency to be swept. This mimics the experimental situation, in which both the input current and the current in the resonator change *continuously*, as the network analyzer progresses from one value of the probe signal frequency to the next one. In particular, the initial conditions for the resonator at each

drive frequency depend on the previous value of the drive frequency, and thus on the direction of the sweep. We must therefore ensure that the drive signal does not change discontinuously in our numerical simulation of the frequency sweep; as we shall see, this can be arranged by choosing the relative phase of the drive signal at frequencies ω and $\omega+\Delta\omega$ appropriately.

The algorithm outlined above is straightforward to implement numerically (for this we use the LabView environment), as we describe in Sec. 4.5. As we shall see there, it yields results that fit our data very well, as shown in Figs. 4.13, 4.18, and 4.20. Before doing that, we explain in simple, physical terms why our model predicts the phenomenology that it does. For ease of presentation, we further simplify the model by neglecting the nonlinear character of the oscillator. The nonlinear element is responsible for the asymmetric nature of the crater, but is otherwise unrelated to the underlying physics. The nonlinear effects have been investigated elsewhere [17].

Basic picture of the oscillatory state

The value $x(t)$ of the supercurrent in the resonator evolves in time t according to the oscillator equation:

$$\ddot{x}(t) + 2\kappa\dot{x}(t) + \omega_0^2 x(t) = Ve^{i\omega t}\Theta(t), \qquad (4.2)$$

where κ is the damping coefficient, ω_0 is the resonance frequency, and $Ve^{i\omega t}\Theta(t)$ is the driving signal, which as an amplitude V and frequency ω and, as indicated by the Θ function, is switched on at time t. The physical current in the resonator is given by the real part of $x(t)$. When the instantaneous value of the real part of the supercurrent in the resonator exceeds the critical current of the nanowire, the following sequence of events occurs:

(1) The nanowire enters the normal state.

(2) The *Q*-factor, and, correspondingly the supercurrent in the resonator and voltage, both drop to zero, thus reducing the total stored energy to zero. All of these quantities remain zero for a time, which we denote t_{hold}.

(3) The *Q*-factor then returns to its equilibrium value (i.e., the value corresponding to small current-oscillation amplitudes), and the current begins to build up in the resonator, according to the oscillator equation.

(4) The current through the nanowire once again reaches its switching threshold, the nanowire switches, and the entire process repeats itself.

This cyclic process has a frequency Ω, which is much lower than the resonance frequency ω of the oscillator. In other words, the frequency Ω is the frequency of the oscillations of the total amount of energy stored in the resonator and, at the same time, of the *amplitude* of the supercurrent oscillations. The time-dependence $x(t)$ of the displacement of the oscillator (i.e., the supercurrent in the resonator) is thus given by

$$x(t) = \cos(\omega t)\sum_{n=0}^{\infty} C_n \cos(n\Omega t) = \frac{1}{2}\sum_{n=0}^{\infty} C_n \left\{\cos\left[(\omega + n\Omega)t\right] + \cos\left[(\omega - n\Omega)t\right]\right\}, \qquad (4.3)$$

where C_n is the n^{th} Fourier component of the amplitude oscillations. Evidently, the Fourier transform of $x(t)$ consists of an array of regularly spaced spikes, offset from the central frequency ω by integer multiples of the amplitude oscillation frequency Ω. Due to the sudden drop of the supercurrent to zero when the supercurrent reaches the critical current, the n^{th} spike is $\sim 1/n$ times the height of the first spike (for $n \geq 1$) [35]– this corresponds to the asymptotic power-law decay behavior of the set of Fourier coefficients, discussed above.

Form of the crater

We now turn to step (3) of the amplitude oscillation cycle, viz., the growth of current in the resonator. Once again, we treat the instructive case of a damped, driven *linear harmonic* oscillator, governed by the oscillator equation

$$\ddot{x}(t) + 2\kappa\dot{x}(t) + \omega_0^2 x(t) = Ve^{i\omega t}\Theta(t)\,.$$

Here, the step function $\Theta(t)$ reflects the fact that the drive begins abruptly at the end of t_{hold}. (Equivalently, and more physically, we could have attached the step function to the inverse of the dissipative term; however, the present form is simpler to analyze and it physically gives the same effect.) The general solution for $x(t)$ may be written in terms of the corresponding Green function $G(t,t')$ as follows:

$$x(t) = \int_{-\infty}^{t} dt' G(t,t') V e^{i\omega t'} \Theta(t') = \int_{0}^{t} dt' G(t,t') V e^{i\omega t'}\,, \qquad (4.4)$$

where G is given (for $t > t'$) by

$$G(t,t') = \frac{1}{2\sqrt{\omega_0^2 - \kappa^2}} \left[\exp\left(-\kappa(t-t')\right)\sin\left(\omega_1(t-t')\right)\right], \qquad (4.5)$$

in which

$$\omega_1 \equiv \sqrt{\omega_0^2 - \kappa^2}\,, \qquad (4.6)$$

is the shifted resonance frequency. Upon performing the relevant integration, one finds that the current is given by

$$x(t) = \frac{V}{2i\omega_1}\left(\frac{e^{i\omega t} - e^{-\kappa t}e^{i\omega_1 t}}{\omega - \omega_1 + i\kappa}\right) - c.c. - r.r.. \qquad (4.7)$$

Note that we have omitted the much smaller, rapidly (counter) rotating (denoted *r.r.* and on the order of GHz), terms, as well as the complex conjugate (*c.c.*) terms as our primary focus is on the shape of the *envelope* of the current, i.e., the manner in which the amplitude grows. Note that $x(t)$ vanishes at $t = 0$, as desired, and that eventually the amplitude saturates to its steady-state sinusoidal form, doing so on a timescale given by $1/\kappa$. In Fig. 4.11 we show the behavior of $x(t)$ at fixed κ for various values of the detuning (with the aforementioned rapidly oscillating and complex conjugate terms omitted), which is given by: $|\omega - \omega_0|$.

We now proceed to explain how the nature of the process by which the current grows explains both the concave-up form of the crater and the existence of hysteresis.

Shape of the crater

The scenario outlined in the previous subsection offers a natural explanation for why the craters predicted by the model are concave *up* rather than concave *down*. From the model, and specifically Eq. 4.7, we know that (a) the r.m.s. value of $x(t)$ grows linearly, for $t << 1/\kappa$, with a frequency-independent slope, and (b) the second derivative of the r.m.s. value of $x(t)$ is *negative* for times until the point at which x saturates at its maximum value x_{max}, which must be greater than some critical value x_c if a crater is to form. [The two typical forms of x are shown in the insets of Fig. 4.11.]

It follows from point (a) that, if x reaches x_c at a very early time (i.e., if the drive power is very large) then the r.m.s. value of $x(t)$ (which we term $\bar{x}$ and define to be the mean taken over the interval $2\pi/\Omega$, i.e., over one cycle of the amplitude oscillation) can be arrived at by expanding the exponential to first order in t:

$$\bar{x} = \frac{x_c}{2}\left(\frac{2\omega_1 x_c/V}{t_{hold} + (2\omega_1 x_c/V)}\right). \qquad (4.8)$$

On the other hand, it follows from point (b) that, as the drive frequency is swept away from resonance, $x(t)$ takes a relatively long time to reach x_c (i.e., when x_{max} is relatively close to x_c, as it would be at driving frequencies relatively far from the resonance) and the average transmission *increases*. This occurs for two reasons: (i) as the amplitude of $x(t)$ saturates toward x_{max}, a larger part of each cycle is spent at higher supercurrent amplitudes [by observation (b); see also Fig. 4.16(c) and (d)]; and (ii) the amplitude oscillation period $2\pi/\Omega$ increases, and therefore t_{hold} occupies a smaller part of the cycle resulting in an increase in transmission. Thus, as one moves away from the resonance, x_{max} decreases, the transmitted power increases, and consequently the crater is concave up.

Hysteresis

Depending on whether or not the detuning exceeds κ, the oscillation amplitude either (i) overshoots its steady-state value or (ii) does not. For instance, if the drive is exactly on resonance, we know from Eq. 4.7 that the envelope behavior of the current amplitude *A(t)* of takes the form

$$A(t) \sim 1 - e^{-\kappa t}, \qquad (4.9)$$

and thus approaches its steady-state value monotonically. By contrast, if the detuning is large compared with κ, the envelope behavior of the supercurrent amplitude exhibits beats, i.e.,

$$A(t) \sim \sin[(\omega - \omega_1)t], \tag{4.10}$$

and can overshoot its steady-state value by up to a factor of two. [Note that if the drive were turned on adiabatically (or, equivalently, the Q-factor were decreased adiabatically), the amplitude would achieve its steady-state value without overshooting. In this case there would be no hysteresis. Therefore, the point at which switching occurs depends on whether the current is increasing rapidly or adiabatically; as we shall see, this leads to hysteresis.]

For large drive strengths as the frequency is swept, x first reaches its critical value relatively *far* from resonance, and case (i) applies. In this case, $x_{\max}$ exceeds the *steady-state* amplitude x_{ss}. If x_c lies between x_{ss} and x_{max} [see Fig. 4.11(b)], the model predicts that bistability occurs—if the system is initialized in its steady state, it can stably continue in the steady-state; however, once the system switches, it cannot re-enter the steady state because to do so it would have to go through the entire transient, which overshoots x_c. Therefore, the sweep *toward* resonance (during which the amplitude adiabatically increases and the resonator enters the bistable region initialized in the steady state) differs from the sweep *away* from resonance (during which the system is initialized in the oscillatory or pulsing regime, and cannot reach the steady state), and the transmission curve thus exhibits hysteresis.

By contrast, for relatively small drive powers, such as those that are barely sufficient to generate a crater, x reaches x_c at frequencies less than κ from the resonance. Now it is case (ii) that is realized, and therefore x is in the monotonic-growth regime, in which $x_{\max} = x_{ss}$, and the

model therefore predicts that no hysteresis should occur—as found in the data.

We conclude this heuristic discussion with some brief remarks on how the inclusion of thermal or quantum fluctuations, or the Duffing nonlinearity, would affect the foregoing arguments. One would expect fluctuations of the photon number in the resonator to cause fluctuations in the current through the nanowire; and these would sporadically drive the current across x_c, and should therefore cause switching between the two stable states in the hysteretic region [see Fig. 4.9(a), Fig. 4.18(a) and Fig. 4.19(d)]; at sufficiently high temperatures this would lead to the disappearance of hysteresis. As for the Duffing nonlinearity, which must be incorporated to achieve *quantitative* agreement with the data, it does not *qualitatively* affect the above considerations: it causes the two sides of the resonance curves to have distinct hysteretic behavior and forms of crater, but each side would still individually behave essentially as one would predict using the linear-oscillator model.

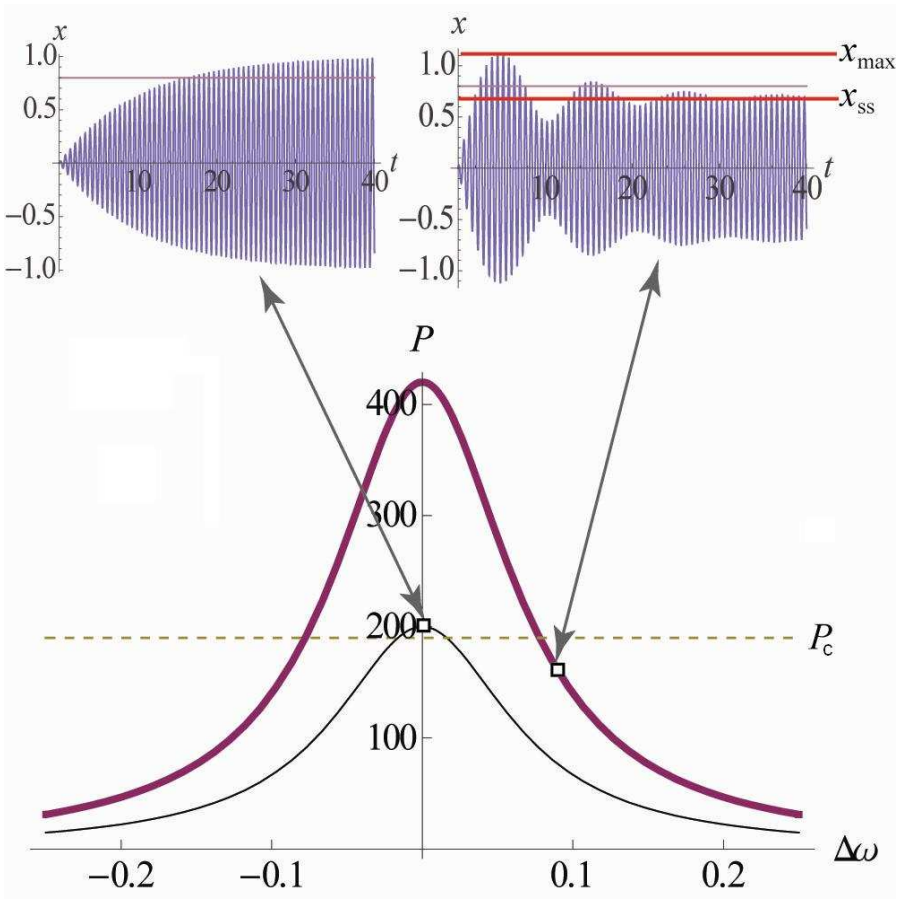

Fig. 4.11: Time averaged transmission characteristic curves (main panel) and the growth of transients (insets) computed for a linear oscillator. The lower panel shows the transmitted power as a function of input frequency for a linear oscillator, for two input-powers; the horizontal line indicates the power required to form a crater. For low input power, the onset of the crater lies near resonance; in this regime, the growth of transients is monotonic, as shown in the upper left panel, and (as explained in the text) no hysteresis occurs. For high input power, the onset of the crater is far from resonance; in this regime, the growth of transients is non-monotonic, as shown in the upper right panel. Hence, the maximal transient amplitude x_{max} exceeds the steady-state amplitude x_{ss}, and thus bistability arises, as explained in the main text. The thin, horizontal lines in the two upper panels correspond to the critical current of the nanowire; the thick lines correspond to x_{max} and x_{ss} as defined in the text.

4.5 Model fits and discussion

We implement the model using a LabVIEW program that solves the circuit sketched in Fig. 4.12, which uses the Josephson junction inductance as the nonlinear Duffing element. The three circuit

parameters used to fit the data—viz., the capacitance, inductance, and resistance—are obtained by fitting the low-power, near-Lorentzian resonance. We model the nanowire as an *effective* Josephson junction having a switching current I_{sw} and kinetic inductance (in the zero current limit) L_k that is determined, as discussed below, by fitting the extent to which the resonance is non-Lorentzian at the onset of the crater. A timestep of 1 ps is used to advance the computation. Using much smaller timesteps results in inaccurate low-power simulations, due to the large periods of the supercurrent oscillations and a loss in accuracy of the order parameter phase due to precision limits within the program. Also, using much larger timesteps results in the breakdown of the approximation used to advance the iterative method in solving the differential circuit equation. The value for the S_{21} parameter is calculated at each particular frequency as $S_{21} = 10\log[\langle I_s^2 \rangle / I_D^2] + offset$, where I_s is the supercurrent in the resonator, I_D is the bias current amplitude applied to the circuit in Fig. 4.12, and the offset is used to account for the reference value of S_{21} effected by the combination of attenuators, isolators, and amplifiers.

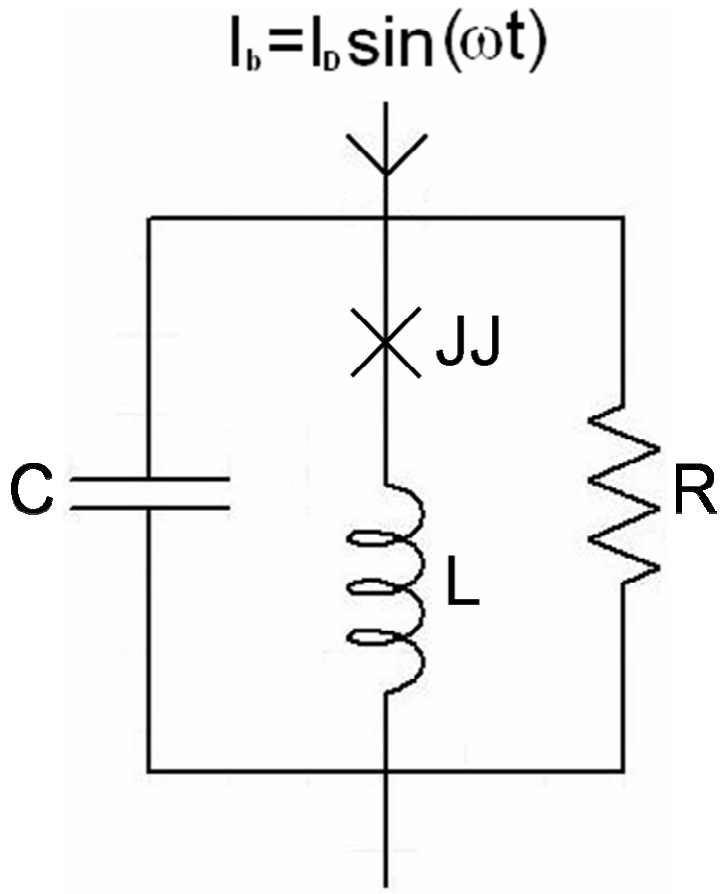

Fig. 4.12: Schematic depiction of the circuit diagram used to model the spectrum of transmission curves. The diagram consists of a resistively and capactively shunted junction (RCSJ) [37, 38] circuit having an inductor inserted in series with the nanowire. The circuit is driven by a sinusoidal bias-current of amplitude I_D and frequency ω.

The model described in Sec. 4.4, if we augment the left-hand side of the oscillator equation with the nonlinearity arising from the wire (as explained below), is able to *quantitatively* reproduce the data taken at various temperatures. In particular at a temperature of 1.5 K, as shown in Figs. 4.13, 4.16, and 4.18, the model quantitatively reproduces the following features: (1) the evolution of the crater shape, as the input power is increased; (2) the dependence of the satellite-peak spacing Δf on the input power at a fixed frequency; and (3) the dependence of the satellite-peak spacing on input frequency at a fixed power.

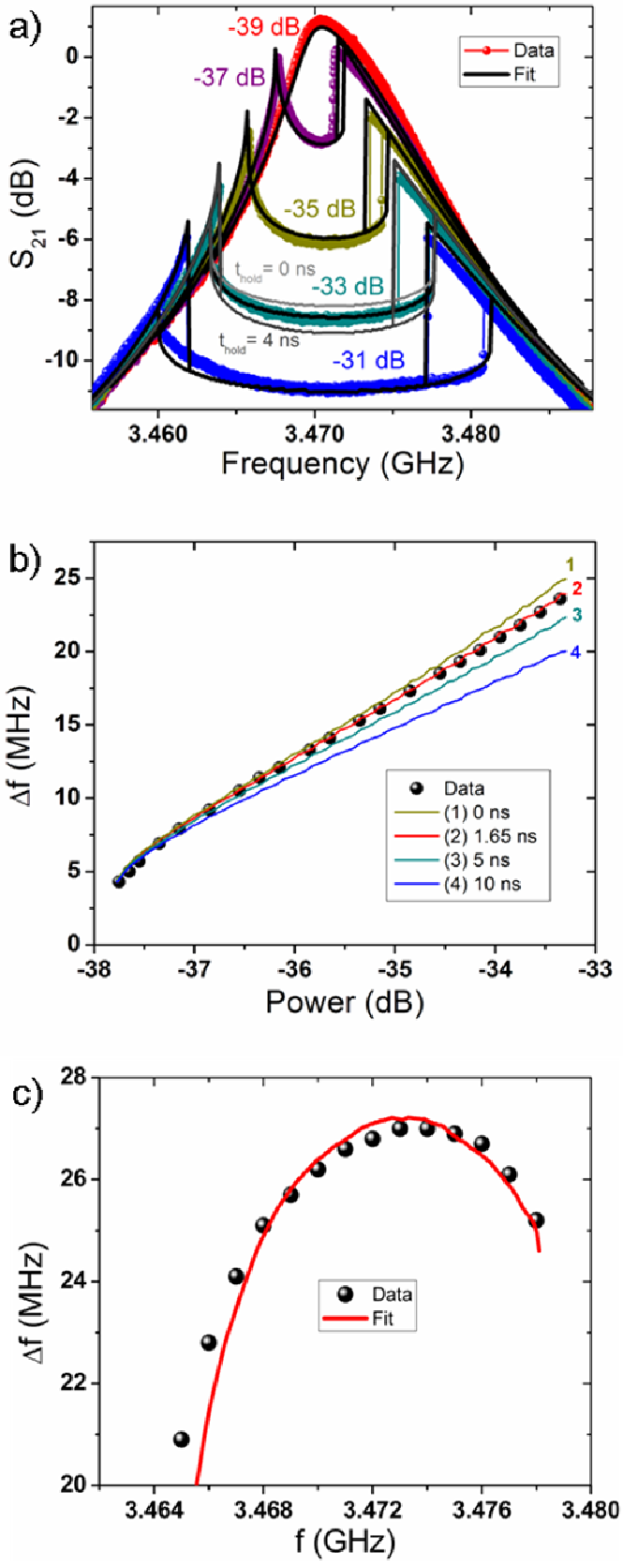

=

Fig. 4.13: Comparison of experimental data for sample S1 and predictions of the model at T = 1.5 K. (a) Transmission characteristics for input powers in 2 dB increments (thick colored lines), and fits to the model (thin black lines). At an input power of -33 dB, two other simulations are shown in grey and dark grey corresponding to t_{hold} = 0 and t_{hold} = 4 ns, respectively. The crater grows deeper (shallower) as the t_{hold} parameter is increased (decreased). Thus, t_{hold} is a sensitive and necessary fitting parameter that only affects the depth of the crater in this graph. Here t_{hold} = 1.65 ns results in the best fit. (b) Satellite peak spacing (Δf) vs. input-power at a fixed input-frequency of 3471 MHz. (c) Satellite peak spacing (Δf) vs. input frequency at a fixed input power of -33.6 dB. All fits were calculated using the following fitting parameters: C = 16.7 pF, L = 0.113 nH, R = 995 Ω, L_k = 13.1 pH, I_{sw} 8.98 μA, and t_{hold} = 1.65 ns.

The supercurrent, which is given by $I_s = I_c \sin(\phi)$, was calculated as a function of time by numerically integrating the circuit equation for Fig. 4.12 to evolve the phase across the junction at each time step according to

$$\ddot{\phi} = \left[\frac{I_{cap}/C + I_c L \dot{\phi}^2 \sin(\phi)}{\hbar/2e + I_c L \cos(\phi)} \right]. \tag{4.11}$$

This equation was derived by equating the voltages on the capacitive and junction branches of the circuit given in Fig. 4.12 and solving for $\ddot{\phi}$. Once $\ddot{\phi}$ is known, Kirchhoff's current law can be used to solve for I_{cap}, which is the current through the capacitor, to advance the computation as follows $I_{cap} = I_b - I_s - I_R$, where each term on the right hand side is known given the value of ϕ or one of its derivatives from the previous timestep. The superconducting phase ϕ and all its derivatives are initialized to zero.

The model presented above can also capture the behavior of S_{21} as a function of single source power at a fixed frequency (Fig. 4.14). In these measurements, the NA frequency is fixed (at three various frequencies) and the NA power is swept while measuring S_{21}. To model these curves, the same fitting parameters as are used in the fit presented in Fig. 4.13 are used here, except in these fits, the drive frequency is fixed while the power is swept. Good agreement between the model and the experiment are found suggesting that our model is correct.

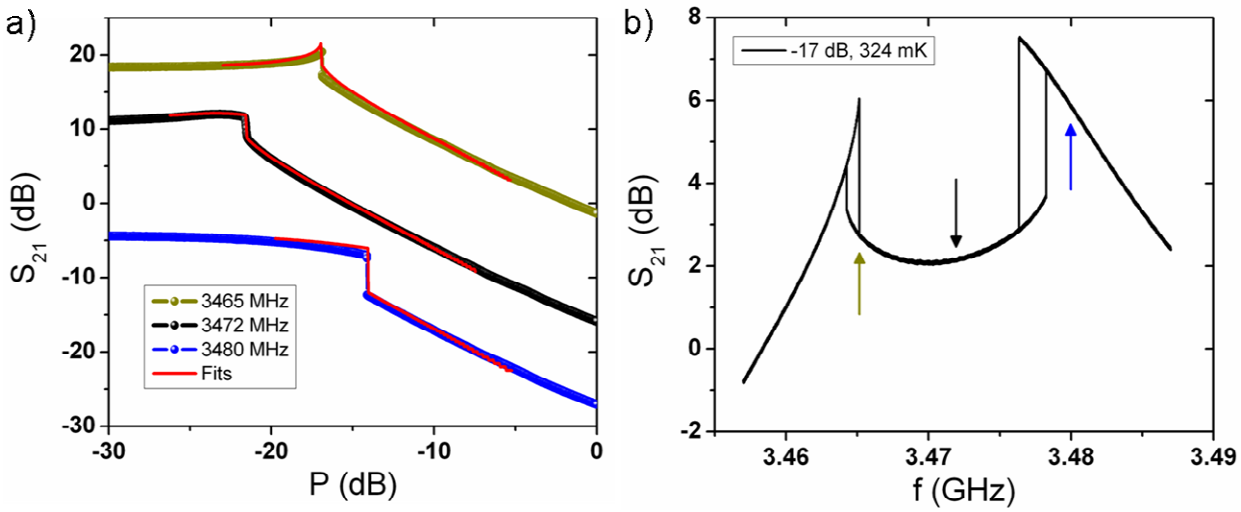

Fig. 4.14: (a) S_{21} as a function of power for three different frequencies, and the corresponding fits from the model using the same fitting parameters as are used in Fig. 4.13. (b) Transmission curve as a function of frequency indicating the frequencies where the microwave signal was applied in (a).

When two sources are applied such that their frequencies and powers make them both supercritical, a series of harmonics and subharmonics are observed in the power spectrum of the satellite peaks as a result of intermodulation (Fig. 4.15). In this figure, additional peaks have been observed in between the standard satellite peaks and have been identified with the 1/2, 1/3, 1/4, 1/5, 1/6, 1/7, 1/8 integer harmonics. These features can be captured using the model as in Fig. 4.15(c). Adding to the model a second supercritical power microwave source at a fixed frequency near to the resonance frequency, results in the same distribution of harmonics i.e. at the 1/2, 1/3, 1/4, 1/5, 1/6, 1/7, 1/8… integer harmonic locations.

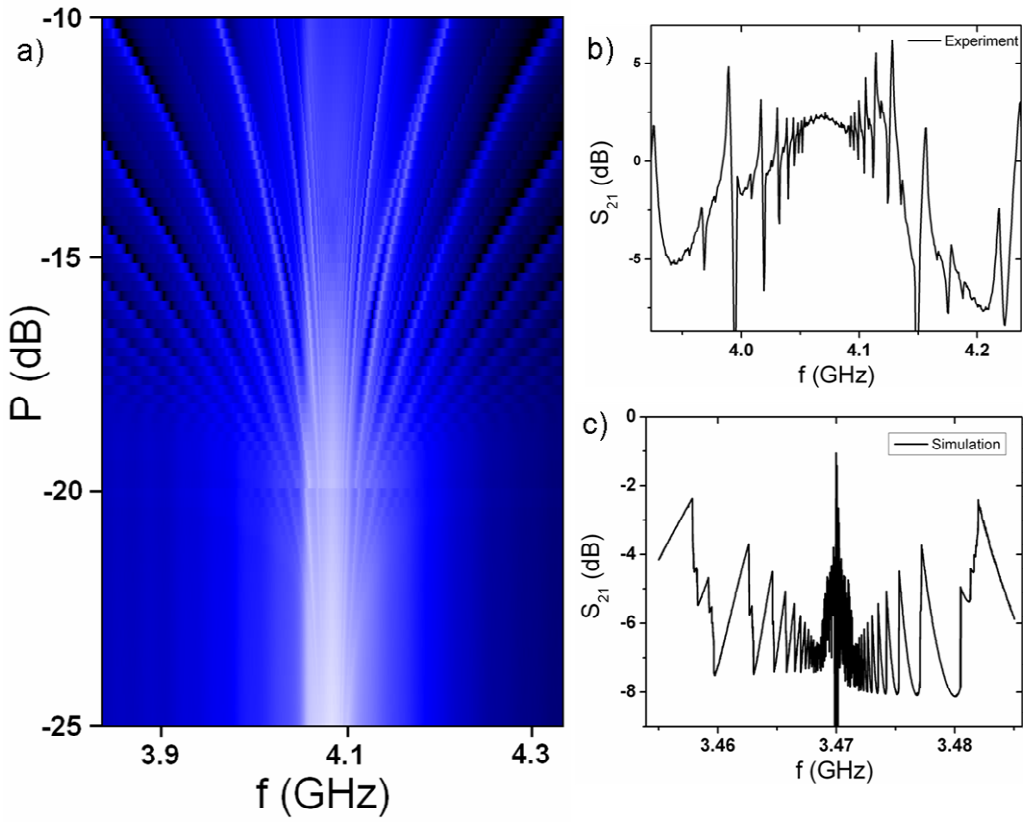

Fig. 4.15: (a) Color plot of a sample measured at 365 mK where the NA power is set to -18 dB and the other source frequency is 4086 MHz while its power is swept. There is a range of powers where both sources are greater than P_c. In between each satellite peak, a number of harmonics can be observed. Light color is a higher transmission in S_{21}. (b) Transmission characteristics as a function of frequency when the source power is set to -13 dB from (a) showing ~ 8 subharmonics. (c) A simulation using the model presented in this chapter where the source frequency is positioned at 3.47 GHz and the power difference between the source and the swept source is ~ 1 dB, while both source powers are supercritical. A similar pattern of harmonics is observed as in (b).

In a frequency and power regime outside the crater and near to the resonance, the model shows the supercurrent monotonically growing [Fig. 4.16(a)] as expected from Eq. 4.9; whereas far from the crater, the model reveals the nonmonotonic growth analogous to that in Fig. 4.11 as expected from Eq. 4.10 [Fig. 4.16(b)]. Inside the crater regime, the supercurrent grows monotonically; even far from the resonance there is monotonic growth, due to the fact that the supercurrent reaches its maximum amplitude before another period in its oscillatory behavior is

reached when the transient would overshoot and cause nonmonotonic growth. Thus, monotonicity is enforced inside the crater. The role of t_{hold} can also be clearly visualized in Fig. 4.16(c) and (d): it corresponds to the interval in which the supercurrent is held at zero after the nanowire switches to the normal state. Once this time is over, the supercurrent begins to grow. Additionally, the satellite peak frequency spacing Δf can be obtained from the model, which are calculated by taking the Fourier transform of the supercurrent versus time profile. These fit the data well, as can be observed in Fig. 4.16(c) and (d).

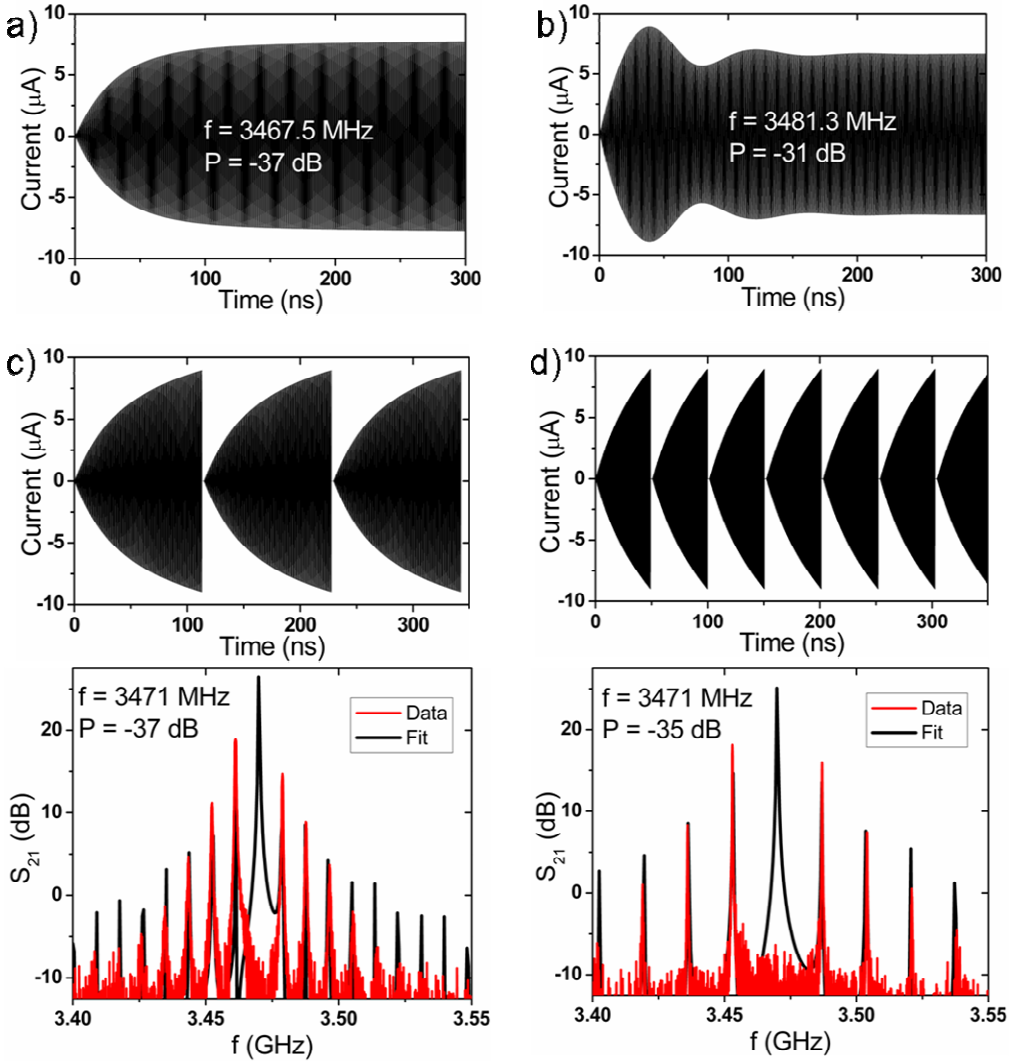

Fig. 4.16: Model prediction of supercurrent growth in the resonator, and comparison between satellite peak data and model for two powers for sample S1. (a) Supercurrent growth in the resonator at a power of -37 dB and frequency of 3467.5 MHz, which is near the resonance and outside, but near the crater shown in Fig. 4.10(a). The supercurrent growth is monotonic in this regime. (b) Supercurrent growth in the resonator at a power of -31 dB and frequency of 3481.3 MHz, which is far from resonance and also outside, but near the crater shown in Fig. 4.10(a). (c) The upper panel shows the supercurrent growth in the resonator inside the crater at a drive power of -37 dB and a frequency of 3471 MHz. The lower panel shows the satellite peaks (i.e., the Fourier transform of the upper panel) at this drive power and frequency and the corresponding fits to the model. (d) Same as (c), except for a drive power of -35 dB. As the drive power is increased, the satellite peak spacing increases, as the model predicts. The central peak in (c) and (d) is too narrow to be observed in the data.

The predictions of the model, namely that driving the system above the critical power P_c results in amplitude oscillations of the supercurrent, was verified using a high frequency oscilloscope (HP/Agilent DSO81004A-001 Infinium Oscilloscope, 10 GHz, 4CH, 40GSa/s) [see Fig. 4.17]. Instead of measuring the transmission as a function of frequency, this device allows us to measure it as a function of time thus allowing us to observe the real-time behavior from the resonator (Fig. 4.17(a)). For lower super-critical powers (powers above the critical power), the behavior is identical to our model prediction in that the transmission gradually increases until it hits a critical value (corresponding to the supercurrent reaching the critical current), then decreases sharply, and remains roughly zero until it begins to grow again. As larger super-critical powers are used, the growth rate increases and becomes more linear and the oscillation period shortens. Within the colored "envelop" showing the measured amplitude oscillations, there is actually a much faster oscillation corresponding to the drive frequency, which is ~ 5 GHz and can be seen in Fig. 4.17(c). In Fig. 4.17(b), the transmission characteristics (satellite-peak spectrum) measured in the frequency domain using the NA is displayed for the various drive powers used. We compared the satellite peak spacing Δf from these measurements for three different super-critical drive powers to the corresponding periods measured using the oscilloscope. For super-critical drive powers of -18, -14 and -10 dB, the measured Δfs were 10.4, 35.0, and 66.3 MHz, while the corresponding periods (and frequency = 1/T) were 103.3 (96.8), 29.0 (34.5), and 15.2 ns (65.8 MHz). Thus, it is clear that the observed satellite peaks are just a result of the oscillatory nature of the supercurrent amplitude.

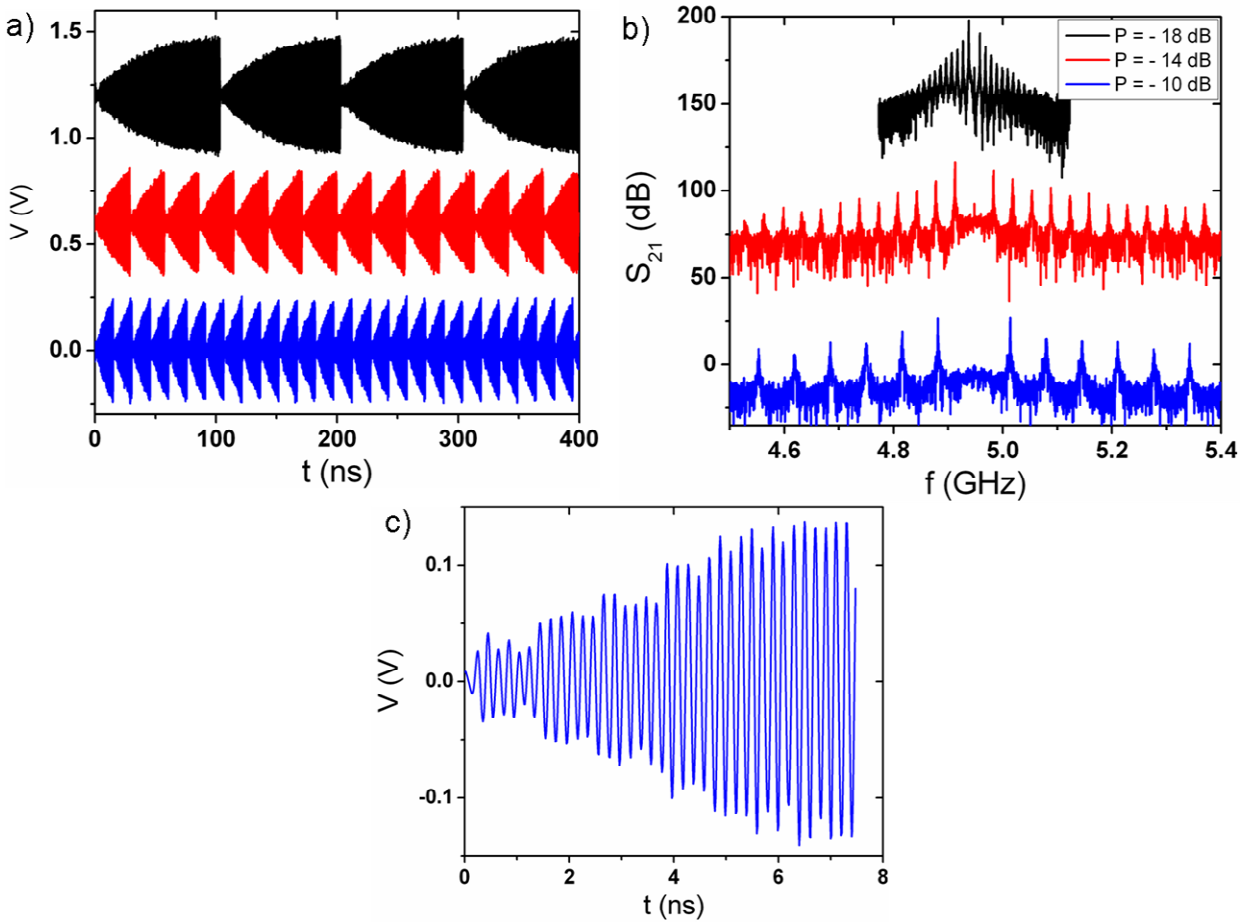

Fig. 4.17: (a) The amplitude oscillations measured in real-time using a high-frequency oscilloscope for three super-critical single drive powers positioned in the crater region. (b) The transmission characteristics (satellite-peak spectrum) for same three super-critical single drive powers as in (a). (c) A zoomed in view of the fast oscillations from (a). The data here is measured using the Infinium oscilloscope HP/Agilent DSO81004A-001, 10 GHz, 4CH, 40GSa/s.

As discussed in Section 4.4, at finite temperatures, thermal fluctuations can reduce the hysteresis by causing switching between the two stable states, which can explicitly be observed in the inset of Fig. 4.19(d). The difference in thresholds the system would exhibit with and without the presence of significant thermal (or quantum) fluctuations on the sweep towards resonance would be greater than on the sweep away from resonance. This can be seen as follows: on the sweep toward resonance, the current grows adiabatically to its critical value, as described in Sec. 4.4, whereas on the sweep away from resonance, the current grows rapidly to

its critical value. In the former case, the current amplitude is constantly near its critical value; therefore, any fluctuation will carry it past this value and cause the system to enter the crater. In the latter case, only fluctuations that occur during the brief interval that the current is near-critical will have an effect. This effect can be seen in Fig. 4.18(a), where for a power of -41 dB, the simulation is shown for both the case of including and not including thermal fluctuations. In these fits, thermal noise can be included by adding a random number with a given amplitude (here, 1.91×10^{-4}) to the phase at each time step. The choice of the phase fluctuation amplitude can then be checked by calculating the resulting supercurrent fluctuations I_{fluct} predicted by the model and comparing it to the estimate from the equipartition theorem: $\frac{1}{2}LI_{fluct}^2 = \frac{1}{2}k_BT$, where L is the total inductance of the resonator-nanowire system. At a temperature of 1.5 K and with an inductance of ~ 0.2 nH, the supercurrent fluctuation in the resonator can be estimated from the equipartition theorem to be $I_{fluct} \approx 300$ nA, which matches the modeled supercurrent fluctuations. This agreement of the predicted fluctuations and the fluctuations needed to produce the best fits confirms that thermal fluctuations are responsible for the observed small value of the hysteresis in this sample with a relatively low critical current.

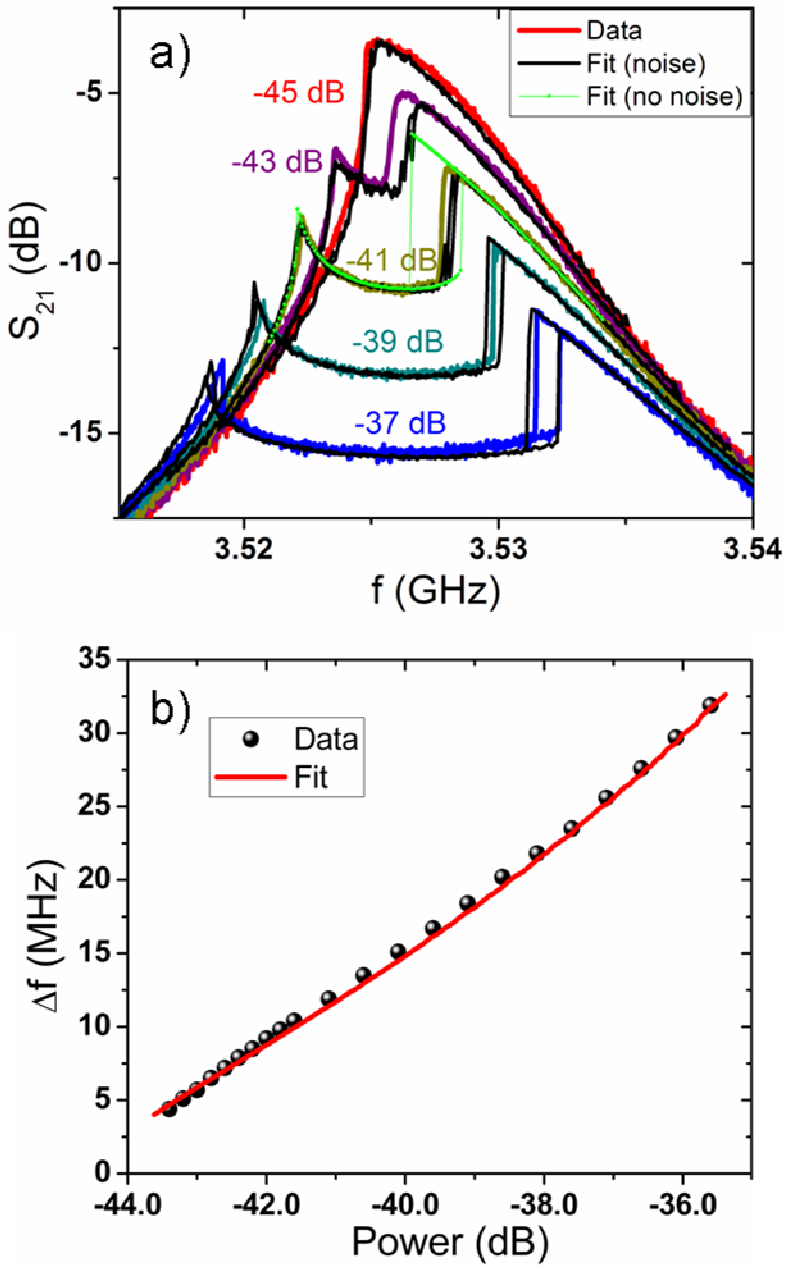

Fig. 4.18: Comparison of experimental data for sample S4, which is a 10 nm thick MoGe resonator/nanowire, and predictions of the model at 1.5 K. (a) Transmission characteristics for input powers in 2 dB increments (colored lines), and fits to the model (black lines). The bright green curve at - 41 dB shows the model simulation upon excluding phase noise. The quality factor is 665. (b) Satellite peak spacing vs. input power at a fixed frequency of 3525 MHz. The data and model show good agreement. All fits were calculated with the following fitting parameters: C = 7.55 pF, L = 0.204 nH, R = 3.2 kΩ, L_k = 65.4 pH, I_{sw} = 1.584 μA, and t_{hold} = 1.8 ns.

In the experiment, there are three main factors that affect the amount of noise in the measurement and can be tuned to reduce noise. (i) The amount of attenuation on each line can be adjusted to block out more thermal noise from the room temperature portion of the experiment. A smaller value attenuator will let more noise in resulting in a reduction in the size of the hysteresis [Fig. 4.19(a)] and a slightly larger width crater when a very small attenuation is used. (ii) The use of a Faraday cage can also help reduce the current noise that the sample experiences. This results in a larger hysteresis and a wider crater [Fig. 4.19(b)]. (iii) The temperature itself can also be a source of noise as in Fig. 4.19(c). As the temperature is increased, the size of the hysteresis reduces and the width of the crater increases drastically. At low noise levels, the frequency width of the hysteresis can be measured as a function of power and fit to the model as in Fig. 4.19(d). Thus, the hysteresis is a well understood phenomena in this experiment, which can be demonstrated both qualitatively and quantitatively.

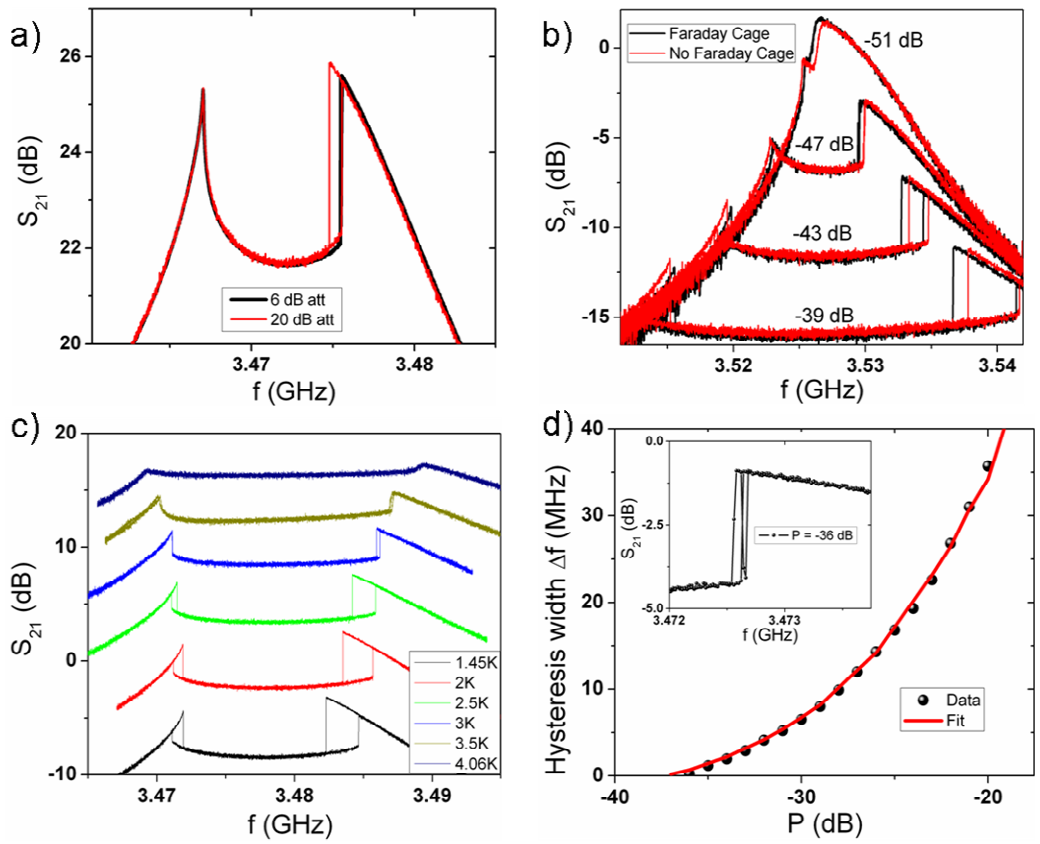

Fig. 4.19: (a) The effect of the amount of attenuation used in the experiment. Using a larger attenuation results in less noise on the sample and a greater hysteresis. (b) Various craters are shown for a sample with (black) and without (red) the use of a Farady cage around the sample. The use of the Faraday cage results in a larger hysteresis and a narrower crater. (c) Craters are shown as a function of temperature at a fixed power. As the temperature is increased, the width of the hysteresis shrinks and the crater width increases due to greater thermal fluctuations. (d) The width of the hysteresis is measured as a function of input power and fit to the model. Thus, the hysteresis is quantitatively understood within the model. Inset: jumps in the bistable region due to thermal fluctuations. All samples where measured here at T = 1.5 K unless otherwise indicated.

The data at much lower temperatures, such as 300 mK, deviate slightly from the model's predictions, in that the crater has a pronounced left-to-right gradient, as shown in Fig. 4.20(b). The origin of this effect is not clear; however, subtracting a linear term (having a coefficient of 87 ndB/Hz) from *all* the resonance data is sufficient to bring the data into good agreement with our model, as shown in Fig. 4.20(a). We therefore believe that this slope is extrinsic to the properties of the nanowire, and is due, instead, to the low-temperature behavior of the two-

dimensional parts of the resonator or to the other circuit elements, or due to parasitic coupling through the vacuum.

Interpretation of fit parameters

In the fits to the data shown in Figs. 4.13(a), 4.18(a), and 4.20(a), the Duffing oscillator parameters are determined by fitting the subcritical (i.e., craterless) resonance data. There are two further fitting parameters: (1) the drive power P_c required for the onset of the crater; and (2) the interval t_{hold}, for which the resonator is taken to be quiescent, once the nanowire enters its normal state. As discussed in Sec. 4.3, our identification of P_c with the power at which the current through the nanowire reaches I_c is supported by the temperature dependence of P_c. In principle, I_c is deducible from the coefficient of the Duffing term, using the current-phase relation (CPR) of the nanowire: however, the CPR appropriate for MoGe nanowires has not been well characterized, to date; we have therefore found it more reliable to determine the coefficient of the nonlinearity experimentally.

Implications for relaxation phenomena in the nanowire

Our other fit parameter, t_{hold}, is sensitive to relaxation processes in the nanowire. Prima facie, it might seem that t_{hold} should depend on the longer of the following intervals: the timescale on which the current in the resonator relaxes to its dissipative steady-state value, and the timescale on which enough heat flows out of the nanowire that it can re-enter the superconducting state after it enters the normal state due to heating. As we can infer from the inductance and normal-state resistance of the nanowire (which is on the order of ~ 100 pH and 1 kΩ, respectively), the former interval is too short to explain the measured value, which can be estimated by

L/R = 0.1 ps; besides, in order to fit the data within our model it is natural to assume that the current in the circuit goes to zero, which would not be the case if the nanowire were to re-enter its superconducting state before the resonator had relaxed. Thus, we can assume that t_{hold} depends on the relaxation rate of the nanowire back into the superconducting state. This being so, one might expect t_{hold} to depend strongly on the temperature of the leads (i.e., the bath temperature), as the thermal conductivity of a gapped BCS superconductor decreases exponentially at low temperatures. In fact, however, t_{hold} does not seem to depend appreciably on the bath temperature at low bath temperatures (i.e. in the range 0.3-1 K), as can be seen from Fig. 4.20(b). (At bath temperatures higher than 2 K, however, our fits find t_{hold} to be zero, to within our uncertainty.)

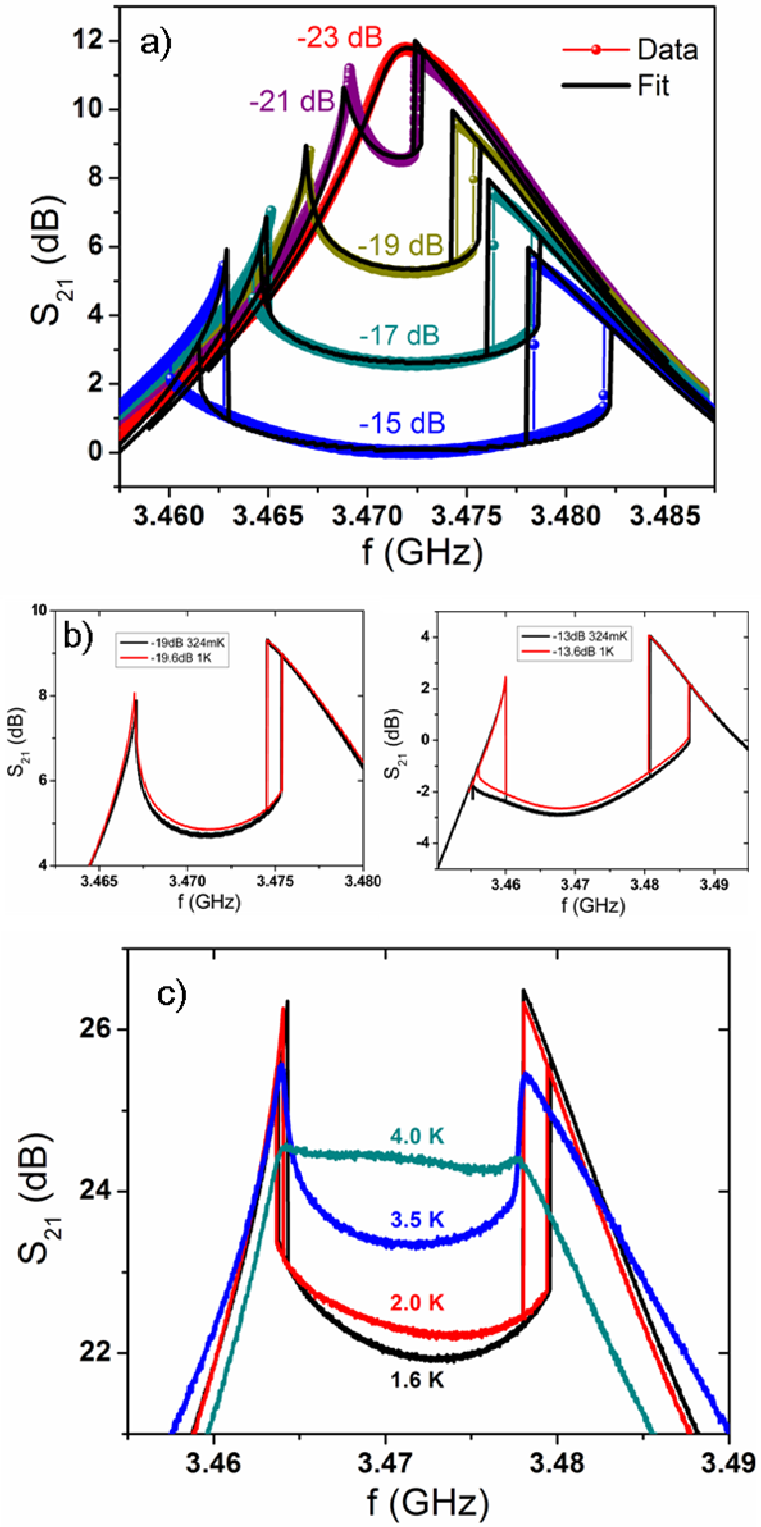

Fig. 4.20: (a) Transmission characteristics of sample S1 at 324 mK for input powers in 2 dB increments (thick colored lines), and fits to the model (thin black lines). At this temperature the thermal fluctuations are negligible and were not included in the modeling. At low power, Q = 425. The fits were calculated using the following fitting parameters: C = 15.2 pF, L = 0.125 nH, R = 1005 Ω, L_k = 13.1 pH, I_{sw} = 10.39 μA, and t_{hold} = 2.9 ns. (b) Dependence of crater depth on temperature for craters of fixed width (for two different widths). Within our model, this depth should be sensitive only to the fit parameter t_{hold}; the very weak temperature dependence of the crater depth indicates that t_{hold} does not depend strongly on temperature, at least over the range 300 mK to 1 K. Two features are of note here: (i) t_{hold} is slightly longer for lower temperatures; and (ii) as the model predicts, the crater depths at higher input power are more sensitive to the value of t_{hold}. (c) Craters at various temperatures that exhibit similar crater widths. At lower temperature the crater can be fit with the model including a nonzero t_{hold}. At slightly higher temperature (~ 2.5 K), t_{hold} begins to decrease towards zero. At still higher temperatures, the current noise in the system becomes comparable to the signal current and the crater becomes flat. Each graph was horizontally and vertically translated to compensate for the temperature dependence of the resonance frequency and other parasitic effects for easier crater-width comparison.

Thus, taken together, our measurements and modeling lead us to the perhaps surprising conclusion that at low enough temperatures the time it takes the nanowire to relax back into the superconducting state, in the absence of a current, does not depend strongly on the bath temperature. A possible scenario that is consistent with this observation goes as follows: in the middle of the nanowire the superconducting gap collapses and reforms essentially immediately (i.e., on the Ginzburg-Landau timescale). This does not give the normal electrons and holes created during the collapse of the gap sufficient time to equilibrate; thus, located near the center of the wire are a substantial number of Bogoliubov quasiparticles, having energies comparable to the gap energy. Within this scenario, the number of quasiparticles created depends only on the highest temperature achieved by the nanowire during the collapse process, and is therefore essentially independent of the bath temperature. Relaxation of the nanowire occurs via the diffusion of these quasiparticles into the leads; this process occurs at a rate that depends on the effective mass of the Bogoliubov quasiparticles, which is proportional to the gap, as illustrated in Fig. 4.21. However, the magnitude of the gap saturates at low temperature, and therefore so does the rate of diffusion of quasiparticles. Thus, the scenario outlined above would suggest that t_{hold} should saturate at low temperatures, as we observe experimentally.

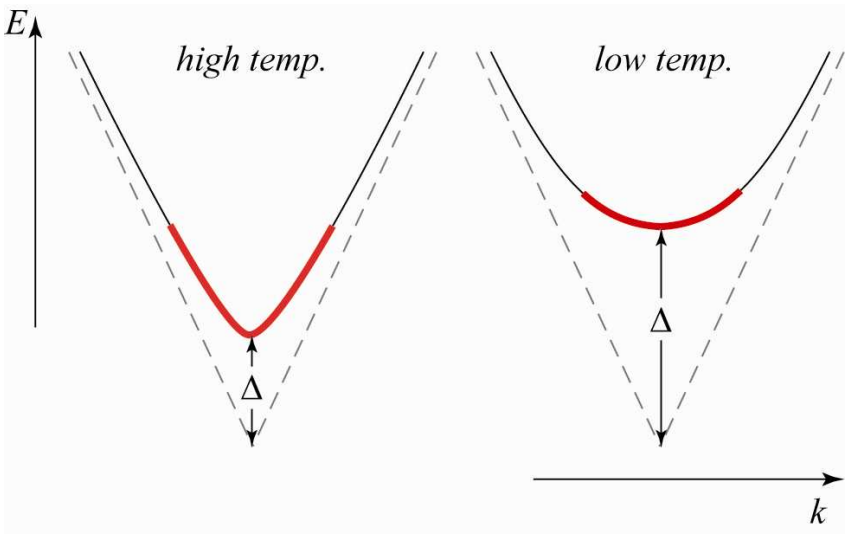

Fig. 4.21: Dispersion relations of trapped Bogoliubov quasiparticles expected under the scenario outlined in the present section, at high and low bath-temperatures. The chief difference between the two cases is the value of the superconducting gap Δ, which is larger at low temperatures. The average quasiparticle velocity (given by $\partial E / \partial(\hbar k)$) decreases as the gap increases, which can be observed in the k-space denoted by the thick red line; hence, the rate at which quasiparticles diffuse into the leads also decreases. However, this diffusion rate, along with the gap, is essentially constant with respect to temperature at low temperatures.

---

[1] J. Bardeen, Rev. Mod. Phys. **34,** 667 (1962).
[2] A. Wallraff, D. I. Schuster, A. Blais, L. Frunzio, R.-S. Huang, J. Majer, S. Kumar, S. M. Girvin and R. J. Schoelkopf. Nature **431**, 162 (2004); R. J. Schoelkopf and S. M. Girvin, Nature **451**, 664 (2008).
[3] By circuit QED we mean situations in which the excitations of the mesoscopic elements interact with the photons of the resonator, thus generating coupled nonequilibrium states of the composite system.
[4] See, e.g., S. Haroche and J.-M. Raimond, *Exploring the Quantum: Atoms, Cavities, and Photons* (Oxford University Press, 2006).
[5] V. Bouchiat, D. Vion, P. Joyez, D. Esteve, and M. H. Devoret, Phys. Scr. **T76**, 165 (1998).
[6] Y. Aharonov and L. Vaidman, arXiv:quant-ph/0105101v2 (2007).
[7] V. E. Manucharyan, E. Boaknin, M. Metcalfe, R. Vijay, I. Siddiqi, and M. Devoret, Phys. Rev. B **76**, 014524 (2007).
[8] M. Metcalfe, E. Boaknin, V. Manucharyan, R. Vijay, I. Siddiqi, C. Rigetti, L. Frunzio, R. J. Schoelkopf, and M. H. Devoret, Phys. Rev. B **76**, 174516 (2007).
[9] N. Bergeal, F. Schackert, M. Metcalfe, R. Vijay, V. E. Manucharyan, L. Frunzio, D. E. Prober, R. J. Schoelkopf, S. M. Girvin & M. H. Devoret, Nature **465**, 64 (2010).
[10] W. A. Little, Phys. Rev. **156**, 396 (1967).
[11] N. Giordano, Phys. Rev. Lett. **61**, 2137 (1988).
[12] C. N. Lau, N. Markovic, M. Bockrath, A. Bezryadin, and M. Tinkham, Phys. Rev. Lett. **87**, 217003 (2001).
[13] A. Bezryadin, C. N. Lau, and M. Tinkham, Nature **404**, 971 (2000).
[14] M. Sahu, M.-H. Bae, A. Rogachev, D. Pekker, T.-C. Wei, N. Shah, P. M. Goldbart, and A. Bezryadin, Nature Physics **5**, 503-508 (2009).
[15] D. Pekker, N. Shah, M. Sahu, A. Bezryadin, and P. M. Goldbart, Phys. Rev. B **80**, 214525 (2009).
[16] N. Shah, D. Pekker, and P. M. Goldbart, Phys. Rev. Lett. **101**, 207001 (2008)
[17] J. Ku, V. Manucharyan, and A. Bezryadin, Phys. Rev. B **82**, 134518 (2010).
[18] F. Brennecke, T. Donner, S. Ritter, T. Bourdel, M. Köhl, and T. Esslinger, Nature **450**, 268 (2007).
[19] P. Domokos and H. Ritsch, Phys. Rev. Lett. **89**, 253003 (2002); J. K. Asbóth, P. Domokos, H. Ritsch, and A. Vukics, Phys. Rev. A **72**, 053417 (2005).
[20] K. Baumann, C. Guerlin, F. Brennecke, and T. Esslinger, Nature **464**, 1301 (2010).

[21] S. Gopalakrishnan, B. L. Lev, and P. M. Goldbart, Nature Physics **5**, 845 (2009).
[22] S. Gopalakrishnan, B. L. Lev, and P. M. Goldbart, Phys. Rev. A **82**, 043612 (2010).
[23] I. B. Mekhov, C. Maschler, and H. Ritsch, Nature Physics **3**, 319 (2007).
[24] A. C. Anderson, R. C. Withers, S. A. Reible, R. W. Ralston, IEEE Trans. on Mag. **19**, 485 (1983).
[25] M. S. DiIorio, A. C. Anderson, B. –Y. Tsaur, Phys. Rev. B **38**, 7019 (1988).
[26] L. Frunzio, A, Wallraff, D. Schuster, J. Majer, R. Schoelkoph, IEEE Trans. on Appl. Superc. **15**, 860 (2005).
[27] E. Boaknin, V. Manucharyan, S. Fissette, M. Metcalfe, L. Frunzio, R. Vijay, I. Siddiqi, A. Wallraff, R. Schoelkopf, and M. H. Devoret, arXiv: 0702445 (2007).
[28] A. Bezryadin, J. Phys.:Condens Matter **20,** 043202 (2008).
[29] A. Bezryadin, A. Bollinger, D. Hopkins, M. Murphey, M. Remeika, and A. Rogachev, "Superconducting Nanowires Templated by Single Molecules," review article in *Dekker Encyclopedia of Nanoscience and Nanotechnology*, James A. Schwarz, Cristian I. Contescu, and Karol Putyera, eds. (Marcel Dekker, Inc. New York, 2004), 3761–3774.
[30] T. Aref and A. Bezryadin, arXiv:1006.5760v2 (2011).
[31] E. Segev, B. Abdo, O. Shtempluck, and E. Buks, J. Phys. C **19**, 096206 (2007).
[32] The quality factor is also observed to drop for higher order modes as it depends on $1/f_0$, where f_0 is the resonance frequency.
[33] S. J. Hedges, M. J. Adams, and B. F. Nicholson, Electronics Letters **26**, 977 (1990).
[34] Michael Tinkham, *Introduction to superconductivity* (Dover, 2004).
[35] M. J. Lighthill, *An Introduction to Fourier Analysis and Generalised Functions* (Cambridge University Press, 1958).
[36] A. H. Nayfeh and D. T. Mook, *Nonlinear Oscillations* (Wiley-Interscience, New York, 1979).
[37] W. C. Stewart, Appl. Phys. Lett. **12**, 277 (1968).
[38] D. E. McCumber, J. Appl. Phys. **39**, 3113 (1968).

Chapter 5

Cratered Lorentzian response of driven microwave superconducting double nanowire-bridged resonators: oscillatory and magnetic-field induced stochastic states

For the case of resonators comprising *two* parallel nanowires and subject to an external magnetic field, we find field-driven oscillations of the onset power for the amplitude oscillations, as well as the occurrence (for values of the magnetic field that strongly frustrate the nanowires) of a distinct steady state in which the pulsing is replaced by stochastic amplitude-fluctuations. It is also demonstrated that a thin-film superconducting Fabry-Perot resonator can be used to reveal the Little-Parks (LP) effect even at temperatures much lower than the critical temperature (where the resistance of the wires is immeasurably low). A pair of parallel nanowires is incorporated into the resonator at the point of a supercurrent antinode. As magnetic field is ramped, the Meissner current develops, changing the kinetic inductance of the wires and, correspondingly, the resonance frequency of the resonator, which can be detected. The LP oscillation are revealed as a periodic set of distorted parabolas observed in the transmission of the resonator and corresponding to the states of the wire loop having different vorticities. We also report a direct observation of single and double phase slip events and their statistical analysis. We conclude by giving a brief discussion of how circuit-QED-based systems have the potential to facilitate

nondestructive measurements of the current-phase relationship of superconducting nanowires and, hence, of the rate at which quantum phase-slips take place in superconducting nanowires.

5.1 Introduction

We find that for resonators that have *two* nanowires embedded in them, the threshold for entering the pulsing state depends periodically on the magnetic field perpendicularly applied, with a period consistent with the predictions and observations given in Refs. [1, 2]. We report on two tantalizing phenomena. First, the appearance, at low temperatures and drive powers, of jumps in the resonance frequency, which are suggestive of a multivalued current-phase relationship in the nanowire. An analysis of the resonance frequency dependence on the magnetic field allows us to measure the Little-Parks effect at temperatures much lower than the critical temperature. Second, the unexpected rise of the crater floor as its width approaches the maximum value, which occurs at the magnetic field such a phase difference of $\pi/2$ is induced between the ends of the wire (i.e. at the maximally frustrated state of the device). This frustrated state is associated with the lowest critical-power value where the energy of the system is the same for the states having a vortex number n and $n + 1$. We will present a qualitative discussion of these phenomena.

5.2 Magnetic-field dependence of resonance and Lorentzian crater

We now turn to the case of resonators that incorporate two wires, as shown in Figs. 5.1(a) and (b). These devices are similar in some respects to the resonators interrupted by SQUIDs that

were studied in Ref. [3, 4]; they differ, however, in two crucial respects. (i) Nanowires, unlike Josephson junctions, can support metastable states having one, or many, virtual vortices trapped in the region between the wires; these devices may therefore enable the study of, e.g., the quantum tunneling of vortices across the nanowires. (ii) If the entire device—resonator, including nanowires—is placed in a perpendicular magnetic field, various properties of the system, such as the intrinsic resistance and the switching current, are periodic in the magnetic field; however, the period is much shorter than what can be estimated by dividing the flux quantum by the area of the loop formed by the nanowires (or, equivalently, the conventional Little-Parks geometrical area dictated value). Suppose that the wires are separated by a distance *a*, and is each of length *b* [see Fig. 5.1(c)], so that the area between the wires is given by *ab*: for the *conventinal* Little-Parks effect, the properties of the wires should oscillate with magnetic field with a period given by $\Delta B = \Phi_0 / ab$, where Φ_0 is the superconducting flux quantum. This effect is, however, greatly modified in situations such as the present one, in which the leads are themselves mesoscopic—i.e., have widths smaller than the perpendicular penetration depth λ. In such cases, it can be shown [1, 5] that the magnetic-field periodicity of the properties of the system as a whole is largely set by screening currents *in the leads*, which do not depend on the length of the wires. Thus, e.g., if the width *l* of the leads is much greater than *a*, the effective periodicity of the physical properties of the wires for small fields is given not by $\Delta B = \Phi_0 / ab$, but by $\Delta B = \Phi_0 / c_1 al$, where c_1 is a geometry-dependent number of order unity. At stronger magnetic fields, vortices enter the leads, and the periodicity changes.

The effects discussed in the preceding paragraph have been explored both experimentally and theoretically for the case of d.c. currents [1, 2, 5]. The experiments reported here confirm that the Lorentzian crater is also periodic in the magnetic field, with the same periodicity.

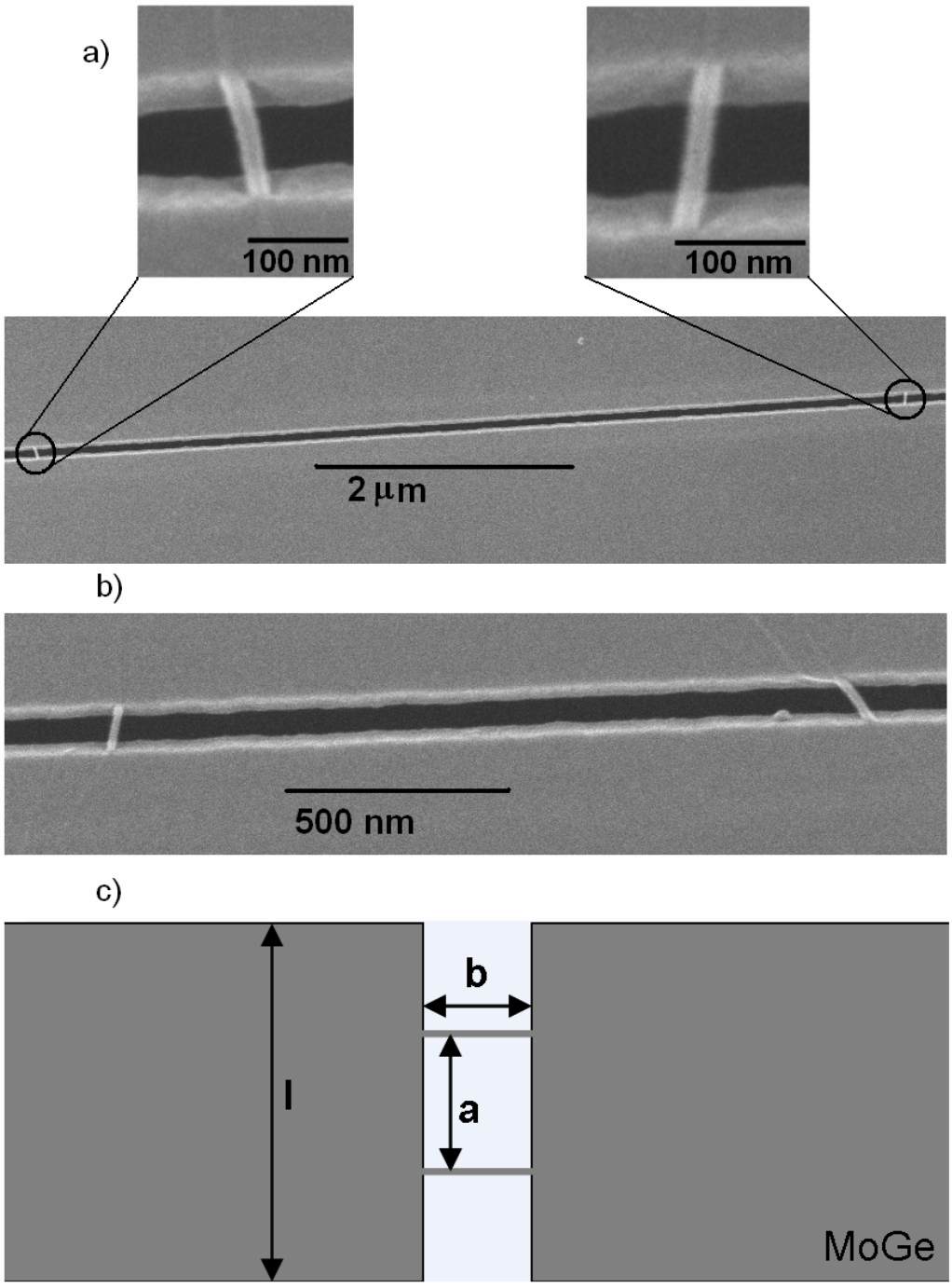

Fig. 5.1: (a) Top panel: Examples of two individual, 25 nm wide, MoGe nanowires. The trench, over which the wires are suspended, appears black. Bottom panel: Double-nanowire sample S5, showing the pair of nanowires, which appear geometrically similar. (b) Double-nanowire sample, S6, showing the pair of nanowires, which appear geometrically somewhat different. (c) Schematic of the center conductor (electrodes) connected by the two nanowires.

Magnetic-field dependence of resonance and Lorentzian crater

Given our previous association—discussed in Ch. 4—of the power required for the onset of the crater with the critical current of the nanowire, one would expect that the power required for the onset of the crater in the two-nanowire situation would depend periodically on the applied magnetic field. We do indeed find such a dependence (Fig. 5.2), with a periodicity consistent with that predicted in [1, 2, 5]. The critical power P_c at the onset of the crater is obtained using the S_{21}-parameter in the dB scale: $P_c = S_{21} + P_{NA}^{out}$. The theoretical period of the magnetic field, for which the sample is tilted at an angle, θ, with respect to the magnetic field in order to fit in our measurement system, is calculated from: $\Delta B = \Phi_0 / c_1 a l \sin|\theta|$. A wire separation of 6.63 μm, a lead width of 10 μm, and an approximate tilt angle of 35-40° results in a theoretical prediction of ΔB = 48.5 to 54.4 μT, assuming $c_1 \approx 1$. This is close to the experimentally measured value of ΔB = 41.4 μT. The small difference in the predicted magnetic field period can be accounted for through the geometric parameter c_1, and through the uncertainty of our knowledge of the exact angle between the resonator surface and the applied magnetic filed (the sample was not horizontal due to practical limitations related to the dimensions of the sample holder and the cryostat).

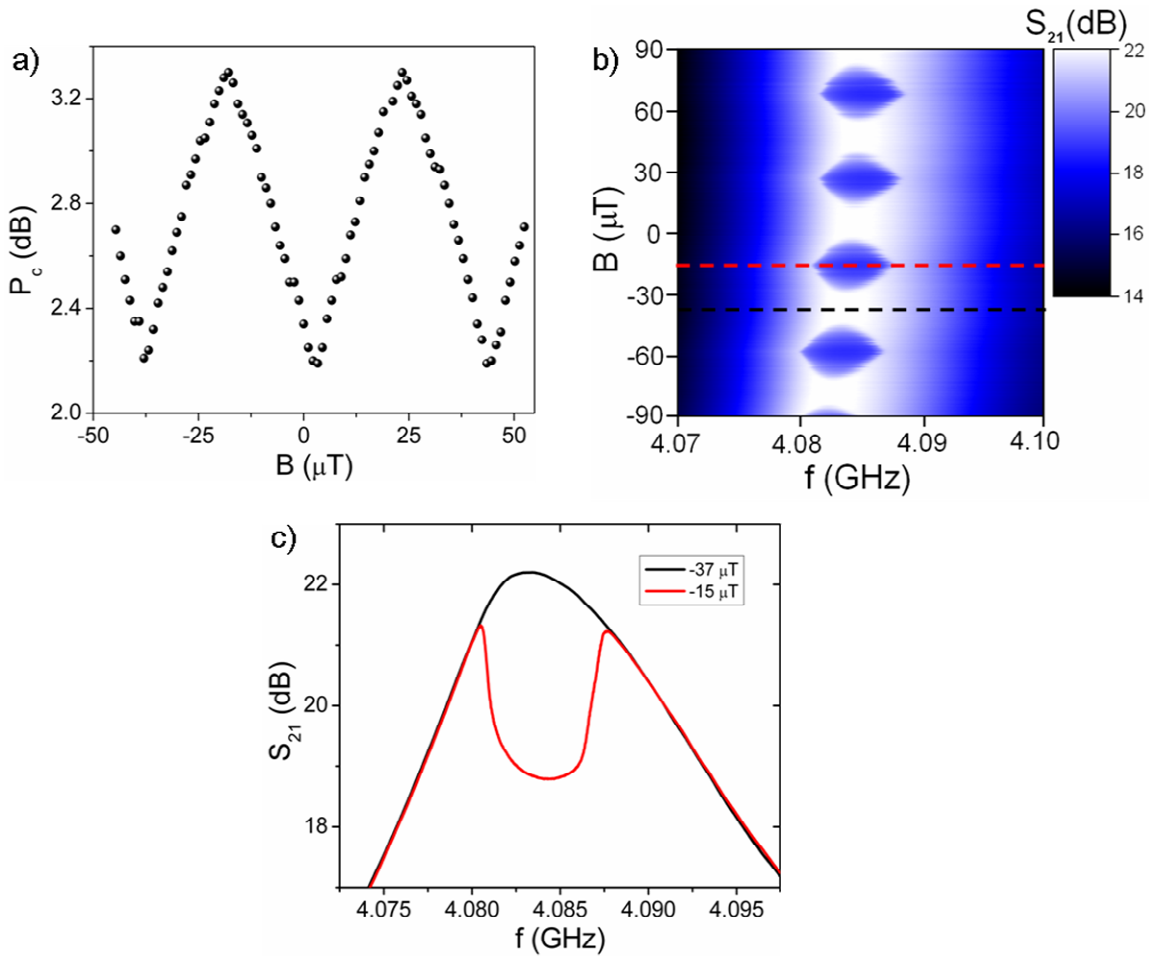

Fig. 5.2: (a) Oscillations of crater onset power P_c as a function of magnetic field for sample S5, which is a 25 nm thick MoGe resonator containing two relatively symmetrical nanowires (having similar critical currents) separated by 6.63 μm and connecting a center conductor that is 10 μm in width. (b) Map of the transmission coefficient as a function of magnetic field and input frequency, at fixed input power, showing the periodic onset and disappearance of the Lorentzian crater (i.e., the dark islands in the middle). Regions of higher transmission are shaded more lightly. (c) Two transmission curves for the same input power but at differing magnetic fields. The input power in this case lies between the minimum and maximum input powers for magnetic field dependent crater onset. The black (red) curve in panel (c) is shown in panel (b) as a dashed black (red) line.

In addition, the resonance frequency for fixed drive power shifts with magnetic field—owing to the fact that the kinetic inductance of the nanowire depends on the supercurrent magnitude in it, which in turn depends on the magnetic field. At low temperature and low power, the shift in the resonance frequency can be as large as ~ 5 MHz (Fig. 5.3), which is easily

detectable. When the drive power is large enough to give rise to a crater, this frequency shift has the same periodicity as that of P_c (see Fig. 5.2) and is continuous. At lower input powers, however, the dependence of the resonance frequency on the magnetic field becomes discontinuous (see Fig. 5.3). At higher powers or higher temperatures (for which the critical current is lower), the barrier to vortex entry is lower; hence one expects the system to return to periodic behavior, as is seen experimentally (see Fig. 5.3). We interpret the discontinuous resonance frequency as a manifestation of the multivalued nature of the current-phase relationship of a long nanowire (i.e., $L/\xi > 4.4$) [6]: there are multiple possible metastable states differing in their values of the current circulating in the nanowires, corresponding to the presence of one or more phase (or coreless) vortices trapped in the area between the wires; the resonance frequency of the resonator is thus shifted by an amount that is related to the number of vortices trapped between the wires, and the entry or exit of vortices corresponds to a jump in the resonance frequency. For a junction with a singled-valued CPR such as a Josephson junction (where $I_s = I_c \sin\phi$ [see Fig. 5.4]) there are no metastable states and the condensate follows the ground state. However, for a multi-valued CPR such as that of our nanowires (where for one stable branch of the CPR: $I_s = (3\sqrt{3}/2)I_c\left[\phi/(l/\xi) - (\phi/(l/\xi))^3\right]$ [see Fig. 5.4]), the jumps enable the system to explore these metastable states which differ by $2\pi n$, where n is the number of vorticies trapped in between the nanowires.

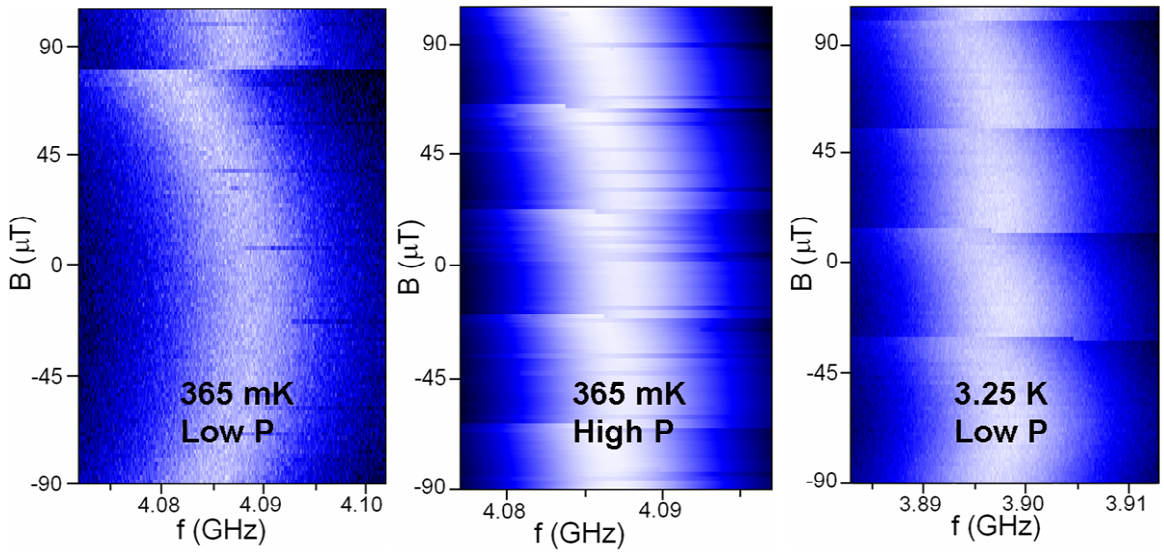

Fig. 5.3: Color map of transmission characteristics as a function of magnetic field and frequency for sample S5. The left graph is measured at 365 mK and an input power roughly 6 orders of magnitude less power than P_c. The middle graph is also measured at 365 mK but at only 3 dB less power than P_c. Here, periodicity returns, as the barrier for vortex jumping into/out of the loop formed by the two nanowiress is reduced. The right graph is measured at 3.25 K and using ~ 4 orders of magnitude less power than P_c. Again, periodicity returns, due to the reduction of the barrier for vortex jumping at higher temperatures. Lighter (darker) color denotes higher (lower) transmission.

The vortex-entry process in a resonator differs crucially from that in the d.c. geometries considered in Ref. [1], in the sense that the overall system is not maintained at a particular bias current: the minimal input current required to observe the resonance shift is far lower than the circulating current. The present a.c. approach therefore raises the prospect of *noninvasive* measurements of phase-slip and vortex dynamics in a two-wire device. It would thus be of considerable interest to perform analogous measurements on resonators containing thinner wires that are closer to the superconductor-insulator transition: we shall return to this idea in future work.

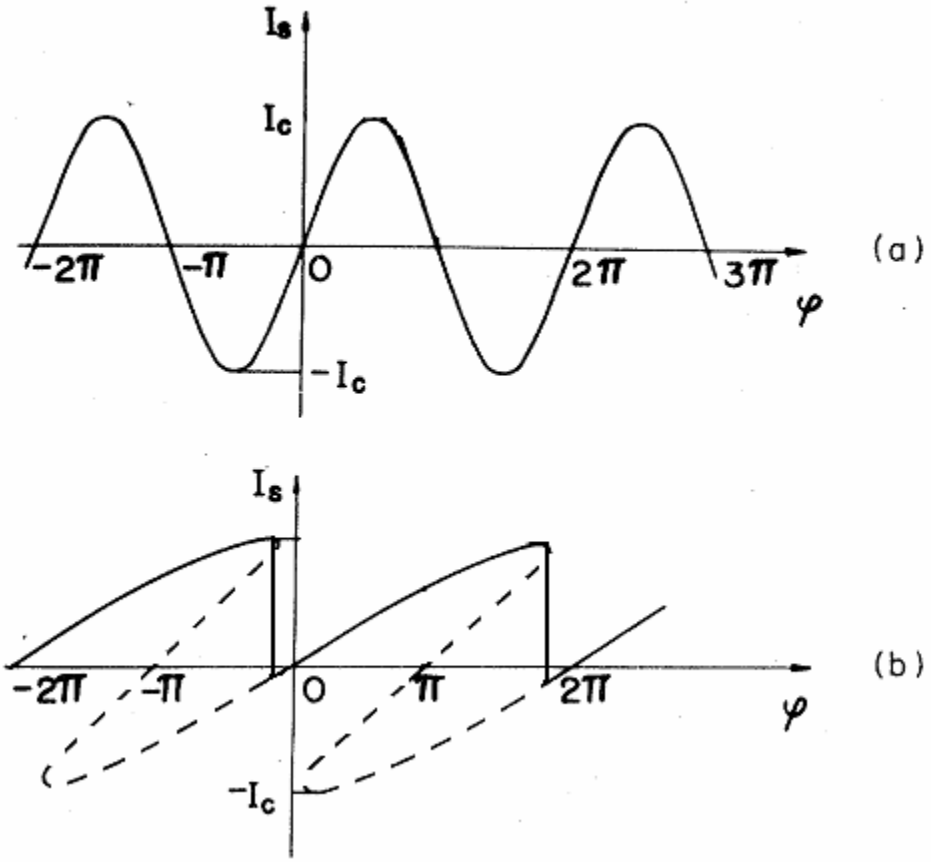

Fig. 5.4 [6]: (a) CPR of a Josephson junction showing its single-valuedness. (b) CPR of a nanowire showing its multi-valued nature. Once the supercurrent reaches I_c, there is a jump to the next stable branch shown by the vertical line. When there are vorticies trapped in between the wires, then jumps in the phase can occur by $2\pi n$, where n is the vorticity.

5.3 Little-Parks oscillations at low temperatures

The phenomenon of magnetic flux quantization in doubly connected superconductors was observed by Deaver and Fairbank [7] and Doll and Nabauer [8]. In these first works the authors investigated magnetic properties of thick ($t >> \lambda$, where t is the wall thickness and λ is the magnetic penetration depth) superconducting tubes. Besides the proof of the flux quantization phenomenon both experiments showed that the magnetic flux quantum size was not *hc/e*, but

rather *hc/2e*. In mesoscopic samples the flux quantization is irrelevant since their dimensions are typically smaller than the magnetic field penetration depth. In this case the principle of fluxoid quantization, which follows from the requirement that the complex wave function of the condensate is single-valued, holds. The experimental demonstration of the fluxoid quantization was first reported by Little and Parks [9] (LP) who demonstrated that the critical temperature of a thin-walled superconducting cylinder is a periodic function of the magnetic flux contained in the cylinder. The phase diagram of the thin hollow ($t << \lambda$) cylindrical superconductor, obtained by LP from multiple resistance vs. temperature (R-T) measurements revealed the presence of clearly defined series of parabolic variations of the critical temperature with magnetic field [10, 11]. More recently, Vakaryuk [12] predicted that at low temperatures the magnetic moment of a superconducting loop should oscillate with the applied field either with the LP period or with a doubled period. This theory can be considered an extension of the LP theory to mesoscopic samples and low temperatures.

So far measurements of the LP effect were mostly concentrated near the critical temperature where the resistance is still high, due to thermal fluctuations for example. At low temperatures the observation of the LP oscillations is challenging since the resistance is immeasurably low. Here we measure the kinetic inductance of a pair of parallel wires, which, together with superconducting electrodes, form a closed loop. These wires and electrodes constitute a superconducting coplanar waveguide resonator (Fig. 5.1). The kinetic inductance variations reveal themselves as changes of the resonance frequency, which, in their turn, produce changes of the transmission of the resonator, measured at a fixed frequency, which equals the resonance frequency at zero field. We show that the transmission coefficient

($S_{21} = 10\ log(P_{out} / P_{in})$), where P_{out} and P_{in} are output and input powers, correspondingly) of the resonator has multiple branches as a function of the external magnetic field. The transition from one branch to the neighbor branch corresponds to a single Little's phase slips [13], taking place in one of the wires. The periodic structure of the $S_{21}(H)$ dependence has the same origin as the Little-Parks critical temperature $T_c(H)$ periodic oscillations, occurring with changing of applied magnetic field H. These oscillations are due to the oscillation of the supercurrent magnitude and correspondingly the free energy of the superconducting condensate with magnetic flux. The periodicity at low temperatures is observed only if the measurement is performed many times, since the states of the system are discrete and are factorized by the number of phase vorticies trapped in the loop.

Our device consists of a pair of parallel superconducting nanowires incorporated in the center of a superconducting coplanar waveguide resonator (Fig. 5.1). The nanowires with thickness ~25 nm and ~100 nm length were produced by molecular templating technique [14, 15]: a carbon nanotube was deposited over a 100 nm wide trench on a Si substrate and sputter-coated with a superconducting alloy of MoGe. Resonators were patterned by means of optical lithography, followed by wet chemical etching in H_2O_2 (Fig. 5.1). The width of the center conductor is 10 μm and the gap between the center conductor and ground plane is 6 μm, the gap between the center conductor and the input (or the output) electrode is 3 μm with corresponding capacitances of about 45 fF. The length of the center conductor between the input and the output "mirrors" is 10 mm, which corresponds to a nominal resonant frequency of ~ 10 GHz (taking into account the dielectric constant of the underlying substrate), which is estimated for the case when the kinetic inductances of the resonator itself and the nanowires are both negligible. The actual resonance frequency is lower than this simple estimation, due to the kinetic inductance of

the thin MoGe film forming the resonator as well as the nanowires. Two samples are measured with different nanowire spacing. In sample A, the distance between nanowires is 6.63 μm, and in sample B the distance between nanowires is 4.26 μm. The resonators are over-coupled and their quality factors are about 500. Each measurement is performed in a ^{3}He cryostat equipped with two semi-rigid coaxial cables with thermalized attenuators and a low temperature GHz amplifier LNF-LNC4_8A, from Low Noise Factory. The transmission measurements are performed using a network analyzer Agilent PNA5230A.

Our measurements, shown in Fig. 5.5(a) for sample A and in Fig. 5.6 for sample B, reveal that $S_{21}(H)$ is a periodic multi-valued function. Each branch of $S_{21}(H)$ corresponds to a state with a particular number of phase vortices (or vorticity) trapped in the nanowire loop (Fig. 5.1).

A single branch of the function $S_{21}(H)$ (for the sample A) obtained at 0.36 K is extracted and plotted in Fig. 5.5(b). As one can see, the transmission function is not truly parabolic but rather it has a flat top. Therefore we will call it a "distorted-parabola". This profile is preserved in a wide temperature interval. For example, the distorted-parabola transmission function is observed on sample B at 0.3 K and 1.8 K, as shown in Fig. 5.6.

To examine the periodicity of the transmission coefficient in the external magnetic field we compare the mean distance in magnetic field between the intersections of branches with the following vorticities: (n,$n+1$) (not shown), (n,$n+2$) (shown as circles in Fig. 5.5(a)) and (n,$n+3$) (shown as triangles Fig. 5.5(a)). This analysis results in the following periodicities: $\langle \Delta H_{n,n+1} \rangle = 0.420\,\text{Oe}$, $\langle \Delta H_{n,n+2} \rangle = 0.423\,\text{Oe}$, $\langle \Delta H_{n,n+3} \rangle = 0.424\,\text{Oe}$, and the mean value of $\langle \Delta H(0.36K) \rangle = 0.422\,\text{Oe}$. A similar analysis for this sample at 1.80 K (not shown) results in the following values for the period: $\langle \Delta H_{n,n+1} \rangle = 0.427\,\text{Oe}$, $\langle \Delta H_{n,n+2} \rangle = 0.427\,\text{Oe}$ and $\langle \Delta H_{n,n+3} \rangle = 0.424\,\text{Oe}$. This yields the mean value of $\langle \Delta H(1.80K) \rangle = 0.426\ \text{Oe}$. Consequently,

the difference between periods of the transmission coefficient function at 0.36 and 1.80 K is less than 1%, which is within the uncertainty of the measurement. Thus we conclude that the period is independent of the temperature in a wide temperature interval. This result agrees with the previous conclusion about independence of the magnetic-field-induced LP oscillations on temperature in systems with two parallel wires connected to wider superconducting electrodes [16]. The value of the period in a magnetic field allows one to establish the relationship between the applied magnetic field and the phase change of the superconducting order parameter (condensate wave function) of the studied double-wire system. Indeed, the period of Little-Parks oscillations corresponds to the phase change of 2π on the closed loop: $\Delta H \cdot \beta = 2\pi$, from where we find the field-phase geometrical parameter $\beta \approx 14.8$ Oe^{-1}. We have also tested that the observed multivalued response function is independent on the input power. The powers tested were -60, -70, and -80 dBm, referring to the output of the network analyzer. This is four, five and six orders of magnitude lower than the critical power at which the current amplitude in the nanowires reaches the critical current. The observed independence of the measured $S_{21}(H)$ on the input power proves that the measurement current (i.e. the induced oscillating current in the resonator) is negligible compared to the magnetic-field-induced Meissner current in the nanowire loop.

If the magnetic field is exactly perpendicular to the sample's surface then the period is given by [16] $\Delta B = \left(\Phi_0 / c_1 a l\right)$, where a is the distance between the wires, l is the width of the electrodes to which the wires are connected and c_1 is a geometry-dependent number of order unity. In the experiment the angle between the magnetic field and the sample's surface was $\theta \approx 35\text{-}40°$. The corresponding expression for the period is $\Delta B = \left(\Phi_0 / c_1 a l \sin|\theta|\right)$. With the wire separation $a = 6.63$ μm and the electrode width $l = 10$ μm, we get $\Delta B = 0.49$ to 0.54 Oe taking

$c_1 \approx 1$. This is close to the experimentally measured vale of $\Delta B = 0.43$ Oe. The small difference in the predicted magnetic field period can be accounted for through the geometic parameter c_1, and through the uncertainty of our knowledge of the exact angle between the resonator surface and the applied magnetic filed.

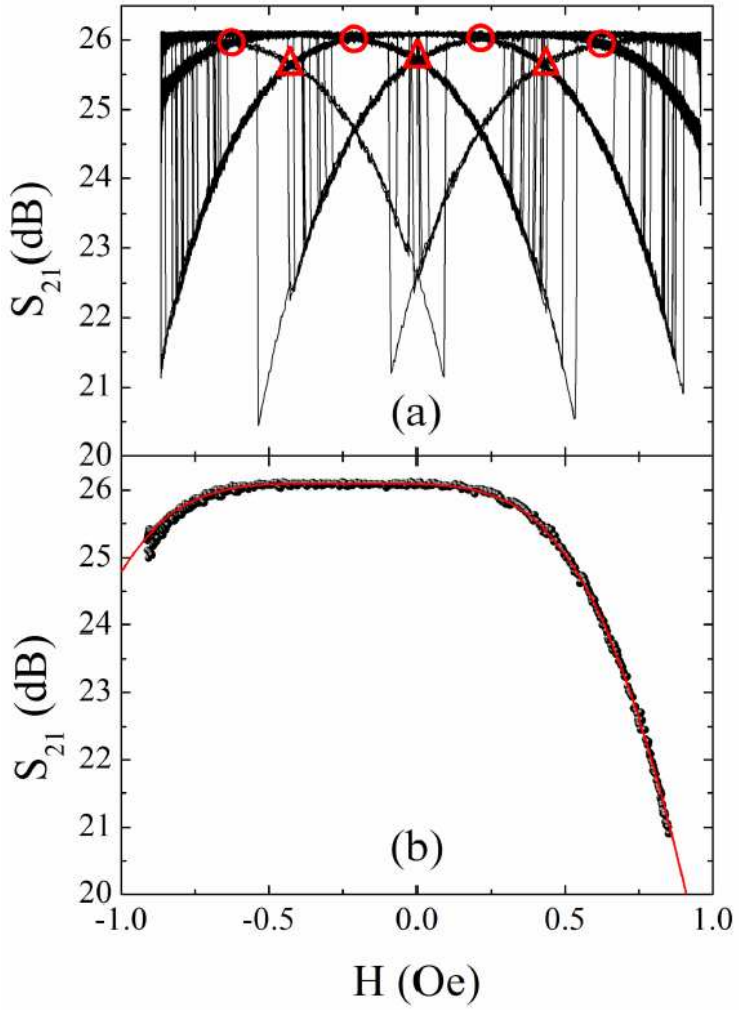

Figure 5.5: (a) The transmission coefficient of sample A as a function of the external magnetic field, measured at 360 mK. Different branches correspond to different numbers of phase vortices trapped in the loop formed by the nanowires and the electrodes (see Fig. 5.1 (a)) The data points are shown by dots connected by straight lines, thus the vertical lines represent abrupt jumps from one parabola to another. Circles and triangles represent the intersections of branches with the vorticities (n,n+2) and (n,n+3), correspondingly. (b) A single branch of the experimental $S_{21}(H)$ dependence (black dots). Red line shows the theoretical fit. An excellent agreement is observed. This graph was measured by A. Belkin at the University of Illinois in Urbana-Champaign.

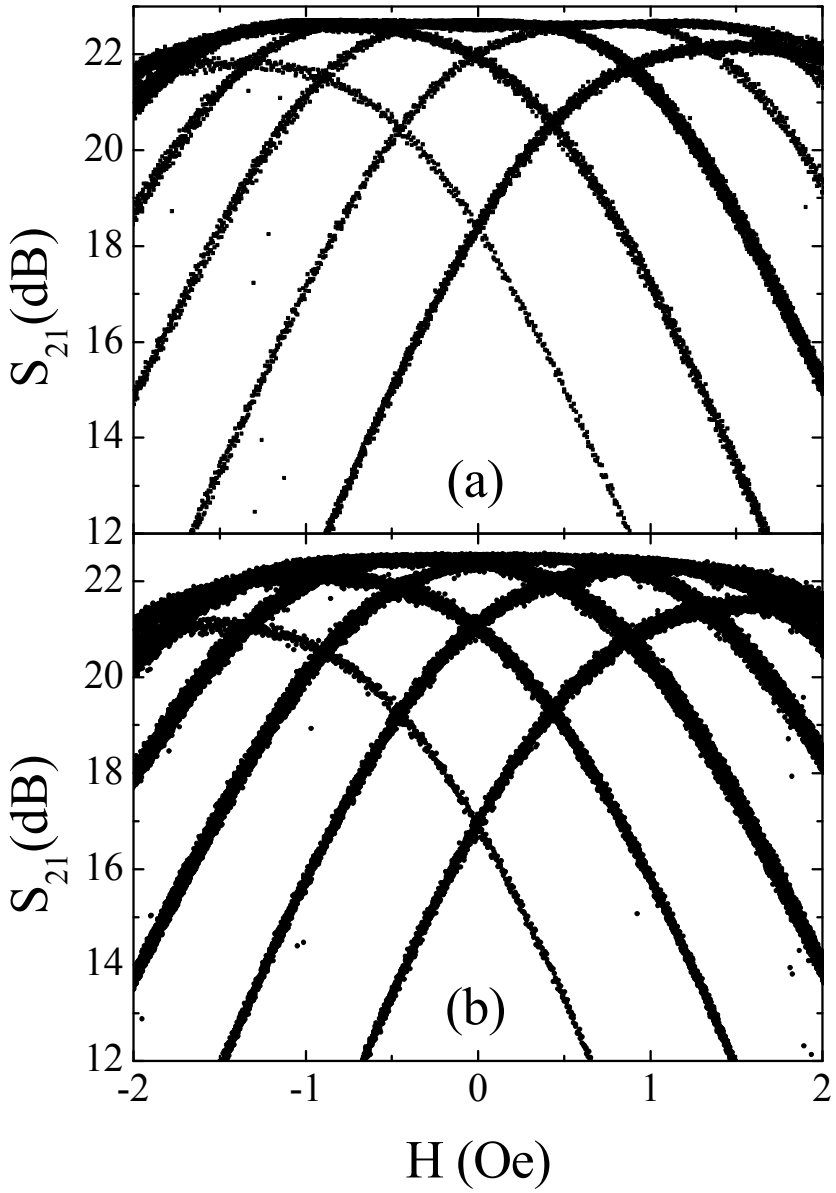

Figure 5.6: The transmission coefficient for sample B as a function of the external magnetic field at two temperatures (a) 0.3 K and (b) 1.8 K. The output power of the network analyzer is -60 dBm. This graph was measured by A. Belkin at the University of Illinois in Urbana-Champaign.

The transmission coefficient of a coplanar waveguide resonator depends on the resonant frequency f_0, the probe frequency f, and the resonator's quality factor Q and is described by Lorentzian:

$$S_{21} = 10\log\left[\frac{A_0}{(f_0/Q)^2 + 4(f - f_0)^2}\right], \tag{5.1}$$

where A_0 is some constant. In a magnetic field the resonance frequency of a superconducting resonator changes (due to the changes of the kinetic inductance of the wires) and the field-dependent transmission coefficient reads:

$$S_{21}(H) = S_{21}(0) - 10\log\left[1 + 4\left(\frac{f_0 - f_0'}{f_0}Q\right)^2\right], \tag{5.2}$$

where f_0' is the field-dependent resonance frequency. Equation 5.2 is derived under the assumption that the probe signal is not changed and fixed at f_0, which is the resonance frequency in zero magnetic field. It is also assumed that the applied field is so weak that the quality factor of the resonator does not depend on the field. The above expression is used to generate the theoretical fit in Fig. 5.5(b) (red curve). The total inductance (L) of the sample can be estimated as a sum of the inductance of a resonator itself (L_{res}) and the kinetic inductance of the nanowires (L_{nw}), $L = L_{res}+L_{nw}$. The kinetic inductance of a nanowire is due to the inertia of the moving condensate (we neglect the magnetic inductance of the nanowire due to its small dimensions and short length). The kinetic inductance of the wire depends on its current-phase relationship (CPR) and is given by the following expression

$$L_{nw} = \frac{\hbar}{2e}\left(\frac{dI}{d\phi}\right)^{-1}. \qquad (5.3)$$

Here e is the electronic charge, $\hbar$ is the reduced Planck's constant, ϕ is the phase difference between the ends of the wire, and I is the supercurrent in the wire. We have performed numerical simulations using the Likharev [17] CPR expression for a long wire ($l >> \xi$, where l is the length of the nanowire and ξ is the coherence length):

$$I = \frac{3\sqrt{3}}{2} I_C \left(\frac{\phi}{(l/\xi)} - \left(\frac{\phi}{(l/\xi)} \right)^3 \right). \qquad (5.4)$$

Here I_C is the critical current of the wire. From the two previous formulas the inductance of the nanowire is:

$$L_{nw}(H) = \frac{\hbar}{3\sqrt{3}e} \frac{1}{I_{C1} + I_{C2}} \frac{1}{\frac{1}{(l/\xi)} - 3\frac{(\beta H/2)^2}{(l/\xi)^3}}. \qquad (5.5)$$

Using the expression for the resonant frequency $f_0 = \left(4\pi^2 LC\right)^{-1/2}$, we obtain the shift of the resonance peak in the magnetic field:

$$f_0 - f_0' = \frac{1}{2\pi C_{res}^{1/2}} \left(\frac{1}{\sqrt{L_{res} + L_{nw}(0)}} - \frac{1}{\sqrt{L_{res} + L_{nw}(H)}} \right) \qquad (5.6)$$

where C_{res} is the capacitance of the resonator with nanowires. In this formula we have assumed that $\phi = \beta H/2$ where the factor 2 originates from the fact that the total phase difference generated

on the wire loop by the applied magnetic field is shared, presumably equally, between the two wires. Using these expressions we are able to fit experimental data with the fitting parameters $I_{C1} = I_{C2} = 33\mu A$, $l/\xi = 20$, $L = 6$ nH and $\beta = 12$. The result is illustrated in Fig. 5.5(b) (red curve).

The experimental approach outlined here allows one to tell exactly how many vortices entered the loop. The vertical lines in Fig. 5.5(a) represent the events when the vorticity changes. The vorticity changes almost instantaneously. The vertical lines in Fig. 5.5(a) appear because in this figure the dots representing the data are connected by straight lines. Thus the lines show from which parabola to which other parabola the jump takes place. If the line connects two neighboring parabolas then one vortex has entered the loop. If the line connects the next to the near neighbor parabola then two vortices have entered, meaning a double phase slip occurred, etc. It was theoretically predicted [18] that transitions between states with different vorticities have unequal probabilities. Under certain conditions the entrance of two vortices at once into a superconducting loop are expected to be more probable. Analysis of our data reveals that in the temperature range $T < 1.5$ K the rate of transition with double phase slip events is significantly higher than rates with single or triple phase slip events (see Fig. 5.7). As we ramp the temperature above 1.5 K the picture changes, namely the frequency of the $n \rightarrow n+2$ jumps decreases while the frequency of the $n \rightarrow n+1$ jumps increases. At approximately 2 K these two rates become equal and $n \rightarrow n+3$ transitions become very rare. A further rise in temperature leaves only $n \rightarrow n+1$ transition possible. This phenomenon is not yet fully understood.

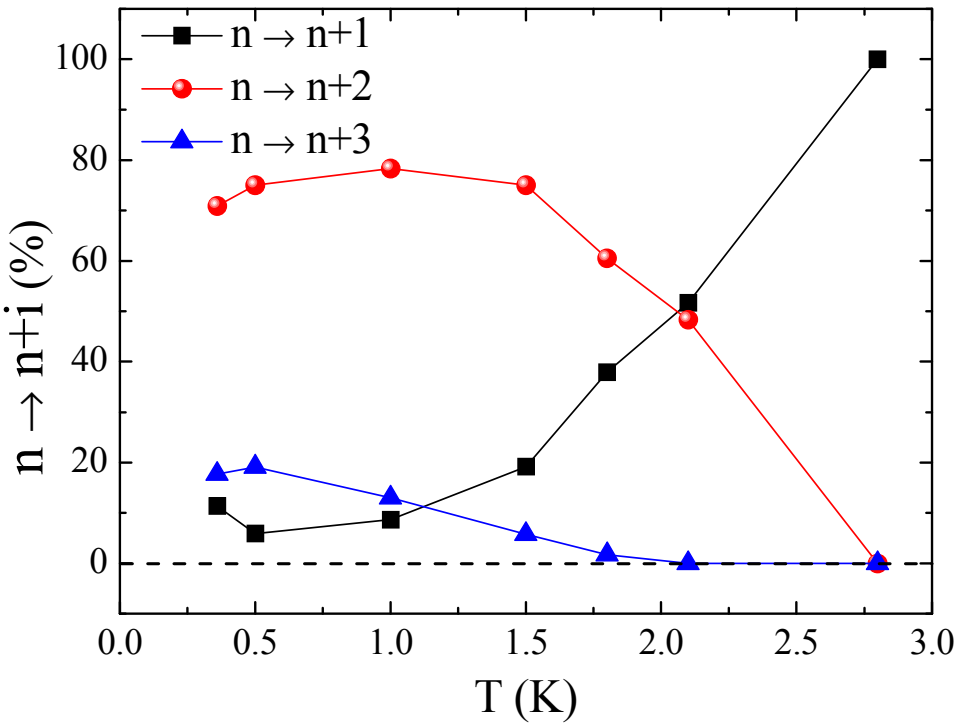

Figure 5.7: Relative frequencies for transitions of the type n→n+1, n→n+2, and n→n+3, calculated for 85 transitions. Here n is the vorticity, i.e. the number of the phase vortices entering the loop. This graph was produced by A. Belkin at the University of Illinois in Urbana-Champaign.

The jumps between parabolas have a one-to-one correspondence with phase slips. Based on our measurement we are able to provide an upper bound to the rate of quantum phase slips (QPS) in nanowires [19]. The conclusion is that in the linear regime the rate of quantum phase slips is extremely low and could be zero. Let us explain this in more detail. The flat top of the parabola [Fig. 5.5(b)] corresponds to a "linear regime", i.e. in such a regime the Meissner current in the loop is weak enough so the kinetic inductance of the wires is not changing significantly. For the single parabola shown in Fig. 5.5(b) the linear regime roughly extends from -0.5 Oe to 0.25 Oe. The regions beyond this interval can be termed "nonlinear regimes", since the magnetic-field-induced circulating current is strong enough to change the inductance significantly. Considering all the data we have obtained on both samples, we conclude that no

phase slips ever happen in the linear regime as defined above, i.e. no jumps from one parabola to another is observed in the linear regime. Experimentally we find that the jumps from one parabola to another can only happen if the field is such that the circulating current is strong enough to significantly change the wire kinetic inductance (i.e. in the "nonlinear" regime). The time it takes the field to sweep near the flat top of the distorted parabolas is ~ 50 s. Since no phase slips are ever observed near the top of the parabola, the rate of QPS is lower than 0.02 s^{-1}. Taking into account the fact that each sample was measured at least 100 times, one concludes that the QPS rate is less than $2 \cdot 10^{-4}$ s^{-1}. This should be compared to the rates predicted by Golubev and Zaikin (GZ) [19], in their Table 1. In sample A wires have the width ~ 25 nm, the thickness ~25 nm and the length of the order of 100 nm, consequently their resistance [15] ~ 0.45 kΩ. Thus, the ratio of resistance to length (R/L) is ~0.0045 kΩ/nm. In equation 50 of the GZ paper, an expression is given to calculate the rate of QPS, $\Gamma_{QPS} = Be^{-S_{QPS}}$, where B is the attempt frequency and S_{QPS} is the QPS action. In equation 47 of the GZ paper, the QPS action is defied as $S_{QPS} = A\frac{R_q}{R}\frac{L}{\xi}$. Thus, from equations 47 and 50 of the GZ paper, one can roughly estimate the rate of phase slips as 10^{-115} s^{-1} for $\xi \approx 5$ nm and $A = 1$, where A is an unknown coefficient introduced by Golubev and Zaikin (we imply that the attempt frequency, B, is equal to the resonant frequency of the resonator, i.e. ~ 5 GHz). This estimate is consistent with our result. A qualitative conclusion is that in a MoGe wire with diameter as small as ~25 nm, QPS do not occur and the wire stays coherent, on a scale of ~1 hour at least, unless a strong current is applied. The robustness of the condensate was even stronger in the sample B having wires with similar width ~26 nm and ~25 nm thick. In this case to initiate the jumps between parabolas and

to obtain the results shown on Fig. 5.6, we had to apply microwave pulses every 100 seconds (the measurements were done after the application of each pulse but not during the pulse).

Generally speaking, we classify the observed periodic set of the distorted parabolas as a manifestation of the Little-Parks effect because it is a reflection of the underlying fact that the thermodynamic potential of our loop formed by wires and electrodes is a periodic set of parabola-like curves, originating from the fundamental principle—single-valuedness of the condensate wave function and the corresponding quantization of the phase increase along the closed path by $2\pi n$ (n is an integer). The same periodic set of parabolas describing the free energy thermodynamic potential is the underlying physical mechanism that leads to the classic Little-Parks oscillation of the critical temperature, observed on empty cylinders [9].

In conclusion, we have shown that a coplanar waveguide resonator can be used to study the Little-Parks periodicity at low temperatures and at low bias by repeating the measurement many times to reveal all possible metastable states. The LP periodicity can be seen in the dependence of the transmission function on the magnetic field as a set of periodically shifted distorted parabolas. Each parabola represents a certain vorticity of the system. Jumps between parabolas allow us to distinguish between single, double and triple phase slip events. The jumps in which the vorticity changes by two (i.e. two vortices enter the closed nanowire loop in one jump) are more frequent at low temperatures.

5.4 Anomalous transmission in the frustrated state

The scenario developed so far, viz., that the magnetic field affects the properties of the resonator by introducing a Meissner current and phase vorticies between the wires (where we understand a "phase vortex" to be a state in which the phase changes by 2π over a loop formed by the wires).

The additional currents flowing through the wires add to the microwave-induced current thus reducing the power P_c at which the crater appears. This leads one to expect that the crater should grow broader and deeper, monotonically, as the magnetic field is swept so as to decrease the critical power P_c. Although this expectation is borne out as regards the *width* of the crater, it is not borne out for the *depth* of the crater under certain conditions. Instead, for a narrow range of magnetic fields near the field corresponding to the lowest critical current (which we refer to as the fully "frustrated" state, i.e. states at which the loop cannot acquire the right number of phase vorticies to compensate the Meissner current; such a state occurs when the leads impose a phase difference of $2\pi n + \pi$ on the wires.), the crater becomes much flatter and *shallower* [see Fig. 5.8(a)], meaning that the average supercurrent amplitude actually becomes *larger* near this frustration point, which seems to go against expectations. Concomitantly, the satellite peaks in the transmitted power spectrum are broadened and decreased in height relative to the unfrustrated state, and a wide feature develops near the drive frequency [see Fig. 5.8(b) and (d)]. At higher temperatures, the satellite peaks disappear altogether at the frustration field. To understand why this effect appears at the frustrated field, we can treat the nanowires in the short, Josephson junction limit, where the energy barrier for vortex movement across the nanowires is given by [1]:

$$\Delta F = \frac{\sqrt{6}\hbar}{2e}\sqrt{\left(I_{c1}+I_{c2}\right)^2\cos^2\left(\frac{\delta}{2}\right)+\left(I_{c1}-I_{c2}\right)^2\sin^2\left(\frac{\delta}{2}\right)}, \qquad (5.7)$$

where I_{c1} and I_{c2} are the critical currents of each nanowire and δ is the phase gain in one lead induced by the magnetic field. Thus from Eq. 5.7, it is clear that the energy barrier for vortex movement across the nanowires is smallest at the frustrated field where $\delta = \pi$.

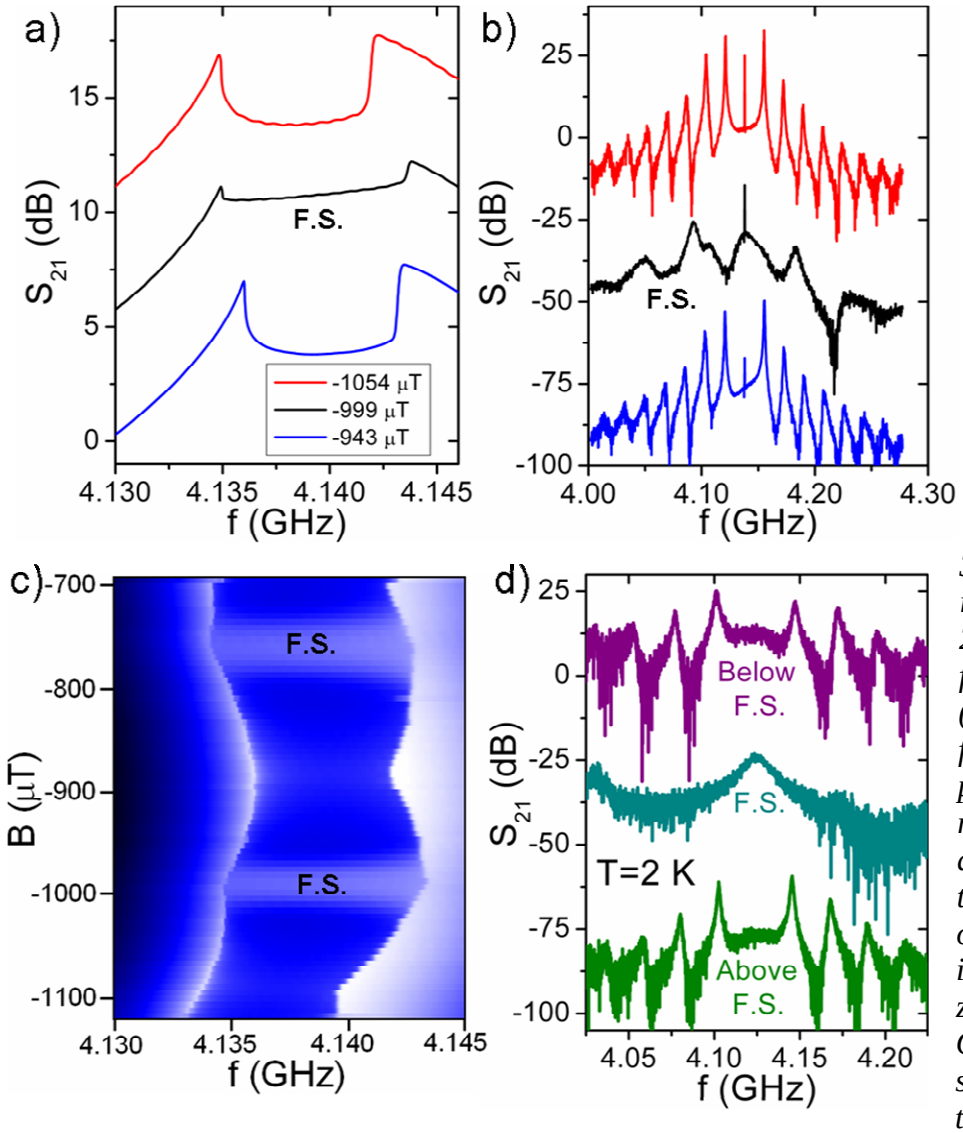

Fig. 5.8: (a) Transmission characteristics for sample S6, which is a two-wire device incorporating somewhat asymmetric nanowires separated by 1.65 μm and connecting a center conductor that is 10 μm in width, measured at 308 mK and at an input power of -21 dB. In the frustrated state (denoted by F. S.), for which the critical power is at a minimum, an anomalous transmission effect is observed. For low input power and at zero magnetic field, Q = 475 for this sample. (b) The transmission power spectrum of the amplitude oscillations when the drive frequency is fixed at 4138 MHz and at a power of -20.8 dB. Near the frustrated state, the satellite peak spacing increases. (c) Color map of the transmission coefficient as a function of magnetic field and frequency, exhibiting the anomalously enhanced transmission effect near the frustrated state (the corresponding regions are marked "F.S"). (d) The transmission power spectrum measured in the crater regime at high temperature (2 K) for drive frequency and power fixed at 4124 MHz and -39 dB. As one tunes the wires to the frustrated state (F. S.; middle curve), the satellite peaks vanish and are replaced by a broad central feature, thus indicating that the periodic superconductor-normal oscillations have been entirely replaced by stochastic dissipative events of a lesser strength. The terms "below" and "above" the F. S. indicate the magnetic field corresponding to the phase induced on the wires that is an integer multiple of 2π, directly below and above the F. S., respectively.

This anomalous transmission effect is most evident at *higher* temperatures. Additionally, of the two samples that we measured, the more *asymmetric* sample (i.e., the one in which the wire critical currents are presumed less similar based on the differences in their physical appearance) exhibited a much more pronounced anomalous transmission feature (i.e. the rise of the bottom of the crater near the frustration point). Whereas, in the more symmetric sample, the anomalous transmission set in only at temperatures above $T \sim 2$ K (Fig. 5.9), in the asymmetric sample this effect persisted down to the lowest temperature at which we took data, i.e., $T = 308$ mK.

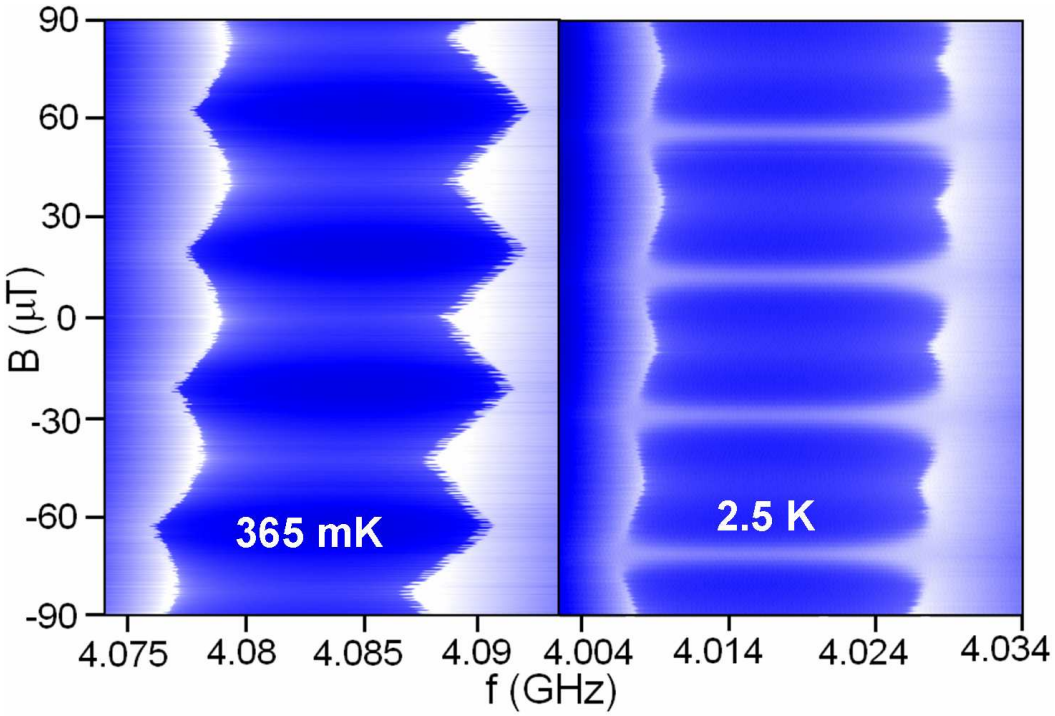

Fig. 5.9: Color maps of the transmission coefficient as a function of magnetic field and frequency, with an input power of -17 dB at the two indicated temperatures for the case of a device incorporating two symmetric nanowires (sample S5). The anomalous transmission effect only appears at higher temperatures.

Qualitative explanation of the anomalous transmission

The anomalous transmission effect seems to depend strongly on the asymmetry between the two wires. Therefore, a natural starting point for explaining it is to consider a resonator containing one wire that is *much* thicker than the other, i.e., the geometry shown in Fig. 5.10. This geometry is related to that of an rf SQUID that is capacitively coupled to the a.c. input. The analogy with an rf SQUID explains how a *plateau* in the transmission could arise: when the driving power exceeds a certain flux-dependent value, vortices are free to enter and leave the circuit via the weak link, thus dissipating energy. In contrast to the process discussed in chapter 4 for the one-wire device, however, this dissipative process does not cause the *Q*-factor of the resonator to drop to zero when the weaker wire undergoes a dissipative process, as the two halves of the resonator remain connected by the stronger nanowire; instead, the current amplitude in the resonator is expected to stay rather large in this regime [20]. This picture also accounts for the broad peak in frequency space near the drive frequency [see Fig. 5.8(d)], as the processes of vortex entry and exit are stochastic. Despite its idealization, therefore, this picture does qualitatively account for the high-temperature, asymmetric-wire data shown in Fig. 5.8(d).

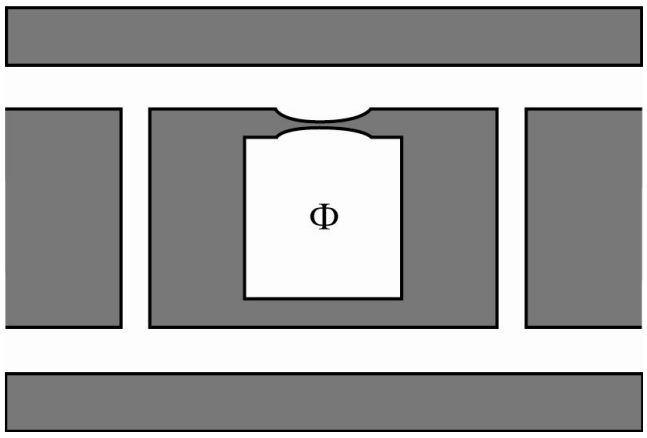

Fig. 5.10: Illustration of a two-wire sample in the "rf SQUID" limit of extreme asymmetry between the wires. The capacitive coupling between the resonator and its input is analogous to the coupling between an rf SQUID and its "tank" circuit [20].

The crucial difference between the scenario considered in the previous paragraph and the one considered in chapter 4 is that in the former case the dissipative processes are concentrated in *one* of the wires. In the experimentally relevant regime, the disparities between the critical currents of the two wires are not as dramatic as in the limit considered in the previous paragraph; the "anomalous" dissipative state, in which only one wire becomes dissipative, must compete with the "normal" dissipative state, in which both wires become dissipative and the phenomenology described in chapter 4 is realized. The critical current I_{c1} in the weaker wire is less than the critical current I_{c2} in the stronger wire, thus thermal (or quantum) phase slips will occur in the weaker wire at a lower current amplitude and drive it to the normal state. If $I_{c1} \approx I_{c2}$, then the change in current amplitude through the stronger wire after the weaker wire switches to the normal state may be enough to drive it to the normal state. However, if $I_{c1} << I_{c2}$, then a switch in the weaker wire might not produce enough of a perturbation in the current amplitude through the stronger wire to also drive it to the normal state. Thus, in less asymmetrical situations, the weaker wire carries an appreciable fraction of the current in the circuit when superconducting; therefore, when the weaker wire switches to the normal state, one would expect the steady-state current in the circuit to drop to some fraction of its maximum achievable value. In particular, it is possible for the weaker wire *alone* to undergo amplitude oscillations (the stronger wire would always remain superconducting), in which case the current amplitudes in the circuit would oscillate between the low value, which equals the supercurrent in the stronger wire, and the high value corresponding to the addition of supercurrents from both wires.

These expectations are borne out by the data shown in Fig. 5.11. The fact that the satellite peaks spacing Δf increases by a factor of ~ 3 in the frustrated state has a natural

explanation in the scenario sketched in the present section: the current should take ~ 1/3 the time to grow from ~ $2I_c/3$ to I_c as it does to grow from 0 to I_c. Therefore, the amplitude oscillation period should be reduced by a factor of ~ 1/3, and the frequency Δf tripled, as the data shown in Fig. 5.11(b) indicates. We are also able to fit the shape of the anomalous crater by using the model presented in Chapter 4 but with a modified switching rule, in which the current is reduced to some fraction of I_c (here ~ 2/3) rather than to zero. In the fits for the frustrated case, the diffusive parameter t_{hold} is not included, so as to simplify the simulation. If t_{hold} were included, it would serve to slightly increase the depth of the crater and would have forced (within the model) the supercurrent to drop to a slightly higher fraction of I_c, resulting in a slightly larger Δf. In the unfrustrated case the model predicts Δf = 44 MHz, whereas the experimental value we have obtained is 50 MHz; in the frustrated state the model predicts Δf = 12.4 MHz, whereas the experimental value is found to be 15 MHz. Therefore, the model has reasonable semi-quantitative agreement with the experiment.

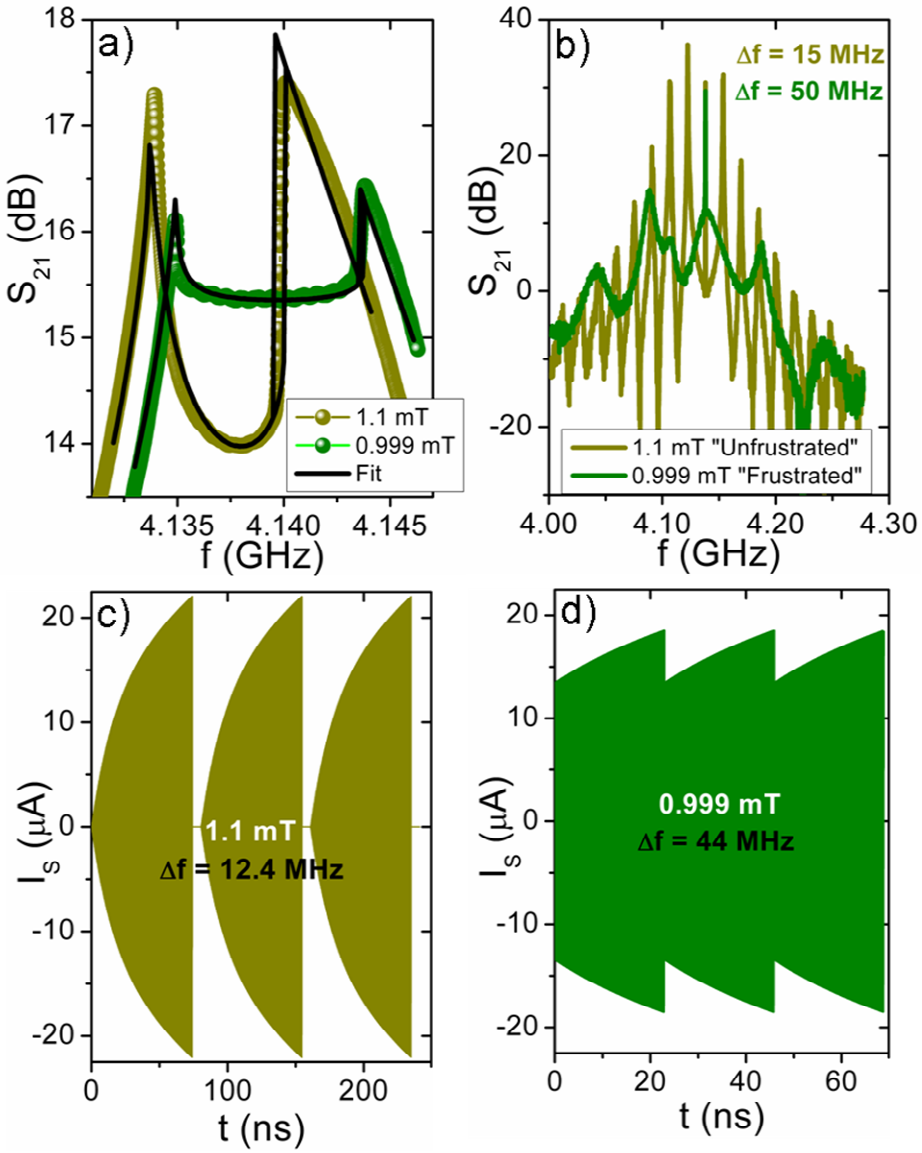

Fig. 5.11: (a) Transmission characteristics for a two-wire sample (S6) having noticeably asymmetric nanowires, measured at 308 mK and at an input power of -21 dB. In the frustrated state an anomalous transmission effect is observed. The model described in Sec. 3 is used to fit the curve, but with a modified switching rule such that when the supercurrent hits I_c, it drops to a fraction of I_c, here, 0.64, because the stronger nanowire maintains superconductivity. The fits were calculated using the following fitting parameters: C = 18.12 pF, R = 545 Ω, L_k = 6.55 pH; and for the unfrustrated (frustrated) state: L = 0.07498 (0.07493) nH; I_{sw} = 22.07 (18.50) μA; t_{hold} = 6.3 (0) ns. Additionally, a small slope of 87 ndB/Hz was subtracted from each set of data to account for low temperature parasitic resonances as discussed in Sec. 4(c). (b) Transmission power spectrum of the amplitude oscillations for drive frequency fixed at 4138 MHz. In the frustrated state, the period of amplitude oscillations is reduced, thus increasing the satellite peak spacing Δf. (c) Model prediction for the supercurrent profile as a function of time at the unfrustrating magnetic field. (d) Model prediction for the supercurrent time evolution at the frustrating field; notice that the supercurrent does not drop to zero after it reaches I_c.

The effective inter-wire asymmetry—parameterized, e.g., by the ratio of the critical currents of the wires—is enhanced at temperatures that are high enough to be comparable to the critical temperature of the weaker of the two wires; thus, the anomalous transmission effect becomes more pronounced at higher temperatures. (The critical temperature is related to the critical current by the Bardeen formula, as discussed in chapter 4.) A further, relatively minor, factor is that at high temperatures the thermal current noise in the resonator becomes comparable to the nanowire's critical current; thus, the deterministic amplitude-growth process delineated in Chapter 4 becomes swamped by the effects of thermal fluctuations. (Thus, one sees behavior that is superficially similar to anomalous transmission at temperatures around 4 K, even in the single-wire case. This effect cannot, however, account for the existence of anomalous transmission presented in this section because (i) at 300 mK in the asymmetric sample the thermal noise is much lower at this temperature and (ii) as the magnetic field is swept away from the frustrated state, the crater is observed to *increase* and not *decrease* in depth, which would be the wrong trend if the anomalous transmission effect were not present. When the anomalous transmission effect is observed in nanowires and the magnetic field is swept away from the frustrated state, the rate of phase vorticies decreases and thus both wires become normal when the supercurrent reaches the critical current, which initially results in a deeper crater. As the magnetic field approaches the integer flux quantum value, the crater floor begins to rise again as the critical current increases to its maximum value. However, for the case where the anomalous transmission effect is not observed, as the magnetic field is swept away from the frustrated field, the critical current increases and thus the crater floor is always observed to increase until it reaches the integer flux quantum value.

5.5 Conclusion

In the present work we have characterized a microwave stripline resonator interrupted by one or two nanowire bridges. We have identified two nonequilibrium steady states, occurring at high current (i.e. very large photon numbers): one, which we have identified as an oscillatory steady state of the resonator-nanowire system, in which the nanowire periodically enters and leaves the superconducting state; and a second, stochastic steady state, which emerges in the two-wire device near what we have termed "frustrating" magnetic fields, and which we conjecture to be associated with vortex (or equivalently: phase slip) motion across the weaker of the two wires. We have presented evidence for the fact that the oscillatory steady state exists in a range of resonators containing quasi-one-dimensional elements, and is associated with the driving of the nanowire (or other quasi-one-dimensional element) being past its critical current. In addition, we have developed a simple phenomenological model that explains the salient features of the oscillatory steady state, and also captures some qualitative features of the stochastic steady state. Moreover, whilst accounting for the features of the oscillatory state, our model also enables us to extract information about the relaxation of heat pulses in nanowires; we find that, contrary to what one might expect, this relaxation does not slow down appreciably at temperatures far below T_c, but rather it saturates. We have also offered a qualitative picture of the "anomalous" stochastic state exhibited by two-wire devices, a feature that we hope to address in more detail in future work.

We believe that the primary avenue for future investigations of nanowires embedded in superconducting resonators should involve the study of nanowires that are much narrower than those measured to date. As discussed in the Introduction to chapter 4, such nanowires would have critical currents that are not much greater than the current due to a single photon in the

resonator. Therefore, resonators containing them could be used both to investigate quantum phase-slips via a novel probe and to explore many-body circuit QED, in which a single photon is coupled to the elementary excitations of an *extended* quantum-mechanical system. Such devices would differ from the artificial-atom-based systems studied to date in a variety of ways; we briefly mention two. First, it has been predicted [21] that successive quantum phase-slip events in nanowires are coherent at low temperatures. As discussed in Refs. [22, 23], such coherence gives rise to an effective energy band structure for the states of the field representing charge transfer across the wire; this effective band structure is accompanied by interband "excitonic" transitions having frequencies in the microwave regime [22]. It is plausible that one could detect such excitonic transitions—which would provide strong evidence for the coherent quantum-mechanical character of phase slips—via their influence on cavity resonances, which would include, e.g., vacuum Rabi splitting [24]. Second, the physics of a single photon coupled to a quantum field (e.g., the superconducting phase fluctuations of the nanowire) would pave the way for realizations of quantum impurity-like models in which the *photon* acts as the impurity and the nanowire acts as a (one-dimensional) environment or bath. Quantum impurity models are believed to exhibit nonperturbative phenomena of considerable theoretical interest, such as the Kondo effect; moreover, the coupling of a low-dimensional system to a controllable "impurity" has been proposed as a method for probing the quantum mechanics of low-dimensional systems [25].

---

[1] D. S. Hopkins, D. Pekker, P. M. Goldbart, and A. Bezryadin, Science **308**, 1762 (2005).
[2] D. S. Hopkins, D. Pekker, T.-C. Wei, P. M. Goldbart, and A. Bezryadin, Phys. Rev. B **76**, 220506 (2007).
[3] A. Lupascu, E. F. C. Driessen, L. Roschier, C. J. P. M. Harmans, and J. E. Mooij, Phys. Rev. Lett. **96**, 127003 (2006).
[4] E. Segev, O. Suchoi, O. Shtempluck, and E. Buks, Appl. Phys. Lett. **95**, 152509 (2009).
[5] D. Pekker, A. Bezryadin, D. S. Hopkins, and P. M. Goldbart, Phys. Rev. B **72**, 104517 (2005).
[6] K. K. Likharev, Rev. Mod. Phys. **51**, 101 (1979).
[7] B. S. Deaver, Jr. and W. M. Fairbank, Phys. Rev. Lett. **7**, 43 (1961).
[8] R. Doll and M. Nabauer, Phys. Rev. Lett. **7**, 51 (1961).

[9] W. A. Little and R. D. Parks, Phys. Rev. Lett. **9**, 9 (1962).
[10] W. A. Little and R. D. Parks, Phys. Rev. **133**, A97 (1963).
[11] R. P. Groff and R. D. Parks, Phys. Rev. **176**, 567 (1968).
[12] V. Vakaryuk, Phys. Rev. Lett. **101**, 167002 (2008).
[13] W. A. Little, Phys. Rev. **156**, 156 (1967).
[14] A. Bezryadin, C. N. Lau and M. Tinkham, Nature **404**, 971 (2000).
[15] A. Bezryadin, J. Phys.:Condens. Matter **20**, 043202 (2008).
[16] D. S. Hopkins, D. Pekker, P. M. Goldbart, and A. Bezryadin, Science **308**, 1762 (2005).
[17] K. K. Likharev, Rev. of Mod. Phys. **51**, 101 (1979).
[18] S. E. Korshunov, JETP Lett. **45**, 434 (1987).
[19] D. S. Golubev and A. D. Zaikin, Phys. Rev. B **64**, 014504 (2001).
[20] Michael Tinkham, *Introduction to superconductivity* (Dover, 2004).
[21] H. P. Büchler, V. B. Geshkenbein, and G. Blatter, Phys. Rev. Lett. **92**, 067007 (2004).
[22] S. Khlebnikov, Phys. Rev. B **78**, 014512 (2008).
[23] J. E. Mooij and Yu. V. Nazarov, Nat. Phys. **2**, 169 (2006).
[24] See, e.g., S. Haroche and J.-M. Raimond, *Exploring the Quantum: Atoms, Cavities, and Photons* (Oxford University Press, 2006).
[25] A. Recati, P. O. Fedichev, W. Zwerger, J. von Delft, and P. Zoller, Phys. Rev. Lett. **94**, 040404 (2005).

Chapter 6

Properties of resistively shunted superconducting nanowires

It is well established that by shunting Josephson junctions the environmental dissipation of the system can be controlled. This effect can be observed in the voltage-current characteristics, which are greatly altered by the amount of dissipation, as described by the McCumber-Stewart model of shunted junctions. The shunting is also known to control the rate of macroscopic quantum tunneling of the phase variable in superconductor-insulator-superconductor (SIS) junctions. On the other hand, the effect of resistively shunting superconducting nanowires has not been explored until now. Here we present such an investigation. We find that resistive shunting stabilizes phase slip centers in the wires and allows us to study them at temperatures much lower than the critical temperature. Among other things, the shunt drives the switching current closer to the depairing current, and shows a temperature dependence in agreement with the Bardeen prediction. We modify the model of McCumber and Stewart to make it applicable to shunted nanowires and successfully describe the experimental voltage-current characteristics. Distributions of the switching and retrapping currents are also analyzed.

6.1 Introduction

It is well known that the Stewart-McCumber model [1, 2] accurately describes the behavior of shunted Josephson junctions (JJs) [3, 4]. The model is very powerful since it allows the analysis

of various fundamental aspects of superconducting devices, including chaotic behavior [5] and high-frequency microwave response [6]. The Stewart-McCumber model can be "quantized" and thus allows one to quantitatively understand the phenomenon of macroscopic quantum tunneling [7, 8, 9, 10, 11], which was also observed experimentally [12, 13]. The analysis of superconducting computational circuits is also done using the Stewart-McCumber model [14].

There have also been many investigations into the statistics of the switching and retrapping behavior in shunted JJs [15, 16, 17, 18, 19, 20, 21]. Many groups have found that a frequency dependent line impedance controlled the level of damping in their system, which is given by the inverse of the quality factor, $Q = \omega_p CZ(\omega)$, where ω_p is the plasma frequency, C is the electrode capacitance, and $Z(\omega)$ is the real part of the frequency dependant impedance of the electrodes [16, 17, 18, 22]. Experimentally, damping has been shown to control the statistics of the switching and retrapping currents [16, 17, 18, 19, 21]. Caldeira and Leggett have theoretically demonstrated that the electromagnetic environment also has a strong impact on the rate of macroscopic quantum tunneling and thus can control the switching and retrapping events in quantum systems [10, 23]. In general, the retrapping current, which is inversely proportional to Q, is more sensitive to the amount of damping than the switching current. A correlation between the retrapping and switching currents was also investigated [20, 21]. It was found that after a switch has occurred out of the superconducting state, if the probability of retrapping is large enough at a given damping strength, the phase particle in the titled washboard model [3, 20] could be retrapped in one of the subsequent wells until the driving current is increased past a critical value that exceeded the level of damping. This observation allows one to understand the role of damping in the behavior of the switching currents. Thus, the Stewart-

McCumber model and the effect of damping have been well characterized for JJs, which can be used in novel ways.

Superconducting nanowires [24] represent another example of a simple superconducting device with potentially important applications, such as in superconducting qubits and current standards [25, 26]. The list of interesting and potentially useful phenomena predicted and/or occurring in junctions involving a superconducting nanowire includes: macroscopic quantum tunneling (MQT) [8, 9, 10, 11] which takes the form of quantum phase slips (QPS) [27, 28, 29, 30], a dissipation-controlled quantum phase transition [31, 32, 33, 34, 35, 36] which is also known as the Schmid-Bulgadaev transition [37], a quantum analogue of the Kosterlitz-Thouless transition [38], a Joule-heating driven hysteresis in voltage-current characteristics [39, 40, 41, 42], and a multi-valued character of the current-phase relationship (CPR) [43]. Nanowires have also been used as photon counters [44], which is an important task in radioastronomy. Additionally, shunting of a superconducting nanowire with a normal resistor should have a strong effect on the superconducting character of the wire. For example, quantum theory shows that the QPS rate as well as quantum phase transition(s) can be controlled by an external shunt [36]. Yet, the behavior of shunted nanowires has not been studied so far and the applicability of the Stewart-McCumber model has not been tested on nanowires either. Here we present results of such a study.

In this paper we study the effects of shunting quasi one-dimensional superconducting nanowires with commercially available external shunt resistors. It is found that at high-bias currents, the nature of the resistive state changes from the Joule-heated normal state (JHNS), which has been observed previously [39, 41], to the phase slip center (PSC) state with the inclusion of a shunt resistor. As the value of the shunt resistance is decreased, the hysteresis

becomes suppressed. The Stewart-McCumber resistively shunted junction (RSJ) model [1, 2] with a multivalued CPR for a nanowire is used to model the observed voltage-current curves in this case, showing excellent agreement with the data. To simulate the behavior of the nanowire as it is shunted with various resistances, such that not every case results in an overdamped junction, the RCSJ model is extended to include an external shunt resistor with a corresponding current noise. These simulations capture the behavior observed in the voltage-current curves and the switching and retrapping distributions and support the conclusion that the insertion of a shunt resistor can change the nature of the normal state. In addition, the temperature dependence of the switching current corresponding to shunt values less than 10 Ω is consistent with the Bardeen prediction for the temperature dependence of the critical current [45]. We also find that the statistics of the switching and retrapping currents significantly depends on the value of the shunt resistance. The deterministic retrapping current observed on our unshunted nanowires (all of which exhibit JHNS when unshunted) becomes stochastic when a resistive shunt is added. A model for stochastic retrapping in hysteretic JJs successfully explains the retrapping distributions measured on the shunted superconducting nanowires [15].

6.2 Sample fabrication and measurement

The nanowires presented in this study were fabricated using molecular templating [24, 46]. Using electron-beam lithography and a reactive ion etch, a 100nm wide trench was patterned in the SiN layer of a Si-SiO_2-SiN substrate. The trench was then etched in a 49% solution of hydrofluoric acid to form an undercut to prevent electrical leakage between the electrodes, which are separated by the trench [47]. Fluorinated single-walled nanotubes, which are insulating, were dissolved in isopropanol and then deposited onto the substrate containing the 100 nm wide trench

in the SiN layer and then dried with nitrogen gas. Randomly, some of the nanotubes cross the trench, creating a scaffold for the nanowires to form as the metal of choice is deposited on the substrate. The samples were then DC sputtered with amorphous $Mo_{76}Ge_{24}$ in a high vacuum (~ 10^{-7} Torr base pressure) chamber, thus coating the substrate and nanotubes with 12-15 nm of MoGe depending on the sample. A scanning electron microscope (SEM) was then used to image the trench until a MoGe coated nanotube (nanowire) is found to be relatively straight, homogeneous, and coplanar with the electrodes [24]. An SEM image of one such nanowire is shown in the inset of Fig. 6.2(a). Contact pads were formed using photolithography and wet etching in a 3% solution of H_2O_2, which etches MoGe rapidly.

The shunt was added by attaching a commercial metal film resistor (ranging from 5 to 200 Ω) parallel to the sample using silver paste (Fig. 6.1(b)). The distance from the nanowire to the shunt was 1-2 cm for all samples and the shunt resistance was measured as a function of temperature down to cryogenic temperatures and found to be constant. Measurements were performed in a ^{4}He or ^{3}He cryostat equipped with base temperature silver paste and copper powder filters and room temperature π-filters. Transport measurements were carried out by current biasing the sample through a large resistor (~1 MΩ) and measuring the voltage with a battery-operated Stanford SR 560 preamp, using the typical film-inclusive four-probe technique as in Fig. 6.1(b) [46]. Resistance vs. temperature (*R*-*T*) curves were measured by applying a small sinusoidal current (~10-100 nA) at a frequency of ~12 Hz and measuring the voltage and then doing a linear fit to the resulting voltage-current data to obtain the resistance. The temperature was measured using a calibrated Cernox thermometer from LakeShore. Voltage vs. current (*V*-*I*) curves were measured by applying a large sinusoidal current in the range of a few μA, at a frequency of 8 Hz, and measuring the voltage simultaneously. The switching

(retrapping) current was measured by sweeping the current as in the *V-I* measurement and recording the current at which the voltage jump (drop) out of the superconducting (resistive) state was the greatest.

6.3 Resistance vs. temperature curves

In Fig. 6.1(a), the sample resistance vs. temperature (*R-T*) is shown, in a log-linear scale for various values of the shunt resistance. As the temperature is lowered below 5.8 K the film becomes superconducting while the wire is still resistive due to the fact that its critical temperature (T_c) is lower than that of the film. Below T_c of the wire, there is a measurable resistance due to phase slips.

To model the measured *R-T* curves, we consider the following. Below T_c of the nanowire the total sample resistance is a parallel combination of the shunt resistance, R_s and the wire resistance, R_w. We model the wire resistance with an empirical formula, $R_w^{-1}(T) = R_N^{-1} + R_{AL}^{-1}(T)$, where R_N is the normal state resistance of the nanowire to account for the quasi-particle resistance channel and R_{AL} is the Arrhenius-Little (AL) resistance occurring due to thermally activated phase slips (TAPS). The AL resistance is estimated, following Little's proposal, by assuming that each phase slip creates a normal segment on the wire of a size equal to the coherence length and for a time interval roughly equal to the inverse attempt frequency [48, 49]. We note that the Langer-Ambegaokar-McCumber-Halperin (LAMH) theory of TAPS is not valid except very near to T_c [35]. So we have to use the phenomenological AL expression: $R_{AL}(T) = R_n \exp\left(-\Delta F(T)/k_B T\right)$, where $\Delta F(T) = \frac{8\sqrt{2}}{3}\frac{H_c^2(T)}{8\pi} A\xi(T)$ is the free energy barrier for a phase slip in the zero-bias regime [50]. Here $H_c(T)$ is the thermodynamic critical field, $\xi(T)$ is the

temperature dependant coherence length, and k_B is Boltzman's constant and they follow the temperature dependence discussed in Chapter 2 in Eqs. 2.28 and 2.27, respectively. The equation for the free energy barrier can be rewritten to include wire parameters more accessible via the experiment as $\Delta F(T) = 0.83 k_B T_C \left(\frac{R_Q}{R_N}\right)\left(\frac{L}{\xi(0)}\right) f(T)$ [51], where L is the length of the nanowire, R_Q ($h/4e^2 \approx 6450\ \Omega$) is the quantum resistance, and $f(T)$ is a function of temperature. Thus, the total temperature dependent sample resistance $R_T(T)$ is:

$$R_T(T) = \left[\frac{1}{R_s} + \frac{1}{R_N}\left(1 + \exp\left(\frac{\Delta F(T)}{k_B T}\right)\right)\right]^{-1}. \qquad (6.1)$$

The fits of the total sample resistance to Eq. 6.1 are presented in Fig. 6.1(c) for the unshunted nanowire ($R_s = \infty$) and the case when the nanowire is shunted with 25 Ω. All the fits are done by measuring the values of R_N, T, L, and R_s from the R-T curve and SEM image and using T_c, and $\xi(0)$ as fitting parameters. The value of the fitting parameters change slightly as the shunt resistance is varied. For instance, in the fitting presented in Fig. 6.1(c), the value of T_c decreased by 10 mK, which can be accounted for slight sample change during thermal cycling. The R-T curves of all the samples presented in this paper were smooth and showed no extra transitions, and the SEM images of these nanowires all confirm that the nanowires are homogenous and well-connected to the electrodes and thus are well suited to study the shunting of quasi one-dimensional nanowires.

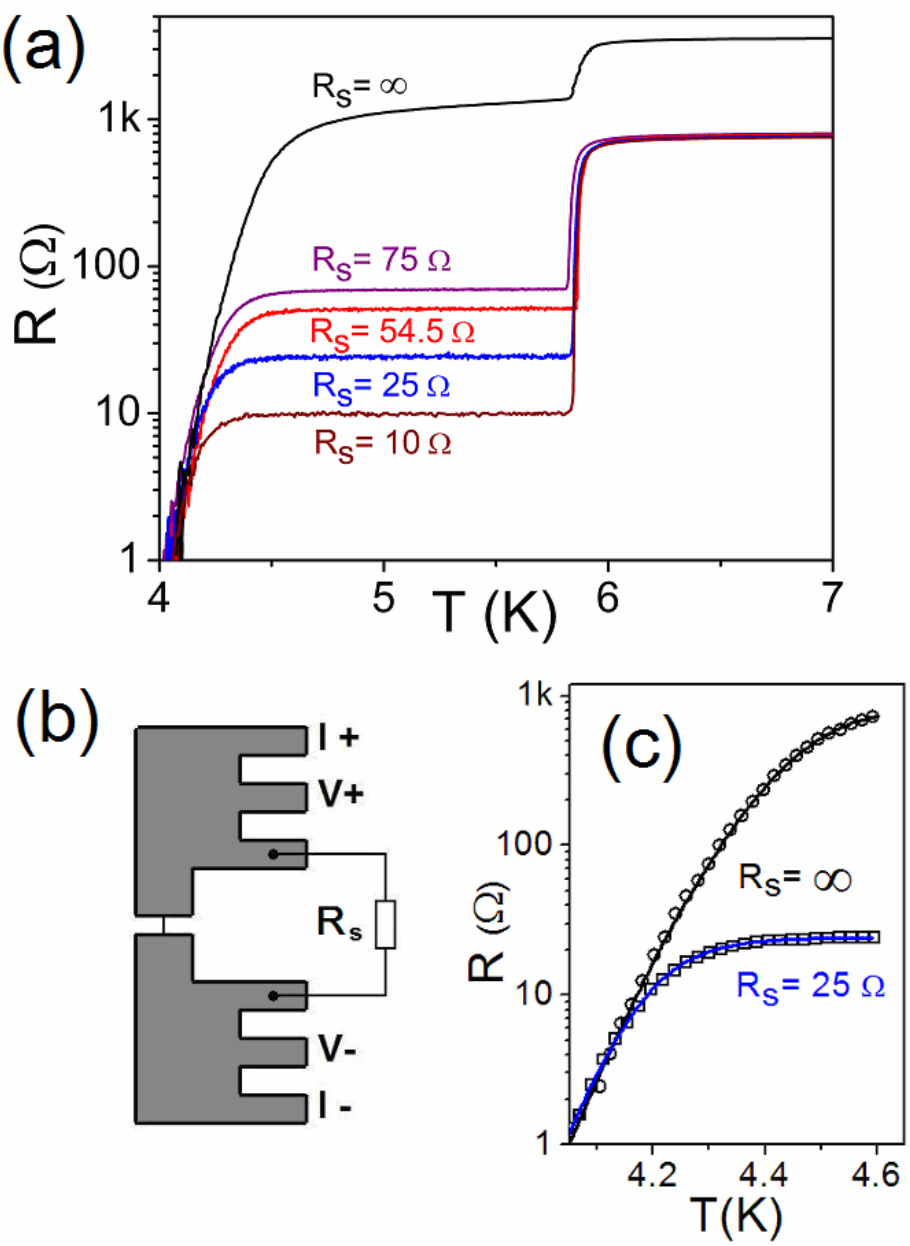

Fig. 6.1: (a) R-T data for sample S1 with various shunt values. The first sharp drop in resistance at ~5.8 K is due to the film electrodes going superconducting. The second, gradual, drop in resistance at lower temperature is the superconducting transition of the nanowire, which is much broader due to TAPS. (b) Sample schematic. The wire is shown as a short vertical line and is shunted by a commercial resistor (R_s). The sample is measured by current biasing the sample and extracting the resistance via a four-probe measurement. (c) R-T curves from (a) for the case of no shunt (circles) and a 25 Ω shunt (squares) compared to the theoretical expression of the total sample resistance given by Eq. 6.1 (solid lines). The known parameters used in each fit were: wire length, L=105 nm, normal state resistance, R_n=1385 Ω, and shunt resistance, R_s=∞ and R_s=25 Ω, respectively. The fitting parameters used for the fits were T_c=4.607 K for the unshunted case and T_c=4.595 for the 25 Ω shunt case, and ξ(0)=7.50 nm for both cases, where ξ(0) is the dirty limit coherence length at zero temperature.

The agreement of the fits with Eq. 6.1 as shown in Fig. 6.1(c) gives evidence that the rate of phase slips does not depend on the shunt at relatively high temperatures ($T > 4$ K in this case). This is an indication that the phase slips are thermally activated and not due to quantum tunneling since the rate of quantum phase slips should depend strongly on the dissipative environment [35, 36]. If QPS were involved at these temperatures, adding a shunt resistor would drop the total sample resistance in Fig. 6.1(a) to a value *lower* than the parallel combination (which is given by Eq. 6.1) of the unshunted nanowire and the shunt resistance. This is not observed in this experiment. Thus we conclude that the observed residual resistance of the wire below T_c is due to TAPS in the high temperature limit of ~ 4-5 K.

6.4 Voltage vs. current characteristics

Fig. 6.2(a) shows *V-I* curves for sample S1 corresponding to various values of the shunt resistor. Consider first the unshunted wire ($R_s = \infty$). As the bias current is increased, thermal fluctuations cause the wire to switch from a superconducting state into a resistive state before the current reaches the critical depairing current. The current at which the wire switches out of the superconducting state is called the switching current (I_{sw}) and is stochastic in nature, i.e. each new current sweep gives a slightly different value for the switching current. The resistive state the wire switches to for unshunted wires is the JHNS. Once in this state, as the current is decreased below some critical value of current, the nanowire experiences retrapping back into the superconducting state. The current at which this happens is called the retrapping current (I_r). For unshunted wires, the retrapping process is non-stochastic since the retrapping occurs from the Joule heating state and not some phase coherent state.

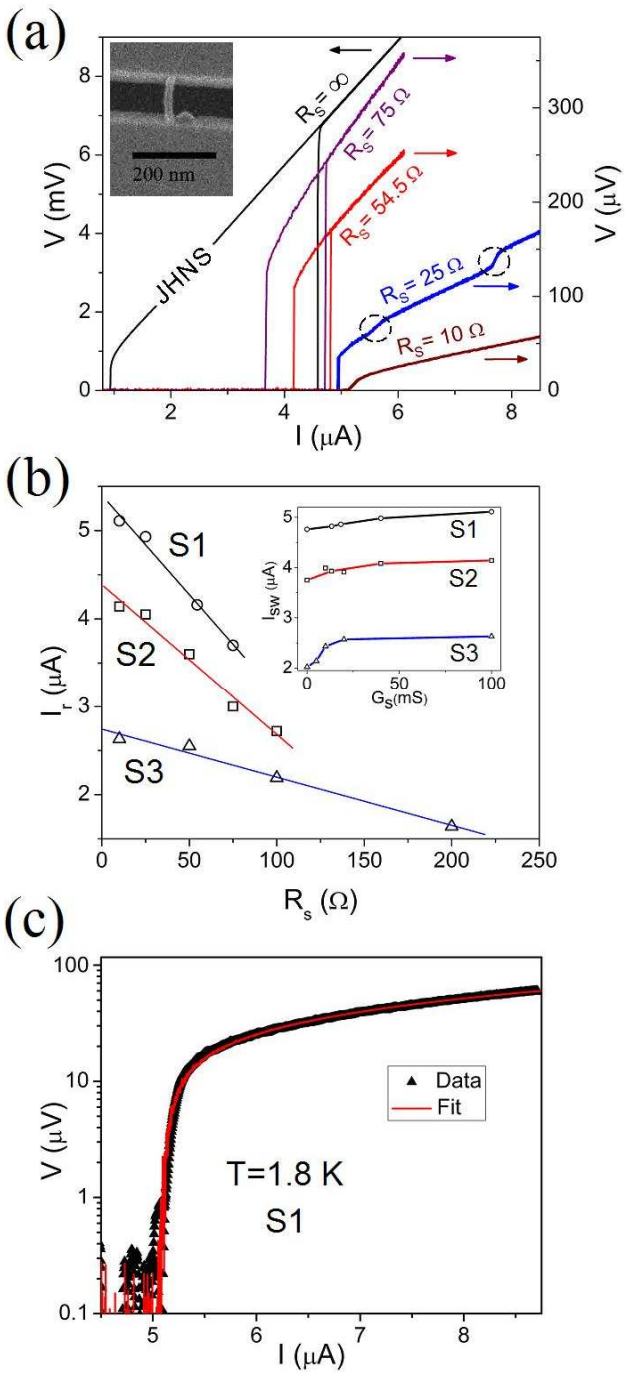

Fig. 6.2: (a) Voltage vs. total current for sample S1 at 1.8 K corresponding to various values of the shunt resistance, R_s. Dashed circles are kinks in the V-I curve occuring for the case when the nanowire is shunted with R_s=25 Ω. Inset: SEM image of the nanowire for sample S1. (b) Average retrapping current (I_r) vs. R_s for three samples (S1 at 1.8 K, S2 at 1.5 K, and S3 at 1.6 K). Inset: The corresponding maximum switching current (I_{sw}) vs. G_s $(\equiv 1/R_s)$ for S1, S2, and S3 at the temperatures given above. (c) Log-linear V-I curve for the case when sample S1 is shunted with 10 Ω. The solid red line is the Stewart-McCumber RSJ fit to Eqs. 6.2 and 6.3 for the R_s=10 Ω case from (a) with fitting parameters: R = 9.25 Ω, I_c = 5.16 μA, and L/ξ = 6.6.

From Fig. 6.2(a), it is clear that the shunting of nanowires results in qualitative changes of the switching and retrapping processes. As the nanowire is shunted with lower values of the shunt resistance, the mean switching and retrapping currents increase while the width of the hysteresis decreases. Additionally, the retrapping current becomes stochastic, indicating the occurance of a PSC. In Fig. 6.2(b), the dependence of the maximum switching (inset) and mean retrapping current on the shunt resistance is shown for different nanowire samples: S1 (R_n = 1385 Ω, T_c = 4.607 K), S2 (R_n = 1434 Ω, T_c = 4.41 K), and S3 (R_n = 1696 Ω, T_c = 3.82 K). The mean switching current increases, at a lower rate than the retrapping current, and saturates for small values of the shunt resistance (see the insert of Fig. 6.2(b)) with a decreasing shunt resistance. Similarly, the retrapping current increases for all wires until it saturates at the switching current as value of the shunt resistance is decreased. As the switching and retrapping current coincide, the hysteresis disappears and the wire becomes overdamped. Nanowires with smaller T_c start showing this saturation behavior at higher shunt values. This saturation effect at low shunt values is a result of high damping (damping ~ R_s^{-1}), caused by the shunt, on the premature switching process, and it indicates that the depairing current is reached for these low values of the shunt.

As mentioned above, below some critical shunt value at a given temperature, the retrapping and switching current become equal and the hysteresis vanishes. For instance, for sample S1 at 1.8 K at a shunt value of 10 Ω., as in Fig. 6.2(a), the *V-I* curve becomes non-hysteretic as the retrapping and switching currents are equal and there is no abrupt switch into the resistive state. As the shunt value is lowered, the damping increases, which changes as ~ $1/R_s$ (since $Q = \omega_p RC$ and damping ~ $1/Q$). Thus, at some critical value of the shunt, the increased damping changes the system from an underdamped junction (with hysteresis) to an overdamped

junction (without hysteresis). In JJs, this transition occurs when $Q \approx 0.84$ [19]. The *V-I* curves showing the dynamics of an over damped system as a function of temperature were measured and can be seen in Fig. 6.3. To observe the *V-I* characteristics across the wire (V_w-I_w), the current through the nanowire can be calculated using Kirchhoff's current law for a parallel shunted element: $I_w = I - V/R_s$.

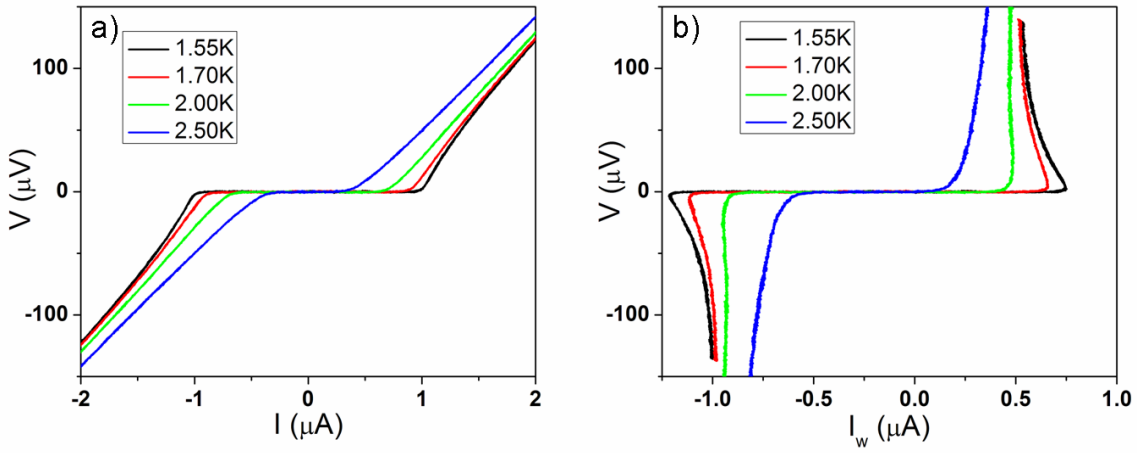

Fig. 6.3: (a) Voltage vs. current (V-I) graphs for a sample measured at various temperatures showing how the overdamped nanowire behaves as a function of temperature. (b). Voltage across the nanowire vs. current through just the nanowire (V_w-I_w) measured at various temperatures where the low temperature curves show a similar behavior to the V_w-I_w plots in [36] in the superconducting regime.

The resistively shunted junction (RSJ) model, which is updated with the specific nanowire CPR [52], can be used to fit the *V-I* curves of overdamped shunted nanowires. The fit to this model is shown in Fig. 6.2(c) (solid red line) for the case of sample S1 shunted with 10 Ω. The RSJ resistance, *R*, is interpreted to be the parallel combination of the shunt resistor and the resistance of the PSC. The thermal fluctuations were accounted for by including a random phase fluctuation with amplitude [53] $(2e/\hbar)/\sqrt{2k_B T R \tau}$, where *e* is the electronic charge, $\hbar$ is Plank's constant divided by 2π, k_B is Boltzman's constant, and τ is the time step of the numerical

integration. Following the Stewart-McCumber model, the fit to the *V-I* curve was calculated by numerically solving the following equation:

$$I = I_S + \frac{V}{R}, \tag{6.2}$$

where I is the total current and V is the voltage given by the Josephson relation [54, 55, 56], $V = (\hbar/2e)(d\phi/dt)$, where ϕ is the phase across the junction. The supercurrent, I_s, comes from the long nanowire $(L >> \xi)$ CPR [52]:

$$I_S(\phi) = \frac{3\sqrt{3}}{2} I_C \left[\frac{\phi}{L/\xi(T)} - \left(\frac{\phi}{L/\xi(T)} \right)^3 \right]. \tag{6.3}$$

Here, I_c is the depairing current of the nanowire. This supercurrent function is multivalued and is 2π periodic. Every time the current reaches the critical current, a phase slip of 2π occurs. In these fits, T, T_c, and L are known while R, I_c, and $\xi(0)$ are used as fitting parameters. For the fit that is presented in Fig. 6.2(c), the value of R used was 9.25 Ω, while the shunt was 10 Ω. This gives the resistance of the PSC to be about 123 Ω, which is roughly 10% of the value of the normal state resistance. The critical current of 5.16 μA obtained from the fit is ~ 70 nA greater than the current at which wire starts to have a resistance above the noise level thus suggesting an agreement between the model and experimental value of the critical current because of their close proximity. The fit also resulted in $L/\xi(T) = 6.6$, resulting in $\xi(0)$ = 12.4 nm which is within a factor of 2 of what the AL fit predicted from Eq. 6.1. This deviation is not really surprising since the fits to the *R-T* curves are based on the assumptions of the Ginzburg-Landau theory, which cannot be quantitatively correct at low temperatures, at which the *V-I* curves are

measured. Thus, we find good agreement between the overdamped *V-I* data and the Stewart-McCumber RSJ model. This indicates that the extension of the Stewart-McCumber RSJ model to shunted superconducting nanowires is reasonable and allows one to estimate the resistance of the PSC stabilized by resistively shunting the nanowire. The PSC shows quite anomalous properties compared to the usual case [3, 57]. In fact, if the effective normal resistance of the PSC is only 123 Ω, then the dissipative size is about 1/10 of the wire length. This small size is roughly equal to the coherence length and is much smaller than the electric field penetration depth, which gives the size of the PSCs in cases studied previously [3]. The anomalously low normal resistance of the PSC can be related to the fact that the PSC is observed at very low temperatures, while all previous studies have been done close to T_c. Further investigations are needed in order to understand the anomalously low resistance of the observed PSC.

When the nanowire is shunted with a ~ 25 Ω resistor or less, kinks in the voltage are also observed (they are marked by dashed line circles in Fig. 6.2(a) for the case where sample S1 is shunted by 25 Ω. The kinks for the 10 Ω shunting case are not shown, but occurs at higher current. This effect can be attributed to the effects of a shunt inductance in series with the shunt resistor. These kinks are not associated with resonance in the system because such a resonance would not depend on temperature as these do. Such inductive effects originate from the fact that the resistor used for shunting has dimensions of a few centimeters and so has a large inductance (~ 20 nH). Inductance connected in series with a shunt resistor is known to cause similar kinks in the *V-I* curves of shunted Josephson junctions due to a complicated dynamic of the phase difference on the junction [58]. Thus, the observation of such kinks confirms that the resistive state in our shunted wires is due to a phase-coherent PSC [3] and not due to Joule heating. Thus

we find an indication that by resistively shunting the nanowire it is possible to change the nature of its resistive state from a phase-incoherent JHNS to a phase-coherent PSC state.

6.5 Joule heating vs. coherent phase dynamics in the normal state probed via single and double nanowire(s)

Recent experiments with microwave radiation and switching events in unshunted wires suggest that the resistive state above the switching current, as shown in Fig. 6.2(a), is the normal state of the wire maintained due to Joule heating, i.e. the JHNS [39, 41, 59]. Wires that are fabricated on the surface of the substrate or are immersed in the liquid helium bath would more easily be able to transfer heat away through those mediums. In these recent experiments as well as in this paper, the nanowires were located in a low-pressure, thermalization helium gas and were fabricated using the molecular templating method resulting in suspended nanowires [46, 49]. Thus most of the heat generated from phase slips flow away through the ends of the wire and Joule heating is expected to be strong.

6.5.1 Joule heating vs. coherent phase dynamics phase diagram

Since Joule heating is involved for unshunted wires, the *V-I* curve is hysteretic and when the current is decreased below a critical retrapping current necessary to sustain the JHNS, the wire switches back to the superconducting state. In unshunted nanowires, retrapping always occurs at the same current, i.e. the transition is deterministic because the transition occurs from the normal

state characterized by a macroscopic number of degrees of freedom corresponding to normal electrons.

In Fig. 6.4, a phase diagram for sample S1 is presented which demonstrates the conditions necessary for the resistive state to be either the JHNS or a coherent phase dynamics state such as a PSC. The power at switching and retrapping is calculated by taking the product of the current through the wire and voltage across the wire, $P = I_w V$, at which the system exhibits switching and retrapping, respectively. Here, $I_w = I - V/R_s$, where I is the total current, which obeys Kirchoff's Law for current conservation ($I = I_{shunt} + I_w$, where $I_{shunt} = V/R_s$ is the current through the shunt). The critical power, P_c, is defined as the minimum power the wire can sustain and still remain in the JHNS and is calculated from the power that the unshunted nanowire exhibits at retrapping. For sample S1, P_c is calculated to be 0.533 nW from the unshunted curve in Fig. 6.2(a). At switching, the unshunted wire has 31 nW of heating, which puts it in the JHNS all the way until retrapping occurs.

With a shunt, the Joule heating power in the wire at switching is reduced, due to a lower equivalent resistance for the system. For example, when shunted with 75 Ω, the Joule heating power at switching is 0.359 nW (compared to 31 nW for the unshunted wire), which is lower than P_c. Thus, the wire switches to the PSC, which is a superconducting dynamic state (and not the normal state), and as the current is reduced, it remains in it until retrapping occurs. Because retrapping occurs from the phase coherent state, stochastic retrapping is expected for sample S1 when shunted with at least a 75 Ω resistor or less. Some heating is also to be expected since the power at retrapping is still comparable to P_c.

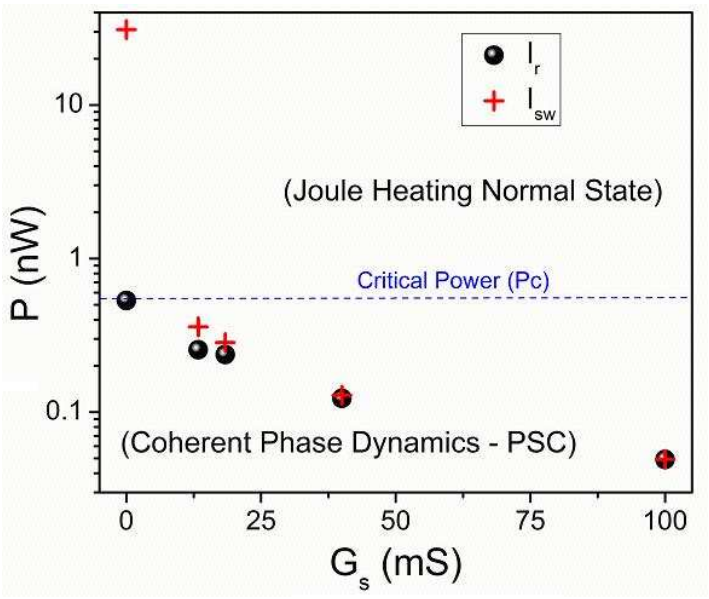

Fig. 6.4: Log-linear plot of average power dissipated in the nanowire immediately after a switching event (crosses) and just before retrapping (circles), plotted versus the shunting conductance (=1/R_s). Above a critical power, P_c, the resistive state of the nanowire is the JHNS while below P_c, the resistive state originates from a coherent phase dynamics. The power is calculated by taking the voltage across the wire times the current through the wire ($P = I_w V_w$) at the retrapping and switching current in the resistive branch of the V-I curve from Fig. 6.2(a).

6.5.2 Response of a resistively shunted double nanowire pair to a small applied magnetic field

So far, we have been able to probe the emergence of a phase coherent state in a shunted superconducting nanowire primarily by analyzing the properties of the retrapping current such as a stochastic distribution and the power of the unshunted wire at the retrapping events. To further probe the existence of phase coherence in the normal state of a highly shunted nanowire, double nanowire devices were fabricated such that there are two nanowires in parallel that bridge the trench, and are separated by some distance *a*. When such a sample is threaded with a small perpendicular magnetic field, oscillations in the resistance and the switching current of the device is observed, while the retrapping current remains at a constant mean value. This effect is different from the typical Little-Parks [60. 61] effect as leads in our sample are themselves

mesoscopic—i.e., have widths smaller than the perpendicular penetration depth λ. In such cases, it can be shown [62, 63] that the magnetic-field periodicity of the properties of the system as a whole is largely set by screening currents *in the leads*, which do not depend on the length *b* of the wires. Thus, e.g., if the width *l* of the leads is much greater than *a*, the effective periodicity of the physical properties of the wires for small fields is given not by $\Delta B = \Phi_0 / ab$, but by $\Delta B = \Phi_0 / c_1 al$, where c_1 is a geometry-dependent number of order unity. At stronger magnetic fields, vortices enter the leads, and the periodicity changes.

In the unshunted nanowire case, the switching current shows an oscillation, which matches the predicted magnetic field period. We measured a sample where the wires are separated by ~ 650 nm and the width of the leads are ~ 20 μm wide. In this geometry, the predicted magnetic field period is ~ 160 μT and the measured period is ~ 240 μT (see Fig. 6.5). The discrepancy between the theoretical value and the measured value can be due to a small tilt of the sample, over-etching of the lead width, and the geometric parameter c_1. It can be noticed from Fig. 6.5(a), that while the switching current shows an oscillation, the mean retrapping current is constant as a function of magnetic field. This phenomena can be explained by an understanding of the nature of the normal state in unshunted nanowires. When the unshunted nanowires switch into the normal state, Joule heating occurs and is preserved [40, 41, 42], while the phase coherence is lost, as the nanowires remain above their critical superconducting temperature until the current is reduced and the wire cools below T_c. We can treat the nanowires in the short, Josephson junction limit, where the energy barrier for vortex movement (phase slips) across the nanowires is given by [62]:

$$\Delta F = \frac{\sqrt{6}\hbar}{2e}\sqrt{(I_{c1}+I_{c2})^2\cos^2\left(\frac{\delta}{2}\right)+(I_{c1}-I_{c2})^2\sin^2\left(\frac{\delta}{2}\right)}, \qquad (6.4)$$

where I_{c1} and I_{c2} are the critical currents of each nanowire and δ is the phase gain in one lead induced by the magnetic field. Thus, during the process of retrapping, the nanowires switches from the JHNS where there is no superconducting free energy barrier since the wires are not superconducting. However, for the switching process, phase coherence is present and the free energy barrier given by Eq. 6.4 is modulated, thus resulting in an oscillation of the switching current.

When the nanowires are sufficiently shunted, both the switching and the retrapping currents as well as the resistance show an oscillation with magnetic field (see Fig. 6.5(b) and the inset of Fig. 6.5(a)). The phase between the oscillation of the switching and retrapping current is zero, as it is with a Josephson junction with an applied perpendicular magnetic field [3]. The switching current shows an oscillation with an applied magnetic field for the same reasons as discussed above for the case of the unshunted nanowires. The oscillation of the retrapping current is only possible because the state that the nanowires retrap from is not the JHNS, but rather it is a phase coherent state where superconductivity is preserved. In this situation, the free energy barrier given by Eq. 6.4 remains valid in the normal state and the nanowires retrap when the dissipation energy becomes equal to the input energy from the current source. The current at which this occurs oscillates as a function of the magnetic field due to the free energy barrier, and thus the retrapping current is observed to oscillate with the same period observed for the switching current oscillations.

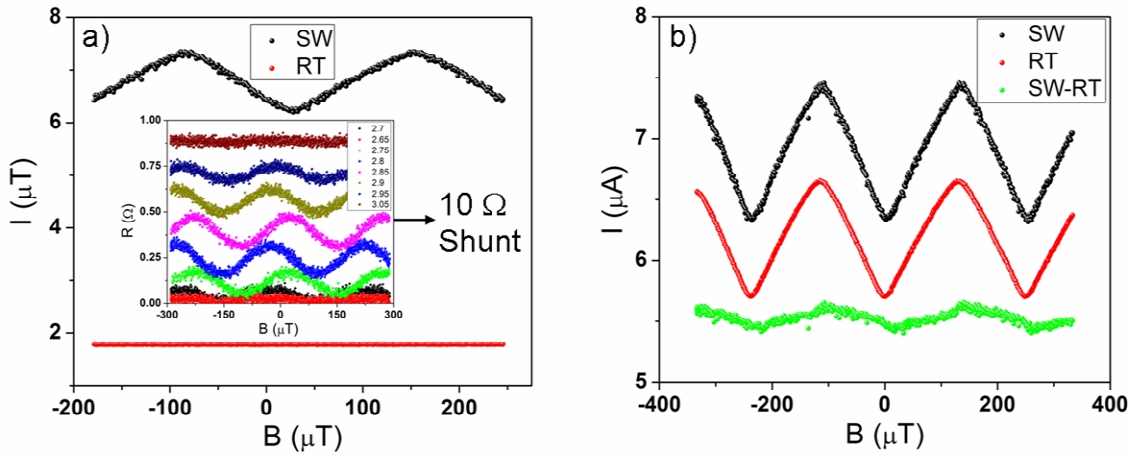

Fig. 6.5: (a) The switching and retrapping currents of the unshunted nanowires as a function of applied magnetic field. Only the switching current shows an oscillation. Inset: The resistance vs. magnetic field for the case where the nanowires are shunted by 10 Ω. (b) The switching and retrapping currents (as well as their difference (green data)) vs. magnetic field for the case where the nanowires are shunted by a 10 Ω resistor. Both the switching and retrapping currents show an oscillation suggesting that phase coherence is preserved in the normal state. All curves were taken at ~ 300 mK.

Before closing out this section, a quick discussion of the effects on the switching and retrapping currents will be made for the case of a single nanowire subjected to larger magnetic fields (up to 9 T). It was demonstrated [64], that magnetic fields can suppress the pair breaking effects of magnetic moments located on the surface of our nanowires and cause an increase in the switching current, especially in thinner wires. While the enhancement of the switching current with high magnetic fields has been studied, the effect on the retrapping current and the switching and retrapping currents in shunted nanowires has not been investigated. In the inset of Fig. 6.6, the retrapping current is plotted as a function of magnetic field. An increase in the mean value of the retrapping current is observed up to magnetic fields of ~ 1.25 T. The same enhancement of the switching and retrapping current is observed for the same sample shunted by a resistor with a value of 100 Ω (see Fig. 6.6), except that the fields where the maximum enhancement occurs is at a higher value of the magnetic field. This phenomena remains unexplained and may be due to

the shifting of magnetic moments due to thermal cycling between measuring the nanowire with and without the shunt.

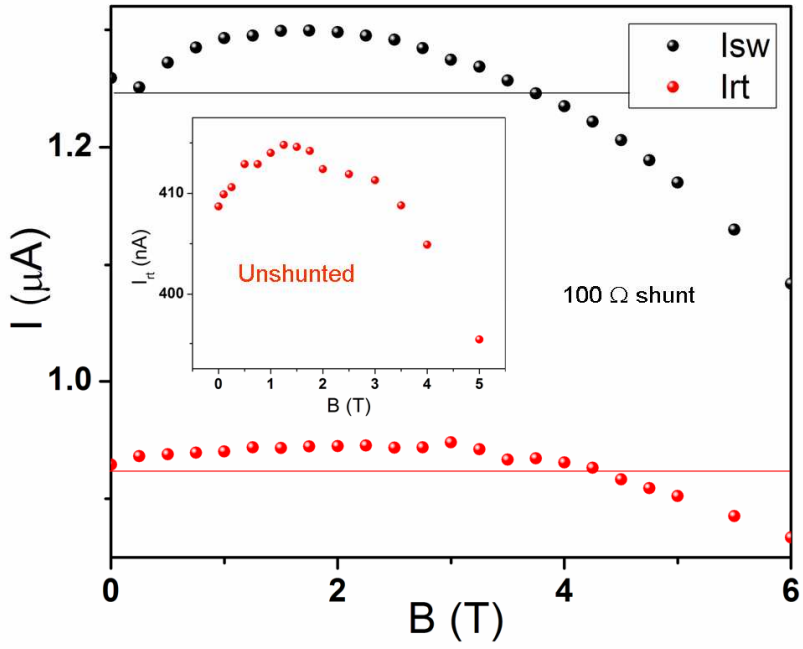

Fig. 6.6: (a) The mean switching and retrapping currents as a function of magneticl field. An enhancement of both quantities is observed. Inset: the mean retrapping current as a function of magnetic field for the nanowire with no shunt.

6.6 Resistively and capacitively shunted junction with an externally applied shunt

To characterize the *V-I* curves obtained in the experiment for the superconducting nanowire we use the Stewart-McCumber model (see Fig. 6.7(a)) which was originally introduced for superconducting Josephson junctions analogous to the driven damped pendulum to study dc *V-I* curves displaying hysteresis for light damping [1, 2]. They consider only the time varying phase difference $\phi(t)$ of the superconducting wave-functions in the weakly coupled superconductors

and neglect any spatial variations of the superconducting wave-functions. The displacement current and "normal" losses (e.g. quasiparticle tunnel currents) are included in the model by the shunting capacitance C and the resistance R_J, respectively. We also include a noise current source I_n associated with the resistance R_J along with the drive current source I [65, 66]. Then applying the usual Josephson dc and ac relations for the current-phase and the voltage-phase relationships given by:

$$I_J = I_0 \sin\phi \tag{6.5}$$

$$\frac{d\phi}{dt} = \frac{2eV}{\hbar}, \tag{6.6}$$

(where I_0 is the critical supercurrent through the junction) we find the equation of motion for ϕ in the circuit in Fig. 6.7(a):

$$\frac{\hbar C}{2e}\frac{d^2\phi}{dt^2} + \frac{\hbar}{2eR_J}\frac{d\phi}{dt} + I_0 \sin\phi = I + I_n, \tag{6.7}$$

along with the Gaussian white noise properties:

$$\langle I_n(t) \rangle = 0 \tag{6.8}$$

$$\langle I_n(t_1) I_n(t_2) \rangle = \frac{2k_B T_J}{R_J}\delta(t_1 - t_2), \tag{6.9}$$

where T_J is the temperature of the JJ and $\langle\ \rangle$ denotes averaging over noise realizations (noise ensemble). The temperature T_J (or $k_B T_J$ where k_B is the Boltzmann constant) can be conceived as the dissipation/losses associated with the quasi-particle tunneling through the junction. The

equation of motion (Eq. 6.7) for the junction phase can be rewritten in terms of dimensionless parameters as

$$Q_0^2 \frac{d^2\phi}{dt'^2} + \frac{d\phi}{dt'} + \sin\phi = i + i_n, \tag{6.10}$$

where $Q_0 = \sqrt{2eI_0R_J^2C/\hbar}$ is the quality factor (inverse of the damping strength) of the linearized equation of motion, $i = I/I_0$ is the normalized dc bias current, $i_n = I_n/I_0$ is the normalized noise current, and $t' = (2eI_0R_J/\hbar)t$ is the normalized time. The equation of motion 6.10 of the JJ is similar to that of a damped oscillator/pendulum (of mass Q_0^2) driven by an external force *i*. The term $d\phi/dt'$ is damping as it breaks the time-reversibility of the equation and introduces dissipation. In this notation, the steady-state junction time-averaged voltage is $V = I_0R_J\langle d\phi/dt'\rangle_{t'}$ and the noise autocorrelation is given by:

$$\langle i_n(t_1')i_n(t_2')\rangle = \frac{2k_BT_J}{E_J}\delta(t_1' - t_2'), \tag{6.11}$$

where the Josephson coupling energy is given as $E_J = \hbar I_0/2e$.

In the absence of thermal noise at zero temperature (also neglecting quantum fluctuations), the zero-voltage state or 0 state is stable at all bias levels less than the fluctuation free critical current ($|i| < 1$), and the voltage state or 1 state is stable at all bias levels greater than a minimum value designated by a fluctuation free retrapping/return current i_{r0}. The value of $i_{r0}(\equiv I_{r0}/I_0)$ is determined entirely by the quality factor Q_0 and decreases with increasing Q_0 as a smaller tilt is sufficient to support the running (finite voltage) state when damping is less. For

$Q_0 < 0.8382$, the damping is sufficient that a running state is not possible unless the potential decreases monotonically and in this case $i_{r0} = 1$. For $Q_0 > 0.8382$, a running state is possible even when the potential has a local minima [67]. In this case $i_{r0} < 1$ and the *I-V* curve is hysteretic. In the limit of large Q_0, $i_{r0} = 4i_0/\pi Q_0$ $(Q_0 > 3)$ [1, 67].

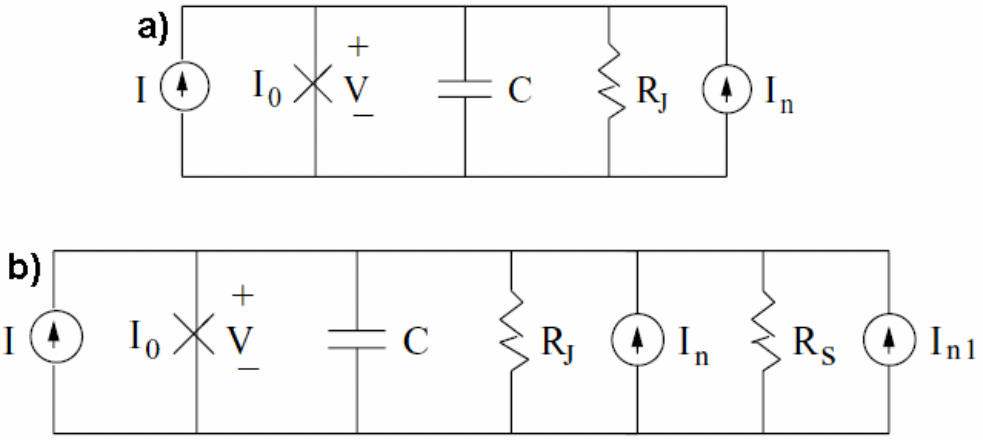

Fig. 6.7: (a) Circuit of the resistively and capacitively shunted Joseph junction (RCSJ) model with the current noise from the resistance included. (b)The circuits of the RCSJ model with an external shunt resistance R_S and current noise I_{n1} included.

The phase dynamics described in Eq. 6.10 can be visualized as the damped motion of a Brownian particle with mass Q_0^2 in the washboard potential $U(\phi) = -(i\phi + \cos\phi)$. In the under-damped regime $Q_0 > 1$, the zero-voltage state and the resistive state correspond to the particle trapped by the energy barrier ΔU and running downward along the tilted potential. Escape from the potential (0 state to 1 state) can occur even for $i < 1$ due to the thermal and the quantum fluctuations.

Next we extend the RCSJ model with an external normal resistance R_S and current noise i_{n1} for the present experimental setup of a shunted nanowire (Fig. 6.7(b)). In this situation, the reduced equation of motion for the phase difference is given by:

$$Q_0^2 \frac{d^2\phi}{dt'^2} + \left(1 + \frac{R_J}{R_S}\right)\frac{d\phi}{dt'} + \sin\phi = i + i_n + i_{n1}, \tag{6.12}$$

where

$$\langle i_{n1}(t_1')\rangle = 0 \tag{6.13}$$

$$\langle i_{n1}(t_1')i_{n1}(t_2')\rangle = \frac{2k_BT_S}{E_J}\frac{R_J}{R_S}\delta(t_1' - t_2'), \tag{6.14}$$

where T_S is the temperature of the shunt resistance R_S. Now if we assume that there is no significant MQT at the temperatures (1.8 K) where the distributions for I_{sw} and I_r are measured, then the distributions are due to the thermal fluctuations.

One can write Eq. 6.12 in a little different from as

$$Q^2 \frac{d^2\phi}{dt'^2} + \frac{d\phi}{dt'} + \sin\phi = i + i_n + i_{n1}, \tag{6.15}$$

where $Q = \sqrt{2eI_0R_T^2C/\hbar}$ and $1/R_T = 1/R_J + 1/R_S$ are respectively the quality factor and the resistance of the full circuit. But the above form in Eq. 6.12 is more useful in simulation.

Now we simulate Eqs. 6.10 and 6.12 and for $T_J = T_S = T_{electrode}$ to calculate the current-voltage characteristics of the RCSJ model for the unshunted and shunted junction/wire in the presence of the current noises from the normal resistances. In the experiment, one changes the bias current with a finite current sweep rate, and measures the corresponding voltages. In the simulation, instead we first fix a bias current, then integrate the above equations of motion (with suitable initial condiaitons and current noises) for a sufficiently long time (this time is the

relaxation time or the transient time), and next calculate the time-averaged voltage by averaging $d\phi/dt'$ over some time interval. For forward current sweep we choose the initial conditions, $\phi(t'=0)=0$ and $\frac{d\phi}{dt'}(t'=0)=0$; and for the backward current sweep we use $\phi(t'=0)\neq 0$ and $\frac{d\phi}{dt'}(t'=0)\neq 0$. We generate the Gaussian white noises i_n and i_{n1} at each time step of the simulation satisfying the noise properties in Eqs. 6.11 and 6.14 following the method described in [68]. The current-voltage characteristics are plotted in Fig. 6.8 for the unshunted junction/wire and the shunted junction with different ratios of the normal resistance of the junction and the shunt resistance. As can be seen from Eqs. 6.10 and 6.12, we really don't need explicit values of the resistances, but we only need the ratios of the two resistances and a quality factor. We choose a quality factor which will show a large hysteresis for the unshunted junction/wire as seen in the experiment. However, we do not expect that the simulation results for the unshunted nanowire should match well to the experimental observations since the switching and retrapping mechanisms in the unshunted nanowire is dominated by overheating [40, 41, 42] and does not involve a coherent phase dynamics. We have also checked that for the quality factor $Q_0 = 7$, the transition from hysteretic behavior to non-hysteretic occurs near the ratio $R_J : R_S = 4:1$.

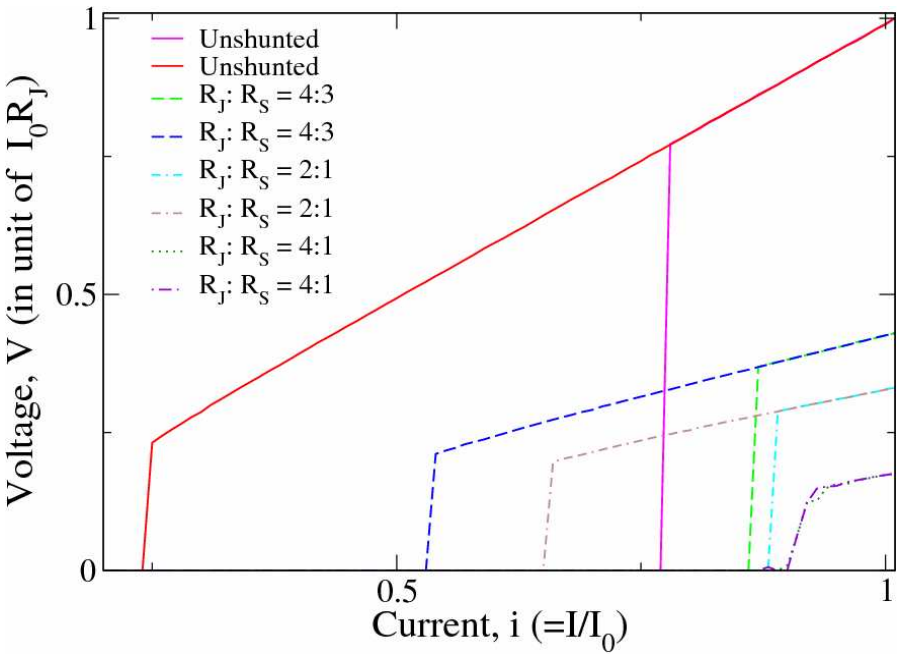

Fig. 6.8: Current-(time-averaged) voltage characteristics of the RCSJ model with an external shunt resistance and current noise. The quality factor used was $Q_0 = 7$ while the temperature used was $T_J = T_S = T_{electrode} = 0.01E_J$. This plot is simulated with a long dwell time (transient time) to obtain a better averaged value for the switching and retrapping currents. This simulation was calculated by R. Dibyendu at the University of Cincinnati.

6.7 Switching and retrapping distributions

In Fig. 6.9(a), switching distributions and the corresponding rates vs. current for sample S1 are plotted. Shunting the nanowire with lower values of the shunt resistance has the effect of narrowing the width, increasing the height, and shifting the distribution to higher currents. The full width of the distribution at half maximum (FWHM) changed from 100 nA to 12 nA due to shunting with a 25 Ω resistor at the same temperature. The asymmetric shape in the distribution for larger shunts changed to a rather symmetric shape with lower shunts. These features indicate that nanowires shunted with smaller resistance results in higher damping as is the case in JJs [21].

The retrapping current shows a dramatic change from deterministic values to stochastic values when shunted with 75 Ω or less. From Fig. 6.4, it is clear that the nature of the resistive state that the nanowire experiences retrapping from can change from the JHNS to a phase coherent state with the inclusion of the shunt resistor. In Fig. 6.9(c), the typical retrapping histogram is plotted for the same wire that in one case is unshunted and in the other case is shunted. The standard deviation of the retrapping current in the unshunted configuration is 1.12 nA, which is the noise limit of our experimental setup. So, this small distribution of retrapping currents is just due to the noise and the point spacing in the current and can be reduced by decreasing the noise and the spacing in between bias-current points. However, when the wire is shunted to drive its resistive state out of the JHNS, a retrapping distribution is observed, with its width being much larger than the experimental setup noise and independent of the bias-current spacing, in this configuration the standard deviation was measured to be 6.3 nA.

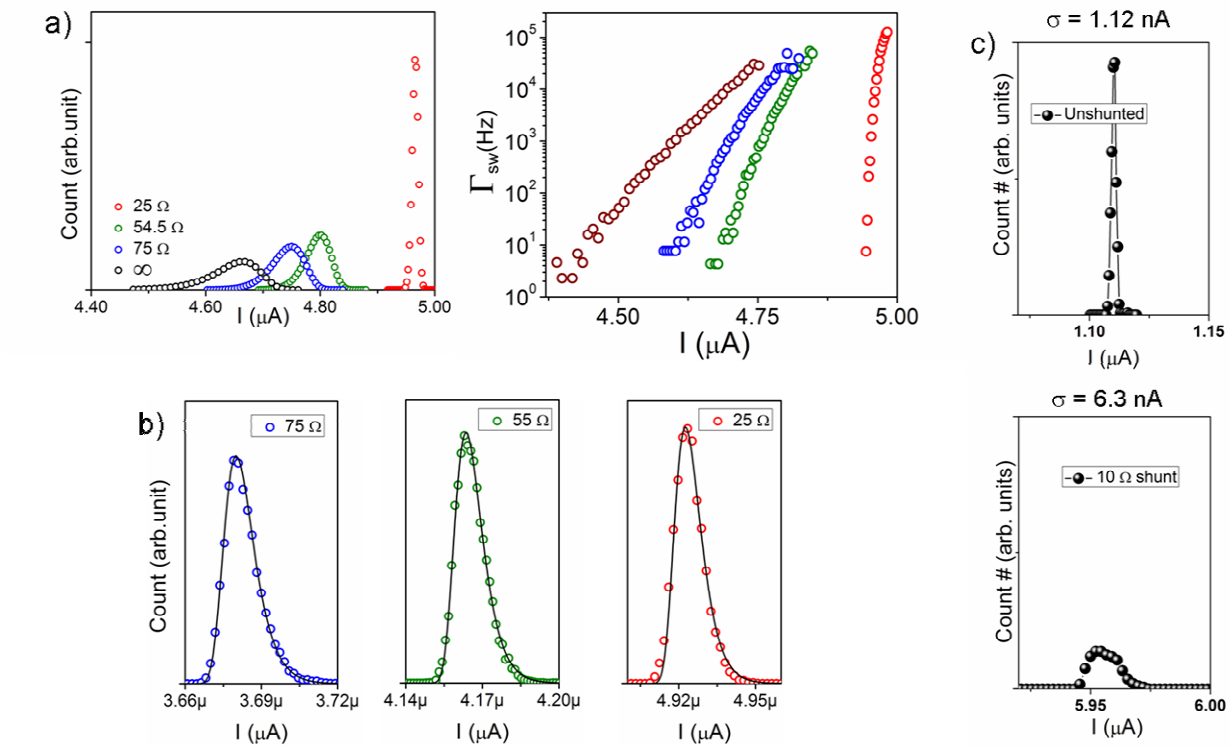

Fig. 6.9: (a) Switching distributions and rates (transformed using the Fulton and Dunkleberger equation [69]). vs. bias current for sample S1 shunted with various R_s values at 1.8 K. All distributions were measured with a sinusoidal current sweep with f = 8 Hz and amplitude of 6.1 μA. Inset: (b) Retrapping distributions vs. I for sample S1 shunted with various R_s values. Solid lines are fits to the retrapping theory of Ben-Jacob et al. from Eq. 6.16 [15] and converted to a distribution using the Fulton-Dunkleberger equations [69]. The fits resulted in I_{ro} = 3.502, 4.004, 4.769 μA and Z(ω)=1200, 1330, 1385 Ω for the case of R_s=75, 54.5, 25 Ω. The mean and standard deviation of the retrapping data are: 3.683, 4.166, 4.925 μA and 7.304, 6.089, and 5.799 nA, respectively. (c) (top panel) Typical retrapping histogram vs. I for the case where the nanowire is unshunted. (bottom panel) The typical retrapping histogram vs. I for a shunted nanowire. The standard deviation in the unshunted sample is about equal to the minimum point separation and thus occurs due to an experimental limitation.

In Fig. 6.9(b), the retrapping current distributions for sample S1 are shown for the nanowire with various resistive shunts. The width of the distribution is slightly sensitive to the value of shunt resistance, but the mean value of the retrapping current changes considerably. It is not surprising that the mean value of the retrapping current is so sensitive to the value of the shunt resistance since for a JJ, the value of the fluctuation free retrapping current, $I_{r0} \sim R^{-1}$.

When shunted with 75 Ω for instance, the standard deviation of the retrapping current increases above the experimental setup noise to 7.3 nA (from ~ 1 nA for the unshunted case under the same conditions). The retrapping current distributions for the shunted nanowire are also asymmetric, suggesting that there is a definite noise-free retrapping current, I_{r0}, where the system is retrapped into the superconducting state. This feature stands in contrast to the retrapping distribution for the unshunted case, as shown in Fig. 6.9(c), where the "distribution" is symmetric.

The retrapping process from a PSC to a zero-voltage state in a nanowire can be explained by the tilted washboard potential model, which has been used to describe the electrodynamics in JJs [3]. Fits to the measured retrapping distributions can be obtained using the theory of retrapping due to by Ben-Jacob *et al.* [15]. This theory is derived for JJs, which are strongly underdamped, and predicts that the rate of retrapping, Γ_r, is given by:

$$\Gamma_{RT} = (I - I_{ro})\sqrt{\frac{1}{\pi C k_B T}}\exp\left(-\frac{(I - I_{ro})R^2 C}{k_B T}\right), \qquad (6.16)$$

where I is the bias current, I_{ro} is the fluctuation free retrapping current, C_j is the capacitance of the junction, and $Z(\omega)$ is the real part of the frequency dependant impedance of the environment [16]. The retrapping rate in Eq. 6.16 can be transformed into a retrapping distribution by the Fulton-Dunkleberger approach [69] and fit to the data, as is shown in Fig. 6.9(b) as solid lines.

Many experiments in JJs have found that the electromagnetic environment plays a large role in the retrapping process [16, 70], and that the damping experienced in the retrapping process is dominated by the low frequency components of the environment. The effective

resistance in this limit is approximately equal to the junction resistance. In this experiment the precise value of the impedance of the electromagnetic environment, $Z(\omega)$, and C_j are unknown. Therefore, C_j was set such that $Z(\omega)$ matched the nanowires' normal state resistance in the limiting case. In the case of sample S1, this occurred when $C_j = 8.5$ fF, which is consistent with the range of capacitances expected for our electrode geometry [71]. The fitting parameters used for each fit were $Z(\omega)$ and I_{ro}. In each fit, I_{ro} was ≈ 175 nA lower than the experimentally measured mean retrapping current and $Z(\omega)$ was close the normal state resistance. As higher shunt values are used, a slight deviation from the normal state resistance is observed in the fitting parameter $Z(\omega)$. This occurs because the retrapping distributions become slightly wider with higher shunt values, which can be understood in terms of the phase diagram presented in Fig. 6.4. When higher shunt values are used, there is more heating in the wire. Even with the resistive state of the nanowire being in a phase coherent state, the shunt is observed to control the amount of heat generated in the wire. With more heat, the distribution of the retrapping currents is wider [3, 15]. Overall, by resistively shunting the nanowire, the retrapping current becomes stochastic and can be modeled by a theory of retrapping developed for underdamped JJs. Another set of switching distributions and rates for various shunt values are displayed in Fig. 6.10 along with a retrapping distribution for the sample S2 shunted with a 25 Ω resistor. Similar behavior as discussed above is observed. Additionally, the switching current can be increased and driven towards the depairing current.

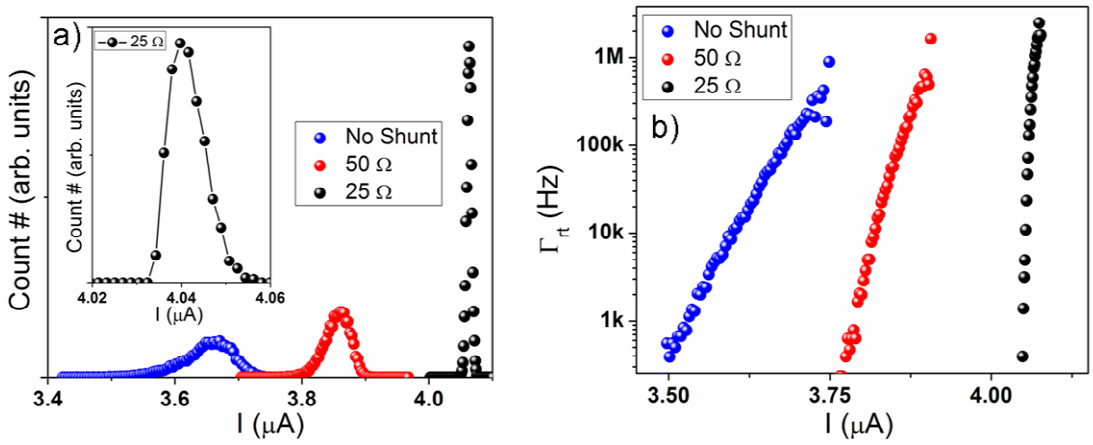

Fig. 6.10: (a) Switching distributions vs. bias current for sample S2 shunted with various R_s values at 1.5 K. Inset: Retrapping distribution vs. I for sample S2 shunted with various R_s = 25 Ω showing a distribution similar to those observed for sample S1. (b) Switching rates vs. bias current for sample S2 shunted with various R_s values at 1.5 K.

The switching and retrapping behavior measured in Figs. 6.9 and 6.10 can be simulated using the model presented in section 6.6. The quality factor was chosen to be $Q_0 = 7$ and the temperatures were initially set to $T_J = T_S = T_{electrode} = 0.01E_J$ to match the model parameters used to simulate the *V-I* curves in Fig. 6.8. The ratio of the junction resistance R_J to the shunt resistance R_S was then adjusted to various values to simulate the effect of changing the shunt resistance in the experiment. In Fig. 6.11(a), the switching distributions are shown for different ratios of resistances. However, due to heating, the temperature in the unshunted sample is expected to be much larger and thus in the right panel, the switching distributions are shown where the temperature of the unshunted samples is increased. In the simulations, as the shunt resistance is decreased in value, the mean switching current increases and the distributions become narrow, as is observed in the experiment. The retrapping current distributions are also simulated and displayed in Fig. 6.11(b). As the shunt value is decreased the mean retrapping current in the simulations increases, however the width of the distributions is observed also to

increase where in the experiment they remain almost constant. Some residual heating is expected to remain even in the shunted samples and when the temperature is increased, the retrapping current becomes wider. The temperature for higher shunt values is expected to be slightly higher and when this heating effect is accounted for, the distributions can be driven to roughly the same height as observed in the experiment. Thus, the simulated switching and retrapping distributions qualitatively show the same behavior as is observed in the experiment with the addition of slight heating in higher shunt values. This agreement suggests that the normal state in shunted superconducting nanowires is phase coherent and that shunting has the effect of increased damping on the phase dynamics.

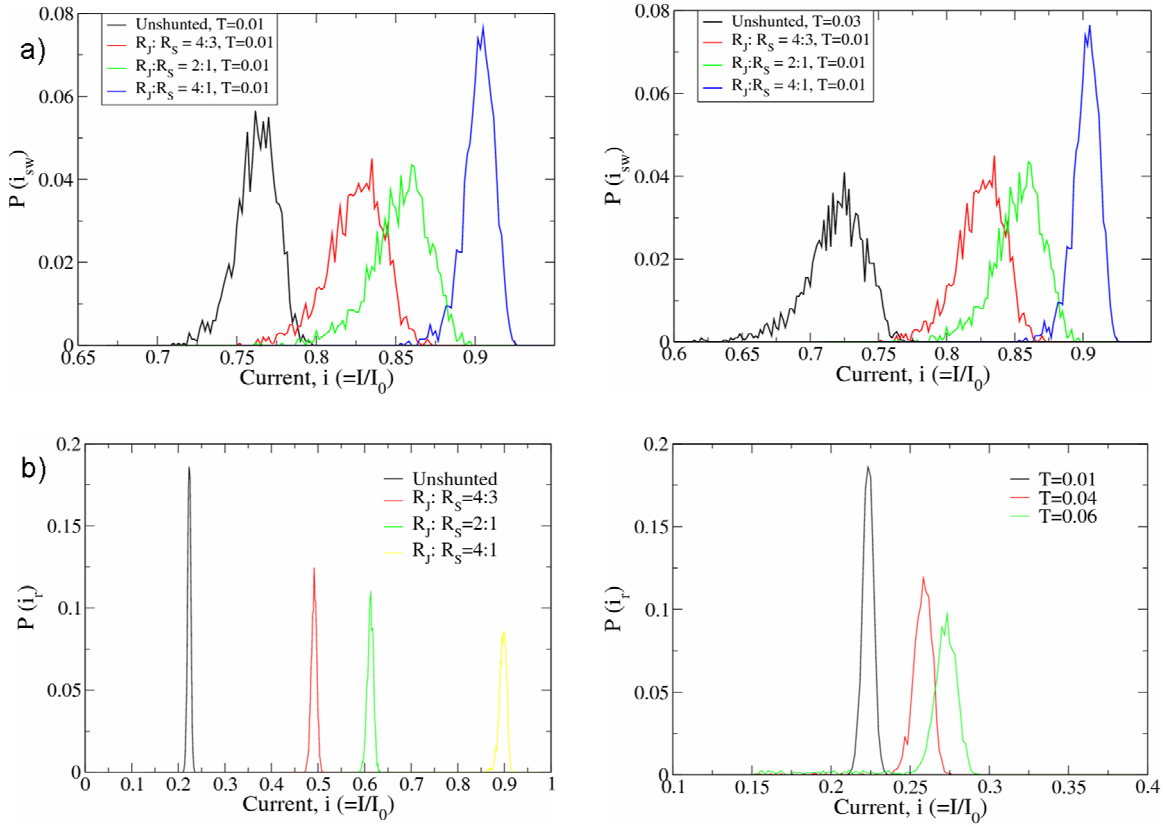

Fig. 6.11: (a) (Left panel) Simulated switching distributions for different values of R_S. (Right panel) Simulated switching distributions for different values of R_S and a higher temperature for the unshunted sample. (b) (Left panel) Simulated retrapping distributions for different values of R_S. (Right panel) Simulated retrapping distributions for the unshunted sample at various temperatures. The quality factor $Q_0 = 7$ was used for all fits. These simulations were calculated by R. Dibyendu at the University of Cincinnati.

6.8 Damping of macroscopic quantum tunneling

The switching mechanism out of the superconducting state can be due to thermal activation over the energy barrier or quantum tunneling through the barrier. Dissipation, which is controlled by the resistance, is expected to damp QPS but not TAPS. In this section, we measure a superconducting nanowire with and without the presence of a shunt and compare the standard deviation of the switching currents as a function of temperature (see Fig. 6.12). We also briefly look at the behavior of the standard deviation of the retrapping current as a function of temperature for the shunted wire.

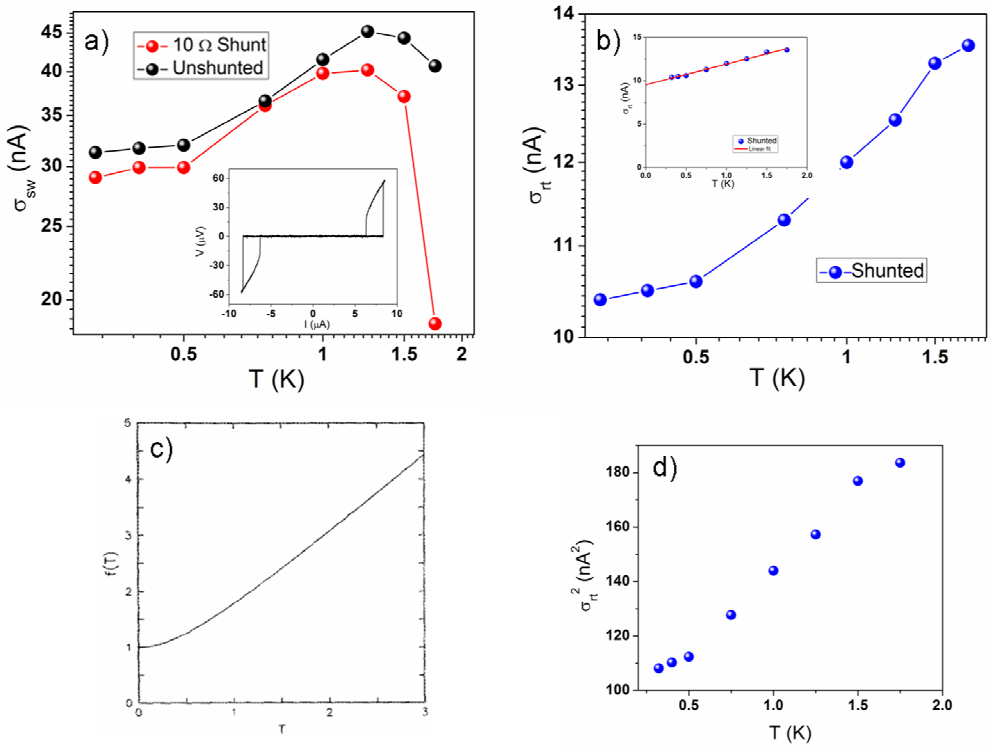

Fig. 6.12: (a) The standard deviation of the switching current for the unshunted and shunted nanowire. Three regimes are observed at different temperatures. Inset: V-I curve of the shunted nanowire sample at 320 mk. (b) The standard deviation of the retrapping current as a function of temperature for the nanowire shunted with 10 Ω plotted in a log-log scale. Inset: Same as in (b) but in a linear-linear scale and linearly extrapolated to zero temperature (red line). (c) The temperature dependence of the square of the standard deviation of the retrapping current taken from ref [72]. (d) The same data from (b) except plotted as the square of the standard deviation vs. temperature in a linear-linear scale.

At higher temperatures, the standard deviation of the switching current increases as the temperature is decreased. When the nanowire is not shunted, this regime can be understood by the overheating model where the heat generated by each phase slip causes an increase in the probability of another phase slip occurring. At some point, a phase slip runaway process occurs and the nanowire overheats [40, 41, 42]. This multiple phase slip switching mechanism has been observed to lead to the trend in the standard deviation discussed above [41]. For the strongly shunted nanowire, the JHNS is replaced by a phase coherent state and the observed regime at higher temperatures where the standard deviation of the switching current increases as the temperature is reduced is due to a multiple retrapping process. Similar to the JHNS, multiple phase slip events must occur before the wire switches to the normal state [19, 20, 21]. The temperature T^*, where the multiple retrapping mechanism switches on, is expected to be a function of the shunt resistance where T^* decreases as the shunt resistor value is decreased. The next regime noticed (between ~ 0.5-1.25 K) is a regime where a single thermally activated phase slip is enough to switch the wire to the normal state [19, 21]. At even lower temperatures (below 500 mK), a saturation in the standard deviation is observed. The regime where the standard deviation becomes independent of the temperature is a property of QPS [13]. In the presence of dissipation, Caldeira and Leggett [10] were able to show that the rate of MQT would be damped. In Fig. 6.12(a), it is clear that the rate of QPS is damped when it is compared to the unshunted case since the standard deviation of the switching current is significantly lower in the shunted case. The lower standard deviation in the shunted sample cannot be accounted for by multiple retrapping because even at higher temperatures in the single TAPS regime, the multiple retrapping mechanism was not observed as the retrapping current became sufficiently distanced in current from the switching current (see the inset of Fig. 6.12(a)). It would be important in

future experiments to apply smaller valued shunt resistors and observe how both T^* and T_{QPS} (the temperature at which QPS sets in) change as a function of temperature. The value of T_{QPS} is expected to be a function of dissipation [19], and follows the following relationship:

$$T_{QPS} = \frac{\hbar\omega_p}{2\pi k_B}\left[\sqrt{1+\frac{1}{4Q^2}}-\frac{1}{2Q}\right]. \qquad (6.17)$$

The standard deviation of the retrapping current was also measured and was observed to decrease as the temperature was decreased until it saturated at lower temperatures as can be seen in Fig. 6.12(b). The decrease in the standard deviation as the temperature is lowered is consistent with a thermal model where the standard deviation decreases as thermal fluctuations are reduced, but the saturation at lower temperatures cannot be understood as a thermal effect. The inset of Fig. 6.12(b) shows the behavior of the standard deviation of the retrapping current as a function of temperature in a linear-linear scale showing that the linear extrapolated curve does not pass through zero at zero temperature thus indicating the presence of QPS. A quantum retrapping model has been proposed [72] in which it has been theoretically predicted that the square of the standard deviation of the retrapping currents should behave according to $A\mu f(T)$, where $f(T)$ is a function of temperature, A is a constant of order unity, and μ is defined as $\hbar\omega_p / I_c\Phi_0$. The function $f(T)$ is plotted in Fig. 6.12(c) while the data is shown in Fig. 6.12(d). The temperature dependence of the theory and data seem to be qualitatively similar indicating that at low temperatures the shunted nanowires experience quantum retrapping. In both the switching and retrapping current measurements, quantum effects do not appear to dominate until ~ 500 mK. Under certain conditions it is predicted by the quantum retrapping model [72] that

the crossover temperature may actually be higher in the retrapping, which is a result of the difference in the plasma frequencies at high and low bias currents.

6.9 Critical current and the Bardeen formula

To check the proximity of the switching current to the depairing current, we measured the switching current as a function of temperature for various samples and compared it with Bardeen's prediction for the temperature dependence of the depairing current. In Fig. 6.13(a), the mean I_{sw} vs. T for sample S1 shunted with 5 Ω and sample S4 shunted with 10 Ω is presented while in Fig. 6.13(b), a continuous distribution of I_{sw} as a function of temperature is presented for sample S5 shunted with a 30 Ω resistor and unshunted. As the temperature is reduced, the switching current for all samples increases and begins to show signs of saturation below ~1 K. The behavior of I_{sw} vs. T in the continuous distribution measurement of sample S5 is similar to samples S1 and S4 where the mean I_{sw} is plotted vs. T as in Fig. 6.13(a), but now the difference in the fluctuation of I_{sw} for the shunted and unshunted nanowire is apparent.

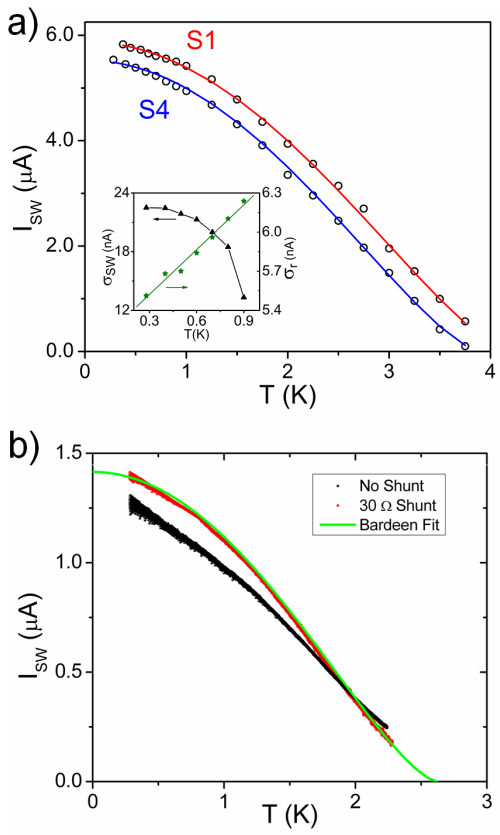

Fig. 6.13: (a) Mean I_{sw} vs. T for samples S1 and S4 shunted with 5 Ω and 10 Ω respectively. The solid lines are fits to the Bardeen prediction (Eq. 6.18) for the temperature dependence of the depairing current, I_c. The fitting parameters used are: $I_c(0)$ = 5.88, 5.53 μA and T_c = 4.2, 3.9 K for samples S1 and S4, respectively. Inset: Standard deviation ($\sigma = \sqrt{\sum_{i=1}^{n}(I_i - \langle I \rangle)^2 / n-1}$) vs. T for the switching and retrapping events of sample S4 shunted with 10 Ω, where for each point σ was calculated using data sets of 10000 points. (b) Distribution of I_{sw} vs. T for sample S5 unshunted (red) and shunted with 30 Ω (black). Each curve contains approximately 20,000 points. The corresponding fit to the Bardeen prediction (green) is presented for the shunted wire. Here $I_c(0)$ = 1.415 μA and T_c = 2.62 K.

In Fig. 6.13 Bardeen's prediction [45] for the temperature dependence of the fluctuation free critical depairing current derived from BCS theory is compared to the temperature dependence of the measured switching current for samples with various small shunts and is given by:

$$I_c(T) = I_c(0)\left[1-\left(\frac{T}{T_c}\right)^2\right]^{3/2}, \qquad (6.18)$$

here $I_c(0)$ is the critical current at zero temperature. Excellent agreement is found, suggesting that the strong dissipation provided by the shunt has driven the switching current very near to the depairing current.

In these fits, T is known while $I_c(0)$ and T_c are used as fitting parameters. Close agreement is found between the theoretical prediction for the depairing current at zero temperature: $I_c(0) = 92\mu A L T_c / R_N \xi(0)$ [51], which is derived from BCS and Ginzberg-Landau theory, and the value of $I_c(0)$ used in the Bardeen fit. Here L and $\xi(0)$ are in nm, T_c in K , and R_N in $\tilde{\Omega}$. Using the fitting parameters from the $R_T(T)$ fit of Eq. 6.1 presented in Fig. 6.1(c), $I_c(0)$ has a theoretical value of 5.48 A, while $I_c(0)$ used in fitting to the Bardeen formula in Fig. 6.13 has a value of 5.88 μA. Thus, excellent agreement is found between the theoretical and experimental value for $I_c(0)$. With regard to T_c, 4.2 K was used to fit the Bardeen formula, while the AL model predicted T_c = 4.717 K. This difference can be accounted for by sample oxidation and thermal cycling between measurements. Thus, by shunting the nanowire with a sufficiently small shunt, the switching current can be controllably driven very near to the depairing current.

The inset of Fig. 6.13 shows the temperature dependence of the standard deviation of the switching and retrapping currents at low temperature for sample S4 shunted with 10 Ω. As the temperature is decreased, the standard deviation of the switching current increases as observed in other experiments with unshunted wires [41], except at low temperatures below ~800 mK at which a saturation effect occurs. The saturation effect occurs as the multiple retrapping regime [19, 20, 21], which is a regime where after a phase slips has occurred due to thermal activation or

QPS the phase particle can be retrapped in a subsequent well, switches to a single phase slip regime where just one phase slip can cause the nanowire to enter the resistive state. In unshunted nanowires, the increase in the standard deviation as the temperature is lowered is a result of a multiple phase slip train that is required to switch the wire into the JHNS [40, 41, 42]. In this same temperature regime for the shunted sample, the standard deviation of the retrapping current shows an opposite trend as it decreases with a decrease in temperature. With less thermal energy, the fluctuation in the retrapping current narrows as the temperature approaches lower values. This decrease in the standard deviation of the retrapping current can thus be explained by the decrease in the thermal fluctuation, which presumably causes the observed temperature dependence of the stochastic behavior of the retrapping current.

6.10 Shunting insulating nanowires and the superconductor to insulator transition

The insulating state is characterized by an increase in the nanowire resistance as the sample is cooled to low temperatures. While the observation of the insulating state can clearly be noticed from the *R* vs. *T* curves, the exact nature of the insulating state is still not clearly understood. In thin inhomogeneous wires, the insulating state can arise due to oxidation of the metal resulting in granularities or non-uniformity. However, even in homogeneous junctions, the insulating state can arise. This could occur to do the Coulomb interaction [73, 74] or weak localization [75], which results in the complete destruction of superconductivity by driving T_c to zero. The insulating state can also arise due to the loss of coherence due to QPS and thus the loss of the capacity for a supercurrent to flow [38, 76, 77]. Within the latter category, Golubev and Zaikin (GZ) [77] calculated the time in between single QPS events ($\tau_{GZ} = \Gamma_{GZ}^{-1}$) for the type of MoGe

nanowires studied in this thesis. Depending on the value of the parameter A_{GZ} used in their theory, they found out that either: (i) the superconducting samples only appear to be superconducting because QPS events are rare while in insulating samples they occur often or (ii) the insulating and superconducting samples should show an insulating behavior due to the proliferation of QPS. However, QPS can still be damped [10] resulting in a dissipative phase transition [34] similar to that observed in the RCSJ model for Josephson junctions. These two possibilities are difficult to distinguish, but some evidence such as the resistance at the transition between the superconducting and insulating state occurring at R_Q points to the dissipative phase transition for the MoGe nanowires studied here [46, 78] and thus a coherent insulating state. However, this is not firmly established yet. To help understand the nature of the insulating state, we shunt an insulating nanowire with other insulating nanowire(s), and in other cases, with a low value resistive shunt to drive the total sample resistance below the quantum resistance.

When an insulating nanowire is shunted by other insulating nanowires such that the parallel combination of the resistance of the nanowires is less than R_Q, an upturn in the sample resistance is till observed as the sample is cooled (see Fig. 6.13(a)). The resistance vs. temperature curves for the insulating nanowire shunted with a normal resistor of ~ 5 Ω does not show a superconducting behavior, but also shows an insulating behavior (see Fig. 6.14(b)). Thus, resistive shunting does not seem to drive the insulating nanowires into the superconducting state.

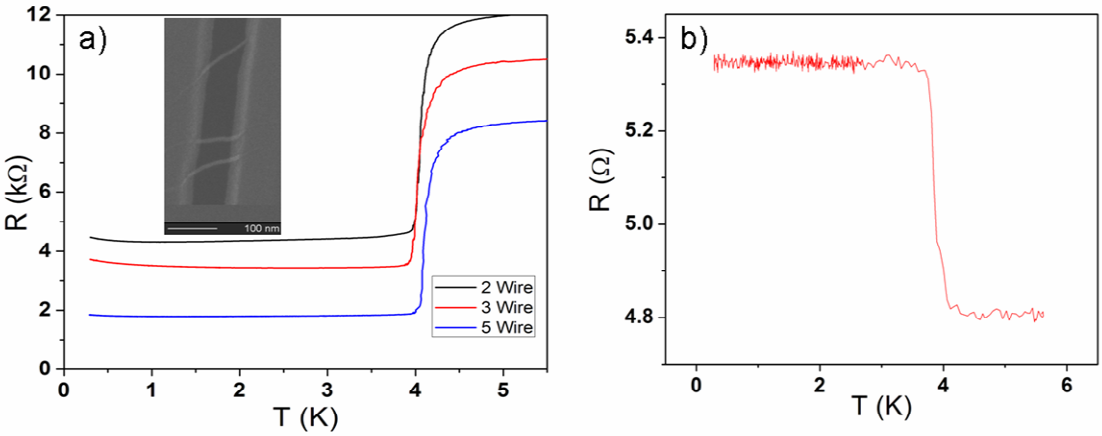

Fig. 6.14: (a) Resistance vs. temperature curves for insulating nanowires shunted by other insulating nanowires. Inset: A SEM picture of a three wire device where each wire is shunted by two others. (b) Resistance vs. temperature of an insulating nanowire that is shunted by a ~ 5 Ω external shunt resistor.

Just as in a single insulating nanowire, the behavior of the resistance vs. temperature curves in our nanowire samples which are shunted by other nanowires follows the predictions of the theory of Coulomb blockade. Weak Coulomb blockade was first demonstrated in tunnel junctions [79] but was then observed in homogeneous normal wires [80]. Golubev and Zaikin [81] were able to extend this understanding by using an effective action technique to derive the temperature dependence of the conductance ($G = R^{-1}$) as well as the current voltage $I(V)$ characteristics. The weak Coulomb blockade occurs when the temperature is high compared with the charging energy E_C. The conductance is given by GZ as:

$$\frac{G(T)}{G_0} \cong 1 - \beta\left[\frac{E_C}{3k_BT} - \left(\frac{3\zeta(3)}{2\pi^4}g + \frac{1}{15}\right)\left(\frac{E_C}{k_BT}\right)^2\right], \qquad (6.19)$$

where G_0 is the conductance in the absence of Coulomb effects, $\beta = 1/3$ for diffusive wires, $\zeta(3) \cong 1.202$, and $g = 4G_0R_Q$. By expanding this expression about E_C, the previous equation can be rewritten as and compared to the experimental data:

$$\frac{G_0}{G_0 - G(T)} = \frac{3k_BT}{\beta E_C} + \frac{9}{\beta}\left(\frac{3\zeta(3)}{2\pi^4}g + \frac{1}{15}\right). \qquad (6.20)$$

The fits to this equation are shown in Fig. 6.15 for the multiple insulating wire samples presented in Fig. 6.14(a).

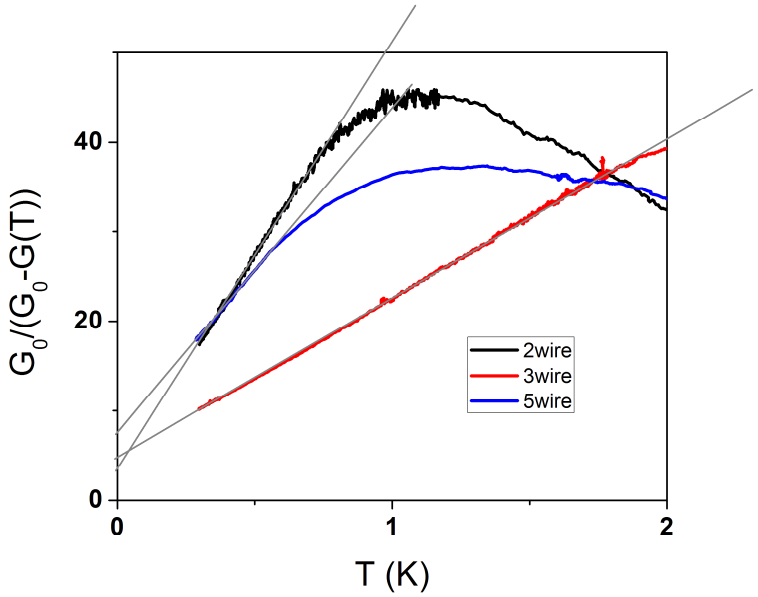

Fig. 6.15: The R-T curves of Fig. 6.14(a) plotted in the normalized conductance units $G_0/(G_0 - G(T))$ and fit to the GZ theory for Coulomb blockade.

There is an excellent agreement between the fits to the GZ theory and the data. The parameter G_0 used for each fit was roughly equal to the inverse of the normal state resistance of the parallel combination of the nanowires ($G_0 \cong R_{N//}^{-1}$, where $G_0^{-1} = 4219\ \Omega$ and $R_{N//} = 4632\ \Omega$ for the 2 wire sample, $G_0^{-1} = 3361\ \Omega$ and $R_{N//} = 3488\ \Omega$ for the 3 wire sample, and $G_0^{-1} = 1740\ \Omega$

and $R_{N//}$ = 1873 Ω for the 5 wire sample). The intercepts given by $\cong 12870(G_0)$ also match well for each sample considered where the measured and theoretical values for each sample are: 3.51 and 3.05, 4.67 and 3.83, and 7.37 and 7.40, for the two, three, and five wire samples, respectively. By analyzing the slope of each plot, the charging energy E_c can be determined and was found to be 16.2 μeV, 43.8 μeV, and 21.3 μeV for the two, three, and five wire samples, respectively. This fits well with the range of the expected charging energies of ~ 8-80 μeV expected from our geometries [71]. Thus, the shunted insulating samples follow the theory of Coloumb blockade of coherent transport through mesoscopic normal metal conductors.

The differential resistance as a function of the bias current can also be measured and compared to GZ theory, where a zero bias anomaly is expected. In Fig. 6.16, differential resistance vs. current curves are shown for the insulating sample containing 3 parallel nanowires at a temperature of 300 mK and at two magnetic field values (where the zero field curve is vertically shifted up 7500 Ω for easier comparison). The curve measured at a magnetic field of 9 T has a noticeably wider zero bias peak. The difference in peak width is related to the ratio e_{eff}/T (the peak becomes narrow as the ratio increases), where e_{eff} is the effective charge and T is the temperature. The GZ theory is derived for normal electrodes, thus at high magnetic field values where the electrodes are normal, the value of the effective charge is close to the electronic charge e. At lower magnetic fields where the electrodes are superconducting, Andreev reflections from the ends of the wire may occur and cause the effective charge to be greater than e but less than $2e$. This has been experimentally verified [71] and can explain the change in the width of the peak at different magnetic field values. The zero bias peak was also studies at various microwave powers at a frequency of 26 GHz and a temperature of 350 mK. As the microwave power was increased, the peak became less sharp at the zero bias point and the height

decreased. This may have occurred due to an increase in the temperature at such high microwave powers.

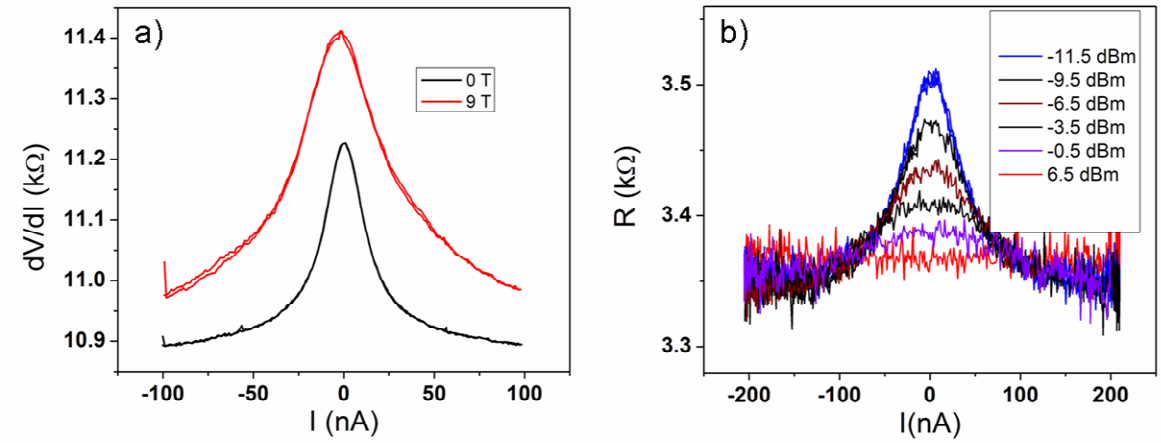

Fig. 6.16: (a) Differential resistance as a function of bias current measured at 300 mK at two magnetic field values. (b) Differential resistance as a function of bias current measured at 350 mK at various microwave powers with a fixed frequency of 26 GHz.

Overall, the shunting of insulating nanowires by other insulating wires and by an external shunt did not drive the nanowire into the superconducting state. However, the GZ theory was applied to the case where insulating nanowires were shunting each other and the equivalent parallel resistance of the nanowires was less than the quantum resistance. Excellent agreement was found between the theory of Coloumb blockade and our data thus suggesting that the transport through our nonsuperconducting nanowires is coherent. Assuming that the resistance of each nanowire in a particular sample was equal, the resistance of the individual nanowire can be calculated and was found to be greater than R_Q. This suggests that the resistance that must be compared to R_Q to determine the phase in the SIT phase diagram is the local resistance of the individual nanowire and not the value of the shunt resistance.

6.11 Conclusion

In summary, the external shunting of quasi one-dimensional superconducting nanowires has no detectable effect on the linear resistance of the wire but has a strong effect on the hysteretic *V-I* curves. We find that hysteresis can be completely eliminated by shunting as the increased damping that the shunt resistance results in drives the nanowire from an underdamped to an overdamped regime and reduces the Joule heating. The switching distributions were also affected by the presence of the shunt and were narrowed and shifted closer to the depairing current as smaller values of the shunt were used. External shunting was also shown to stabilize the PSC regime against JHNS and thus allows us to study the switching and retrapping statistics within the RCSJ model adapted to include the external shunt resistor. The PSC state was further demonstrated by the observation of oscillations in the retrapping current of a double nanowire as a function of magnetic field, a phenomena that is not observed in unshunted nanowires [62, 63] whose normal state is the JHNS. While being shunted, the nanowire retrapping current became stochastic and its mean value increased with a decreasing shunt resistance. With small shunt resistances, the switching current was driven very near to the depairing current and found to be in agreement with the Bardeen formula for the depairing current as a function of temperature in a large temperature interval. The dissipation of QPS was also qualitatively demonstrated for a shunted nanowire. Finally, when insulating nanowires shunted each other such that the total resistance was below the quantum resistance, the behavior of the nanowires did not exhibit superconducting properties. The model of Coloumb blockade was applied to fit the resistance vs. temperature curves with excellent agreement suggesting that the transport is coherent and that the nanowires truly are in an insulating state.

[1] W. C. Stewart, Appl. Phys. Lett. **12,** 277 (1968).
[2] D. E. McCumber, J. Appl. Phys. **39,** 3113 (1968).
[3] M. Tinkham, Introduction to Superconductivity (McGraw-Hill, New York, 1996), 2nd ed.
[4] K.K. Likharev, Dynamics of Josephson junctions and circuits (Gordon and Breach Science Publishers, New York, 1981).
[5] S. Al-Khawaja, Chaos, Solitons & Fractals, **36,** 382 (2008).
[6] S. Naito and Y. Higashino, Jpn. J. Appl. Phys. **23,** 861 (1984).
[7] S. Takaqi, Macroscopic Quantum Tunneling (Cambridge University Press July 2005)
[8] A. J. Leggett, J. Phys. (Paris), Colloq. **39,** C6–1264 (1978).
[9] A. J. Leggett, *Lesson of Quantum Theory. N. Bohr Centenary Symposium*, 35–57 (1986).
[10] A. O. Caldeira and A. J. Leggett, Phys. Rev. Lett. **46,** 211 (1981).
[11] A. J. Leggett, S. Chakravarty, A. T. Dorsey, M. P. A. Fisher, A. Garg, and W. Zwerger, Rev. Mod. Phys. **59,** 1 (1987).
[12] R. F. Voss and R. A. Webb, Phys.Rev.Lett. **47,** 265 (1981).
[13] J. M. Martinis, M. H. Devoret, and J. Clarke, Phys. Rev. B **35,** 4682 (1987).
[14] B. Dimov, et al., IEEE Transactions on Applied Superconductivity, **15,** 2 (2005).
[15] E. Ben-Jacob, D. J. Bergman, B. J. Matkowsky, and Z. Schuss, Phys. Rev. A **26,** 2805 (1982).
[16] J. M. Martinis and R. L. Kautz, Phys. Rev. Lett. **63,** 1507 (1989).
[17] D. Vion, M. Götz, P. Joyez, D. Esteve, and M. H. Devoret, Phys. Rev. Lett. **77,** 3435 (1996).
[18] J. M. Kivioja, T. E. Nieminen, J. Claudon, O. Buisson, F. W. J. Hekking, and J. P. Pekola, Phys. Rev. Lett. **94,** 247002 (2005).
[19] V. M. Krasnov, T. Golod, T. Bauch, and P. Delsing, Phys. Rev. B **76,** 224517 (2007).
[20] J. Männik, S. Li, W. Qiu, W. Chen, V. Patel, S. Han, and J. E. Lukens, Phys. Rev. B **71,** 220509(R) (2005).
[21] V. M. Krasnov, T. Bauch, S. Intiso, E. Hurfeld, T. Akazaki, H. Takayanagi, and P. Delsing, Phys. Rev. Lett. **95,** 157002 (2005).
[22] Myung-Ho Bae, M. Sahu, Hu-Jong Lee, and A. Bezryadin, Phys. Rev. B **79,** 104509 (2009).
[23] J. M. Martinis and H. Grabert, Phys. Rev. B **38,** 2371 (1988).
[24] A. Bezryadin, J. Phys.:Condens. Matter **20,** 043202 (2008).
[25] Mooij J E and Harmans C J P M, New J. of Phys. **7,** 219 (2005).
[26] Mooij J E and Nazaron Y V, Nature Physics **2,** 169 (2006).
[27] N. Giordano, Phys. Rev. B **41,** 6350 (1990).
[28] M. Zgirski, K.-P.Riikonen, V.Touboltsev and K.Yu.Arutyunov, Phys. Rev. B **77,** 054508 (2008).
[29] F. Altomare, A.M. Chang, M. R. Melloch, Y. Hong and Charles W. Tu, Phys. Rev. Lett. **97,** 017001 (2006).
[30] M. Tinkham, C. N. Lau, and N. Markovic, Physica E **18**,308 (2003).
[31] A. Schmid, Phys. Rev. Lett. **51,** 1506 (1983).
[32] S. A. Bulgadaev, JETP Lett. **39,** 315 (1984).
[33] S. Chakravarty, Phys. Rev. Lett. **49,** 681 (1982).
[34] J.S. Penttilä, Ü. Parts, P. J. Hakonen, M. A. Paalanen, E. B. Sonin, Phys. Rev. Lett. **82,** 1004 (1999).
[35] D. Meidan, Y. Oreg and G. Refael, Phys Rev. Lett. **98**, 187001 (2007).
[36] H. P. Büchler, V. B. Geshkenbein, G. Blatter, Phys. Rev. Lett. **92**, 067007 (2004).
[37] P. Werner and M. Troyer, Phys. Rev. Lett. **95**, 060201 (2005).
[38] A. D. Zaikin, D. S. Golubev, A. van Otterlo, G. T. Zimányi, Phys. Rev. Lett. **78**, 1552 (1997).
[39] M. Tinkham, J. U. Free, C. N. Lau and N. Markovic, Phys. Rev. B **68**, 134515 (2002).
[40] N. Shah, D. Pekker, P. M. Goldbart, Phys. Rev. Lett. **101,** 207001 (2008).
[41] M. Sahu, Myung-Ho Bae, A. Rogachev, D. Pekker, Tzu-Chieh Wei, N. Shah, Paul. M. Goldbart, A. Bezryadin, Nat. Phys. **5,** 503 (2009).
[42] D. Pekker, N. Shah, M. Sahu, A. Bezryadin, and P. M. Goldbart, Phys. Rev. B **80**, 214525 (2009).
[43] A. A Golubov, M. Yu. Kupriyanov, E. Il'ichev, Rev. Mod. Phys. **76,** 411 (2004).
[44] A.J. Kerman, E. A. Dauler, W. E. Keicher, J. K. W. Yang, K. K. Berggren, G. Gol'tsman, B. Voronov, Appl. Phys. Lett. **88,** 111116 (2006).
[45] J. Bardeen, Rev. Mod. Phys. **34,** 667 (1962).
[46] A. Bezryadin, C. N. Lau, M. Tinkham, Nature **404,** 971 (2000).
[47] A. Bezryadin and C. Dekker, J. Vac. Sci. Technol. B **15,** 793 (1997).

[48] W. A. Little, Phys. Rev. **156,** 396 (1967).
[49] A. Bezryadin, J. Phys.: Condens. Matter **20,** 043202 (2008).
[50] J. S. Langer and A. Ambegaokar, Phys. Rev. **164,** 498 (1967).
[51] M. Tinkham and C. N. Lau, Appl. Phys. Lett. **80,** 2946 (2002).
[52] K. K. Likharev, Rev. Mod. Phys. **51,** 101 (1979).
[53] W. T. Coffey, Y. P. Kalmykov, J. T. Waldron, *The Langevin Equation* (World Scientific, New Jersey, 1996).
[54] L. P. Gor'kov, Sov. Phys. JETP **7,** 505 (1958).
[55] B. D. Josephson, Phys. Lett. **1,** 251 (1962).
[56] P. W. Anderson and A. H. Dayem, Phys. Rev. Lett. **13,** 195 (1964).
[57] R. Tidecks, Current-Induced Nonequilibrium Phenomena in Quasi-One-Dimensional Superconductors (Springer-Verlag, New York, 1990) Vol. 121.
[58] A. B. Cawthorne, C. B. Whan, and C. J. Lobb, J. Appl. Phys. **84,** 1126 (1998).
[59] R. C. Dinsmore III, Myung-Ho Bae, A. Bezryadin, Appl. Phys. Lett. **93**, 192505 (2008).
[60] W. A. Little and R. D. Parks, Phys. Rev. Lett. **9**, 9 (1962).
[61] W. A. Little and R. D. Parks, Phys. Rev. **133**, A97 (1963).
[62] D. S. Hopkins, D. Pekker, P. M. Goldbart, and A. Bezryadin, Science **308**, 1762 (2005).
[63] D. Pekker, A. Bezryadin, D. S. Hopkins, and P. M. Goldbart, Phys. Rev. B **72**, 104517 (2005).
[64] A. Rogachev, T.-C. Wei, D. Pekker, A. T. Bollinger, P. M. Goldbart, and A. Bezryadin, Phys. Rev. Lett. **97**, 137001 (2006).
[65] V. Ambegaokar and B. I. Halperin, Phys. Rev. Lett. **22**, 1364 (1969); **23**, 274 (1969).
[66] J. Kurkijarvi and V. Ambegaokar, Phys. Lett. **31A**, 314 (1970).
[67] R. L. Kautz and J. M. Martinis, Phys. Rev. B **42**, 9903 (1990).
[68] M. P. Allen and D. J. Tildesley, *Computer Simulation of Liquids, Clarendon Press.*
[69] T. A. Fulton and L. N. Dunkleberger, Phys. Rev. B **9,** 4760 (1974).
[70] A. T. Johnson, C. J. Lobb, and M. Tinkham, Phys. Rev. Lett. **65,** 1263 (1990).
[71] A. T. Bollinger, A. Rogachev, and A. Bezryadin, Europhys. Lett. **76,** 505 (2006).
[72] Y. C. Chen, M. P. A. Fisher, and A. J. Leggett, J. Appl. Phys. **64**, 3119 (1988).
[73] Y. Oreg and A. M. Finkel'stein, Phys. Rev. Lett. **83**, 191 (1999).
[74] H. Ebisawa, H. Fukuyama, and S. Maekawa, J. Phys. Soc. Jpn. **55**, 4408 (1986).
[75] Y.-J. Kim and K. J. Chang, Mod. Phys. Lett. B **12**, 763 (1998).
[76] N. Giordano, Phys. Rev. Lett. **61**, 2137 (1988).
[77] D. S. Golubev, and A. D. Zaikin, Phys. Rev. B **64**, 014504 (2001).
[78] A. T. Bollinger, R. C. Dinsmore III, A. Rogachev, and A. Bezyradin, Phys. Rev. Lett. **101**, 227003 (2008).
[79] J. P. Pekola, K. P. Hirvi, J. P. Kauppinen, and M. A. Paalanen, Phys. Rev. Lett. **77**, 3889 (1994).
[80] Y. V. Nazarov, Phys. Rev. Lett. **82**, 1245 (1999).
[81] D. S. Golubev and A. D. Zaikin, Phys. Rev. Lett. **86**, 4887 (2001).

Chapter 7

Superconducting graphene proximity junctions

Since the pioneering work by R. Holm and W.Meissner [1], who observed zero resistance in SNS pressed contacts, many manifestations of the superconducting proximity effect have been reported. Recently it was shown that when closely spaced superconducting leads are placed on graphene, the proximity effect is induced and a supercurrent can flow between the electrodes. Here we fabricate graphene proximity-effect junctions (GPJ) and compare them to Josephson junctions (JJ). As the bias current is increased to near the critical current, a thermal escape over the barrier or a quantum tunneling through the barrier defined by the washboard potential, can occur driving the junction into the runaway voltage state. The standard deviation of the switching current is measured as a function of temperature and compared to the thermal and quantum escape models for JJs. We find that the temperature dependence of the standard deviation of switching currents of graphene proximity junctions is qualitatively different from the well-studied behavior of the insulator-based JJs, at least in the case of wide junctions. Also our results strongly indicate that thermal activation (TA) dominates the process of escape to the normal state, and that macroscopic quantum tunneling (MQT), down to temperatures of ~ 275 mK, is not observed.

7.1 Introduction

With the discovery of a method to extract single atomic layers of graphite [2, 3], an intense effort is currently underway to explore the physical properties of graphene, which is a monatomic layer of carbon atoms arranged in a honeycomb lattice. When graphene is doped with electrons or holes, they travel through the material at the Fermi velocity $v_F = 10^6$ m/s, which is only a small fraction of the speed of light. However, the interesting fact is that the electrons and holes have a velocity that is energy independent and the energy spectrum is gapless as the conduction and valence bands touch at discrete points called Dirac points [4]. Thus, the quasiparticles in graphene follow a linear energy-momentum dispersion relation and thus behave like relativistic massless particles traveling at the speed of light and are described by the Dirac equation, which is a relativistic wave equation. Many other interesting properties of graphene include the observation of Andreev reflection [5, 6], evidence of a finite lower bound in conductivity of order $4e^2/h$ at charge neutrality point [3, 7], an anomalous integer quantum Hall effect [3, 7, 8, 9], and the suppression of weak localization [10].

Graphene itself is not superconducting, but when placed between two superconductors, the proximity effect drives the graphene into the superconducting state [11, 12]. Therefore, graphene is an interesting material as it allows a study of the interplay between superconductivity and relativity. Many of the superconducting properties of the graphene proximity junction, such as the critical current and normal state resistance, are a function of the charge density, which can be controlled through applying a gate voltage to the system. Thus, the graphene proximity junctions are promising candidates to be used to study the physics of Josephson junctions which includes the phase diagrams for the superconductor to insulator (SIT) transition and the crossover from overdamped dynamics to the underdamped phase diffusion branch, and then

finally to the running state [13]. Many other applications and interesting points of the physics of graphene proximity junctions rely on the presence of macroscopic quantum tunneling (MQT), which has been observed in Josephson junctions [14]. The process of MQT occurs when the phase particle in the washboard potential tunnels from one stable potential well to another, and undergoes a phase change of 2π. This, however, is not the only mechanism by which the phase can change. The phase particle can also hop over the barrier via a thermal activation process. It is an important task to detect the mechanism by which the graphene proximity junction undergoes phase changes and thus shows a finite resistance.

One technique to investigate the process by which the phase particle transverses along the phase axis is to study the statistics of the switching of the graphene junction from the superconducting state to the normal state. The process is stochastic and can be analyzed and compared to switching rates for the processes of thermal activation or MQT, which show distinct differences. When the phase particle is thermally activated, the standard deviation of the switching current as a function of temperature follows a power law of $T^{2/3}$ [15], while for the MQT process, the standard deviation saturates at low temperatures [14]. Thus, by analyzing the statistics of the switching current, one can distinguish the mechanism by which the phase particle in the graphene junction system can change its phase by 2π. It will be discussed in this chapter that our graphene junctions do not show the characteristic saturation of the standard deviation of switching currents as a function of temperature, but instead, it shows a power law dependence similar to the standard Josephson junction case except where the power of 2/3 is replaced by 1/3. Possible reasons will be discussed and are related to the length of the junction.

7.2 Sample fabrication

The graphene proximity junctions are fabricated (by Ulas Coskun at the University of Illinois in Urbana-Champaign) using an electron beam lithography process, which is used to define a small gap in two superconducting electrodes with graphene in the gap connection the two electrodes. We start with a four inch diameter silicon wafer purchased from Silicon Quest International, Inc., with a 280 nm SiO_2 layer deposited on each side. The wafer is then cleaned by a five step cleaning process where it is agitated for one minute in each of the following in order: acetone, deionized water, nitric acid, deionized water, and then finally isoproponal. After this, the wafer is diced into smaller chips with a dimension of 5 by 20 µm. The wafer is now ready to have graphene deposited on its surface.

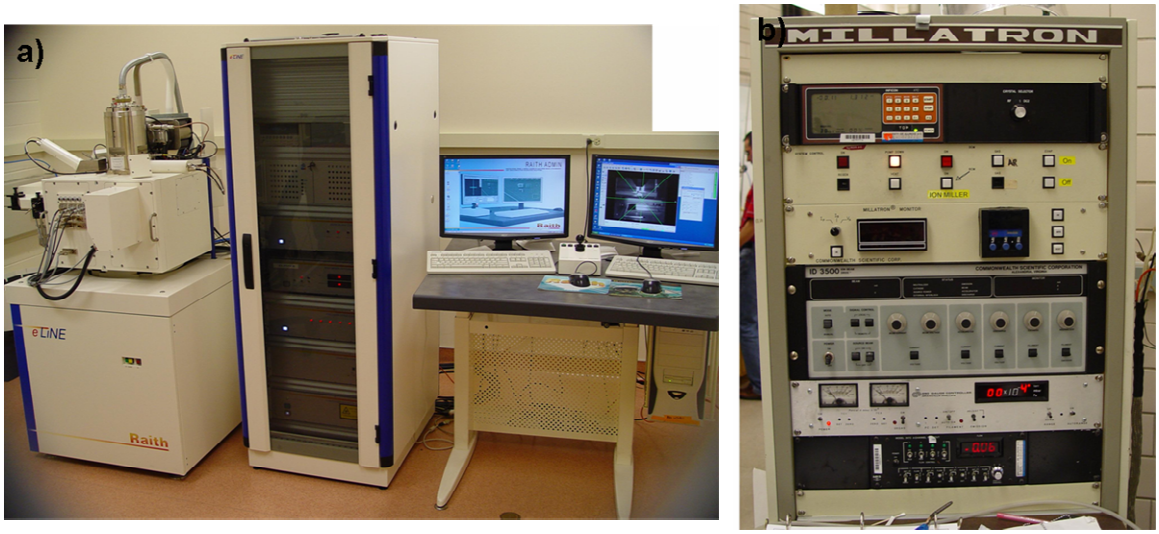

Fig. 7.1: (a) The Raith E-line ebeam writer which is used to expose the sample to perform the ebeam lithography step in the sample fabrication. (b). The Common Wealth Scientific Thermal Evaporator used for Pd and Pb metal deposition.

The graphite used to produce the graphene for our junctions is purchased from NGS Naturgraphite GmbH and contains graphite flakes with a size of 10-20 mm and 50-100 µm thick. The graphene is exfoliated using a scotch tape method [2]. After each attempt to get graphene,

the graphite on the tape is held in front of a light source to estimate the graphite thickness. After many attempts to get graphene (10-20), the graphite looks thin enough that the tape is applied to the surface of the SiO_2, where both thin graphite and graphene sticks to the surface. The SiO_2 sufrace is then scanned with an optical microscope while monitoring the transparency of the graphite flakes. The darker and more purple the color of the flake, the thicker and more layered the graphite is. Thus, a nearly transparent flake is selected as it is graphene [16] and the optical microscope is used to roughly determine the coordinates of the graphene flake. The graphene can also be checked using Raman spectroscopy. In Fig. 7.2, the Raman spectroscopy results are plotted for two different thin graphite flakes. In the thicker flake, the peak profile is non-Lorentzian and even shows a small side peak. However, in the thin flake, the peak profile is Lorentzian and located between 2600 and 2700 cm^{-1}, which is suggestive that the thin flake is graphene [17].

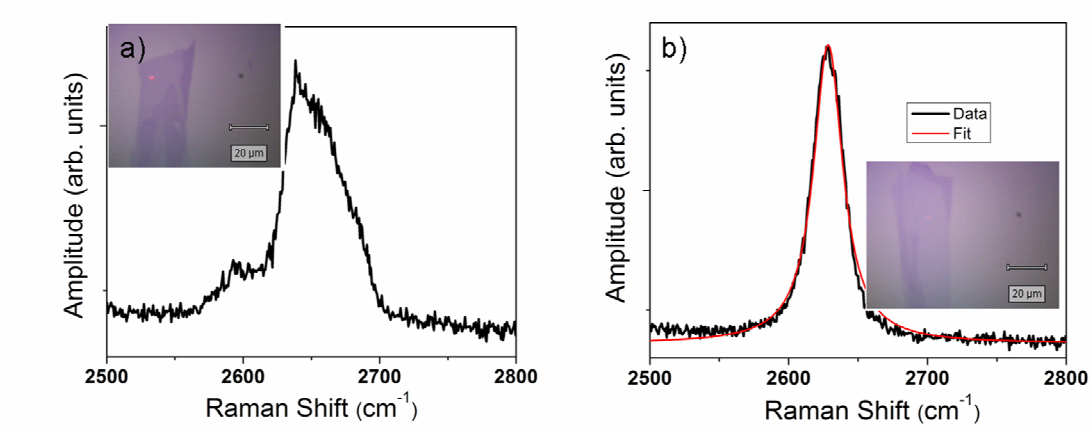

Fig. 7.2: (a) Raman spectroscopy for a thick graphite flake showing a double peak. Inset: optical image of the thick graphite flake. (b). Raman spectroscopy of a thin graphite flake showing a single peak. The peak is fit to a Lorentzian curve centered about 2628.5 cm^{-1} with a quality factor of Q = 4 suggesting that it is graphene. Inset: optical image of the graphene flake. This data was measured by U. Coskun at the University of Illinois in Urbana-Champaign.

The next step in the fabrication process is to deposit ebeam resist on the surface of the SiO_2 chip containing the graphene. We use the ebeam resist 495 PMMA A8, which is deposited on the chip and then spun at 4000 rpm for 40 seconds and then baked on a hotplate at 180 °C for 2 minutes. Since the location of the graphene is roughly known, we put a search pattern of 1.2 by 1.2 mm centered on the approximate location of the graphene (see Fig. 7.3). The resist is then placed in the Raith E-line ebeam writer (see Fig. 7.1) and exposed to a total charge of 300 $\mu C/cm^2$ with an accelerating voltage of 20 keV and a total current of 340 pA. After the exposure, the chip is agitated in MIBK: Isopropanol (1:3 ratio) for 75 seconds to develop the search pattern markers, which are spaced out by ~50 μm. The chip is then studied under the optical microscope to find the graphene, which is visible even under the PMMA, and an optical picture of the graphene is taken and the location of the graphene is recorded. The picture is then loaded into an AutoCad program, and the electrode pattern is drawn on top of the picture (see Fig. 7.3(b) and (c)).

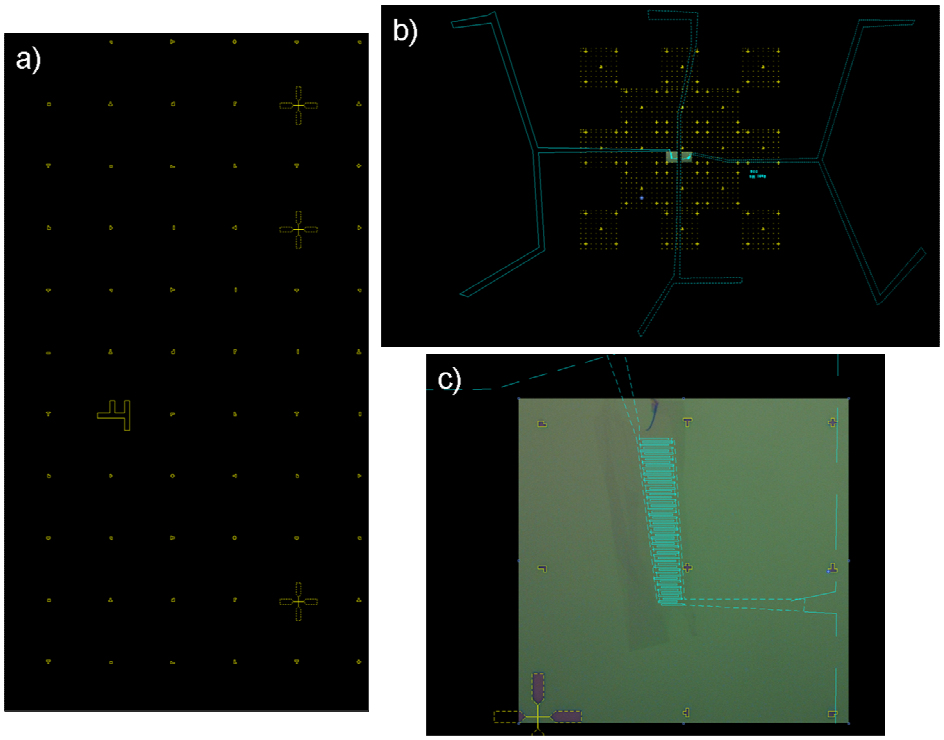

Fig. 7.3: (a) An AutoCad image of the 1.2 by 1.2 mm search pattern. The various shaped markers are used to locate the graphene. (b) The electrode pattern is drawn in AutoCad on top of the the optical picture of the graphene. (c) A zoomed in view of the center of the picture from (b) showing the electrode pattern drawn on top of the graphene.

The sample is then placed back into the ebeam machine where the sample is aligned using the alignment markers. The ebeam then exposes the section of the pattern drawn in AutoCad that does not contain the electrodes, in order to facilitate the liftoff process to be performed later. Metal deposition is done in the Common Wealth Scientific Thermal Evaporator (see Fig. 7.1). A cold trap is used to pump down the O_2 level in the vaccum chamber and a small amount (~ $5x10^{-5}$ Torr) of Ar or N_2 gas is leaked into the chamber to help reduce granular films which we believed is helped by cooling the sample stage. Initially, ~ 5 nm of Pd is evaporated on the surface, to be used as a wetting layer for the Pb, at an evaporation speed of 0.5-1 Å/s to avoid any damage to the graphene. After this, ~ 100 nm of Pb is evaporated at a much larger rate of 10-30 Å/s. Next, the liftoff process is done in a hot bath of acetone. The sample is placed in the acetone, which is heated to 60 °C for 1 minute, and then the sample is sonicated for

10 seconds. This process is repeated 3 times to ensure a complete liftoff process. Afterwards, the sample is agitated in a separate room temperature bath of acetone for 5 minutes before rinsing it for 30 seconds with isoproponal. Finally the sample is ready (an SEM image of the Pb electrodes placed over graphene for a sample can be seen in Fig. 7.4) and is mounted on a chip carrier with gold wires in a process identical to that outline in chapter 3. The gate electrode is added by using a fast drying silver paint to attach a gold wire from the pin on the chip carrier to the side and bottom of the doped silicon chip. The sample is now ready to be inserted to our ^{3}He system for measurements.

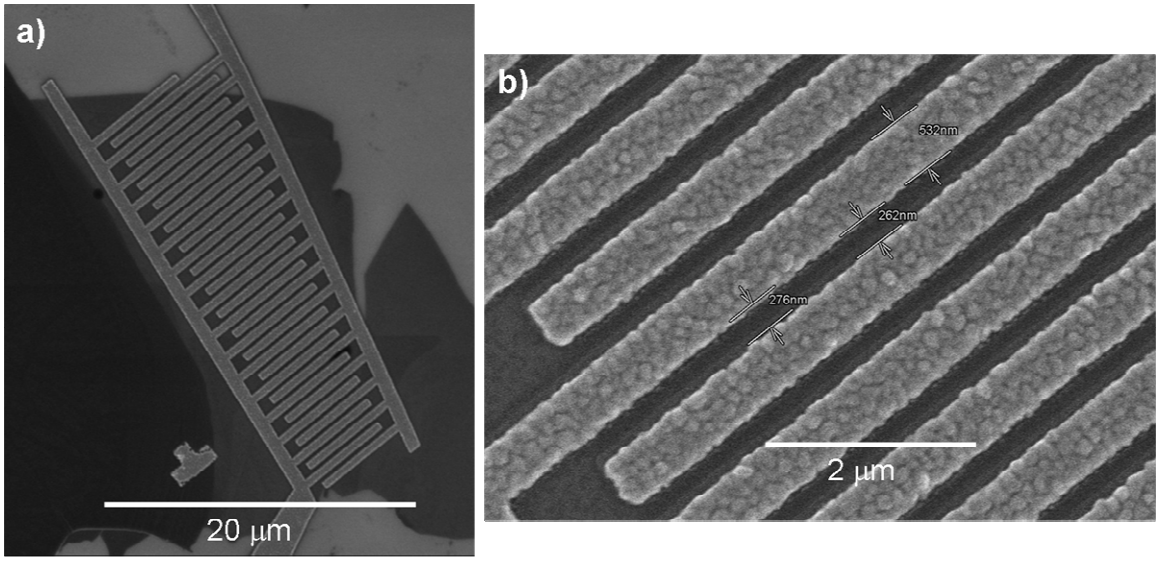

Fig. 7.4: (a) A SEM image of a graphene proximity junction. The Pb electrod pattern (some Pb granularity is visible on it) is shown on top of the graphene. The Pb thickness is 100 nm and the darker regions to the side are multilayer graphite. (b). A zoomed in picture of the electrodes from (a) where the electrode spacing is ~ 275 nm.

7.3 Characterization of graphene proximity junctions

In this section, the basic characterization of the electronic transport properties of graphene proximity junctions will be presented. As the sample is cooled from room temperature, the total resistance of the sample is the resistance of the Pb electrodes and the graphene junction. As the

sample is further cooled, the resistance shows a relatively sharp drop around a temperature of 7 K, which is the critical temperature of the Pb electrodes and the resulting resistance is just the resistance of the graphene proximity junction (see Fig. 7.5(a)). The resistance of the sample after the film becomes superconducting is the normal resistance R_N (see Fig. 7.5(b)). As the temperature is reduced, the graphene junction decreases in resistance until it is below the experimentally measureable limit of our system. When the gate voltage is changed from the Dirac point, it has the effect of reducing the normal state resistance and increasing the critical temperature of the graphene junction (see Fig. 7.5(a)). This is a further indication that our graphene consists of at most a few layers of graphene.

The resulting resistance vs. temperature (*R*-*T*) curve of the graphene junction can be fit by employing an Arrenehus law for the thermal activation of phase slips given by Little [18]:

$$R_{Little}(T) = R_N \exp\left(-\frac{\Delta F}{k_B T}\right), \tag{7.1}$$

where ΔF is the free energy barrier for a thermally activated phase slip and is given by:

$$\Delta F(T) = \frac{\hbar I_c(T)}{2e}, \tag{7.2}$$

where *h* is Planks constant, *e* is the electronic charge, $I_c(T)$ is the temperature dependent critical current. The fit to Little's equation is plotted in Fig. 7.5(c) where good agreement is found particularly at lower temperatures with the parameters $R_N = 110\ \Omega$, $T_c = 3.9$ K, and $I_c(T) = 0.3\mu\text{A}(3.9 - T)$. The deviation at higher temperatures is a result of the modeling of the temperature dependence of the critical current. We model the critical current as a linear function of temperature with the endpoints being the switching current at the highest temperature we have

measured [here, ~ 2 K (see Fig. 7.5(d))] and a critical current of zero at the T_c from the fit. At a temperature of ~ 2 K, the slope from the switching current vs. temperature (I_{sw} vs. T) plot is ~ 0.3 μA/K, which matches the value used in the Little fit. However, as the temperature increases to the critical temperature of the fit T_c = 3.9 K, the slope must decrease, which would force the fit to match the data better at higher temperatures. Thus, the good agreement between the data and the fit suggest at temperatures above ~2 K, only thermal activation is present and macroscopic quantum tunneling is not observed (MQT).

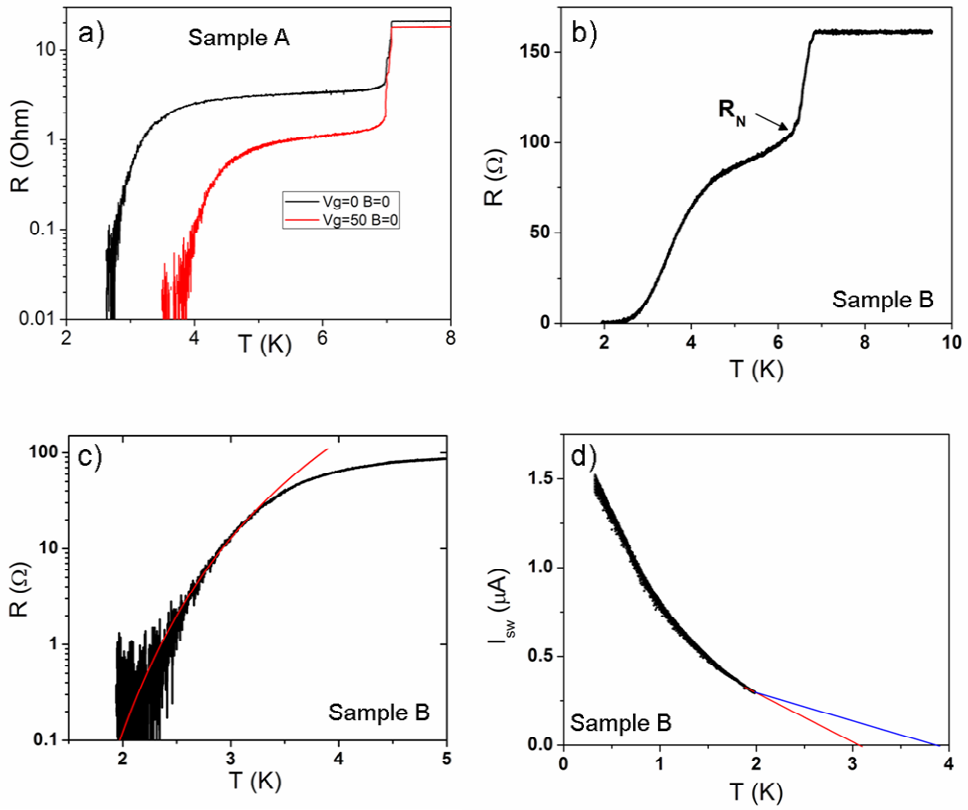

Fig. 7.5: (a) R-T curves for graphene proximity junction biased with two different gate voltages. Higher gate voltages reduces the normal state resistance and increases the critical temperature of the junction. (b) An R-T curve showing the definition of the normal state resistance. (c) An R-T curve showing a fit to the Little model describing the resistance vs. temperature resulting from thermal activation. (d) The switching current as a function of temperature showing the instantaneous slope at a temperature of 2 K (red) and the slope if the curve were to be extended to zero critical current at the critical temperature (blue).

Below the critical temperature of the graphene junction, we measure voltages vs. current curves at various gate voltage biases (see Fig. 7.6). A proof that our graphene becomes superconducting is that we observe a Josephson supercurrent below the switching current. As we ramp up the bias current, the junction switches at a particular current, we call the switching current, to the normal state where a nonzero voltage is measured. For underdamped junctions, as the bias current is reduced below the switching current, the junctions stays in the normal state until a different and lower current value is reached. At this current, we call the retrapping current, the junction is "retrapped" back into the superconducting state. Both the switching and retrapping currents are stochastic in nature and can be analyzed to understand the transition mechanism between the two states. As the gate voltage is increased from 10 to 50, both the mean retrapping and switching current values are observed to increase while the normal state resistance, measured as the slope of the *V-I* curve in the normal state, is observed to decrease. This is further evidence that the graphene junction responds to a change in gate voltage and thus must at the most be a few graphene sheets thick.

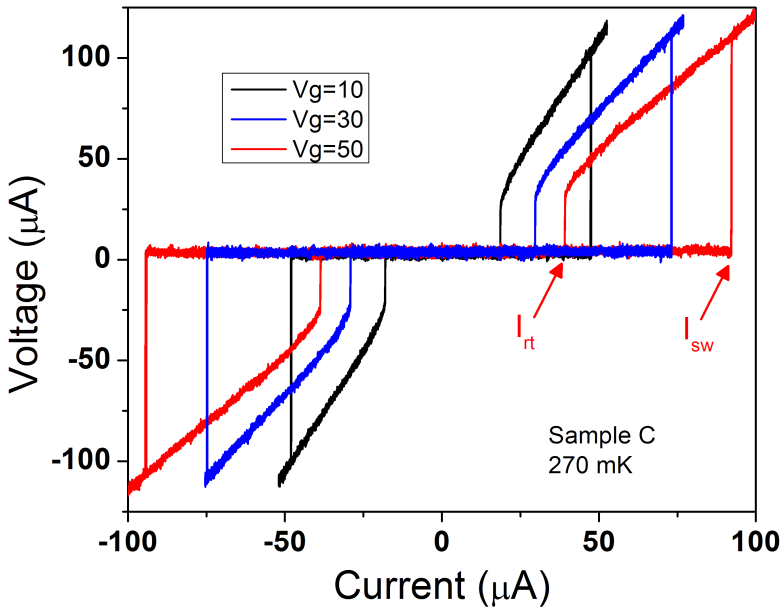

Fig. 7.6: The V-I curves at various gate voltage biases for a graphene proximity junction. The switching I_{sw} and retrapping I_{rt} currents are shown and this junction is determined to be underdamped by the observed hysteresis. This data was measured by U. Coskun at the University of Illinois in Urbana-Champaign.

The observation of hysteresis reveals the fact that this junction is underdamped. The quality factor can be calculated by $Q = \omega_p RC$ where $\omega_p = \sqrt{(2eI_c/\hbar C)}$, however, the exact value of the capacitance of the junction is not well-known. Another way to calculate the *Q*-factor is through the ratio of the fluctuation free critical and retrapping currents by $Q = (4I_c/\pi I_{r0})$ [19], where I_{r0} is the fluctuation free retrapping current. At first glance, the *Q*-factor can be underestimated by taking the observed mean value of the stochastic switching and retrapping current from Fig. 7.6. Doing this results in a *Q*-factor of 3.00, 3.14, and 3.20 for the applied gate voltages of 50, 30, and 10 V, respectively. Thus, our quality factor suggests that our graphene junction is moderately underdamped. To be overdampted, the quality factor should satisfy the relationship $Q \leq 0.84$. Using the estimates for the quality factor above, the

capacitance of the junction can be estimated to be ~ 15 pF. The capacitance can also be estimated by considering the geometry of our sample as in Fig. 7.7. An estimate of the capacitance across the graphene sheet suggested by our geometry is to use a formula for coplanar electrodes [20] $C = \varepsilon_r \varepsilon_0 L K(k) \big/ K\left(\sqrt{1-k^2}\right)$, which leads us to the conclusion that the electrode capacitance should be ~ 10 fF, where ε_0 is the permittivity of free space, ε_r is the relative permittivity of silicon ~ 4, L is the junction length given by ~ 300 μm, and $K(k)$ are the complete elliptical integrals of modulus $k = \left(1 + d_{gap}/w\right)^{-1}$, where d_{gap} is the gap between electrodes and w is the width of the electrods. However, the two electrodes have a capacitive coupling through the gate and thus Fig. 7.7(b) gives the proper geometry and electrical schematic for calculating the capacitance across the junction. In this geometry, d is 280 nm, and the area of each electrode (including the presence of a pressed indium dot to facilitate the electrical connection to the pins on the chip carrier) is 2.9 and 2.27 m^2. Thus the capacitance of each electrode to the gate is 36.7 and 28.7 pF, which is calculated from the formula $C = \varepsilon_r \varepsilon_0 A/d$. Using the circuit schematic in Fig. 7.7(c), the total capacitance is found to be 16 pF, which is close to the value of 15 pF that we obtained using the quality factor. Thus, our quality factor is close to its true value and our junction shows underdamped dynamics.

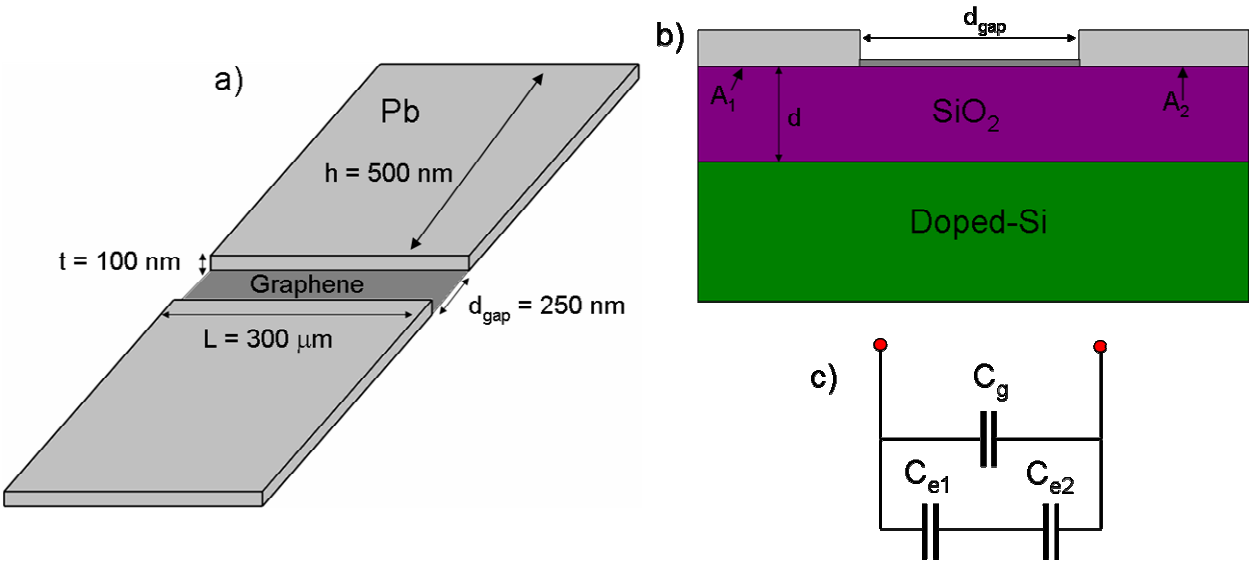

Fig. 7.7: (a) The capacitance across the graphene, C_g, can be calculated using the cross sectional area of the Pb film and the distance between the Pb electrodes. (b) The Pb electrodes form capacitors through the SiO_2 with a plate separation of d. (c). The electrical schematic of the capacitance through the graphene and the two capacitors formed between the electrodes and the gate. The equivalent capacitance is $C_g + C_{e1}C_{e2}/(C_{e1} + C_{e2})$.

If we assume that the amount of the reduction of the switching current is ~ 20% and that the increase in the retrapping current is ~ 10% higher than its fluctuation free value then, using these estimates, the *Q*-factor increases to $Q = 4$, 4.19, and 4.27 for the applied gate voltages of 50, 30, and 10 V, respectively. Given that the reduced normal state resistance increases the damping and thus drives the switching and retrapping current closer to their fluctuation free values, the amount the *Q* factor should be higher than the above analysis predicts should be greater for higher applied gate voltages. If the gate voltage were reduced even more, the hysteresis in some cases can be eliminated altogether and the *Q*-factor would be less than 1 and the phase dynamics switch to an overdamped regime. In either case, the *Q*-factor estimates show that our junctions are underdamped at these low temperatures and that an applied gate voltage can be used to tune the quality factor which opens up many potential applications for graphene proximity junctions to be used to better understand interesting Josephson junction physics [13].

As the temperature is reduced, the switching and retrapping currents are both observed to increase, until the retrapping current finally saturates (see Fig. 7.8). The stochasticity can be observed in this plot as the switching and retrapping currents are measured at a frequency of 8 Hz as the temperature was continuously lowered. However, a more precise analysis of the width of the stochastic switching and retrapping current distributions will be presented in the next section. For sample B, above ~ 2 K, the switching and retrapping currents become less defined and our measurement setup cannot easily measure these values. Below 2 K, we can easily obtain these values and the switching current is observed to continually increase, even at low temperatures, without much saturation. Our curves look similar to those derived by Kulik and Omel'yanchuk [21, 22], which are valid all the way to zero temperature. This is suggestive that we are in the clean limit where the electron mean free path is sufficiently short to justify the diffusive approximation. At low temperatures, the retrapping current is observed to saturate suggesting that the dissipation reaches a constant value.

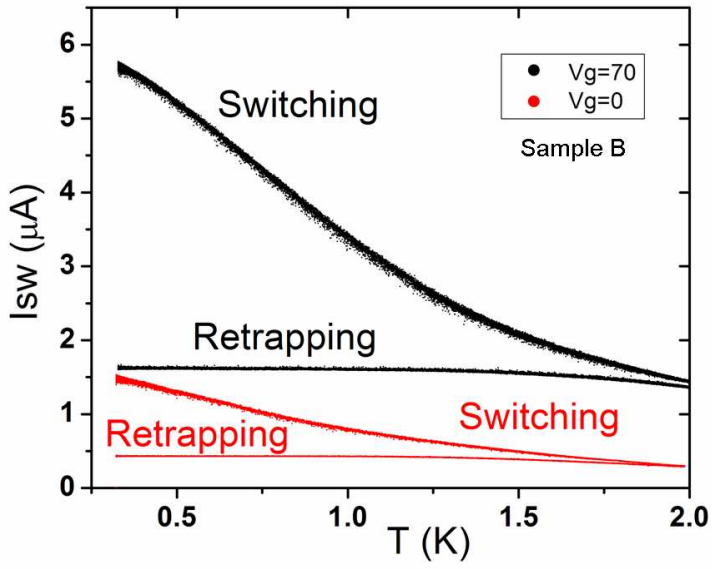

Fig. 7.8: The switching and retrapping currents as a function of temperature for sample B shown for two different values of the gate voltage.

The magnetic field dependence of the switching current can be measured and compared to Josephson junction theory. In an extended Josephson junction, the maximum (or critical) current as a function of applied magnetic flux can be fit to a Fraunhofer function:

$$\frac{I_m(\Phi)}{I_m(0)} = \left| \frac{\sin(\pi\Phi/\Phi_0)}{\pi\Phi/\Phi_0} \right|, \qquad (7.3)$$

where Φ is the magnetic flux through the junction which is given by $\Phi = BL(d + 2\lambda)$ (the effective area is larger than just Ld due to the penetration into the electrodes by a distance equal to the penetration depth), where L is the total length of the junction, d is the distance between the electrodes, B is the magnetic field, and Φ_0 is the magnetic flux quantum given by $\Phi_0 = h/2e$. The fit of our data to the Fraunhofer pattern can be seen in Fig. 7.9(a), where a good fit is obtained using an area that is estimated from the junction area of ~10^{-10} m^2 which results in a magnetic field period of ~ 20 μT. A vertical shift of 2.5 μA was also used to obtain the fit to account for the supercurrent observed even at the Dirac point. The magnetic field period obtained from the experimental data is somewhat small at about 7 μT. This discrepancy between the fitted and measured value can be traced to an understanding of the effective area of the junction given by $A_{eff} = L(d + 2\lambda)$. Using a penetration depth of 120 nm [23] results in an effect area of ~2x10^{-10} m^2 and a magnetic field period of 9 μT. If the area of the entire electrode plus junction were used, the magnetic field period would be ~7.8 μT. Thus, to fit to the Fraunhofer period the penetration depth in our samples should be larger than 120 nm in order to increase the effective area of the junction. The differential resistance of the junction can also be measured as a function of bias current and magnetic field. Again, the Fraunhofer pattern is observed, with a

slightly reduced value of the switching current even at a applied gate voltage of 50 V due to a shift of the Dirac point due to thermal cycling.

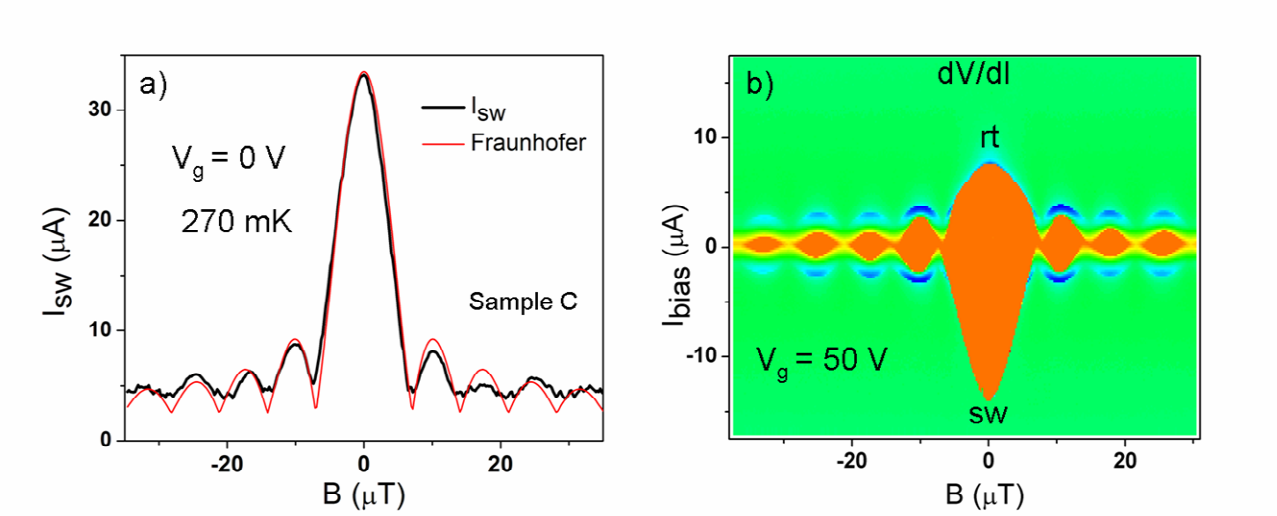

Fig. 7.9: (a) The switching current as a function of magnetic field with the corresponding Fraunhofer fit. The effective area of the junction needed to obtain a good fit is ~ the area of the entire junction suggesting that the penetration depth of our sample is ~200 μm. (b) A color plot of the differential resistance vs. bias current vs. magnetic field. The orange color is zero differential resistance while the green is the normal state resistance. Thus plot also shows the expected Fraunhofer fit. This data was measured by U. Coskun at the University of Illinois in Urbana-Champaign.

The switching current and resistance as a function of gate voltage are displayed in Fig. 7.10. As the gate voltage is swept away from the Dirac point, the total carrier concentration increases and thus, the switching current is expected to increase as well, which is confirmed in Fig. 7.10(a). In Fig. 7.10(a) the Dirac point is observed to be at ~ 21 V and above this value the Fermi energy is shifted to the conduction band and thus the charge carriers are primarily electrons while below 21 V, the Fermi energy is shifted to the valence band and the charge carriers are mostly holes. Thus, this figure confirms that our junctions are capable of carrying a bipolar supercurrent [12]. The differential resistance as a function of bias current and gate voltage is shown in Fig. 7.10(b) at a higher temperature and also after undergoing a change in the Dirac point due to thermal cycling of the sample. The red is zero differential resistance and the

yellowish-green is the normal state resistance at this temperature. Thus, it is clear that the gate voltage can be used to tune the critical current of our graphene proximity junctions, which can be a used as a tool to study the escape dynamics in our junctions.

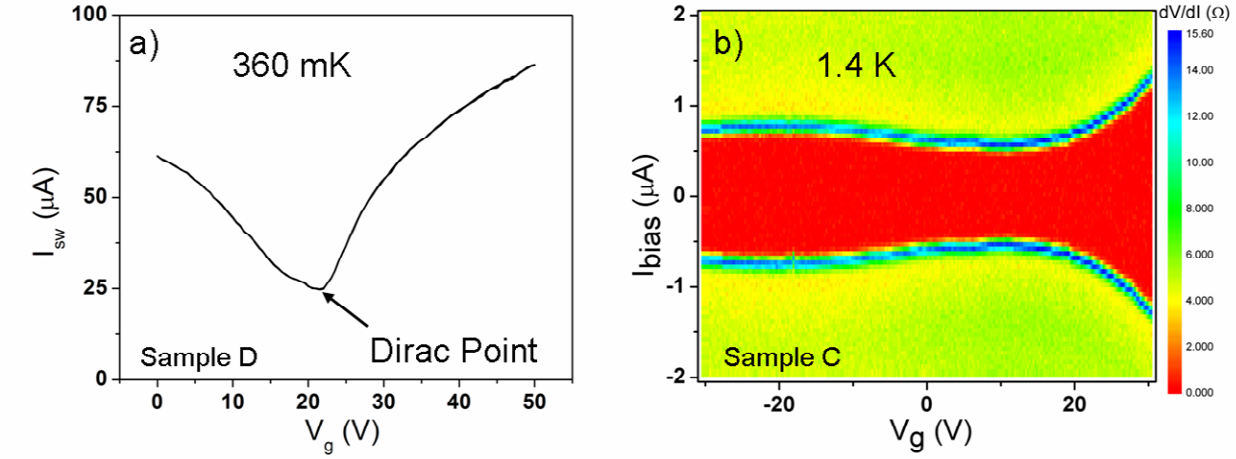

Fig. 7.10: (a) The switching current as a function of gate voltage. As the gate voltage is swept from the Dirac point, the switching current increases. (b) The differential resistance vs. bias current vs. gate voltage. The red color is zero differential resistance and the yellowish-green color is the normal state resistance at the given temperature of 1.4 K. This data was measured by U. Coskun at the University of Illinois in Urbana-Champaign.

7.4 Analysis of switching currents in graphene proximity junctions: thermal activation

In this section, we will present and analyze the measurements of the switching current in our graphene proximity junctions. As the current through the junction is increased (decreased), a switch to the normal (superconducting) state occurs at a current we call the switching (retrapping) current, which is stochastic in nature. This stochasticity in the switching current can be a result of a thermal activation process over the barrier, or MQT through the barrier. An analysis of the statistics of the switching current distributions gives us insight into the mechanism by which the normal state arises.

In section 7.3 we saw how the mean value of the switching current changed as a function of the gate voltage. As the gate voltage moved away from the Dirac point, the mean switching current increased. In Fig. 7.11, the switching and retrapping current distributions are plotted for three different applied gate voltages at 270 mK. The junction was biased using a sinusoidal current with a frequency of 8 Hz and recording the value of the current when the junction switches (retraps) to the normal (superconducting) state. To construct the distribution, 10,000 switching and retrapping currents were measured. A different current cell size was used for each distribution, thus the distributions were normalized by their total area to facilitate direct comparison between various distributions. The results are clear, as the gate voltage is increased, the mean switching and retrapping currents increase as well as the width of each distribution. The increase in the standard deviation at a given temperature as a function of gate voltage is not surprising since some theories predict that the standard deviation is a function of the critical current [24]. However, it is difficult to check this dependence on our data as the exact critical current is unknown. The standard deviation of our data is visually linearly proportional to the switching current for high switching currents, but then begins to dip to lower values as the switching current approaches zero (see Fig. 7.11(c)).

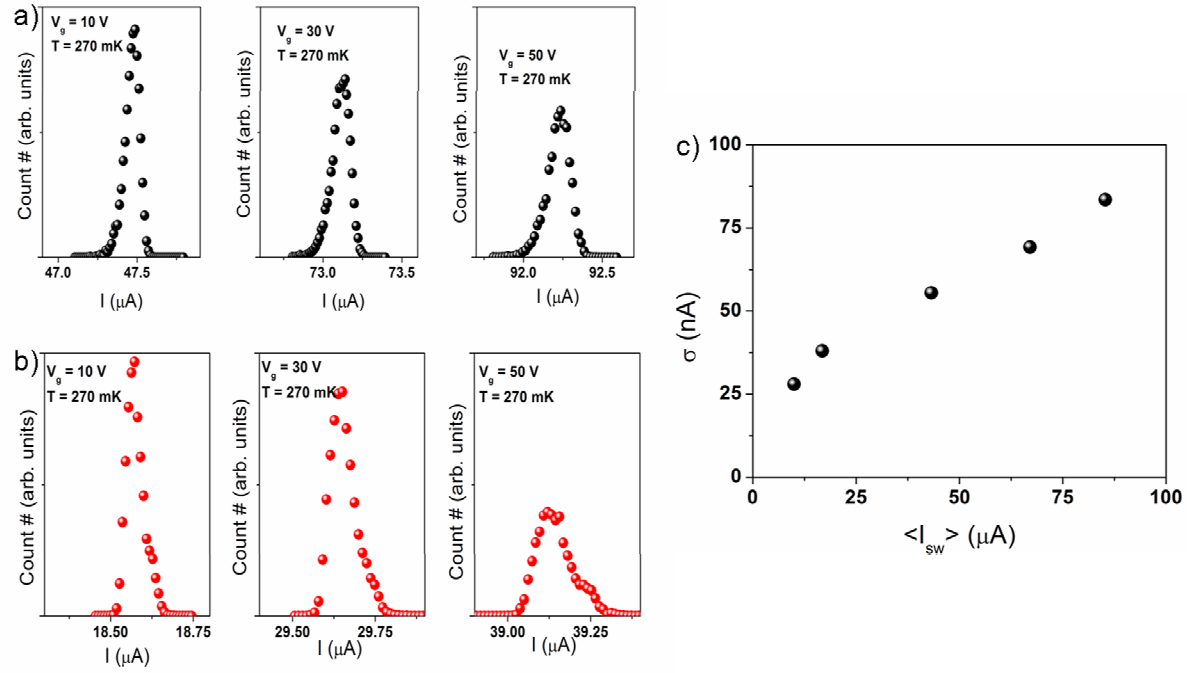

Fig. 7.11: (a) Switching distributions for sample C for various gate voltages measured at 270 mK. As the mean switching current increases with an increasing gate voltage, the width of the distribution also increases. (b) The corresponding retrapping distributions for sample C for various gate voltages. (c) The behavior of the standard deviation of the switching currents as a function of mean switching current at 320 mK. The distributions were measured using a bias current with a frequency of 8 Hz. This data was measured by U. Coskun at the University of Illinois in Urbana-Champaign.

The behavior of the switching current distributions has a temperature dependence such that an increase in temperature has a similar effect as an increase in the gate voltage except that the mean value of the switching current decreases instead of increases. Thus, as the temperature is increased the width of the switching curves increases, while the width of the retrapping current distributions increases slightly and mean of the retrapping current also changes only slightly indicating that the quality factor of the system does not change much in this temperature range. The decrease in the mean value of the switching current can naturally be understood by observing how the switching current behaves as a function of temperature as plotted for a different sample in Fig. 7.8. At higher temperatures, there is more thermal energy which results

in a greater amplitude of thermal fluctuations. For junctions that are in the single phase slip regime (which is a regime such that for each phase slip event, when the phase particle escapes from a potential minimum it continuously runs down the washboard without damping causing it to be retrapped) as the thermal fluctuations increase, the relative probability of switching to the normal state becomes higher at lower currents. It is therefore expected and predicted by Josephson junction theory [24] that in the single phase slip thermally activated regime, the width of the switching current distributions should increase as the temperature increases. We will investigate this more by analyzing the standard deviation of the switching currents and comparing the results to well known theory for the thermally activated and MQT regime in Josephson junctions.

A fit to the retrapping distribution is plotted in Fig. 7.12(b) which is compared to the data measured with an applied gate voltage of 50 V and at a temperature of 500 mK. The fit can be obtained by the theory of Ben-Jacob *et al.* [25], where the retrapping rate can be expressed as:

$$\Gamma_{RT} = (I - I_{ro})\sqrt{\frac{1}{\pi C k_B T}} \exp\left(-\frac{(I - I_{ro})R^2 C}{k_B T}\right), \qquad (7.4)$$

where I_{ro} is the fluctuation free retrapping current, C is the capacitance of the junction, R is the resistance of the junction, and T is the temperature. This rate can be converted into a retrapping distribution by using the Fulton and Dunkelberger [26] expression:

$$P(I) = \frac{\Gamma(I)}{\dot{I}}\left(1 - \int_0^I P(u)du\right). \qquad (7.5)$$

A comparison of the data and the theory using C = 15 pF, T = 500 mK and the fitting parameters I_{ro} = 36.22 μA and R = 1.8 Ω, results in a good fit suggesting that our graphene junctions behave

like Josephson junctions and experience retrapping in the thermal regime. This also supports our earlier claim that the retrapping current is not enhanced by a significant amount from the fluctuation free value. It has been theoretically predicted [27] that MQT can be observed through an analysis of the statistics of the retrapping current. Here, no such analysis has been done as the point spacing of current in the *V-I* curve was comparable to the standard deviation of the retrapping current preventing an accurate measurement of the standard deviation of the retrapping current.

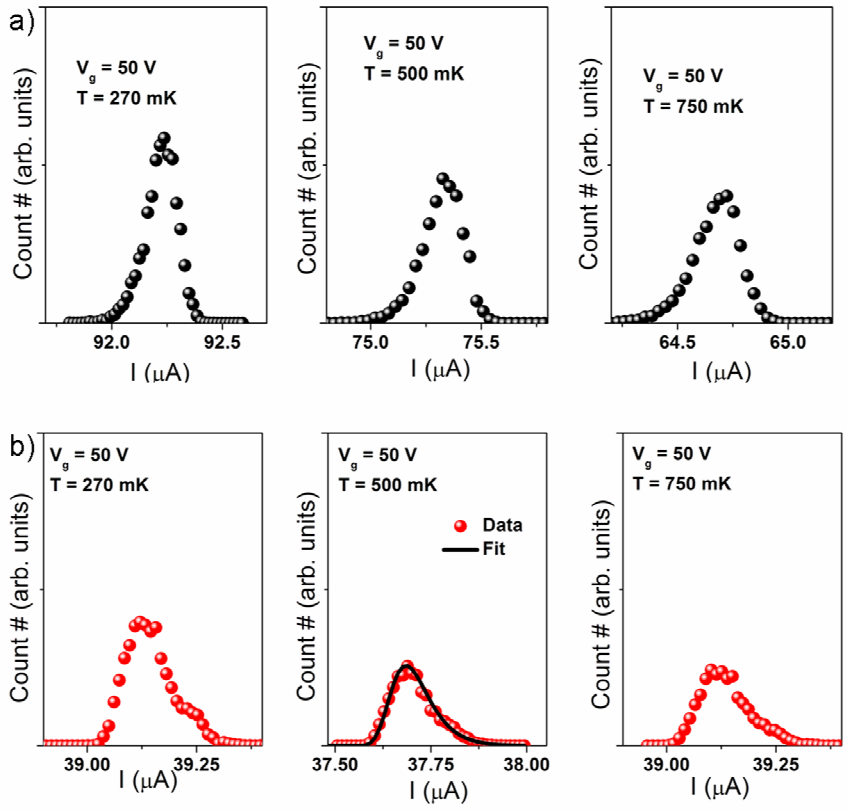

Fig. 7.12: (a) Switching distributions for sample C for various temperatures measured at an applied gate voltage of 50 V. As the mean switching current decreases with an increasing temperature, the width of the distribution increases. (b) The corresponding retrapping distributions for sample C for various temperatures at an applied gate voltage of 50 V. A fit to the retrapping distribution is shown at a temperature of 500 mK. This data was measured by U. Coskun at the University of Illinois in Urbana-Champaign.

The standard deviation of switching current was measured for various samples as a function of temperature and for various applied gate voltages. For all samples, two regimes were observed (i) a regime at lower temperatures where the standard deviation increased with an increase in temperature and (ii) a regime at higher temperatures where the standard deviation decreased with an increase in temperature. We identify the first regime as being related to thermal activation over the barrier [28, 29, 30]. In sample B, which was a junction with a separation of ~ 250 nm and a shorter length compared to the other junctions measured of ~ 10 μm, the log of the standard deviation shows a linear dependence on the log of the temperature (see Fig. 7.13 (a)). This demonstrates that the standard deviation has a power law dependence on the temperature, where the power is equal to the slop from the log-log plot. It has been theorized that the standard deviation should follow a power law dependence on the temperature as $\sim T^{2/3}$ [31] or for junctions where the critical current has not saturated as a function of temperature as $\sim T^{2/3} I_c^{1/3}$ [24]. In sample B, the standard deviation followed a power law dependence on the temperature as $\sim T^{0.6}$, which is close to what is expected from the Josephson junction theory in the thermal activation region. For longer junctions with a length of ~ 300 μm, the same features are observed in the standard deviation vs. temperature curves (see Fig. 7.13(b)) as in the short sample with one noticeable difference: the power law dependence on the temperature is not ~ 2/3, but is closer to the anomalous value of ~ 1/3, which has been measured on multiple long-junction samples. This deviation from the expected value of 2/3 can be due to nonuniformity of the gap distance or the effective gate voltage along the length of the junction. It may also be related to the temperature dependence of the critical current, which has not saturated at low temperatures (see Fig. 7.8) and may change the power in the power law dependence on temperature as the standard deviation is related to $T^{2/3} I_c^{1/3}$ [24]. The deviation

from the expected power of 2/3 in the longer junctions cannot be accounted for by changing the sweep speed as Fig. 7.13(c) shows.

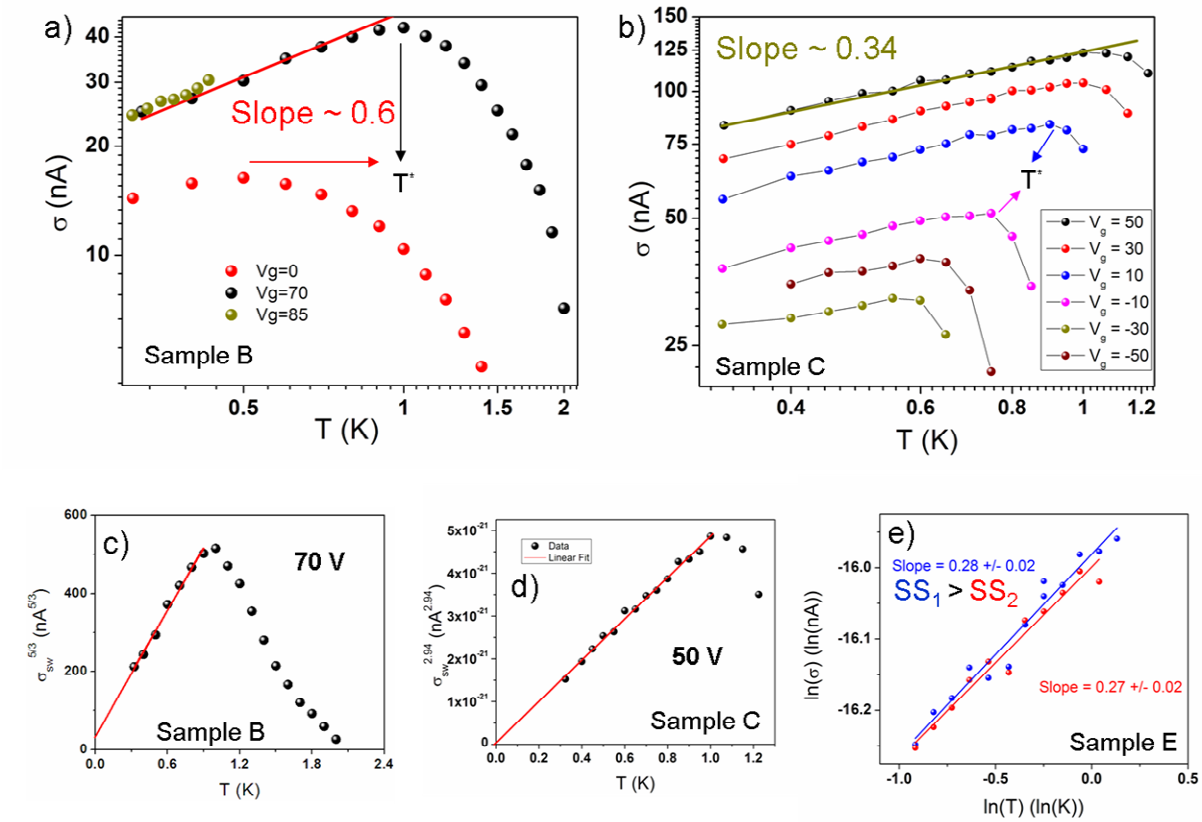

Fig. 7.13: (a) The standard deviation as a function of temperature plotted in a log-log scale for a short length junction. In the region of thermal activation, a simple power law dependence is observed as the standard deviation is proportional to ~ $T^{0.6}$. (b). The standard deviation as a function of temperature plotted in a log-log scale for a long length junction. In the region of thermal activation, a simple power law dependence is observed as the standard deviation is proportional to ~ $T^{0.34}$. The parameter T^* is the crossover from the thermally activated region to the multiple retrapping regime. (c) The standard deviation of the switching current raised to the 5/3 power measured with an applied gate voltage of 70 V plotted in a linear-linear scale and extrapolated to zero temperature. (d) The standard deviation of the switching current raised to the 2.94 power measured with an applied gate voltage of 50 V plotted in a linear-linear scale and extrapolated to zero temperature. (e) A ln-ln plot of the standard deviation as a function of temperature for a long junction with two sweep speeds (sinusoidal current biases with a frequency of 3.4 Hz and current amplitude of $1.3I_{sw}$ (blue) and $1.15I_{sw}$ (red)) that were held fixed as a function of temperature. The slope is independent of the sweep speed to within the noise level. Here, SS is the sweep speed. The data in (b) and (e) was measured by U. Coskun at the University of Illinois in Urbana-Champaign.

In sample D, which is another long junction, a different behavior was noticed in the standard deviation vs. temperature behavior. With all the other samples measured and thus far discussed, the gate voltage tuned the critical current but had no effect on the standard deviation behavior as a function of temperature, i.e. the slope of ~1/3 or ~ 2/3 was constant as a function of gate voltage in the log-log plots of σ vs. T. However, in sample D, the slope (in the log-log scale) changed continuously from ~ 0.15 to ~1.7 as the gate voltage was incremented from -26.5 to 62.5 V (see Fig. 7.14). The mechanism for this is unclear as is the difference between this junction and the other long junctions that showed a constant behavior. It was observed that the shape of the slope of the log-log plot as a function of gate voltage looked visually similar to the shape of switching current as a function of gate voltage plot as can be seen in Fig. 7.14(b) and its inset. This suggests that the slope should be proportional to the critical current. The reason for this remains unclear.

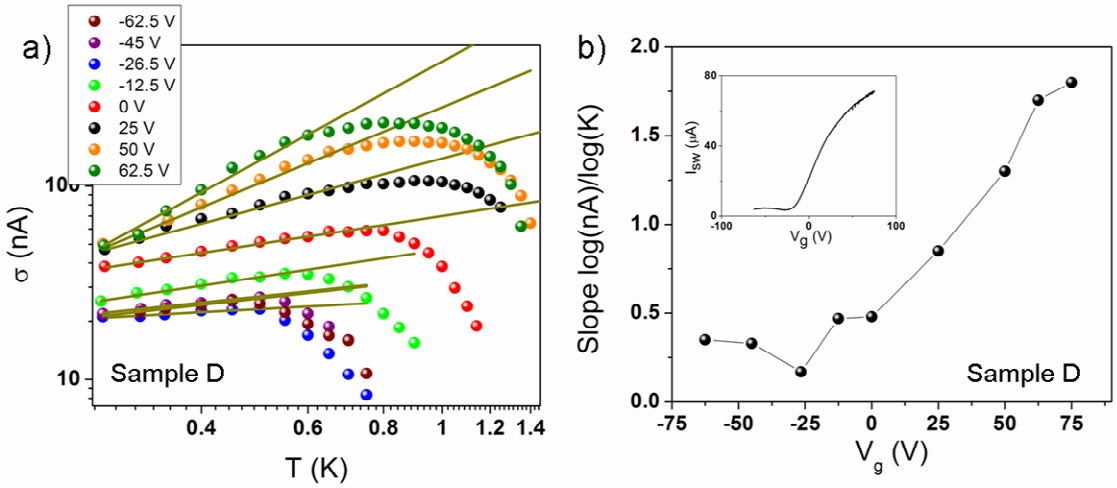

Fig. 7.14: (a) The standard deviation as a function of temperature plotted in a log-log scale for a long length junction for various gate voltages. In the region of thermal activation, a simple power law dependence is observed as the standard deviation is proportional to ~ T^{α}, where α is the slope and is a function of the applied gate voltage. (b) The dependence on the slope α as a function of gate voltage. Inset: The switching current as a function of gate voltage for this sample. The shape of this curve is similar to the shape of the curve shown in (b) suggesting that the slope is proportional to the value of the critical current.

In all the samples we have measured, there is a gate dependent crossover temperature T^* between the region where the standard deviation increases and decreases with an increasing temperature. The first region has already been discussed as the region where the phase particle is thermally activated over the energy barrier and freely slides down the washboard potential. The second region can be identified as the multiple retrapping region [28, 29, 30]. In this region, once the phase particle is excited over the energy barrier, damping can cause the phase particle to be retrapped in one of the subsequent potential wells. This usually occurs at higher temperature where the switching current is lower and there is less energy gained. The multiple retrapping regime is therefore likely to be observed when the quality factor is low, or equivalently, when the retrapping and critical currents are close. The result is that the phase particle experiences a higher damping and the standard deviation begins to decrease with an increasing temperature. An interesting feature of the samples that we have studied is the crossover temperature T^* dependence on the gate voltage (and switching current) which can be seen in Fig. 7.15. This is not surprising since other groups have predicted and measured a critical current dependent crossover temperature [29, 30].

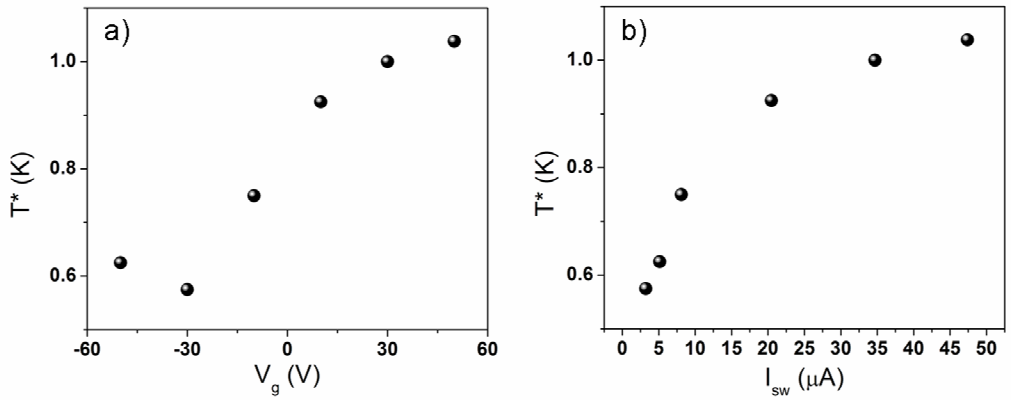

Fig. 7.15: (a) The crossover temperature dependence on the applied gate voltage. (b) The crossover temperature dependence on the switching current measured at the given crossover temperature.

From the experiments presented above, it is well demonstrated that the mechanism by which our graphene proximity junctions enter the normal state is by thermal activation. In order to see evidence of MQT, a temperature independent standard deviation should be observed. Down to temperatures of ~ 270 mK, we still measure a temperature dependent standard deviation which has a power law dependence on the temperature. Additionally, in Figs. 7.13(c) and (d), the standard deviation of the switching current raised to a power (to make it linear in the low temperature "single thermal escape" regime) is plotted for two different samples in a linear-linear scale and extrapolated to zero temperature. In each case, the extrapolated curve roughly hits zero standard deviation at zero temperature indicating that the switching mechanism is dominated by thermal escape. In order for the effects of MQT to be observable, Leggett [32, 33, 34] first suggested the following two constrains must be satisfied (i) the thermal energy must be sufficiently low to avoid the incoherent mixing of eigenstates and (ii) that the macroscopic degree of freedom must be sufficiently decoupled from the other degrees of freedom for the quantum states to have a lifetime long enough to be on the time scale of the system. For a Josephson junction this means that (i) $\hbar\omega_0 >> k_B T$ to prevent incoherent mixing between quantum states, (ii) the circuit dimensions should be small compared to the wavelength, and (iii) $R >> Z_0$ to ensure that the level width is small than the level separation, where $\omega_0 = (LC)^{-1/2}$ and $Z_0 = \sqrt{L/C}$, and R is the resistance governing the coupling to the environment, L is the inductance, and C is the capacitance. With the junction parameters discussed in this chapter, the two constrains above result in an inequality for the inductance (which is unknown for our samples) that is not possible to realize. Thus, it is not surprising that we do not observe MQT. The damping of MQT [35] is another mechanism that can result in the presence of MQT in graphene junctions going undetected. The value of T_{QPS}, the temperature at

which the crossover from the TA to the MQT regime, is expected to be a function of damping parameterized by the quality factor [30], and follows the following relationship:

$$T_{QPS} = \frac{\hbar\omega_p}{2\pi k_B}\left[\sqrt{1+\frac{1}{4Q^2}}-\frac{1}{2Q}\right]. \qquad (7.6)$$

The plasma frequency can be estimated from $\omega_p = \sqrt{(2eI_c/\hbar C)}$, where the capacitance can be taken from Section 7.3 and the critical current from the current section. The quality factor is also known from Section 7.3. Thus, dissipation slightly reduces the value of T_{QPS} (here by ~ 15%), which is estimated for our graphene proximity junctions to be ~ 100 mK, a temperature we are unable to reach in our experiment.

[1] R. Holm and W.Meissner, Z. Physik. 86, 787 (1933)
[2] K. S. Novoselov, A. K. Geim, S. V. Morozov, D. Jiang, Y. Zhang, S. V. Dubonos, I. V. Grigorieva, and A. A. Firsov, Sci. **306**, 66 (2004).
[3] K. S. Novoselov, A. K. Geim, S. V. Morozov, D. Jiang, M. I. Katsnelson, I. V. Grigorieva, S. V. Dubonos, and A. A. Firsov, Nat. (London) **438**, 197 (2005).
[4] M. Wilson, Phys. Today **59**, 21 (2006).
[5] A. F. Andreev, Sov. Phys. JETP **19**, 1228 (1964).
[6] C. W. J. Beenakker, Phys. Rev. Lett. **97**, 067007 (2006).
[7] Y. B. Zhang, Y. W. Tan, H. L. Stormer, and P. Kim, Nat. **438**, 201 (2005).
[8] V. P. Gusynin, and S. G. Sharapov, Phys. Rev. Lett. **95**, 146801 (2005).
[9] N. M. R. Peres, F. Guinea, and A. H. Castro Neto, Phys. Rev. B **73**, 125411 (2006).
[10] S. V. Morozov, K. S. Novoselov, M. I. Katsnelson, F. Schedin, L. A. Ponomarenko, D. Jiang, and A. K. Geim, Phys. Rev. Lett. **97**, 016801 (2006).
[11] M. Titov and C. W. J. Beenakker, Phys. Rev. B **74**, 041401(R) (2006).
[12] H. B. Heersche, P. Jarillo-Herrero, J. B. Oostinga, L. M. K. Vandersypen, and A. F. Morpurgo, Nat. (London) **446**, 56 (2007).
[13] J. M. Kivioja, T. E. Nieminen, J. Claudon, O. Buisson, F. W. J. Hekking, and J. P. Pekola, Phys. Rev. Lett. **94**, 247002 (2005).
[14] J. M. Martinis, M. H. Devoret, and J. Clarke, Phys. Rev. B **35**, 4682 (1987).
[15] J. Kurkijarvi, Phys. Rev. B **6**, 832 (1972).
[16] D. S. L. Abergel, A. Russell, and V. I. Fal'ko, Appl. Phys. Lett. **91**, 063125 (2007).
[17] D. Graf, F. Molitor, and K. Ensslin, Nano. Lett. **7**, 238 (2007).
[18] W. A. Little, Phys. Rev. **156**, 396 (1967).
[19] Michael Tinkham, *Introduction to superconductivity* (Dover, 2004).
[20] Y. Song, J. Appl. Phys. **47**, 2651 (1976).
[21] I. O. Kulik and A. N. Omel'yanchuk, JETP Lett. **21**, 96 (1975).
[22] I. O. Kulik and A. N. Omel'yanchuk, Sov. J. Low Temp. Phys. **3**, 459 (1978).
[23] C. M. Ojeda-Aristizábal, M. Ferrier, S. Guéron, and H. Bouchiat, arXiv:0903.2963v1 (2009).
[24] J. Kurkijarvi, Phys. Rev. B **6**, 832 (1972).
[25] E. Ben-Jacob, D. J. Bergman, B. J. Matkowsky, and Z. Schuss, Phys. Rev. A **26,** 2805 (1982).

[26] T. A. Fulton and L. N. Dunkleberger, Phys. Rev. B **9** 4760 (1974).
[27] Y. C. Chen, M. P. A. Fisher, and A. J. Leggett, J. Appl. Phys. **64**, 3119 (1988).
[28] J. Männik, S. Li, W. Qiu, W. Chen, V. Patel, S. Han, and J. E. Lukens, Phys. Rev. B **71,** 220509(R) (2005).
[29] V. M. Krasnov, T. Bauch, S. Intiso, E. Hurfeld, T. Akazaki, H. Takayanagi, and P. Delsing, Phys. Rev. Lett. **95,** 157002 (2005).
[30] V. M. Krasnov, T. Golod, T. Bauch, and P. Delsing, Phys. Rev. B **76,** 224517 (2007).
[31] T. Aref, PhD thesis, *University of Illinois at Urbana-Champaign* (2010).
[32] A. J. Leggett, Prog. Theo. Phys. (Suppl.) **69**, 80 (1980).
[33] A. J. Leggett, Contemp. Phys. **25**, 583 (1984).
[34] A. J. Leggett, J. Phys. (Paris) Colloq. **39**, C6-1264 (1980).
[35] A. O. Caldeira and A. J. Leggett, Phys. Rev. Lett. **46,** 211 (1981).

Vita

Matthew Brenner was born on September 19th, 1980 in Arlington Heights, IL. He graduated from the University of Illinois at Urbana-Champaign with a B. S. in General and Electrical engineering in 2003. He was always interested in the fundamental aspects of the science behind the engineering he studied and decided to pursue graduate studies in physics at the University of Illinois beginning in 2003. He earned his masters degree in physics in 2004 and was attracted to the study of nanoscale superconductivity and eventually joined the research group of Alexey Bezryadin in 2005. In the Bezryadin research group, he learned how to fabricate superconducting nanowires using the molecular templating method as he began to study the superconductor to insulator transition in nanowires where it was found that the normal state resistance of the nanowire determined the nanowire phase at low temperatures. This project motivated the study of resistively shunting nanowires, which he began to investigate. He found that the nanowire environment could affect the switching and retrapping behavior in nanowires and that the nature of the resistive state can be changed with the inclusion of a shunt resistor. He gradually moved into the field of microwave measurements with nanowires and incorporated a nanowire inside a superconducting resonator. Here he discovered a new pulsing state involving a large nonlinearity that could potentially be used in many applications. He was also able to use double nanowire embedded resonators to detect phase slip events. After completion of his Ph.D., Matthew will look for a job in industry and pursue a masters degree in theology.